LOCATION SPECIFIC PROPERTIES IN AN AEROSPACE ALLOY

by

Gavin Yearwood

A thesis submitted to the
University of Birmingham
for the degree of
DOCTOR OF PHILOSOPHY

School of Metallurgy & Materials
University of Birmingham
April 2019

UNIVERSITY OF
BIRMINGHAM

University of Birmingham Research Archive

e-theses repository

This unpublished thesis/dissertation is copyright of the author and/or third parties. The intellectual property rights of the author or third parties in respect of this work are as defined by The Copyright Designs and Patents Act 1988 or as modified by any successor legislation.

Any use made of information contained in this thesis/dissertation must be in accordance with that legislation and must be properly acknowledged. Further distribution or reproduction in any format is prohibited without the permission of the copyright holder.

Abstract

In this work a physics based creep model is presented to predict the behaviour in the Nickel based superalloy RR1000. The model presented takes into account the strengthening mechanisms active during high temperature deformation, associated with interactions between dislocations and γ' precipitates. In the creep conditions examined the γ' precipitates act as pinning points to dislocations gliding in the matrix where the primary method for overcoming these obstacles is through vacancy assisted climb. This creep constitutive model is also coupled with a mean field approximation to capture how the microstructure is evolving during the creep process. The macroscopic creep predictions are obtained through a scale invariance argument where component-level creep rates are assumed to have the same functional form as the shear rates active slip system. Crystal plasticity simulations have been carried out to assess the validity of this assumption.

To validate the model, experiments were done comprising creep and tensile tests to better understand the mechanisms which are occurring during deformation and the effect of ageing and pre-straining on this behaviour. Also both SEM and TEM were carried out to better capture the γ' dispersion and obtain mean sizes for both the tertiary and secondary γ'. Model predictions of lifetimes and minimum creep rates over a range of temperature and stresses are shown to be in good agreement with the available experimental data on RR1000. Simulations of the creep response with different starting γ' dispersions, obtained from a disc, have been carried out. The dispersions investigated had similar volume fractions and particle size,

however they differed in size distribution. The mean field model predicts faster coarsening/dissolution rates for a broad distribution when compared to a narrow one. This results in a size distributions giving different creep rates and allowing the model to capture experimental creep scatter

Acknowledgements

I could not have completed this work all alone and I have to give thanks to all the various groups and people for their help in completing my work. I would like to thank my supervisor Dr Hector Basoalto and co supervisor Prof Jeff Brooks for the opportunity, help and support. My industrial sponsors Rolls-Royce the funding and materials needed to complete this project especially Dr Christos Argryakis and Dr Ben Saunders. General thanks to everyone in the PRISM2 office for all their help particularly with discussion on dislocations and crystal plasticity and particularly: Dr Magnus Anderson for all the help with the Mean Field work, Dr Yu Lu and the EM center facilities for help with the microscopy work and Dr Richard Turner for help with bluebear. Finally thanks to my friends and family for all their patience and support.

Contents

1 Introduction 11

2 Literature review 16

2.1 Turbine discs and Nickel superalloys 16

2.2 Creep phenomena 19

2.3 Creep mechanisms 20

2.3.1 Ashby Maps 21

2.3.2 Dislocation climb 22

2.4 Creep Physics 23

2.4.1 Creep theory development 23

2.5 Empirical creep models 27

2.5.1 Power Law Creep 27

2.5.2 Larson-Miller parameter & Robinson's life fraction law . . . 28

2.5.3 Empirical damage mechanics 30

2.5.4 Theta projection 31

2.5.5 Omega parameter 34

2.6 Physics based model 37

2.6.1 Single crystal superalloy approach 38

2.6.2 Constitutive developments 45

2.7 Microstructure evolution 49

2.8 Dislocation Background 52

2.8.1 Dislocation interactions 54

2.8.2 Forces (PK-Force and Peierls Force) 59

3 Theoretical framework 61

3.1 Kinematics of deformation 61

3.1.1 Objectivity 64

3.2 Micro- to Macroscale viscoplastic modelling 67

3.2.1 Taylor Factor 70

3.2.2 J2 theory and Scale invariance 73

3.3 Microstructure explicit shear rate model 74

3.4 Stress Partitioning 78

3.4.1 Back Stress 78

3.4.2 Misfit 81

3.5 Dislocation Density 82

3.6 Spacing 85

3.6.1 Lattice Square Spacing 85

3.6.2 Freidel spacing 87

3.6.3 Spacing in a multimodal system 87

4 Experimental Procedure 89

4.1 Theoretical basis for experimental programme 89

4.2 Method 92

4.2.1 Creep tests 92

4.2.2 Tensile tests 94

4.2.3 Pre-strained Creep tests 97

4.2.4 Microstructure analysis 98

5 Experimental Results 100

5.1 Creep experimental results 100

5.2 Tensile Flow Stress 110

5.3 Pre-strained Creep tests 118

5.4 Microstructure Characterisation 122

6 Numerical implementation and results 142

6.1 Identification of model parameters 142

6.2 Mean field predictions of the γ' evolution 146

6.3 Experimentally derived distributions 149

6.4 Lifetime and MCR 155

6.5 Prediction of strain-time trajectories 158

6.6 Simulations of the flow stress 176

7 Discussion on experiments 184

7.1 Mechanical characterisation 184

7.2 Microstructure characterisation 187

8 Discussion on numerical simulations 189

8.1 Constitutive modelling 189

8.1.1 Stress Partitioning 189

8.1.2 Mobile dislocation density 192

8.2 Towards location specific property predictions 193

8.3 Microscale to macroscale transition: Scale Invariance 196

9 Conclusion and Future work 198

9.1 Conclusion 198

9.2 Future Work 200

9.2.1 Crystal Plasticity 200

9.2.2 Primary Creep 201

9.2.3 Cutting γ' 201

10 Bibliography 207

List of Figures

1.1 Microstructure variation along a RR1000 turbine disc [2] 12

1.2 Length scales and the associated areas of focus 15

2.1 Superalloy alloying elements [11] 17

2.2 Key crystal structures found in RR1000 where (a) is the FCC γ phase and (b) is the $L1_2$ γ' phase. 18

2.3 Schematic creep curves for constant tensile load [12] 19

2.4 Ashby map for the Ni-superalloy material MAR-M200 21

2.5 Influence of particle size, d on the creep rate at a constant stress according to different physics interpretations [15] 26

2.6 Theta projection predictions of minimum creep rate and rupture life of IN 100 [5] 33

2.7 Comparison of different creep life predictions against measured data [35] 35

2.8 Creep predictions of different Omega formulations at different conditions (a) low temperature power-law, (b) low temperature hyperbolic sine law, (c) high temperature power-law and (d) high temperature hyperbolic sine law. [35] 36

2.9 Similarity of creep curves from different materials [36] 37

2.10 Different damage mechanisms and categories that could potentially be used to predict creep behaviour in Continuum Damage Mechanics [8] 38

2.11 Dislocations gliding to particle getting pinned and climbing until they can climb again. 39
2.12 Effect of atomic percentage Al+Ti+Nb+Ta on solvus temperature experimental results compared against predictions from equation (2.56) 45
2.13 Creep predictions at various stresses showing the effect of the inclusion of misfit on material creep response [43] 48
2.14 Burgers circuit image before a closed loop and after the introduction of a dislocation [54] 53
2.15 Images of 2 dislocations with the same sign repelling 54
2.16 Images of 2 dislocations with the opposite sign attracting to each other and when they reach each other they annihilate each other . . 54
2.17 Images of 2 dislocations at 45° to each other climbing through the emission and absorption of vacancies 55
2.18 Images of a Frank-Read source in silicon decorated with copper by Dash [58] 56
2.19 Slip lines formed in aluminium from work by Jaul [59] 57

3.1 Diagram of neighbourhood $\mathbf{X}$ in Ω_0 being deformed and at time $t + \delta t$ body becomes Ω_1 and points become $\mathbf{X}_{(t+\delta t)}$ 62
3.2 Schematic of Lee's decomposition showing breaking down the transition of deformation into plastic and elastic components 68
3.3 Image showing all the combined constitutive effects in the proposed creep formulation 75
3.4 Distribution of particle spheres on a plane 76
3.5 Figure of loading effect on γ and γ' 78

4.1 Creep tests done in this project and given in the PANACEA project [1] 92
4.2 Creep test piece geometry. 93
4.3 Uniaxial tensile test piece geometry. 95

4.4 Temperature measurements to ensue sample reaches correct cooling rate 96
4.5 Flow stress test matrix for this study. Also indicated are exisiting Rolls-Royce plc. data. 97

5.1 All experimental lifetime data against amount of elongation 100
5.2 Creep experimental results 700°C 700 MPa 101
5.3 Creep experimental results 700°C 900 MPa 102
5.4 Creep experimental results 700°C 1050 MPa 103
5.5 Creep experimental results 750°C 460 MPa for both SHT and MHT 104
5.6 Creep experimental results 775°C 200 MPa 105
5.7 Creep experimental results 775°C 600 MPa 106
5.8 Creep experimental results 800°C 300 MPa 107
5.9 Creep experimental results 800°C 500 MPa 108
5.10 Creep experimental results 600°C 500 MPa for both SHT and MHT 109
5.11 Tensile 650°C, $\dot{\varepsilon} = 0.01s^{-1}$ 110
5.12 Tensile 650°C, $\dot{\varepsilon} = 1s^{-1}$ 111
5.13 Tensile 700°C, $\dot{\varepsilon} = 10^{-4}s^{-1}$ both SHT and MHT 112
5.14 Tensile 700°C, $\dot{\varepsilon} = 10^{-3}s^{-1}$ both SHT and MHT 112
5.15 Tensile 700°C, $\dot{\varepsilon} = 0.01s^{-1}$ 113
5.16 Tensile 700°C, $\dot{\varepsilon} = 1s^{-1}$ both SHT and MHT 113
5.17 Tensile 750°C, $\dot{\varepsilon} = 10^{-4}s^{-1}$ both SHT and MHT 114
5.18 Tensile 750°C, $\dot{\varepsilon} = 0.01s^{-1}$ 115
5.19 Tensile 750°C, $\dot{\varepsilon} = 1s^{-1}$ both SHT and MHT 115
5.20 Tensile 800°C, $\dot{\varepsilon} = 10^{-4}s^{-1}$ both SHT and MHT 116
5.21 Tensile 800°C, $\dot{\varepsilon} = 10^{-3}s^{-1}$ both SHT and MHT 117
5.22 Flow stress experimental curves for 700°C,750°C and 800°C all with a strain rate of 10^{-4} s^{-1} 118

5.23 1 % pre-strain at both room temperature and 800°C and creep tested at 750°C 231 MPa 119
5.24 1 % pre-strain at both room temperature and 800°C and creep tested at 750°C 460 MPa 120
5.25 All the experimental data including old and new, and the effect of ageing temperature at the condition 750 $^{\circ}C$ 460 MPa 121
5.26 TEM image of SHT from pancake forging at 74000× (1) 122
5.27 TEM image of MHT from pancake forging at 12000× (2) 123
5.28 TEM image of thread area for 600°C 500 MPa at 22500x SHT . . . 124
5.29 TEM image of test area for 600°C 500 MPa at 36000x SHT (2) . . 124
5.30 TEM image of thread area for 600°C 500 MPa at 36000x MHT . . . 125
5.31 TEM image of thread area for 600°C 500 MPa at 22500x MHT . . . 125
5.32 TEM image of test area for 600°C 500 MPa at 22500x MHT 126
5.33 TEM image of thread area for 775°C 200 MPa at 28500x 127
5.34 TEM image of test area for 775°C 200 MPa at 22500x 127
5.35 TEM image of thread area for 750°C 460 MPa RT pre-strain at 36000x 128
5.36 TEM image of test area for 750°C 460 MPa RT pre-strain at 28500x 129
5.37 TEM image of thread area for 750°C 460 MPa 800°C pre-strain at 14000x 129
5.38 TEM image of test area for 750°C 460 MPa 800°C pre-strain at 22500x 130
5.39 TEM image of thread area for 800°C $\dot{\varepsilon} = 10^{-3}$ at 17500x 131
5.40 TEM image of thread area for 800°C $\dot{\varepsilon} = 10^{-3}$ at 36000x (1) 131
5.41 TEM image of thread area for 800°C $\dot{\varepsilon} = 10^{-3}$ at 36000x (2) 132
5.42 TEM image of test area for 800°C $\dot{\varepsilon} = 10^{-3}$ at 36000x (1) 133
5.43 TEM image of test area for 800°C $\dot{\varepsilon} = 10^{-3}$ at 36000x (2) 133
5.44 TEM image of test area for 800°C $\dot{\varepsilon} = 10^{-3}$ at 28500x 134

5.45 Size distribution of secondary γ' from the test ring: (a) SHT sample, (b) MHT sample; and (c) number density distribution 136
5.46 Size distribution of tertiary γ' from the test ring: (a) SHT sample (b) MHT sample; and (c) number density distribution 137
5.47 Size distribution of secondary γ' from the pancake forging: (a) SHT sample; (b) MHT sample; and (c) number density distribution . . . 139
5.48 Size distribution of tertiary γ' from the pancake forging: (a) SHT sample; (b) MHT sample; and (c) number density distribution . . . 140

6.1 Data capturing RR1000 Young's modulus, Poisson's ratio and Misfit strain and how these vary with temperature 145
6.2 Tertiary γ' size distribution, showing mean field predictions and experimental data from the PANACEA programme [[1]]. 147
6.3 Mean Field predictions of γ' evolution predictions validated against PANACEA experimental data in [1] 148
6.4 Distribution for secondary γ' measurements from sample 1 figure 5.45 150
6.5 Distribution for tertiary γ' measurements from sample 1 figure 5.46 151
6.6 Distribution for secondary γ' measurements from sample 2 figure 5.45. 151
6.7 Distribution for tertiary γ' measurements from sample 2 figure 5.46 152
6.8 Distribution for secondary γ' measurements from sample 3 figure 5.47 152
6.9 Distribution for tertiary γ' measurements from sample 3 figure 5.48 153
6.10 Distribution for secondary γ' measurements from sample 4 figure 5.47 153
6.11 Distribution for tertiary γ' measurements from sample 4 figure 5.48 154
6.12 Lifetime model predictions against experimental data, also showing the effect of no tertiary γ' and no coarsening on lifetime predictions 156
6.13 Minimum creep rate predictions from the constitutive equation description 157
6.14 Creep prediction at 650°C 700 MPa 159
6.15 Creep prediction at 650°C 900 MPa 159

6.16 Creep prediction at 675°C 590 MPa 160
6.17 Creep prediction at 675°C 930 MPa 160
6.18 Creep prediction at 700°C 500 MPa 161
6.19 Creep prediction at 725°C 263 MPa 161
6.20 Creep prediction at 725°C 655 MPa 162
6.21 Creep prediction at 725°C 831 MPa 162
6.22 Creep prediction at 750°C 200 MPa 163
6.23 Creep prediction at 750°C 231 MPa 163
6.24 Creep prediction at 750°C 900 MPa 164
6.25 Mean Field prediction of secondary γ' at 700°C showing the different distribution shapes: (1) = Base, (2) = Narrow and (3) = Broad, all with the same mean size and volume fraction 165
6.26 Mean Field prediction of tertiary γ' at 700°C showing the different distribution shapes: (1) = Base, (2) = Narrow and (3) = Broad, all with the same mean size and volume fraction 166
6.27 Creep prediction at 700°C 500 MPa from different distribution sizes (1) = Base, (2) = Narrow and (3) = Broad, all with the same mean size and volume fraction 167
6.28 Prediction of creep behaviour at $600°C$ 500 MPa with different starting particle size distributions 168
6.29 Prediction of creep behaviour at $700°C$ 700 MPa with different starting particle size distributions 169
6.30 Prediction of creep behaviour at $700°C$ 900 MPa with different starting particle size distributions 170
6.31 Prediction of creep behaviour at $700°C$ 1050 MPa with different starting particle size distributions 171
6.32 Prediction of creep behaviour at $750°C$ 460 MPa with different starting particle size distributions 172

6.33 Prediction of creep behaviour at 775°C 200 MPa with different starting particle size distributions 173
6.34 Prediction of creep behaviour at 775°C 600 MPa with different starting particle size distributions 174
6.35 Prediction of creep behaviour at 800°C 300 MPa with different starting particle size distributions 175
6.36 Prediction of creep behaviour at 800°C 500 MPa with different starting particle size distributions 176
6.37 Boundary conditions used in crystal plasticity model 177
6.38 Crystal plasticity simulations showing stress using creep constitutive equations: (a) [001] orientated single crystal, (b) 100 grains RVE and (c) 1000 grains RVE. All simulations correspond to an applied strain rate of $10^{-3}s^{-1}$ at 700°C. 178
6.39 Comparing grain size effects to tensile load at 700°C and $\dot{\varepsilon} = 10^{-3}$. 179
6.40 Slip activity in a random grain (1) 180
6.41 Slip activity in a random grain (2) 180
6.42 Slip activity in a random grain (3) 181
6.43 Slip activity in a random grain (4) 181
6.44 Slip activity in a random grain (5) 182
6.45 Average slip activity in polycrystalline CP simulations 183

8.1 Plot showing the effect of temperature and stress on stress partition parameters σ_k and σ_{mis} 191
8.2 Loading of test piece for creep at 750°C/460MPa. 192

9.1 Sphere being cut into planes (a) shows the sphere (b) the appearance of planes on the 3d structure. (c) and (d) show depending where the plane is that the size of the visible particle can change . . 202
9.2 Logarithmic CDF of the sizes gathered through the 2D planes for a 3D spherical particle 203

9.3 Situation for a bimodal distribution 204
9.4 When there is a size distribution of particles both unimodal and bimodal 205

List of Tables

2.1 At % of RR1000 nominal composition [1] 16

2.2 FCC slip planes and slip directions 58

4.1 Creep test matrix x = SHT and o = MHT 94

4.2 Tensile test plan x = SHT and o = MHT 96

4.3 Test for sample which would first undergo a 1% tensile test pre-strain then a creep test 98

5.1 Volume fraction of tertiary γ' and area fraction for secondary γ' for each of the different samples 141

6.1 Mean field parameters 143

6.2 List of creep model parameters 144

6.3 Mean values from each microstructure distribution 155

Nomenclature

List of Symbols

The next list describes several symbols that will be later used within the body of the document

$\dot{\sigma}_0$	Stress Constant
$\dot{\varepsilon}_0$	Strain Constant
$\dot{\varepsilon}_i$	Curren Creep Strain
$\overset{\nabla}{\boldsymbol{\sigma}}$	Jaumann Stress Rate
α	Fractional Constant
α	Material Constant
α_w	Scale Parameter
$\bar{M}$	Taylor Factor
$\bar{v}_c$	Mean Climb Velocity
$\bar{v}_g$	Mean Glide Velocity
β	Material Constant
β_w	Shape Parameter
$\boldsymbol{\beta}$	Displacement Gradient Tensor
$\boldsymbol{\varepsilon}$	Strain Tensor

$\dot{\boldsymbol{\sigma}}$	Cauchy Stress Rate
$\dot{\gamma}$	Shear Strain
η	Geometry Factor
γ	Stacking Fault Energy
Γ^{+}	Frequency of Dislocation Release Events
γ_w	Location Parameter
γ_{APB}	Anti-Phase Boundary Energy
$\grave{A}_i$	Material Constant
$\grave{A_{\Omega_p}}$	Material Constant
$\grave{C}$	Material Constant
$\grave{K}$	Function of Shear Modulus of Matrix and Secondary Phase Volume Fraction.
$\grave{n}_i$	Material Constant
$\grave{n_{\Omega_p}}$	Material Constant
λ_2	Spacing Between Secondary γ' Particles
λ_3	Spacing Between Tertiary γ' Particles
λ_l	Spacing Between Large Particles
λ_s	Spacing Between Small Particles
λ_{eff}	Effective Particle Spacing
λ_{FR}	Frank-Read Pinning Point Spacing
ν	Material Constant

ν	Poisson's Ratio
Ω_0	Original Body Configuration
Ω_1	Current Body Configuration
Ω_p	Composite Damage Term
Ω_p	Intermediate Configuration
ϕ_a	Area Fraction Left After Cutting
ϕ_p	Volume Fraction
ϕ_s	Area Fraction of Particles
$\phi_{p,2}$	Volume Fraction of Secondary γ' Particles
$\phi_{p,3}$	Volume Fraction of Tertiary γ' Particles
$\phi_{s,2}$	Area Fraction of Secondary γ' Particles
$\phi_{s,3}$	Area Fraction of Tertiary γ' Particles
ρ_c	Climbing/Waiting Dislocation Density
ρ_g	Gliding Dislocation Density
ρ_I	Impedance Factor
ρ_m	Mobile Dislocation Density
ρ_{m0}	Initial Mobile Dislocation Density
σ	Stress
σ^H	Hydrostatic Stress
σ^α	Stress σ to the power of Material Constant α
σ^γ	Stress σ to the power of Material Constant γ

σ^{∞} Sum of All Stress States

σ_k Back Stress

σ_{eff} Effective Stress

σ_{mises} Von Mises Stress

σ_{mis} Misfit Stress

τ Shear Stress

τ_c Cutting Stress

τ_{FR} Frank-Read Critical Stress

$\mathbf{C}$ Compliance Matrix

$\mathbf{D}$ Stretch Tensor

$\mathbf{D}^e$ Elastic Stretch Tensor

$\mathbf{D}^p$ Plastic Stretch Tensor

$\mathbf{E}$ Green-Lagrange Stain Tensor

$\mathbf{F}$ Deformation Gradient Tensor

$\mathbf{F}^e$ Elastic Deformation Gradient Tensor

$\mathbf{F}^p$ Plastic Deformation Gradient Tensor

$\mathbf{L}$ Velocity Gradient Tensor

$\mathbf{L}^p$ Plastic Velocity Gradient Tensor

$\mathbf{n}$ Slip Normal

$\mathbf{P}$ Intermediate Location of Points between and $\mathbf{x}$

$\mathbf{Q}$ Transformation Matrix

$\mathbf{S}$ Deviatoric Stress

$\mathbf{s}$ Slip Direction

$\mathbf{u}$ Displacement vector

$\mathbf{W}$ Spin Tensor

$\mathbf{X}$ Collection of Points in a Neighbourhood

$\mathbf{x}$ New Location of Points $\mathbf{X}$

θ_1 Strain Related Parameter

θ_2 Parameter Representing Micromechanisms

θ_3 Strain Related Parameter

θ_4 Parameter Representing Micromechanisms

θ_L, ψ_L, ϕ_L Euler Angles

ε Creep Rate

ε_p Primary Creep Strain

ε_t Tertiary Creep Strain

ξ Line Tangent Vector

ζ_p Centre to Centre Particle Spacing

A Current Test Piece Cross-Sectional Area

A Material Constant

A_0 Original Test Piece Cross-Sectional Area

A_i Material Constant

A_{Ω_p} Damage Constant

B Material Constant

b Burgers Magnitude

C Dislocation Multiplication Parameter

C Material Constant

C_0 Atomic Concentration

C_e Equilibrium Matrix Concentration

c_j Jog Concentration

C_{L-M} Larson-Miller Constant

D Accumulated Damage

D Diffusion Coefficient

d Grain Diameter

D_i Damage

D_s Self Diffusion Coefficient

D_v Vacancy Diffusion

$D_{v,0}$ Vacancy Diffusivity

E Young's Modulus

e Strain Tensor

F Force

F Size Distribution Frequency

$F_{peierls}$ Peierls Force

F_{PK} Peach-Koehler Force

F_{plane} Probability Density Function on a Plane

G Shear Modulus

H Back Stress

H^* Back Stress Saturation Term

H_s Enthalpy

K Material parameter equal to $\frac{\pi b^3}{2kT}$

K_B Boltzmann Constant

k_p Coarsening Constant

K_{CF} Constraint Factor

n Material Constant

n_i Material Constant

N_p Number of Particles

N_v Number of Particles per Volume

n_{Ω_p} Damage Constant

n_{FR} Number of Frank-Read Sources

$N_{p,A}$ Number of Particles per Unit Area

P_{L-M} Larson-Miller Parameter

Q Activation Energy

Q_d Activation Energy

Q_i Activation Energy

Q_k Activation Energy for Kinc Formation

Q_r Activation Energy

Q_{Ω_p} Activation Energy

R Particle Radius

r_c Critical Particle Radius

R_g Molar Gas Constant

r_p Particle Radius

R_t Test Piece Radius

$r_{p,0}$ Initial Particle Radius

$r_{p,2}$ Mean Radius of Secondary γ' Particles

$r_{p,3}$ Mean Radius of Tertiary γ' Particles

S Entropy

S Size measurements of Points $\mathbf{X}$

s Points in medium Γ

s Size measurements of Points $\mathbf{x}$

T Absolute Temperature

t Time

t_i Accumulated Time

T_s Solvus Temperature

t_{climb} Climbing Time

$t_{r,i}$ Rupture Time

u Displacement

v	Velocity
z	Correction Factor
γ^p	Plastic Shear Strain
ε^p	Plastic Strain

Chapter 1

Introduction

Development of a robust lifing assessment capability for critical aero-engine components depends critically on understanding the underlying physics driving the high temperature behaviour of superalloys used in turbine blades and disc components. In particular, the effect of the various microstructural changes that are known to occur in these materials on life is fundamental in developing realistic and reliable lifing methodologies.

Mechanistically, the high temperature creep strength of nickel-based alloys is governed by the interactions of dislocations with the γ' particle dispersion. At stresses well below the yield stress of the alloy, the γ' particles act as barriers to continual dislocation glide, since the formation of complex stacking faults associated with the slip transfer of $< 110 >$-type dislocations from the disordered fcc γ matrix into the ordered structure of the $L1_2$ γ' intermetallic provides an energy cost that needs to be overcome.

Traditionally, the problem of creep in aero-engines was mainly focused on the turbine blades, but due to the ever increasing demands on fuel efficiency at reduced cost, is leading to higher operating temperatures in aero engines. As a consequence creep is becoming an important issue in discs.

Alloys used in disc applications differ greatly from those found in the blades, which typically have unimodal sized cuboidal γ' with a volume fraction of 70%. In

contrast, disc alloys have a smaller γ' volume fraction with a multi-modal particle size distribution.

In a disc alloy such as RR1000, the size distribution consists of the primary γ' found on the grain boundaries typically with a size greater than 300 nm and a 10 % volume fraction. The secondary γ' is found within the grains and its size ranges from 30 nm to 300 nm at 30-35 % volume fraction. The final distribution is the tertiary γ' which is also found within the grains and are the smallest precipitates with a size less than 30 nm and less than 5 % volume fraction [1].

In dual microstructure RR1000, significant variations in the γ' dispersion are observed. Figure 1.1 shows such observed process-induced variations in the γ' distribution, which arise from non-uniform thermomechanical histories across the disc during manufacture. Such microstructure distributions will give rise to variations in the creep and fatigue response that are location specific. Thus, the constitutive descriptions must go beyond using simple measures of the microstructure, such as mean values, if they are to capture scatter in material properties and provide statistical lifing methodologies that exploit location specific properties.

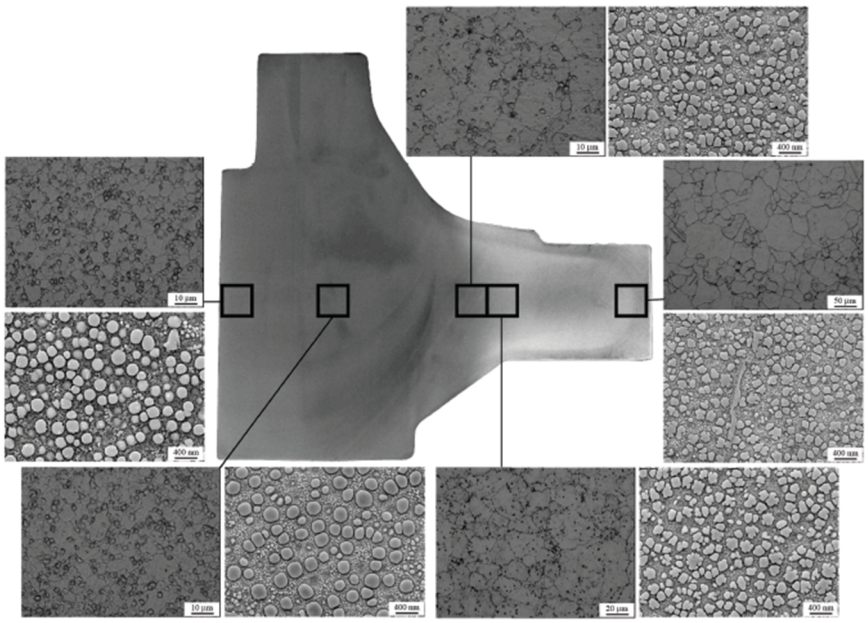


Figure 1.1: Microstructure variation along a RR1000 turbine disc [2]

Predictive modelling of the high temperature behaviour of nickel-base superal-

loys is challenging. A number of approaches have been developed over the last few decades for modelling viscoplastic response of materials. Many of these approaches have been empirical with no reference to the microstructure [3] [4] [5], while more phenomenological models based on state variable approaches have model parameters that have no physical meaning [6] [7]. In both of these cases model parameters are identified through a numerical fit of the model to an existing creep database. Furthermore, the lack of uniqueness of the model parameters resulting from physical interpretations means that such methods cannot be used reliably for extrapolating behaviour beyond the database. Thus, the ability to reliably predict behaviour requires the development of physics-based constitutive models that explicitly link the creep response of the material to potential micromehanisms driving it. Such a micromechanics approach will naturally identity model parameters that have direct physical meaning and consequently such a theory is able to provide an *a priory* parameter set.

This thesis is concerned with the development of a physics-based constitutive description of creep in nickel-based superalloys that allows location specific property predictions.

In particular, micromechanics will be formulated that couple dislocation based plasticity to the relevant microstructural elements influencing component level behaviour.

The micromechanistic approach of Dyson and co-workers [8] [9] is one of the first to derive microstructure-sensitive mathematical expressions of the creep rate in precipitate strengthened alloys. The approach has been successfully applied to unimodal γ' nickel-based superalloys such as Nimonic 90 [9]. However, such a framework cannot be used to simulate the creep response of a multimodal precipitate size alloy such as RR1000. Thus, this work aims to extend the micromechanics of precipitate strengthened alloys to complex multimodal dispersions. This will involve the development of a mean field modelling framework for modelling the temporal evolution of the γ' size distribution.

Following a literature review on nickel-based superalloys and constitutive models outlined in Chapter 2, the theoretical framework for the proposed micromechanics is developed in Chapter 3. Material mechanics over a number of length scales need to be addressed in the derivation of such a constitutive theory. These are shown in Figure 1.2 and key elements of the theory include derivation of the dislocation density, γ' dispersion and back stress evolutions. Shear rates on active slip systems are determined by the dislocation flux, which is defined as the product of the mobile dislocation density and their mean velocity. Dislocation evolution is expressed as a continuity condition that accounts for generation (Frank-Read sources) and trapping/annihilation (formation of dipoles) of dislocation segments. However, not all of the mobile segments will be gliding at any given time since they will be intersected by the γ' particles.

The mobile scalar dislocation density can be decomposed into two populations: gliding and waiting densities.

Reaction equations are established that describe the transition between gliding and waiting (climbing) dislocation segments. The macroscale creep rates are obtained through a scale invariance argument which assumes that the functional form of the macroscale creep rate is the same as that on active slip systems.

The approach is extended into a crystal plasticity (CP) formulation to simulate the flow stress response of an agglomerate of grains. The CP model will be used to validate some of the assumptions behind scale invariance of constitutive descriptions.

The γ' evolution of a multimodal size dispersion is simulated using a mean field model that accounts for composition, nucleation, dissolution and coarsening of the particle dispersion. The approach will be used to assess the impact of the shape of the particle size distribution on the evolution rate of the γ' dispersion and how it influences the creep response.

Mechanical and microstructure characterisation of the alloy RR1000 is presented in Chapters 4 and 5. Creep tests were carried out for a number of stress

and temperature conditions. The test matrix focused on the temperature range 600-800°C. In addition, a number of tensile tests were also carried out for different temperatures and applied strain rates. These were used to validate model predictions.

Scanning and transmission electron microscopy was also carried out to measure the γ' size dispersion and obtain the mean size of tertiary and secondary particles as well as their volume fraction. Information on dislocation activity in the γ and γ' phases is also presented.

Comparison of mean field and micromechanics models of the precipitation and deformation kinematics are presented in Chapter 6. The main outputs from the experimental and modelling activities are discussed in Chapters 7 and 8. Finally, conclusions and future work from this study are outlined in Chapter 9.

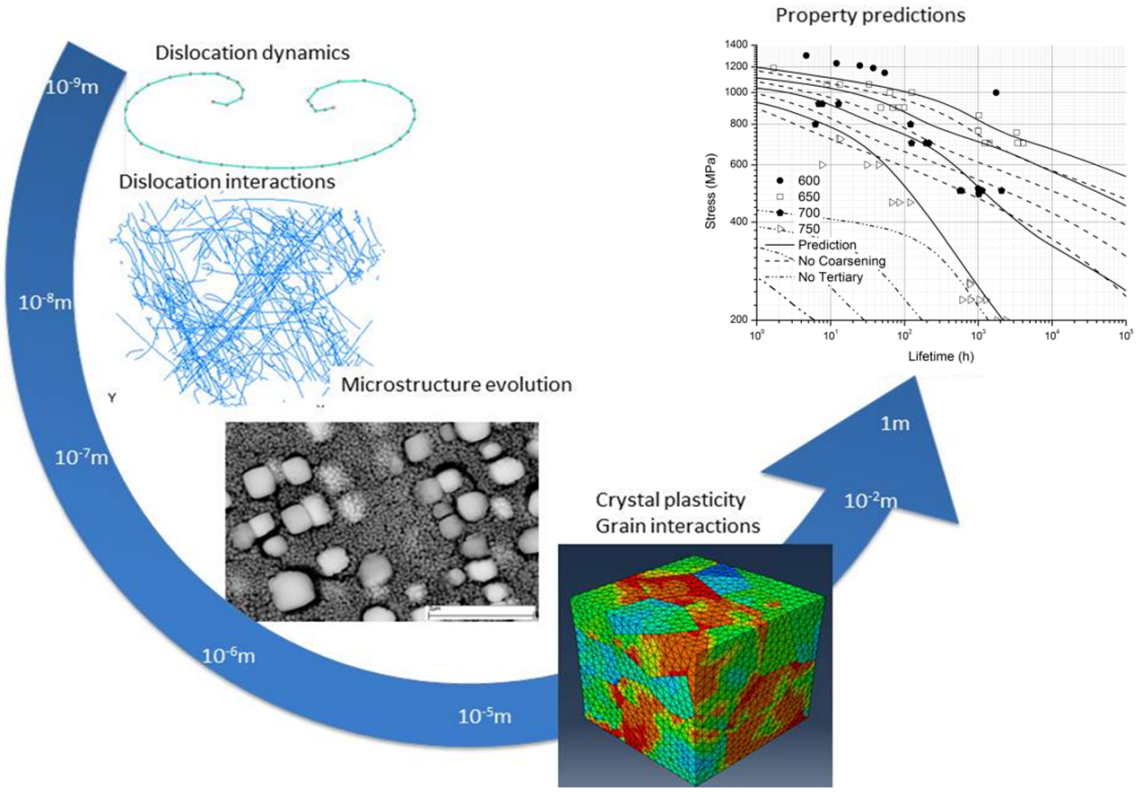


Figure 1.2: Length scales and the associated areas of focus

Chapter 2

Literature review

2.1 Turbine discs and Nickel superalloys

Superalloy is a term used to describe a class of material known for being chemically complex with multiple alloying elements and having relatively high mechanical strength and surface stability at elevated temperatures. Superalloys can be split into three groups depending on which of the group VIII elements are the base/balance element i.e. Iron based superalloys, Cobalt based superalloys and Nickel based superalloys. The focus of this work is on a nickel based superalloy. Out of the three groups these have shown the greatest high temperature strength, which has seen them used as the main component in gas turbine high pressure turbine discs and blades. Nickel based superalloys will usually be comprised of more than one phase. There is the γ matrix phase and, depending on the alloy and outlined in great detail by Donachie [10], either one or multiple phases known as: γ', γ", δ, ν, σ, borides, nitrides, carbides and the less desirable topologically closed packed (TCP) and Laves phases. In regards to RR1000 the only phases that are important with regards to creep properties are the γ and γ' phases.

Al	B	C	Co	Cr	Hf	Mo	Ni	Ta	Ti	Zr
6.35	0.08	0.13	17.94	16.49	0.16	2.98	bal	0.63	4.29	0.04

Table 2.1: At % of RR1000 nominal composition [1]

Table 2.1 shows the elemental composition for RR1000, the material of study in this work. Figure 2.1 gives a general outline of the effect of typical alloying elements in superalloys. Each element at the right wt% has a specific purpose in giving RR1000 its properties: Aluminium is used to improve oxidation resistance and is a fundamental component in γ' formation. Boron is added as a grain boundary refiner and will improve both creep and rupture properties. Carbon forms carbides and acts as a grain boundary refiner. Cobalt is used as a solid solution strengthener that raises the solvus temperature of γ' and improves hot corrosion resistance. Chromium strengthens the γ phase, can form carbides, improves oxidation and hot corrosion resistance. Hafnium is a grain boundary refiner and will also form carbides. Molybdenum is used for solid solution strengthening and can also potentially form carbides. Tantalum is used for improving the creep strength and in solid solution strengthening. Titanium is used to form γ' and can also potentially form carbides. Zirconium is added for its grain boundary refinement properties. The combination of all these elements in their concentrations will also influence the material properties and the phases that will be present.

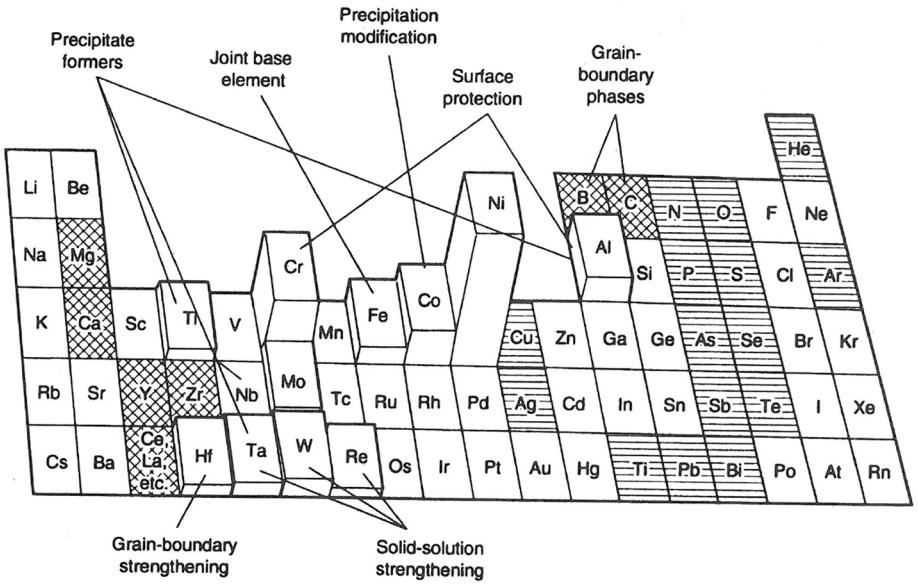


Figure 2.1: Superalloy alloying elements [11]

RR1000, thanks to its composition, has a couple of strengthening mechanisms

which give it such desirable properties. The γ matrix is face centred cubic (FCC) (figure 2.2(a)) in structure and with the addition of some of the elements explained above it is solid solution strengthened. The addition of these elements cause:

- Distortion of atomic lattice by addition of alloying elements of various sizes inhibits dislocation movement: increased drag.
- High melting point elements increase lattice cohesion and reduce diffusion.
- Decreased stacking fault energy decreases mobility (inhibits cross slip).
- Solid solution hardening only valid up to 815°C [11] .

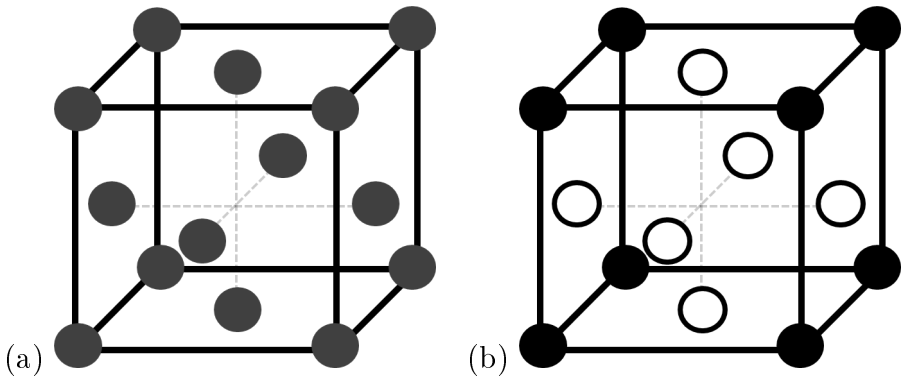


Figure 2.2: Key crystal structures found in RR1000 where (a) is the FCC γ phase and (b) is the $L1_2$ γ' phase.

Precipitate strengthening is the formation of the ordered $L1_2$ γ' precipitate seen in figure 2.2(b). It shows for the Ni_3Al the Al as the black circles and the Ni as the white circles. A coherency strain is generated due to the difference in lattice parameters between γ and γ'. The precipitates act as pinning points of dislocations impeding their motion; if the stress is high enough to cut them, due to the ordered nature of γ' a dislocation can only cut in pairs with an antiphase-boundary (APB) between them. Much like the stacking fault energy the APB energy is determined by the alloy composition, though a higher APB energy is more ideal as it is harder to then cut precipitates. In the case of RR1000 the γ' precipitate is split into three classifications based on the precipitate size and location.

2.2 Creep phenomena

Material deformation can be categorised as having two distinct regions; there is the reversible elastic region and the permanent plastic region. There are a lot of physical processes occurring in the material some of which will be covered later on. The transition from elastic to plastic behaviour will occur at a certain stress: this transitional point is known as the yield stress. Creep is a time dependent thermally activated process where plasticity occurs below the yield stress. During the creep process there are three key stages during a material's creep lifetime: primary, secondary (steady state) and tertiary creep.

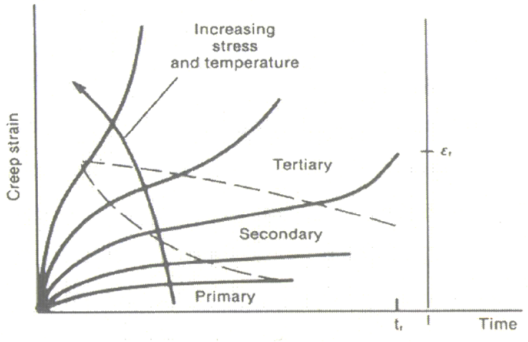


Figure 2.3: Schematic creep curves for constant tensile load [12]

The extent of each region seen in figure 2.3 is heavily dependent on the loading conditions. Upon loading there is an instantaneous strain brought on by loading, then in the primary creep region time dependent deformation occurs at a continually decreasing rate. The instantaneous loading will generate a lot of dislocations. In the primary region of creep the rate at which dislocations are being generated decreases, as well as the dislocations forming complex 3 dimensional networks and substructures. This can be based on dislocation-dislocation interactions such as the formation of dipoles or on dislocation interaction with second phase particles. Secondary creep is also known as steady state creep, and is a region where the creep rate is constant. It is a transitional region between primary and tertiary regions; in pure metals this can be a significant portion of a creep curve and in

complex alloys such as the Nickel based superalloy RR1000 the secondary region is just a transitional point observed by finding the minimum creep rate in a creep curve.

Nabarro [13] points out that the minimum creep rate is not exactly the steady state creep and will exceed it as it contains components from the decelerating primary creep and accelerating tertiary creep. The tertiary region in complex alloys is the most extensive.

The increasing creep rate in the tertiary regime is due to 'damage' evolution occurring during creep. These damage mechanisms are dependent on the material, loading conditions and the environmental conditions the material is under. Such mechanisms include: the evolution of the microstructure where secondary phases evolve such that the amount of plasticity is increasing. Void formation and their expansion at grain boundaries which act as localised stress concentrations and created zones of increased plasticity whilst also changing the cross sectional area. Corrosion damage is based upon the material being in an environment where corrosion can occur. This result in loss of material as with the formation of voids results in high stress regions around the corroded zone resulting in a high stress region. Changes in the cross sectional area reduce the area the the load is is being placed under and thus increases the stress locally which in turn will increase the creep rate.

2.3 Creep mechanisms

Creep can occur over a wide spectrum of conditions at different intensities of stress and temperature. This gives rise to different creep mechanisms which are dependent on those conditions and the material microstructure.

As observed in the work of Whittaker et al [14] high stress (approaching yield)

behaviour for superalloys transitions from a glide-climb based strengthening to one dependent on forest hardening from the increasing dislocation density. The high stress enables the dislocations to bypass obstacles, overcoming most dislocation-dislocation interactions and cutting or bowing around precipitates. There will also be the nucleation of twins based on the dissociation of a dislocation and the movement of these partial dislocations. Whilst twinning is more of a low temperature phenomenon it is also dependent on the material crystal structure, being more prevalent in HCP and BCC structures. Examination of RR1000 tensile test results which are discussed later show that twinning can occur.

2.3.1 Ashby Maps

Ashby maps can tell, based on the loading condition and a lot of prior experimental data, the different mechanisms, that can occur during thermomechanical loading.

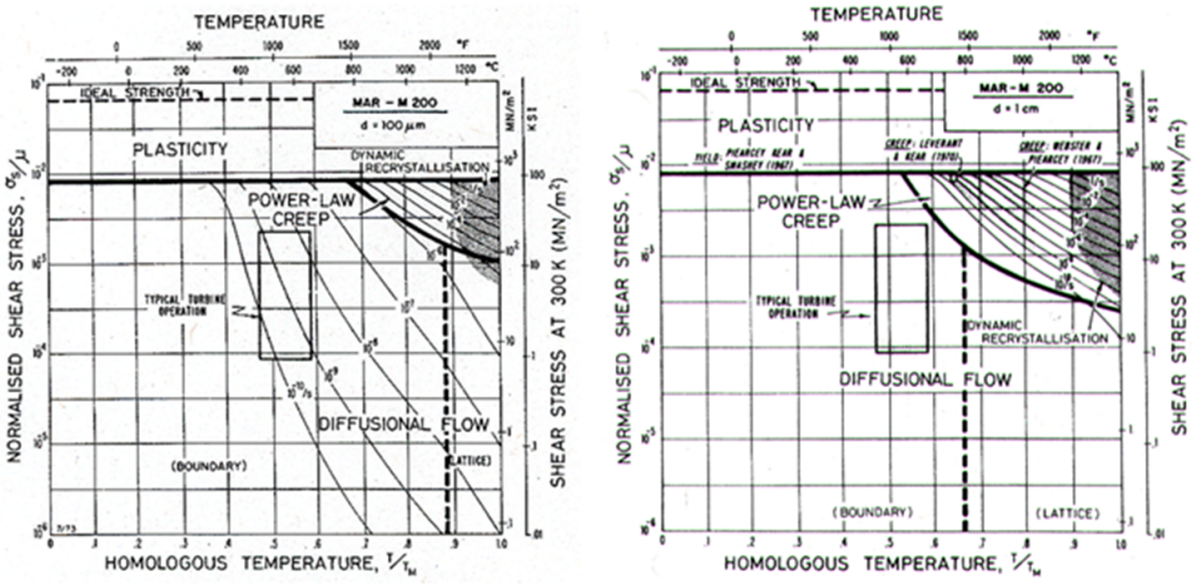


Figure 2.4: Ashby map for the Ni-superalloy material MAR-M200

Figure 2.4 covers the key deformation mechanisms that can occur depending on the thermomechanical conditions which are:

- Theoretical shear stress.
- Plasticity (with twinning).
- Power law creep (climb model) for edge dislocations.
- Climb model based on jog formation on screw dislocations.
- Harper-Dorn Creep.
- Diffusion based creep (both lattice (Nabarro-Herring) and grain boundary (Coble creep) flow).

At very low stresses diffusional flow becomes the prominent method of creep; the temperature of the creep test will determine where the diffusion will be most prominent. The effect of an applied stress will create a chemical potential this helps facilitate diffusional creep processes at high temperatures.

The Nabarro-Herring creep is a diffusional based creep mechanisms, where diffusion in the lattice is facilitated by dislocation core acting as sites for vacancy diffusion, this mechansism is described below:

$$\dot{\varepsilon} = \frac{ADb^3}{K_B T d^2} \tag{2.1}$$

Where D is a diffusional constant, d is the grainsize and A is a material constant ranging from 10-15. This predicts that the steady state creep rate is inversely proportional to the grain diameter squared $\dot{\varepsilon} \propto \frac{1}{d^2}$.

2.3.2 Dislocation climb

In the Ashby maps (figure 2.4) the power law region is the most important area for this study as it covers both stress and temperature regimes that will be examined. The power law regime describes a multitude of mechanisms that can occur the one that will be studied here is dislocation climb.

There are two climb based mechanisms that could be the creep rate determining factor. One mechanism is based upon the nucleation of jogs on a screw dislocation segment. The jog segment would be of an edge orientation and would constrain the gliding of the screw dislocation [15]. This can be overcome by the emission and absorption of vacancies. This same process of vacancy diffusion is used in the second mechanism; this is based on gliding edge dislocations which are being pinned by second phase particles or trapped in a locking configuration. The ability for the edge dislocations to climb enables them to continue to glide. This latter mechanism is the main focus for the predictive model developed in this work.

2.4 Creep Physics

2.4.1 Creep theory development

One of the earliest theorised methods explaining dislocation climb is by Weertman [16] It is based on relating the physics to an empirical derived equation set obtained from low stress experiments by Dorn [17]. The derived theory is based upon key principles: dislocations are held up by obstacles, they are circumvented via climb; this climb process is facilitated by the absorption or emission of vacancies. The obstacles outlined by Weertman [16] are assumed to be from bisecting slip planes forming a Lomer dislocation. This theory creates a power law stress dependence equation:

$$\dot{\varepsilon} = C\frac{\sigma^{\alpha}}{K_B T}\exp\frac{-Q}{K_B T}\ for\ \frac{n_{FR}\sigma b^3}{kT} < 1 \tag{2.2}$$

$$\dot{\varepsilon} = \grave{C}\frac{A\sigma^{\gamma}}{K_B T}\exp\frac{-Q}{K_B T}\ for\ \frac{n_{FR}\sigma b^3}{K_B T} > 1 \tag{2.3}$$

A common aspect in the equation set is the activation energy; at low temperatures this would be temperature dependent, but at $0.5T_m$ and above it no

longer varies with temperature and it approaches the value of the activation energy for self-diffusion [13, 15]. There is an assumption that the number of Frank-Read sources are independent of stress. This is a suitable assumption, but it must be noted that there is a competing theory put forward by Kocks et al [18–20] and explained below that the number of sources is proportional to the stress and as the stress increases so does the number of sources.

Work by Weertman [21] is extended to include annihilation from neighbouring Frank-Read sources leading dislocations via climb and is not dependent on the production of immobile dislocations, to produce:

$$\dot{\varepsilon} = A\sigma^3 \sinh\left(\frac{B\sigma^{1.5}}{K_B T}\right) \exp\left(\frac{-Q}{K_B T}\right) \tag{2.4}$$

The Weertman climb model is not the only climb based framework developed. Another method was derived by Ardell and Sherby [22], with the expression relating creep rate to the stress being accomplished using Gilman's model for dislocation glide deformation [23]. Gilman's model assumes that glide creep is controlled by nucleation of kink motion at dislocation sites, leading to the expression:

$$\dot{\varepsilon} = C \exp\left(\beta\sigma\right) \exp\left[-\frac{\left(Q_k + \frac{\nu}{\sigma}\right)}{R_g T}\right] \tag{2.5}$$

Competing physical mechanisms for the most prevalent mechanism in creep is a common issue addressed in this work; the work from Weertman [16, 21, 24, 25]; though was the starting physical framework from which the final derived expression used in this work is derived, so his equation and theoretical evolution will be focused upon. A later evolution in the Weertman theory is the inclusion of the effect of dislocations which dissociate to form partial dislocations. The resulting partial dislocation and stacking fault increase the difficulty of climb: [25]

$$\dot{\varepsilon} = AD_s\gamma^{3.5}\left(\frac{\sigma}{E}\right)^5 \tag{2.6}$$

This effect of dislocation dissociation, which for FCC materials have typically a higher stacking fault energy, and a resultant higher creep resistance than BCC materials.

This climbing over an obstacle framework was then extended to include precipitates in the study of dispersion hardened aluminium alloys [26]. Depending on the stress state different assumptions are made: at low stresses it is assumed that the dislocation interaction with the particles is such that there is no bowing around the precipitates and no pile-up to form:

$$\dot{\varepsilon} = KD_s \left(\frac{\sigma}{r_p^2} \right) \tag{2.7}$$

while at higher stresses the stress enables the initial particle dislocation reaction resulting in an Orowan loop around the particle. This loop has a stress field which opposes further bowing around those particles:

$$\dot{\varepsilon} = \grave{K} r_p D_s \sigma^4 \tag{2.8}$$

Both equations (2.7) and (2.8) predict how the creep rate scales with the particle size; as the particles coarsen the creep rate decreases at low stresses with the opposite effect at high stresses. This though, does not accurately portray experimental results which when comparing the lifetime prediction of an as-received material and an over-aged material. The prediction would indicate that the over-aged material would have the longer lifetime, but the experiments show the opposite.

Other theoretical models predicting creep behaviour in dispersion hardened alloys were developed by McLean [27] and Grant [28].

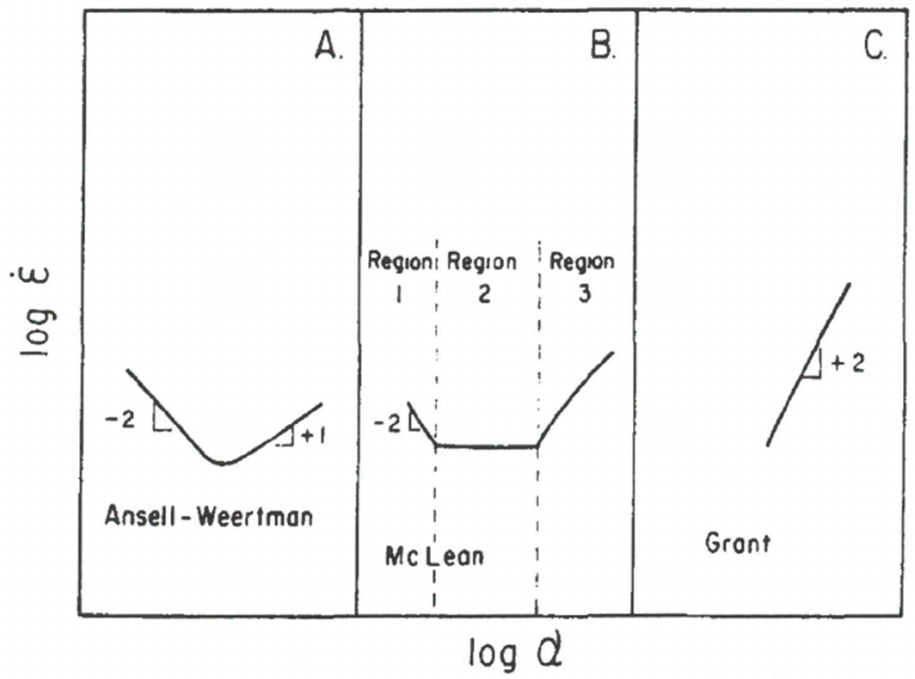


Figure 2.5: Influence of particle size, d on the creep rate at a constant stress according to different physics interpretations [15]

A comparison of creep rate evolution with particle size is displayed in figure 2.5. The prediction by Mclean has the creep rate and particle size relationship divided into three regions which indicate:

1. Creep rate decreases with increasing particle size; this assumes that the dislocations move by pushing particles. Creep rate is controlled by vacancy migration from the tension side of the particle to the compression side. It is described in an equation similar to Nabarro-Herring creep:

$$\dot{\varepsilon} = \left(\frac{k}{r_p^2}\right) \tag{2.9}$$

2. This region assumes no dependence of creep with particle size: dislocations will climb a particle and will glide a distance λ to another particle. Here $\dot{\varepsilon} \propto \lambda/d$.

3. When the particles are large which is in agreement with the Ansell and Weertman theory [26] the dislocations will bow around the particles.

Grant introduces the influence of dislocation subgrains which he claims match the mean free path of the particles also aiding the impingement of gliding dislocations:

$$\dot{\varepsilon} = kr_p^2 \tag{2.10}$$

Here the creep rate is proportional to the square of the particle size. All three theories are examined by Shelby and Burke [15] who indicate the limitations due to a lack of understanding of the underlying physics, but when comparing them all the dislocation climb theory from Weertman is the best fit from the phenomenological observations on creep.

2.5 Empirical creep models

Dyson [8] outlines and expresses the need for transitioning from popular empirically based creep models to a physics based continuum damage mechanics (CDM) approach. This section seeks to examine some of empirical methods to understand what they are capable of and why they are not sufficient when wanting to truly predict material behaviour.

2.5.1 Power Law Creep

Power law creep is the most prevalent equation used to describe creep data. The equations are usually in the form of an Arrhenius type of equation. Whilst the equation changes in appearance there are some key concepts present in all equations. Brown and Ashby [29] present the power law equation in the form:

$$\dot{\varepsilon} = \dot{\varepsilon}_0 \left(\frac{\sigma}{\sigma_0}\right)^n \tag{2.11}$$

where if the conditions are such that there are temperature dependent processes:

$$\dot{\varepsilon_0} = B \exp\left(\frac{-Q}{R_g T}\right)$$

Most uses of the power law equation are to fit experimental data, and the constants will change with different testing conditions. This method is usually used to describe and show comparative relationships with a minimal physical basis for a lot of the constants.

2.5.2 Larson-Miller parameter & Robinson's life fraction law

The Larson-Miller parameter P_{L-M} is a method to predict creep behaviour via extrapolating existing short term creep data and is represented in the form:

$$P_{L-M} = T(C_{L-M} + \ln t) \tag{2.12}$$

Where the Larson-Miller constant C_{L-M} was initially seen as a material constant = 20, but later uses determine this value via a least squares analysis [8]. Equation (2.12) is then set as a replacement of the stress function in a creep equation described by an Arrhenius equation [30], and equations (2.2) and (2.3).

This prediction method was examined by Dyson [8] and it was found to have three major limitations:

1. Valid when there is no ageing of particles.

2. Applies only to constant ductility behaviour.

3. Primary creep has to be saturated.

These are major limitations for its use in predicting creep behaviour in a superalloy as if there is no particle ageing then it will only be valid in the case of RR1000 at temperatures $\leq 700°C$ where there are little or no microstructural

changes. This prediction method is also only able to predict when there is an existing data range; a true predictive model should be able to go beyond the data available as it would ideally be relying on the underlying physics and not the test data at hand. Another issue outlined by Dyson [8] with the Larson-Miller parameter is that it will not give rupture lifetimes and will extrapolate indefinitely. This is not really an issue in this work, but to overcome this issue this model would be coupled with a lifetime prediction model such as Robinson's rule.

Robinson's rule is a method with which the rupture lifetimes can be obtained; it is based on the temperature and loading history of the creep testing sample. It is the first method examined that brings up the concept of damage. This will be looked at in greater detail in some of the prediction examples later in this work. It has two assumptions for this rule to be valid; the first:

$$D_i = \frac{t_i}{t_{r,i}} \tag{2.13}$$

This states that the damage D_i that has accumulated after time t_i is proportional to the rupture time $t_{i,r}$. The second assumption indicates that:

$$\sum \frac{t_i}{t_{r,i}} = 1 \tag{2.14}$$

Damage from each loading period is independent and rupture will occur when the summation over each period is unity. Dyson [8] indicates that the best conditions for Robinson's law are when there is one dominant damage mechanism and when dealing with a changing temperature rather than a changing stress. The model also struggles to handle a condition when the damage mechanism will change during testing. This is a major drawback as the dominant damage mechanism can be dependent on test time, temperature or stress, which could potentially all evolve

during a real component working scenario.

2.5.3 Empirical damage mechanics

With the concept of damage being introduced above it will be outlined in more detail here. Damage is the effect that is happening to the material which is accelerating the creep rate seen in most prominence during the tertiary region of a creep curve seen in figure 2.3. There are three different methods damage can be induced during creep explained by Dyson [8]:

1. Strain induced damage $= \dot{D}(\sigma, T, H, D)$
2. Thermally induced damage $= \dot{D}(T, D)$ damage rate is independent of stress and will occur on thermal exposure alone
3. Environmentally induced damage $= \dot{D}(\sigma, T, H, D, R_t)$ or $= \dot{D}(T, D, R_t)$ Is influenced by chemical interaction between the test piece and containment fluid/environment

Kachanov [31] and Robotnov built a continuum damage approach based upon void formation of the sample during creep which is one of the most commonly explored and utilised damage mechanisms. The damage parameter D is a function of the area of the voids. When the voids form and grow the area A increases until it reaches a value of A_0, at which point failure is assumed to have occurred. Therefore:

$$D = \frac{A}{A_0} \tag{2.15}$$

This can then be related to the stress applied under a constant load situation so:

$$\sigma = \frac{F}{A} = \frac{F}{A(1-D)} \tag{2.16}$$

This will modify the power law expression of creep rate based on the amount of damage incurred in the material to form:

$$\dot{\varepsilon} = \dot{\varepsilon}_0 \left(\frac{\sigma}{\sigma_0 (1 - D)} \right)^n \tag{2.17}$$

As creep evolves so too does the damage parameter in a similar power law relation as in equation (2.17)

$$\dot{D} = \dot{D}_0 \left(\frac{\sigma}{\sigma_0 (1 - D)} \right)^m \tag{2.18}$$

Constants $\dot{\varepsilon}_0$, $\dot{D}_0$ and σ_0 are all obtained by empirically fitting the above equations and extrapolating to experimental data. Dyson [8] outlines key flaws with this prediction method primarily being its limitation to a single damage mechanism. This will lead to poor extrapolations in instances where there are multiple mechanisms. The biggest fault Dyson outlines is the large number of fitting parameters that would be needed in the case of complex alloys. This would make it difficult to be used for RR1000, the material in this study, which has a lot of alloying additions and multiple phases present.

2.5.4 Theta projection

This prediction method introduced by Wilshire and co-workers [5, 32, 33] is a method of extrapolating short term creep data to generate long term predictions. Key strengths of this prediction method are its applicability to complex alloys and ability to operate under varying loading and temperature conditions. The Theta projection works by splitting the creep curve into 2 distinct regions, the primary creep region:

$$\dot{\varepsilon}_p = \theta_1 \theta_2 \exp^{-\theta_2 t} = \theta_2 (\theta_1 - \varepsilon_p) \tag{2.19}$$

and the tertiary creep region

$$\dot{\varepsilon}_t = \theta_3\theta_4 \exp^{\theta_4 t} = \theta_4(\theta_3 - \varepsilon_t) \tag{2.20}$$

The overall creep strain is given by the the addition of both primary and tertiary creep integrating equations (2.19) and (2.20). Setting the boundary condition $\varepsilon_p = \varepsilon_t = 0$ at $t = 0$ will produce the following equation form

$$\varepsilon = \theta_1 \left(1 - \exp^{-\theta_2 t}\right) + \theta_3 \left(1 - \exp^{\theta_4 t}\right) \tag{2.21}$$

θ_1 and θ_3 are strain related parameters that are used to scale their respective regions. θ_2 and θ_4 represent micromechanisms of deformation that are represented as first order rate constants. Note both θ_2 and θ_4 are temperature dependent. The dependency of θ_2 is easily identified and the impact is the same as the temperature effects on matrix self diffusion; for θ_4 this is not the case and due to its dependence on damage it could also have a stress dependency that would need to be factored in. Each θ parameter can be obtained from extrapolating experimental data to typically get a linear function of stress and temperature:

$$\log \theta_i = a_i + b_i T + c_i \sigma + d_i \sigma T = h(\sigma, T) \tag{2.22}$$

Evans and Wilshire [5] outline the best way to find these parameters is through multi-linear least squares regression. Together this means that 16 constants need to be found. If the creep rupture strain is constant then that number could be as high as 17; this is much higher then the number of constants needed in the Larson-Miller predictions which is 3. This makes it a lot more time consuming to determine the parameters and also has the potential for errors to accumulate. From equation (2.21) a lot more elements of a creep curve can be obtained such as the minimum creep rate which is obtained by differentiating that equation:

$$\dot{\varepsilon} = \theta_1\theta_2 \exp(-\theta_2 \grave{t}) + \theta_3\theta_4 \exp(\theta_4 \grave{t}) \tag{2.23}$$

where

$$\grave{t} = \frac{1}{\theta_2 + \theta_4} \ln \frac{\theta_1 \theta_2^2}{\theta_3 \theta_4^2} \tag{2.24}$$

Evans and Wilshire [5] show the proficiency of the theta prediction and how well it has matched experimental data for the Nickel superalloy IN 100

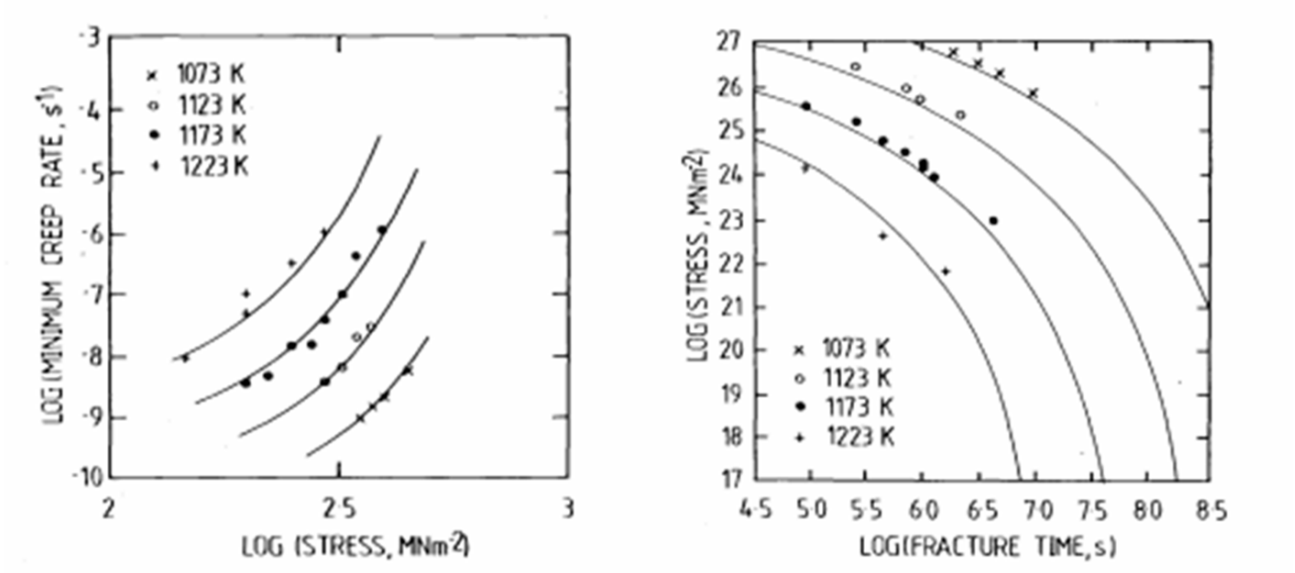


Figure 2.6: Theta projection predictions of minimum creep rate and rupture life of IN 100 [5]

The theta method as shown above in figure 2.6 is very accurate in predicting the material behaviour. Dyson [8] did outline that the tertiary proportion of the theta projection can be re-written into a CDM (Continuum Damage Mechanics) framework to form:

$$\dot{\varepsilon} = \dot{\varepsilon}_i (1 + C\varepsilon) \tag{2.25}$$

Where the expression from equation (2.20) would become:

$$\dot{\varepsilon} = \theta_3 \theta_4 \left(1 + \frac{\varepsilon}{\theta_3}\right) \tag{2.26}$$

Both of the above equations can be identical when $C = \frac{1}{\theta_3}$ and $\theta_4 = C\dot{\varepsilon}$; while the theta projection represents the data well it does not form any constitutive relationship and the parameters do not have any real physical meaning so even

though it is a method of interpreting existing data it is not a fully predictive expression, which limits its usage.

2.5.5 Omega parameter

The Omega parameter is a creep prediction approach by Prager [34] used to characterise and assess creep behaviour. The model is based on the observation that a material's ability to resist plastic deformation at a given stress decreases with increasing creep strain. The creep strain rate is based on the current creep strain and a composite damage term Ω_p; for a constant load creep test the creep rate can be expressed as:

$$\dot{\varepsilon} = \dot{\varepsilon}_i \exp^{\Omega_p \varepsilon} \tag{2.27}$$

Where the damage term can be expressed as three components

$$\Omega_p = n + p + c \tag{2.28}$$

The stress and temperature dependency of both the initial imaginary creep strain ε_i and the damage parameter Ω_p has been expressed by Yeom et al [35] as Arrehenius equations:

$$\dot{\varepsilon}_i = A_i \sigma_0^{n_i} \exp\left(\frac{-Q_i}{R_g T}\right) \tag{2.29}$$

$$\Omega_p = A_{\Omega_p} \sigma_0^{n_{\Omega_p}} \exp\left(\frac{Q_{\Omega_p}}{R_g T}\right) \tag{2.30}$$

In regards to applying equations (2.29) and (2.30) to the Nickel superalloy 718 (which shows significant coarsening of its γ' precipitates at and above 650°C) Yeom et al [35] found it deviating from the experimental data which is a problem with the initial explanation of the Omega parameter also outlined by Dyson [8] that the stress exponents are no longer constant. Yeom et al state that a hyperbolic

sine formulation is much more accurate:

$$\dot{\varepsilon}_i = \grave{A}_i \left[\sinh(\alpha \cdot \sigma_0)\right]^{\grave{n}_i} \exp\left(\frac{-Q_i}{R_g T}\right) \tag{2.31}$$

$$\dot{\Omega}_p = \grave{A}_{\Omega_p} \left[\sinh(\beta \cdot \sigma_0)\right]^{n\grave{\Omega}_p} \exp\left(\frac{-Q_{\Omega_p}}{R_g T}\right) \tag{2.32}$$

Where all the parameters $\left[\grave{A}_i, \grave{A}_{\Omega_p}, \grave{n}_i \; and \; n\grave{\Omega}_p\right]$ as well as α and β are material constants. A comparison of this Omega method prediction and the Larson-Miller method in equation (2.12) where compared against both power law (equations (2.29) and (2.30)) and sinh law (equations (2.31) and (2.32)).

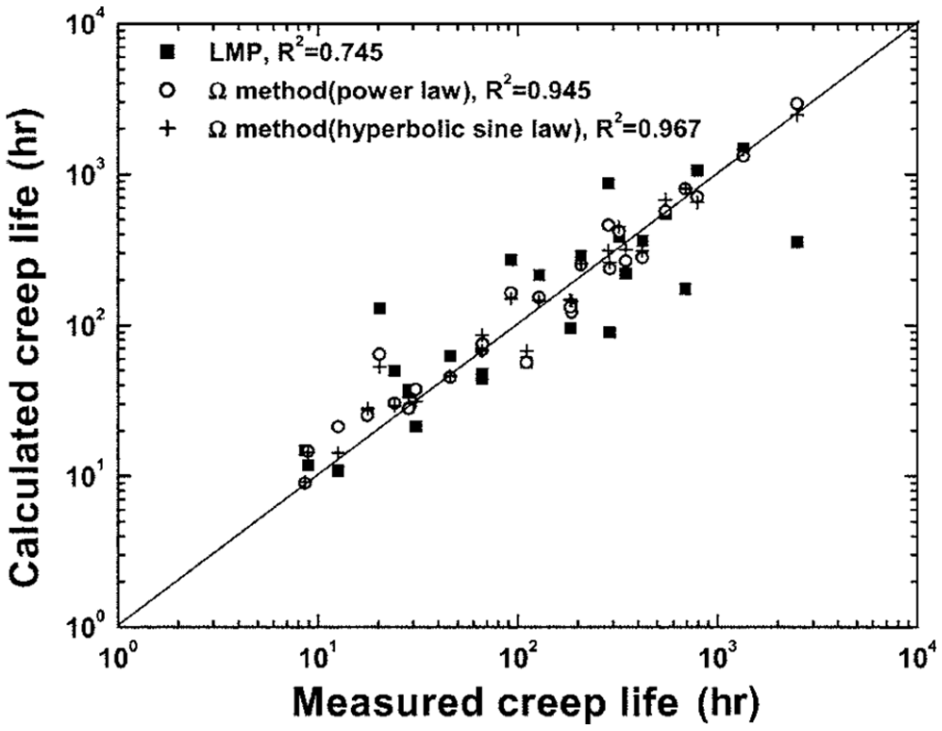


Figure 2.7: Comparison of different creep life predictions against measured data [35]

Yeom et al [35] show that the Larson-Miller method has the greatest deviation and is thus less accurate than both Omega methods. A better comparison of the two Omega methods can be seen in looking at how they predict individual creep curves as shown below in figure 2.8.

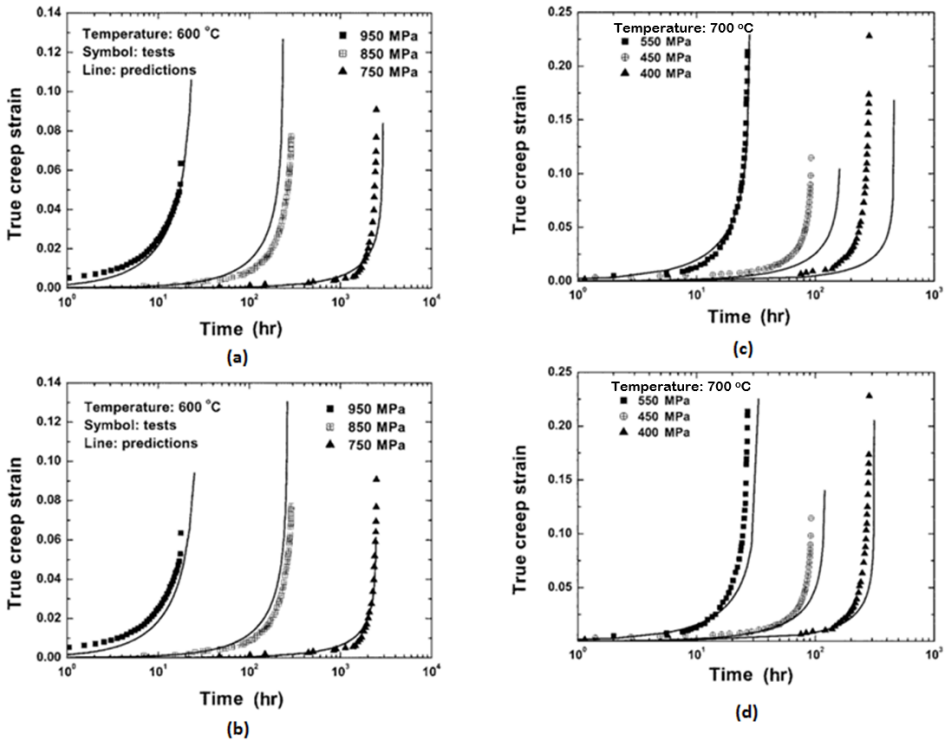


Figure 2.8: Creep predictions of different Omega formulations at different conditions (a) low temperature power-law, (b) low temperature hyperbolic sine law, (c) high temperature power-law and (d) high temperature hyperbolic sine law. [35]

At the lower temperature both methods predict well, but at the higher temperature 700°C which is at a high enough temperature for microstructural evolution of γ' to occur the accuracy is reduced. At lower stresses which result in longer creep lifetimes the power law method equations (2.29) and (2.30) show a greater deviation from experimental results. This was also mentioned by Dyson [8] that the Omega parameter in exponential form is not suitable for thermally degrading materials. This model has many strengths; being both very accurate and capable at modelling creep curves, a flaw again is that this method is not predictive and requires experiments at all temperatures as all the material constants are temperature dependent. This limits the range of uses for this model.

2.6 Physics based model

The previous examples are only some emperical methods used for creep and while this work acknowledges there have been advancements in emperical models since the work of Dyson [8] the central point of that work remains true. There are different aims in the development of empircal models and physics based modes. Empircal models aim to properly capture experimental data which they do very well, this can then enable extrapolation of the data to get a greater understanding of the material behaviour. Physics based model aims to start from trying to describe the physics of the process and then compare it against the experimental data or use that data to callibrate parameters and confirm assumptions. Thist section will describe physics based models their description of material behaviour during creep and model developments.

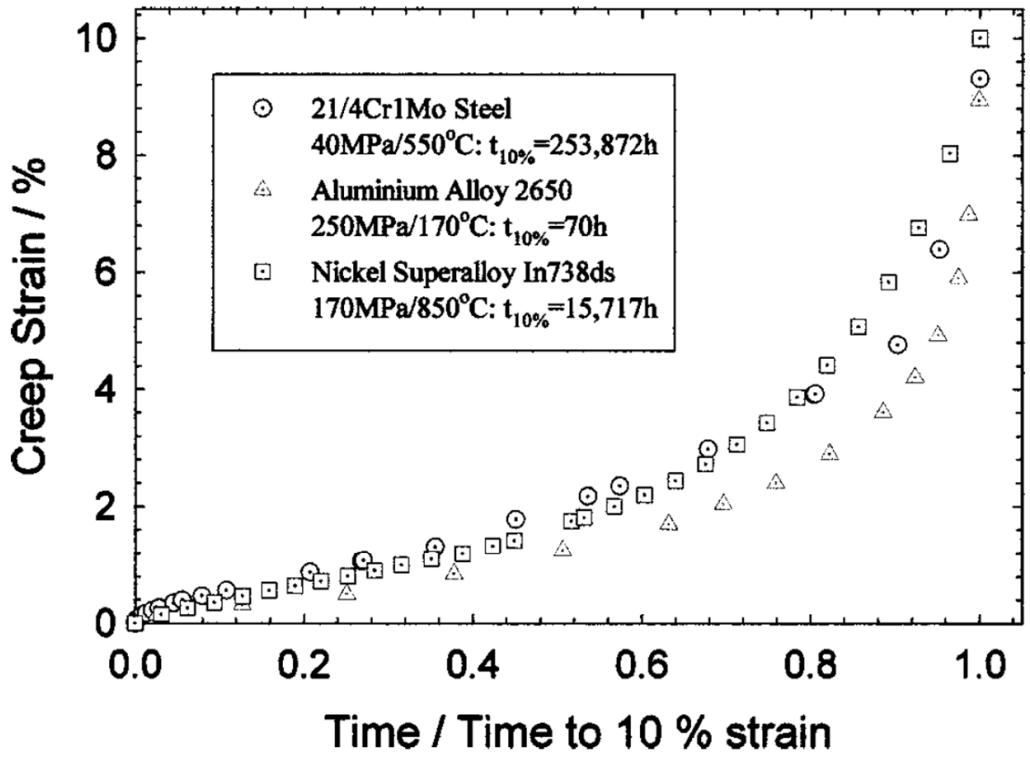


Figure 2.9: Similarity of creep curves from different materials [36]

Figure 2.9 outlined by McLean and Dyson [36] shows three different creep

curves which look very similar, but have different damage mechanisms. This outlines the false ideal based on trying to create a model from data points. As for select conditions the empirical method may fit well, but changing the temperature or stress the model will be unable to capture that behaviour. A physics based creep approach relies on an accurate portrayal of the material behaviour where, independent of the thermomechanical loading, it should still predict the material behaviour. An outline of some of the damage mechanisms outlined by Dyson are displayed below in figure 2.10.

CREEP DAMAGE CATEGORY	DAMAGE MECHANISM	DAMAGE PARAMETER	DAMAGE RATE	STRAIN RATE
Strain-Induced $\dot{D} = \dot{D}(\sigma,T,H,D)$	Creep-Constrained Cavity Nucleation-Controlled	$D_N = \frac{\pi d^2 N}{4}$	$\dot{D}_N = \frac{k_N}{\varepsilon_{f,u}}\dot{\varepsilon}$	$\dot{\varepsilon} = \dot{\varepsilon}_0 \sinh\left[\frac{\sigma(1-H)}{\sigma_0(1-D_N)}\right]$
	Creep-Constrained Cavity Growth-Controlled	$D_N = \frac{\pi d^2 N}{4}$ $D_G = \left(\frac{r}{\ell}\right)^2$	$\dot{D}_N = 0$ $\dot{D}_G = \frac{d}{2\ell D_G}\dot{\varepsilon}$	$\dot{\varepsilon} = \dot{\varepsilon}_0 \sinh\left[\frac{\sigma(1-H)}{\sigma_0(1-D_N)}\right]$
	Dynamic Subgrain Growth	$D_{sg} = 1-\left(\frac{r_{sg,i}}{r_{sg}}\right)$	?	?
	Multiplication of Mobile Dislocations	$D_d = 1-\frac{\rho_i}{\rho}$	$\dot{D}_d = C(1-D_d)^2\dot{\varepsilon}$	$\dot{\varepsilon} = \frac{\dot{\varepsilon}_0}{(1-D_d)}\sinh\left[\frac{\sigma(1-H)}{\sigma_0}\right]$
Thermally-Induced $\dot{D} = \dot{D}(T,D)$	Particle-Coarsening	$D_p = 1-\frac{P_i}{P}$	$\dot{D}_p = \frac{K_p}{3}(1-D_p)^4$	$\dot{\varepsilon} = \dot{\varepsilon}_0 \sinh\left[\frac{\sigma(1-H)}{\sigma_0(1-D_p)}\right]$
	Depletion of Solid-Solution Elements	$D_s = 1-\frac{\bar{c}_i}{c_0}$	$\dot{D}_s = K_s D_s^{1/3}(1-D_s)$	$\dot{\varepsilon} = \frac{\dot{\varepsilon}_0}{(1-D_s)}\sinh\left[\frac{\sigma(1-H)}{\sigma_0}\right]$
$\dot{D} = \dot{D}(\sigma,T,D,H,R)$ **Environmentally-Induced** $\dot{D} = \dot{D}(T,D,R)$	Fracture of Surface Corrosion Product	$D_{cor} = \frac{2x}{R}$	$\dot{D}_{cor} = \frac{1}{R}\left(\frac{K_c\dot{\varepsilon}}{\varepsilon^*}\right)^{1/2}$	$\dot{\varepsilon} = \dot{\varepsilon}_0 \sinh\left[\frac{\sigma(1-H)}{\sigma_0(1-D_{cor})}\right]$
	Internal Oxidation	$D_{ox} = \frac{2x}{R}$	$\dot{D}_{ox} = \frac{K_{ox}}{R^2 D_{ox}}$	$\dot{\varepsilon} = \dot{\varepsilon}_0 \sinh\left[\frac{\sigma(1-H)}{\sigma_0(1-D_{ox})}\right]$

Figure 2.10: Different damage mechanisms and categories that could potentially be used to predict creep behaviour in Continuum Damage Mechanics [8]

2.6.1 Single crystal superalloy approach

An extensive approach to predicting the behaviour of the single crystal unimodal nickel superalloy Nimonic 90 was presented by Dyson, [9] showing a generic kinetic creep equation using the climb/glide bypass micromechanism. Understanding of the equations used was vital in knowing what needed to be taken into account

with regards to building a model for RR1000. Dyson starts off forming the creep equations by stating that the mobile dislocation density is split into two categories; those which are gliding and those which are climbing:

$$\rho_m = \rho_g + \rho_c \tag{2.33}$$

These gliding dislocations contribute to the plastic shear strain via the Orowan relationship:

$$\dot{\gamma} = b\rho_g \bar{v}_g \tag{2.34}$$

This gliding dislocation density will evolve: some will be generated from those that are climbing over the precipitates, some will be trapped as they reach a particle and must start climbing,

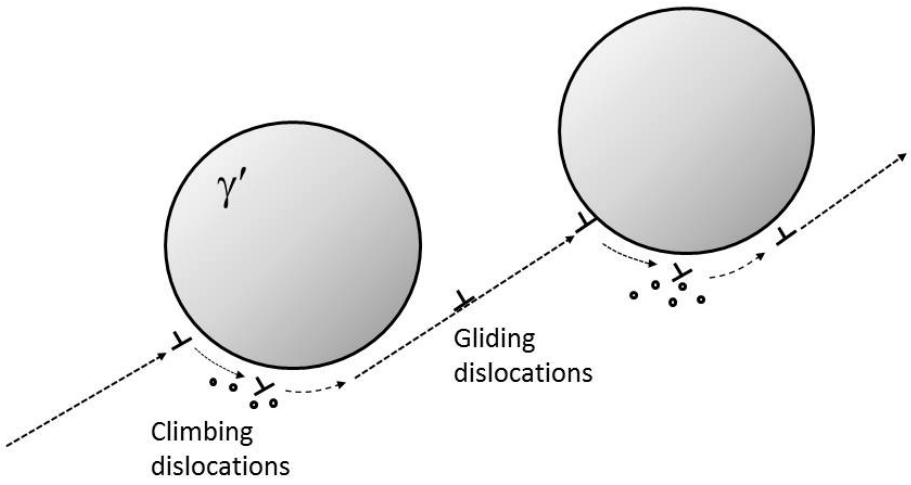


Figure 2.11: Dislocations gliding to particle getting pinned and climbing until they can climb again.

Figure 2.11 shows a visualisation of the jerky glide method and below it is shown via the equation:

$$\dot{\rho}_g = \rho_g^+ + \rho_g^- \tag{2.35}$$

A general rule for working out the evolution of something be it generated or annihilated is:

$$\rho_g^{\pm} = number\ available\ \times\ probability\ (\pm)\ \times\ frequency\ of\ event$$

For trapping a dislocation: the number available is all the gliding dislocations, the probablility of a trapping event occuring is assumed to be 1 meaning all gliding dislocations will eventually be trapped. The frequency that this occurs is dependent on the gliding dislocation velocity and the particle spacing:

$$\rho_g^- = \rho_g \times 1 \times \frac{\bar{v}_g}{\lambda_p} \tag{2.36}$$

For generation the number of dislocations available are those waiting to glide which we can assume are therefore in the process of climbing, and the frequency is the inverse of the climbing time. The probability has two distinct sections: the first is the probability of an encounter, which is based on where the dislocations are climbing, which is at the particles, and the volume fraction of particles. The second is based on where these release events are taking place, this is for the dislocations that are one climb event away from being free of the particle and gliding, which is assumed to be $\approx \frac{b}{r_p}$. This results in the equation or gliding dislocation generation being:

$$\rho_g^+ = \rho_c \times \frac{\phi_p b}{r_p} \times \frac{1}{t_{climb}} \Rightarrow \rho_c \times \phi_p \times \frac{1}{r_p} \times \frac{b}{t_{climb}} \Rightarrow \rho_c \times \phi_p \times \frac{\bar{v}_c}{r_p} \tag{2.37}$$

Combining both equation (2.36) and equation (2.37) to get the rate of change

of gliding dislocations and equation (2.35) becomes:

$$\dot{\rho}_g = \rho_c \phi_p \frac{\bar{v}_c}{r_p} - \rho_g \frac{\bar{v}_g}{\lambda_p} \tag{2.38}$$

Through integrating equation (2.38)

$$\rho_g = \frac{\rho_c \phi_p \frac{\bar{v}_c}{r_p}}{\bar{v}_p \lambda_p} \left[1 - \exp\left(\frac{-\bar{v}_g}{\lambda_p} t \right) \right] \tag{2.39}$$

Multiplying equation (2.39) by the mean glide velocity $\bar{v}_g$ the equation becomes:

$$\rho_g \bar{v}_p = \frac{\rho_c \phi_p \frac{\bar{v}_c}{r_p}}{\lambda_p} \left[1 - \exp\left(\frac{-\bar{v}_g}{\lambda_p} t \right) \right] \Rightarrow \rho_c \phi_p \left(\frac{\lambda_p}{r_p} \right) \bar{v}_c \left[1 - \exp\left(\frac{-\bar{v}_g}{\lambda_p} t \right) \right] \tag{2.40}$$

Using the Orowan relation in equation (2.34) the shear strain is determined to be:

$$\dot{\gamma} = b \rho_c \phi_p \left(\frac{\lambda_p}{r_p} \right) \bar{v}_c \left[1 - \exp\left(\frac{-\bar{v}_g}{\lambda_p} t \right) \right] \tag{2.41}$$

From analysis of creep behaviour the term in the [] brackets in equation (2.40) has only a small influence on a material's creep behaviour, mainly as a transient effect at the beginning of creep. To simplify the problem this term can be excluded so that equation (2.41) becomes:

$$\dot{\gamma} = b \rho_c \phi_p \left(\frac{\lambda_p}{r_p} \right) \bar{v}_c \tag{2.42}$$

The equation for dislocation climbing velocity is explained later on. Dyson [9] makes the assumption that both vacancy absorption and vacancy emission are occurring at the same frequency; the climb equation thus becomes:

$$\bar{v}_c = \frac{4\pi D_v c_j}{b} \sinh\left(\frac{\tau \lambda b^2}{K_B T} \right) \tag{2.43}$$

With c_j being the jog concentration and is taken to be unity, and the vacancy

diffusion D_v is described as:

$$D_v = D_{v,0} \exp\left(\frac{-Q}{R_g T}\right) \tag{2.44}$$

With λ_p in equation (2.43) being the mean lattice spacing

$$\lambda_p = 2\sqrt{\frac{2}{3}} r_p \left(\frac{\pi}{4\phi_p} - 1\right) \tag{2.45}$$

and can be rearranged into

$$\frac{\lambda_p}{r_p} = 2\sqrt{\frac{2}{3}} \left(\frac{\pi}{4\phi_p} - 1\right) \tag{2.46}$$

Substituting both equations (2.43) and (2.46) into equation (2.42) and assuming that the majority of the dislocations present will be at the particles so $\rho_c \approx \rho_m$ the equation for the creep strain becomes:

$$\dot{\gamma} = \rho_m \phi_p 2\sqrt{\frac{2}{3}} \left(\frac{\pi}{4\phi_p} - 1\right) D_v c_j \sinh\left(\frac{\tau \lambda b^2}{K_B T}\right) \tag{2.47}$$

Under uniaxial tension the shear components are transformed using the Taylor relationship [37]:

$$\gamma = \bar{M}\varepsilon$$

$$\tau = \frac{\sigma}{\bar{M}}$$

It should also be noted that the effects of creep are only impacting the matrix whilst the γ' particles are only deforming elastically which will result in both only an effective stress σ_{eff} being applied and an area application parameter $(1 - \phi_p)$, so the creep equation becomes:

$$\dot{\varepsilon} = \rho_m \bar{M}^{-1}(1 - \phi_p)\phi_p 2\sqrt{\frac{2}{3}} \left(\frac{\pi}{4\phi_p} - 1\right) D_v c_j \sinh\left(\frac{\sigma_{eff} \lambda b^2}{\bar{M} K_B T}\right) \tag{2.48}$$

To simplify equation (2.48) the pre-sinh term is grouped together to form the strain constant ε_0 and inside the sinh function terms are grouped to form the stress constant σ_0

$$\dot{\varepsilon} = \varepsilon_0 \sinh\left(\frac{\sigma_{eff}}{\sigma_0}\right) \tag{2.49}$$

where:

$$\varepsilon_0 = \rho_m \bar{M}^{-1}(1-\phi_p)\phi_p 2\sqrt{\frac{2}{3}}\left(\frac{\pi}{4\phi_p} - 1\right) D_v c_j$$

and

$$\sigma_0 = \frac{\bar{M} K_B T}{\lambda b^2}$$

Where $\sigma_{eff} = \sigma - \sigma_k$; this equation is coupled with other damage evolution mechanisms such as those found in [36]. σ_k is the back stress which is due to the loading of stress from the plastically deforming matrix onto the elastically deforming particles:

$$\dot{\sigma}_k = E\phi_p\left(1 - \frac{\sigma_k}{\sigma H^*}\right)\dot{\varepsilon} \tag{2.50}$$

The maximum proportion of the stress the particles can absorb is based upon the material microstructure and assuming the precipitates are spherical then:

$$H^* = \frac{2\phi_p}{1+2\phi_p} \tag{2.51}$$

During creep the mobile dislocation density will evolve proportional to the creep rate. The implementation is based on an empirical formulation undertaken in previous work [36]

$$\dot{\rho}_m = C\dot{\varepsilon} \tag{2.52}$$

With C being of the order $300 \times \rho_{m0}$ where the initial dislocation density $\rho_{m0} = 1E10$.

The microstructure of the material is also changing over time at the elevated temperature. The initial microstructure was obtained from experimental data and the mean particle size measurements obtained from extensive work by Heslop

and Betteridge [38] to give an initial particle radius $r_{p,0} = 12.5\,nm$. The volume fraction data was determined by fitting experimental data for In597 by Gibbons and Hopkins [39]. Using the Lever rule equation the volume fraction at any creep operating temperature can be determined by:

$$\phi_p(T) = \frac{C_0 - C_e(T)}{\alpha - C_e(T)} \tag{2.53}$$

Where α was determined to be 0.23 and the equilibrium matrix concentration C_e is:

$$C_e(T) = \exp\left(\frac{S}{R_g}\right) \times \exp\left(\frac{-H_s}{R_g T}\right) \tag{2.54}$$

and the atomic concentration C_0 is:

$$C_0(T) = \exp\left(\frac{S}{R_g}\right) \times \exp\left(\frac{-H_s}{R_g T_s}\right) \tag{2.55}$$

From the experimental data, Dyson found:

$$\exp\left(\frac{S}{R_g}\right) = 17 \;\&\; H_s = 7250$$

This was validated by rearranging equation (2.52) at the solvus temperature where $\phi_p(T_s) = 0$ and $C_0 = C_e(T_s)$ to form:

$$T_s = \frac{7250}{\ln\left(\frac{17}{C_0}\right)} \tag{2.56}$$

Equation (2.56) is compared against experimental data for a range of superalloys and it shows that for Nimonic 90 the prediction matches the data as shown in figure 2.12.

With the initial microstructure obtained an accurate description of the γ' evolution was presented:

$$r_p^3 - r_{p,0}^3 = k_p \exp\left(\frac{-Q_r}{R_g T}\right) \tag{2.57}$$

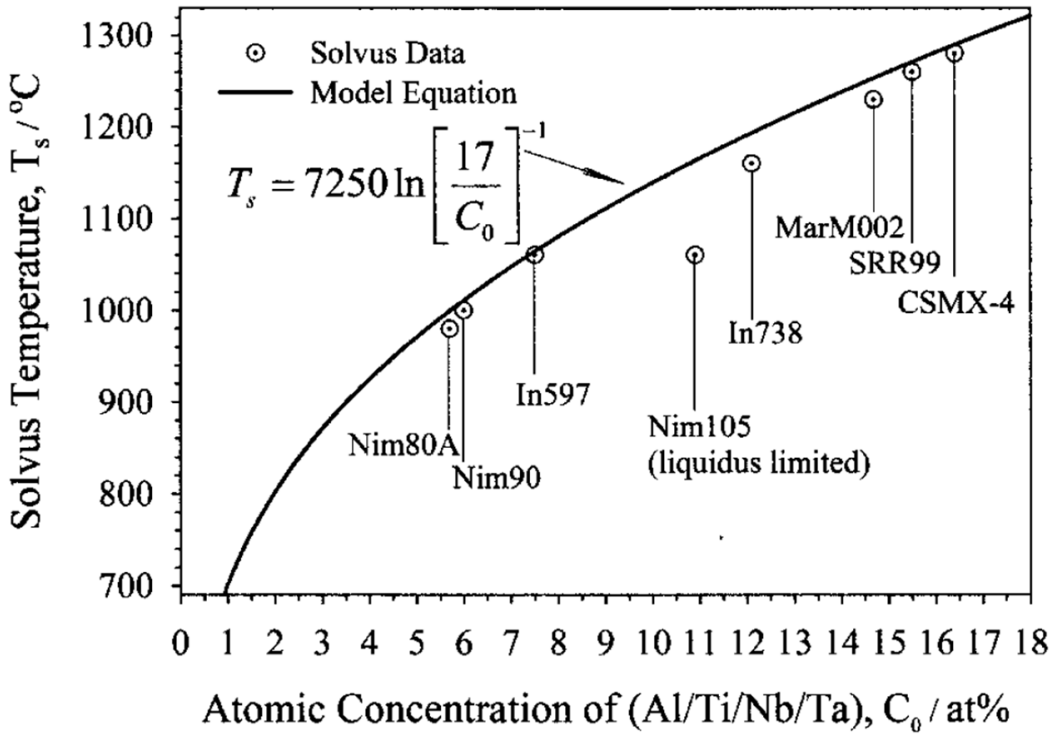


Figure 2.12: Effect of atomic percentage Al+Ti+Nb+Ta on solvus temperature experimental results compared against predictions from equation (2.56)

Describing the Ostwald ripening process, when equation (2.57) is differentiated with respect to time it becomes:

$$\dot{r}_p = \frac{k_p}{3r_{p,0}^2} \exp\left(\frac{-Q_r}{R_g T}\right) \tag{2.58}$$

2.6.2 Constitutive developments

Equations (2.50), (2.52) and (2.58) represent 3 constitutive descriptions that are also evolving over time. Greater detail on constitutive descriptions is found later on in this work.

Literature on the development of constitutive descriptions to describe different alloys and microstructures was reviewed. Early work by Dyson [8] outlines an important damage feature mentioned in early creep examples; the nucleation of

cavities on grain boundaries:

$$\dot{D}_n = \frac{k_N}{\varepsilon_{fu}}\dot{\varepsilon} \tag{2.59}$$

This constitutive equation is difficult to implement as it requires knowledge of the material failure strain and therefore cannot be used to be fully predictive. Work by Kachanov [31] outlines the essence of cavitation damage having no effect on the associated creep rate, but will impact the failure strain. This is very important to be addressed as a common misconception is that grain size affects creep rate; this is not the case. RR1000 the main focus material in this study comes in two forms, coarse grain and fine grain. Coarse grain is known for having a better creep response: this is purely because of the difference in their respective microstructures within the grain and not their grain sizes.

The physics based approach is also examined in work by Basoalto et al [40] which follows a similar approach to [9], but adds the interesting concept of constraint. The idea of a constraint factor was devised by Pollock and Argon [41] and is for high volume fraction materials such as superalloys where the dislocations are only able to move (in a single crystal Ni superalloy) through the γ channels. These channels can only allow a certain amount of gliding dislocations through them at one time. The higher the strain rate and the faster the dislocations are moving through the γ channels the more of an effect the constraint factor will have. This is expressed as a function of the volume fraction:

$$K_{CF} = \begin{cases} \frac{1+2\phi_p^{\frac{1}{3}}}{3\sqrt{\pi}\left(1-\phi_p^{\frac{1}{3}}\right)} \\ 1 \qquad\qquad \text{for } \phi_p \leq 0.3 \end{cases} \tag{2.60}$$

This constraint factor is then included in the calculation of the stress constant which then becomes:

$$\sigma_0 = \frac{K_{CF}(\phi_p)\bar{M}K_BT}{\lambda b^2} \tag{2.61}$$

This an important physical process that if in place will increase the creep

lifetime.

Other aspects captured are the effect of temperature and stress on the different mechanisms that could occur.

At high temperatures (in the case of CMSX-4 $\geq 0.6T_m \approx 850°C$ [42]) and low stresses, not only is there significant coarsening of the γ', but there is a shape factor evolution. This is when the γ' in the superalloy, CMSX-4 [43] change from there cuboidal shape to platelets. This shape change will affect the amount of stress partitioning in the material. This effect was pointed out and acknowledged and should be considered when capturing high temperature behaviour in RR1000.

Later in the work by Basoalto et al [43] the concept of misfit is introduced and added as an additional constitutive law. As explained previously misfit between the γ and γ' is alleviated at elevated temperatures in an Arrehenius style equation:

$$\dot{\sigma}_{mis} = A \exp\left(\frac{-Q_d}{R_g T}\right) \sigma_k \tag{2.62}$$

It is also incorporated in the back stress evolution and modifies equation (2.50). The misfit strain term $\frac{\sigma_{mis}}{E}$ is added on as an extra strain term to equation (2.49). The effect of the inclusion of misfit in the case presented by Basoalto et al [43] is an extension in the material creep lifetime.

This extension is because misfit supplements the loading from the matrix to the precipitates. Dislocations climbing at the γ/γ' interface are formed from the concentration gradient of vacancies from around the dislocations to the bulk material. The resultant effect is localised diffusional creep which occurs as a mechanism similar to Nabarro-Herring diffusional creep to alleviate the misfit. The greater the misfit the more alleviation is needed and thus the longer the creep lifetime predicted. The importance of considering this effect is shown in figure 2.13. The application of misfit extends creep strength and does better capture the creep data examined.

Cutting of the γ' is also considered as an additional mechanism which will

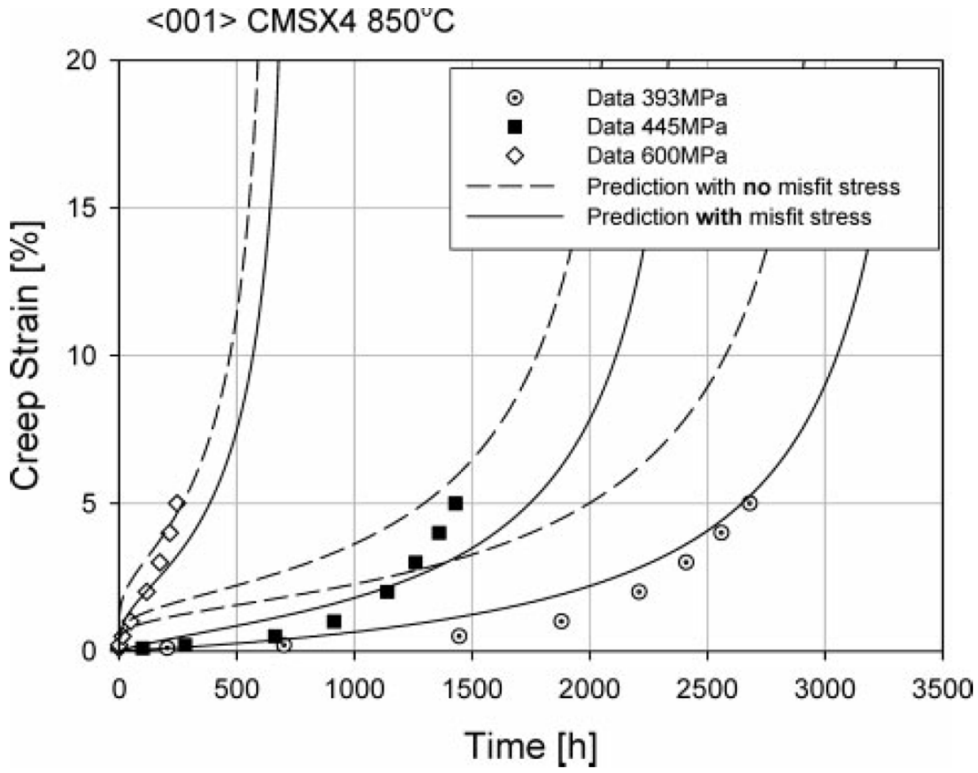


Figure 2.13: Creep predictions at various stresses showing the effect of the inclusion of misfit on material creep response [43]

occur at higher stresses and is dependent on the material microstructure. Cutting of γ' will be looked at in more detail, but work by Coakley et al [44] shows that cutting can and should be addressed when predicting creep in Ni superalloys. To do so a cutting formulation first obtained by Brown and Ham [45] was utilised for dislocations in order to cut a γ' particle must enter in pairs and form an anti-phase boundary, where the cutting stress is:

$$\tau_c = \frac{\gamma_{APB}}{2b}\left[\left(\frac{8\gamma_{APB}\phi_p r_p}{\pi G b^2}\right)^{\frac{1}{2}} - \phi_p\right] \tag{2.63}$$

The material of choice examined by Coakley et al [44] was Nimonic 115, which is a polycrystalline material and the concept of a bimodal distribution was also examined. The cutting stress was examined for each independent distribution. With regards to the particle descriptions two different systems were employed. Since the LSW (Lifshiitz, Slyozov and Wagner) equation (2.58) is not valid for a

bimodal distribution attempts were made to group both distributions and have a total mean radius. These were inaccurate at low temperatures, but at higher temperatures which had rapid dissolution of the smaller precipitates it did better. Another aspect examined was the interparticle spacing: instead of a spacing based on the mean particle size an effective spacing based on each individual distribution was calculated:

$$\frac{1}{\lambda_{eff}^2} = \frac{1}{\lambda_s^2} + \frac{1}{\lambda_l^2} \tag{2.64}$$

Each respective mean lattice spacing is dependent on both the particle size and volume fraction. During creep this will evolve, as will the effective spacing.

Examination of the above constitutive descriptions provides a framework of potential physical process occurring during creep. This helps decide for the model what processes should be added and what as in the case of cavity formation may not need to currently be considered.

2.7 Microstructure evolution

A method to capture and predict the temporal and spacial evolution of γ' particles is vital for an accurate model which will predict plastic deformation. At an elevated temperature Ostwald ripening will occur when in order to lower the total surface free energy of the system larger particles will coarsen at the expense of the smaller ones. This act has been described as a carnivorous process with the larger particles feeding off the smaller particles; this results in an increase in the average particle size, but decrease in volume fraction.

One of the earliest methods which advanced the Ostwald ripening theory and built a framework to predict this process was done by Lifshitz and Slyozov [46], extended with independent work of Wagner [47], to form the LSW theory. Voorhees [48] explains that there are three governing equations that any particle coarsening

theory must solve to be valid:

1. Kinetic equation which describes the growth and shrinkage rate of individual particles.

2. Configuration equation that describes the temporal evolution of the particle size distribution.

3. A mass conservation equation which (1) and (2) must satisfy to be acceptable.

The LSW is valid, but makes a few simplifying assumptions: it operates on spherical particles in a stress free infinite matrix with an infinitely dilute (volume fraction near zero) system. There is a relationship between how the cubed mean particle size evolves linearly with time such that $\bar{r} \propto t^{\frac{1}{3}}$.

Baldan [49] provides a thorough outline on work and modifications to the LSW theory. The modified LSW (MSLW) theory by Ardell furthers the LSW work, by introducing volume fraction effects. This work concludes that the coarsening rate increases with the volume fraction and the theoretical size distribution broadens rapidly with increasing volume fraction. Baldan [49] covers the Lifshitz-Slyozov Encounter Modified (LSEM) theory which is for materials with a large volume fraction. The work describes coarsening of two particle diffusion fields with the possibility of these particles coalescing. Baldan compares this method with the MSLW theory finding the particle size distribution shape and evolution to match better with the experimental data [49].

The situation that has to be modelled is a lot more complex than the earlier theories describe. In the case of RR1000 we are dealing with a moderate volume fraction, highly alloyed material that forms a multi-modal particle size distribution. The modelling aspect is based upon the Onsager extreme principles modified for use in describing nucleation and Ostwald ripening as described by [50] and

used within a Mean Field approach. An in house code was developed based on the work found in [46, 47, 51] and presents the particle size distribution in the form:

$$\frac{\partial F(r,t)}{\partial t} + \nabla.(F(r,t)v(r,t)) = 0 \tag{2.65}$$

A multi-modal distribution means that in viewing the size distribution multiple distinct populations can be identified. In the case of fine grain RR1000 there would be three distinct γ' populations: primary, secondary and tertiary (in coarse grain there is no primary). There are a few ways to discern each population, from finding local minima to, if the material is well known, the distributions can be separated by size giving each distribution a critical radius where: $0 < r_p < r^*_{p,3}$ describes the tertiary γ' distribution, $r^*_{p,3} < r_p < r^*_{p,2}$ for secondary γ' distribution and primary γ' is $> r^*_{p,2}$. The growth rate shown in equation (2.65) is a description of Ostwald ripening as presented by [49]:

$$v(r,t) = \frac{A(t)}{r}\left(\frac{1}{r_c(t)} - \frac{1}{r}\right) z(r,t) \tag{2.66}$$

A lot of work has gone into trying to describe $z(r,t)$ which is a correction factor derived by Marqusee and Ross [52]. This model uses a modification of $z(r,t)$ that accounts for overlapping diffusion fields for neighbouring particles undertaken by Chen and Vorhees [51]).

$$z = 1 + r\sqrt{4\pi N_v \langle r_p \rangle} \tag{2.67}$$

From the distribution generated from equations (2.65) to (2.67) taking moments from $F(r,t)$ will give information on the number of particles per volume N_v, the mean particle size r_p and the volume fraction ϕ_p:

$$N_v = \int F(r,t)dr \tag{2.68}$$

$$r_p = \int rF(r,t)dr \tag{2.69}$$

$$\phi_p = \frac{4\pi}{3}\int r^3 F(r,t)dr \tag{2.70}$$

2.8 Dislocation Background

Previously dislocations have been described by their effect on plastic deformation. In this section dislocations will be examined in greater detail and also the localised effects of the dislocations on other dislocations and their surrounding environment. The term dislocation was first coined by A.E.H.Love [53] and was a renaming of the term "distorsioni" coined by E.Cesaro. This was work progressed from V. Volterra's general description of a resultant stress state due to a localised deformation initially described as the removal of a small piece of material in a cylindrical medium. It was not until 1934 that dislocations started to be described in a more recognised format by Orowan, Polyani and Taylor (1934) as a way to describe material behaviour during plastic deformation. In a medium Γ without a dislocation loop (a perfect crystal) there is no net displacement hence

$$\oint_0^\Gamma \left(\frac{\partial u}{\partial s}\right) ds = 0$$

When there is a displacement effect due to the addition of the dislocation loop this will be the magnitude **b**

$$\oint_0^\Gamma \left(\frac{\partial u}{\partial s}\right) ds = -b$$

Figure 2.14 visualises the introduction of a dislocation into the crystal where the crystal open space between 19-1 is of the magnitude b.

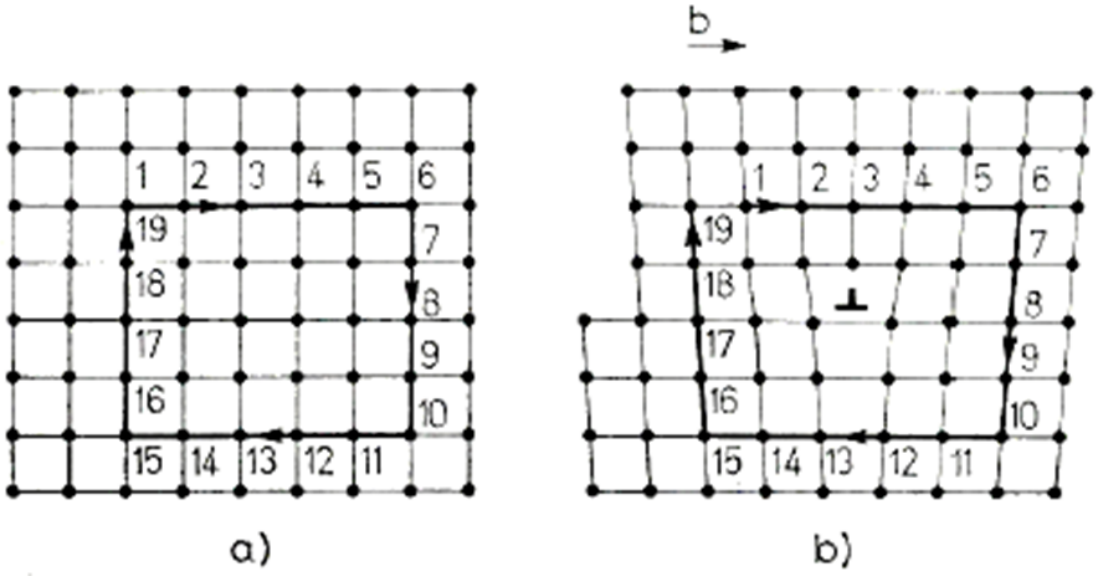


Figure 2.14: Burgers circuit image before a closed loop and after the introduction of a dislocation [54]

Crystallographically a dislocation will typically be confined to the material's crystallographic planes the active of which are known as the slip planes. If a component of the dislocation line is parallel to the slip direction then it is known as a screw dislocation or screw component along the dislocation line. If the dislocation is perpendicular to the slip direction then it is an edge dislocation or edge component along the dislocation line. If the dislocation line component is in between then it is said to be of mixed character For example if the slip direction was (0,0,1) then an edge dislocation would be (b,0,0) and a screw dislocation would be (0,0,b).

One common method to describe a dislocation and its general properties is the Taylor model [55]. This model shows the insertion of a half plane of atoms simulating an edge dislocation moving and shearing the crystal. A similar atomic distortion was built up by Burgers and it shows the displacement effects of inserting a screw dislocation in a crystal. A lot of the work on dislocations was vital in improving the scientific understanding in key areas:

- Crystal physics
- Geometrical and elastic theory

- Crystal growth
- Grain boundary energies (particularly low angle grain boundaries)

2.8.1 Dislocation interactions

The essence of plastic deformation is in the motion of a dislocation (the edge component) equation (2.34). One crucial difference between edge and screw dislocations is their influence on plastic deformation and the conservation of motion. For an edge dislocation the number of atoms is maintained only when the dislocation moves along the glide plane. For the edge to move out of its glide plane there would have to be the emission or absorption of vacancies. This is called climb and it is non-conservative motion. For screw dislocations they are free to move conservatively in any plane that contains **b**, this enable the screw dislocations to glide and to move from one slip plane to another via cross-slip.

A dislocation can have a sense of direction along the slip plane meaning that at a given stress dislocations in one sense will move in the direction of the stress or they will move in the opposite direction. Based on this, dislocations can be classified as either positive or negative. This charge-like attribute affects the dislocation in other ways as well.



Figure 2.15: Images of 2 dislocations with the same sign repelling



Figure 2.16: Images of 2 dislocations with the opposite sign attracting to each other and when they reach each other they annihilate each other

On the same slip plane 2 dislocations of the same sign will repel each other shown in figure 2.15 and if they are of opposite signs they will attract (figure 2.16) until they reach each other and then they annihilate. Dislocations on parallel slip planes if close enough will cause a locking behaviour This will typically be seen in the form of a dipole figure 2.17. Multiple edge dislocations lining up on parallel glide planes will typically be at 45° to each other.

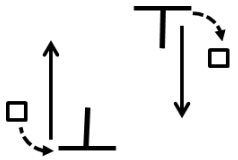


Figure 2.17: Images of 2 dislocations at 45° to each other climbing through the emission and absorption of vacancies

If the stress is large enough this 'wall' of dislocations can move as a single entity [56]. At lower stresses this dislocation 'wall' can act as a pinning point for any dislocations approaching. In regards to pinning dislocations if there are a number of dislocations moving along the glide plane and the leading dislocation is pinned the dislocations will pile up. This will lead to a large stress concentration at the head of the pile up and is a cause for the production of far field effects. Pile-ups can be behind a lot of deformation phenomena, from slip transmission to even crack initiation.

Generation and Annihilation

Dislocations and the material microstructure can act as a source of dislocations which will enable dislocations to be generated and travel throughout the material. Dislocations can originate from the microstructure e.g. at grain boundaries as well as from the interface of secondary phases. If the external stress is very high dislocations moving very quickly will generate dislocations when striking the material surface or even another dislocation.

A Frank-Read source, one of the more commonly explored generation mechanisms, first viewed experimentally when studying the effect which secondary phase precipitates have on dislocations in Al-Cu alloys by H.Wilsdorf and D.Kuhlmannn-Wilsdorf [57]. An image showing an FR loop in silicon is displayed in figure 2.18 below:

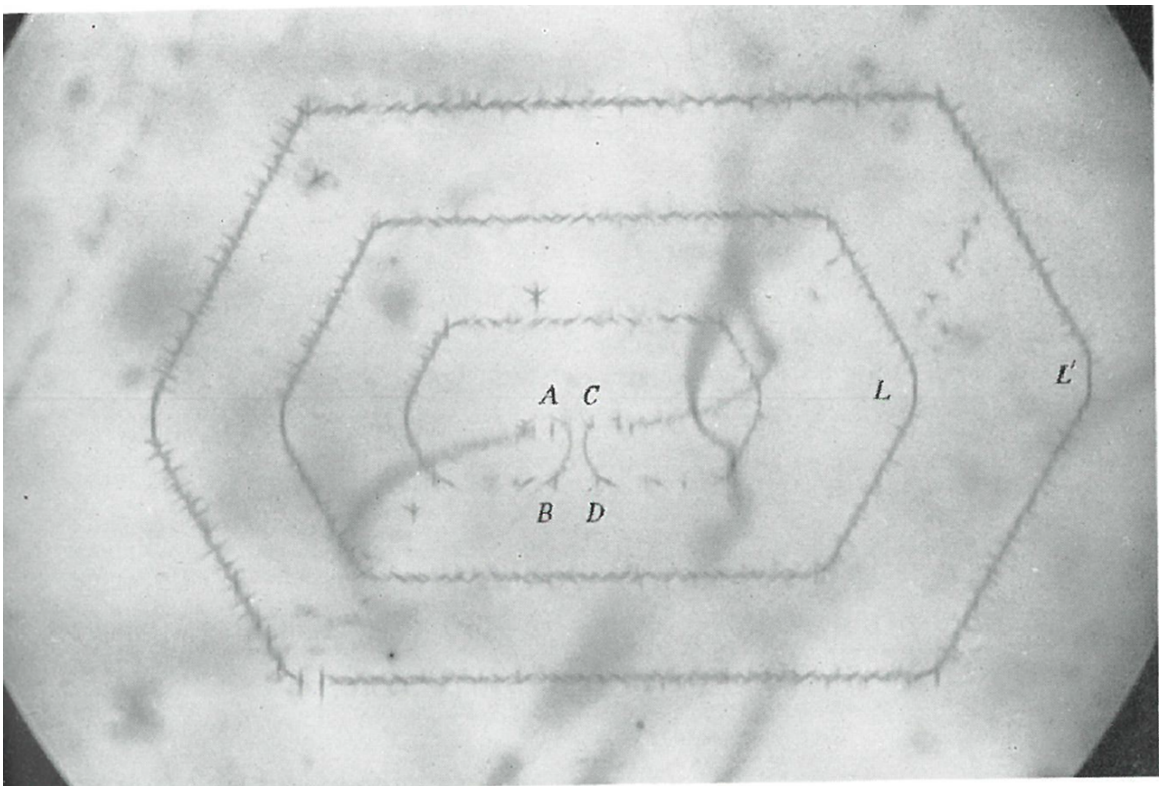


Figure 2.18: Images of a Frank-Read source in silicon decorated with copper by Dash [58]

When a dislocation line meets two pinning points the line within the points will bulge out two corners of the dislocation line in figure 2.18. Points $A\vec{B}$ and the points $C\vec{D}$ will eventually meet, they will then annihilate due to these opposing points having opposite Burgers vector and form a new line to bow at and create another loop. This leaves a loop L in figure 2.18. This loop will grow as seen in L' and move throughout the material. This leaves a dislocation loop free to expand in the glide plane and the dislocation line will generate again.

As mentioned above dislocations can annihilate if the conditions are right. This annihilation process can occur when 2 dislocations of opposite sign meet on the same glide plane and glide into each other. Dislocations will also annihilate when they approach a grain boundary or the surface of the material. In these cases of annihilation these areas are known as sinks. Dislocations can meet each other by escaping their respective planes either via cross slip, or if the temperature is high enough the edge portions will climb and meet each other. It is a common method of dislocation annihilation that a dipole of two opposite sign edge dislocations will climb towards each other until they annihilate as in figure 2.17.

Slip

Plastic deformation and the resultant effects of slip are observable, the ease of which is dependent on the test and the material.

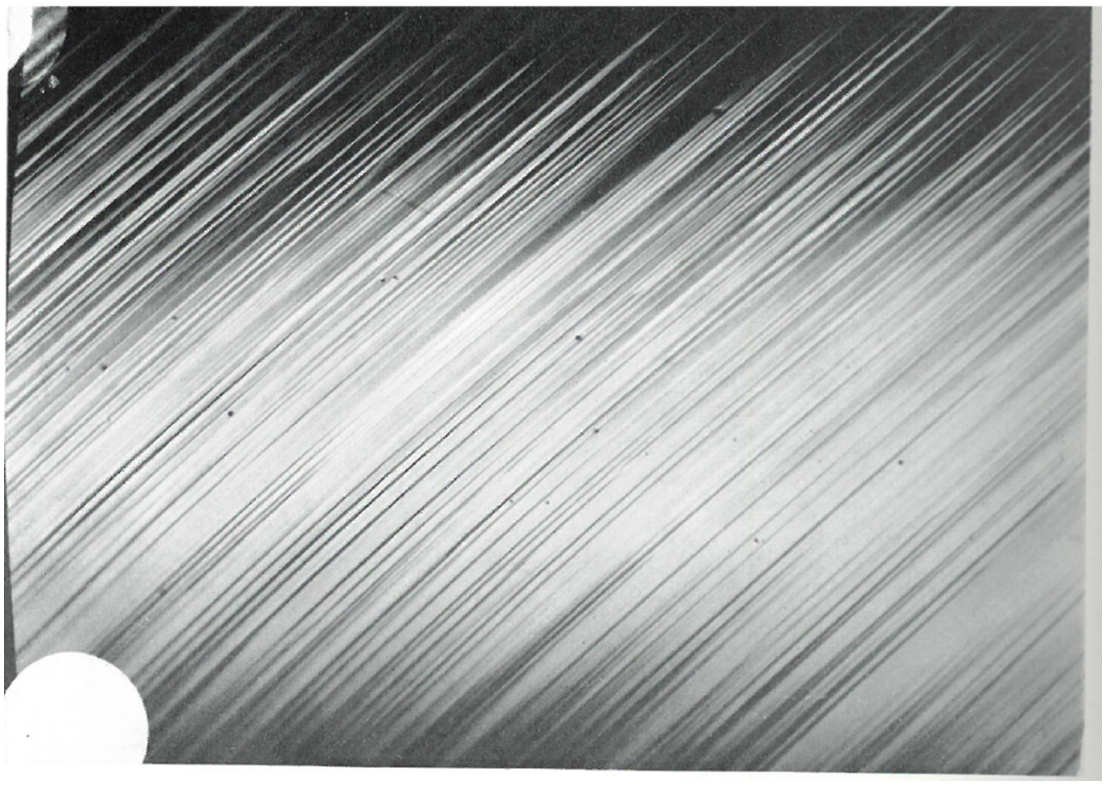


Figure 2.19: Slip lines formed in aluminium from work by Jaul [59]

These experimental results as in figure 2.19 are evidence that slip is localised.

Dislocations are confined to specific planes which if active will allow dislocations to glide. There are a different number of slip planes depending on the material crystal structure. Face Centered Cubic (FCC) is the crystal structure of the material of choice in this study (γ phase in RR1000). There are 4 $\{111\}$ planes and on each slip plane there are 3 $< 011 >$ directions. This gives a total of 12 slip directions the dislocations can move shown in table 2.2. Which slip planes are active depends on the orientation of the crystal in regards to the loading direction.

Planes	(111)	$(11\bar{1})$	$(1\bar{1}1)$	$(\bar{1}11)$
Dimensions	$[1\bar{1}0]$	$[1\bar{1}0]$	$[110]$	$[110]$
	$[10\bar{1}]$	$[101]$	$[10\bar{1}]$	$[0\bar{1}1]$
	$[0\bar{1}1]$	$[0\bar{1}\bar{1}]$	$[0\bar{1}\bar{1}]$	$[\bar{1}0\bar{1}]$

Table 2.2: FCC slip planes and slip directions

Line Tension

The dislocation line itself can also impede its motion due to a line tension effect. The dislocation strain energy is proportional to the dislocation line length as if the dislocation line grows then so does its strain energy. In Hull and Bacon [60], it is explained how both the geometry of the dislocation line and the dislocation component can effect the line tension: it is found that the line tension in a screw dislocation component is $4\times$ that in an edge. A common and simplified version of the line tension equation is given to be [18] [60]:

$$T = \alpha G b^2 \tag{2.71}$$

Where the term α is based on the line geometry and ranges from $0.5 - 1$.

2.8.2 Forces (PK-Force and Peierls Force)

For slip to be achieved the dislocation must move throughout the lattice, but there are certain aspects of the material that impinge dislocation motion. The Peierls force is a force derived from an energy barrier that must be overcome for the dislocations to move. This energy is formed from the configurational changes that are formed with an edge dislocation with the half plane of atoms moving from a stable symmetrical configuration to an unstable unsymmetrical configuration and back to a symmetric configuration. Nabarro [61] gives the derivation of the maximum Peierls force to be:

$$F_{peierls} = \frac{2bG}{1-\nu} \sin 2\pi \exp\left(-\frac{4\pi \frac{2\pi 1-\nu}{b}}{b}\right) \tag{2.72}$$

If the force is large enough to overcome the Peierls barrier the moving dislocation also has a drag that will impinge its movement.

The motion of the dislocation is based on the forces acting on it; one such force is based upon the interaction between dislocations known as the Peach-Koehler force. The idea of such a force was first introduced by Taylor. The force on one dislocation is dependent on the geometry of the other dislocations and the force **F** is comprised of components on all three principal axes.

$$F_{PK} = (\sigma^{\infty} : b) \times \xi \tag{2.73}$$

In instances when dislocation movement is constrained to the glide plane (no climb) then the first component of **F** is considered where if the Burgers vector for example was $(b, 0, 0)$ then:

$$F_x = \sigma_{12} b \; or \; \tau b$$

The above form is typically seen in work [18] when working out shear based on dislocation motion as in the Orowan relation equation (2.34).

Chapter 3

Theoretical framework

This chapter focuses on the derivation of a micromechanics formulation for creep in multimodal precipitate strengthened alloys. First general mathematical considerations of the kinematics of deformation in continuous media are presented (section 3.1), which introduces important measures of elastic and plastic distortions. The principle of objectivity is reviewed in section 3.1.1 from which Jaumann rates are defined and used to calculate the stress rate. A crystal plasticity formulation is outlined (section 3.2) which is used to establish a link between microscale fields and macroscale properties. The creep constitutive model is introduced in section 3.3.

3.1 Kinematics of deformation

Consider a collection of points $\mathbf{X}$ making up a continuum body Ω_0 as shown in figure 3.1. A deformation is any mapping f of the original configuration (reference) Ω_0 to a new configuration (current) Ω_1, i.e., $f : \Omega_0 \mapsto \Omega_1$. Physically this corresponds to a transformation, where all the points $\mathbf{X} \in \Omega_0$ at a time t in the continuum are displaced to a new position $\mathbf{x} \in \Omega_1$ at a later time $t + \delta t$. Points in the current configuration and the reference configuration are related through the expression:

$$\mathbf{x} = \mathbf{u} + \mathbf{X} \quad (\mathbf{x} \in \Omega_1, \mathbf{X} \in \Omega_0) \tag{3.1}$$

Focusing on the mapping of a neighbourhood of $\mathbf{X}$, that is $f : d\mathbf{X} \mapsto d\mathbf{x}$, then for small deformations

$$d\mathbf{x} = d\mathbf{u} + d\mathbf{X} \tag{3.2}$$

$$d\mathbf{x} = (\boldsymbol{\beta} + \mathbf{1})d\mathbf{X} \tag{3.3}$$

$$d\mathbf{x} = \mathbf{F}.d\mathbf{X} \tag{3.4}$$

where $\mathbf{F} = d\mathbf{x}/d\mathbf{X}$ is the deformation gradient tensor, $\boldsymbol{\beta} == \nabla\mathbf{u}$ and $\mathbf{1}$ is the identity tensor. The deformation gradient tensor $\mathbf{F}$ contains all relevant information of the mapping connecting the two configurations and from equation (3.1) we have:

$$\frac{\partial \mathbf{x}}{\partial \mathbf{X}} = \mathbf{1} + \frac{\partial \mathbf{u}}{\partial \mathbf{X}} \Longrightarrow \mathbf{F} = \mathbf{1} + \nabla\mathbf{u} \tag{3.5}$$

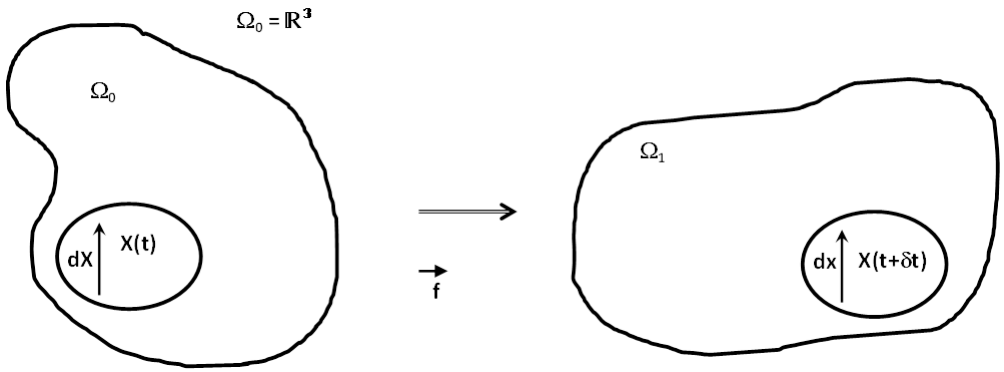


Figure 3.1: Diagram of neighbourhood $\mathbf{X}$ in Ω_0 being deformed and at time $t + \delta t$ body becomes Ω_1 and points become $\mathbf{X}_{(t+\delta t)}$

Let dS and ds be measures of the size of the neighbourhoods in the reference and current configurations, respectively. These are defined as $dS^2 = d\mathbf{X}.d\mathbf{X}$ and $ds^2 = d\mathbf{x}.d\mathbf{x}$. The strain associated with such a deformation is defined in terms of changes in the length of the neighbourhood. This is estimated to be given by

$$ds^2 - dS^2 = d\mathbf{x}.d\mathbf{x} - d\mathbf{X}.d\mathbf{X} \tag{3.6}$$

Inserting equation (3.4) for $d\mathbf{x}$ we obtain:

$$ds^2 - dS^2 = (\mathbf{F}.d\mathbf{X}).(\mathbf{F}.d\mathbf{X}) - d\mathbf{X}.d\mathbf{X} \tag{3.7}$$

$$\begin{aligned} ds^2 - dS^2 &= (d\mathbf{X}^T.\mathbf{F}^T).(\mathbf{F}.d\mathbf{X}) - d\mathbf{X}.\mathbf{1}.d\mathbf{X} \\ ds^2 - dS^2 &= d\mathbf{X}^T(\mathbf{F}^T.\mathbf{F}).d\mathbf{X} - d\mathbf{X}.\mathbf{1}.d\mathbf{X} \end{aligned} \tag{3.8}$$

Take out a $d\mathbf{X}$

$$ds^2 - dS^2 = d\mathbf{X}^T(\mathbf{F}^T.\mathbf{F} - \mathbf{1}).d\mathbf{X} \tag{3.9}$$

Equation (3.9) now becomes:

$$\begin{aligned} ds^2 - dS^2 &= 2d\mathbf{X}^T\left(\mathbf{F}^T.\mathbf{F} - \mathbf{1}\right).d\mathbf{X} \\ ds^2 - dS^2 &= d\mathbf{X}^T.2\mathbf{E}.d\mathbf{X} \end{aligned} \tag{3.10}$$

where the Green-Lagrange strain tensor $\mathbf{E}$ is defined as:

$$\mathbf{E} = \frac{1}{2}\mathbf{F}^T.\mathbf{F} - \mathbf{1} \tag{3.11}$$

The Green-Lagrange strain tensor can also be interpreted in terms of the gradient of displacement from equation (3.5):

$$\mathbf{E} = \frac{1}{2}\left(\left[\mathbf{1} + \mathbf{u}\nabla\right].\left[\mathbf{1} + \nabla\mathbf{u}\right] - \mathbf{1}\right) \tag{3.12}$$

$$= \frac{1}{2}\left(\mathbf{1} + \mathbf{u}\nabla + \nabla\mathbf{u} + \mathbf{u}\nabla.\nabla\mathbf{u} - \mathbf{1}\right) \tag{3.13}$$

$$= \frac{1}{2}\left(\mathbf{u}\nabla + \nabla\mathbf{u} + \mathbf{u}\nabla.\nabla\mathbf{u}\right) \tag{3.14}$$

In a small strain approximation the second order terms of the displacement

gradient can be ignored and the strain tensor becomes

$$\boldsymbol{\varepsilon} = \frac{1}{2}\left(\mathbf{u}\nabla + \nabla\mathbf{u}\right) \tag{3.15}$$

The velocity gradient tensor $\mathbf{L}$ measures the rate of deformation in the deformed body Ω_1 and is defined as:

$$\mathbf{L} = \nabla\mathbf{v} = \frac{\partial\mathbf{v}}{\partial\mathbf{x}} \tag{3.16}$$

Inserting the definition of the deformation gradient tensor:

$$\dot{\mathbf{F}} = \frac{\partial}{\partial t}\left(\frac{\partial\mathbf{x}}{\partial\mathbf{X}}\right) \tag{3.17}$$

from which the following evolution law for the deformation rate is obtained

$$\dot{\mathbf{F}} = \mathbf{L}\mathbf{F} \tag{3.18}$$

and in rearranging the above equation:

$$\mathbf{L} = \dot{\mathbf{F}}\mathbf{F}^{-1} \tag{3.19}$$

The symmetric and antisymmetric parts of the velocity gradient tensor give the stretch tensor $\mathbf{D}$ and the spin tensor $\mathbf{W}$ respectively:

$$\mathbf{D} = sym\left(\mathbf{L}\right) = \frac{1}{2}\left(\mathbf{L} + \mathbf{L}^T\right) \tag{3.20}$$

$$\mathbf{W} = Asym(\mathbf{L}) = \frac{1}{2}\left(\mathbf{L} - \mathbf{L}^T\right) \tag{3.21}$$

3.1.1 Objectivity

During the deformation process the concept of objectivity must be addressed. This is due to the transformation from one coordinate system to another during defor-

mation. Objectivity is the condition of frame invariance where the transformation of vector $\mathbf{v}$ and tensor $\mathbf{A}$ becomes:

$$\begin{aligned} \mathbf{v}^* &= \mathbf{Q}.\mathbf{v} \\ \mathbf{A}^* &= \mathbf{Q}.\mathbf{A}.\mathbf{Q}^T \end{aligned} \tag{3.22}$$

To determine whether or not the deformation gradient tensor is objective first consider the coordinates to affine mapping such that the transformation is:

$$\mathbf{x}^* = \mathbf{Q}(t).\mathbf{x} + c(t) \tag{3.23}$$

$$d\mathbf{x}^* = \mathbf{Q}.d\mathbf{x} = \mathbf{Q}.\mathbf{F}.d\mathbf{X} \tag{3.24}$$

$$\begin{aligned} \mathbf{F}^*.d\mathbf{X} &= \mathbf{Q}.\mathbf{F}.d\mathbf{X} \\ \mathbf{F}^* &= \mathbf{Q}.\mathbf{F} \end{aligned} \tag{3.25}$$

Equation (3.25) shows that the deformation gradient tensor transforms like a vector and is thus objective. A similar procedure is applied to the velocity gradient tensor described in equation (3.19)

$$\mathbf{L}^* = \dot{\mathbf{F}}^*.\mathbf{F}^{*-1} = \dot{\mathbf{Q}}.\mathbf{Q}^T + \mathbf{Q}.\mathbf{L}.\dot{\mathbf{Q}}^T \tag{3.26}$$

This shows that the velocity gradient tensor is not objective, the impact on the stretch and spin tensors is:

$$\mathbf{D}^* = sym\,(\mathbf{L}^*) = \mathbf{Q}.\mathbf{D}.\mathbf{Q}^T \tag{3.27}$$

$$\mathbf{W}^* = Asym\,(\mathbf{L}^*) = \mathbf{Q}.\mathbf{W}.\mathbf{Q}^T + \dot{\mathbf{Q}}.\mathbf{Q}^{-1} \tag{3.28}$$

This shows that the stretch tensor $\mathbf{D}$ is objective, but the spin tensor $\mathbf{W}$ is not. With regards to the stress, the stress tensor is objective

$$\boldsymbol{\sigma}^* = \mathbf{Q}.\boldsymbol{\sigma}.\mathbf{Q}^T \tag{3.29}$$

$$\dot{\boldsymbol{\sigma}} = \dot{\mathbf{Q}}.\boldsymbol{\sigma}.\mathbf{Q}^T + \mathbf{Q}.\dot{\boldsymbol{\sigma}}.\mathbf{Q}^T + \mathbf{Q}.\boldsymbol{\sigma}.\dot{\mathbf{Q}}^T \tag{3.30}$$

from equation (3.28) rearranged to form

$$\mathbf{W}^*.\mathbf{Q}^{T-1} = \mathbf{Q}.\mathbf{W} + \dot{\mathbf{Q}}$$

Since $\mathbf{Q}$ is orthogonal matrix the inverse transpose is the matrix

$$\therefore \dot{\mathbf{Q}} = \mathbf{W}^*.\mathbf{Q} - \mathbf{Q}.\mathbf{W} \tag{3.31}$$

$$\dot{\mathbf{Q}} = (\mathbf{W}^* - \mathbf{W})\,\mathbf{Q}$$

It should be noted that

$$\mathbf{Q}.\mathbf{Q}^T = \mathbf{1}$$

$$\dot{\mathbf{Q}}^T = -\mathbf{Q}^T.\mathbf{W}^*.\mathbf{Q}.\mathbf{Q}^T + \mathbf{Q}^T.\mathbf{Q}.\mathbf{W}.\mathbf{Q}^T$$

$$\therefore \dot{\mathbf{Q}}^T = -\mathbf{Q}^T.\mathbf{W}^* + \mathbf{W}.\mathbf{Q}^T \tag{3.32}$$

Feed equations (3.31) and (3.32) into equation (3.30)

$$\dot{\boldsymbol{\sigma}}^* = \mathbf{W}^*.\mathbf{Q}.\boldsymbol{\sigma}\mathbf{Q}^T - \mathbf{Q}.\mathbf{W}.\boldsymbol{\sigma}\mathbf{Q}^T + \mathbf{Q}\dot{\boldsymbol{\sigma}}.\mathbf{Q}^T + \mathbf{Q}.\boldsymbol{\sigma}.\mathbf{W}.\mathbf{Q}^T - \mathbf{Q}.\boldsymbol{\sigma}.\mathbf{Q}^T.\mathbf{W}^* \tag{3.33}$$

Rearrange and group terms to get:

$$\dot{\boldsymbol{\sigma}}^* = \mathbf{Q}.\left(\boldsymbol{\sigma}.\mathbf{W} - \mathbf{W}.\boldsymbol{\sigma} + \dot{\boldsymbol{\sigma}}\right).\mathbf{Q}^T + \mathbf{W}^*.\mathbf{Q}.\boldsymbol{\sigma}.\mathbf{Q}^T - \mathbf{Q}.\boldsymbol{\sigma}.\mathbf{Q}^T.\mathbf{W}^* \tag{3.34}$$

Substituting equation (3.29) into equation (3.34)

$$\boldsymbol{\sigma}^*.\mathbf{W}^* - \mathbf{W}^*.\boldsymbol{\sigma}^* + \dot{\boldsymbol{\sigma}}^* = \mathbf{Q}.\left(\boldsymbol{\sigma}.\mathbf{W} - \mathbf{W}.\boldsymbol{\sigma} + \dot{\boldsymbol{\sigma}}\right).\mathbf{Q}^T \tag{3.35}$$

The last result shows that the term in the brackets is objective, the co-rotational stress state is known as the Jaumann rate:

$$\overset{\nabla}{\boldsymbol{\sigma}} = \dot{\boldsymbol{\sigma}} - \mathbf{W}.\boldsymbol{\sigma} + \boldsymbol{\sigma}.\mathbf{W} \tag{3.36}$$

To update the stress state at any point in the material uses Hooke's law

$$\overset{\nabla}{\boldsymbol{\sigma}} = \mathbf{C} : (\mathbf{D} - \mathbf{D}^p) = \mathbf{C} : \mathbf{D}^e \tag{3.37}$$

Where $\mathbf{C}$ is the compliance tensor and $\mathbf{D}^e$ is the elastic portion of the stretch tensor. The stress rate is then calculated from the Jaumann stress rate:

$$\dot{\boldsymbol{\sigma}} = \overset{\nabla}{\boldsymbol{\sigma}} - \mathbf{W}.\boldsymbol{\sigma} + \boldsymbol{\sigma}.\mathbf{W} \tag{3.38}$$

3.2 Micro- to Macroscale viscoplastic modelling

Crystal plasticity is a general kinematic description for lattice distortion first given by Rice [62]. A neighbourhood is identified, from which the macroscale properties can be derived. Such a neighbourhood is a representative volume element (RVE) and contains a polycrystalline grain structure. Dislocation slip is allowed to occur along certain closed packed crystallographic planes and directions. The resulting shear rates are used to determine the microscale stress tensor through application of Lee's decomposition (section 3.2) of the deformation gradient tensor into elastic and plastic parts. The macroscale stress state is obtained through a volume average of the microscale stress field. For further details on the general theory and its implementation into finite element calculations see Dunne and Petrinic [63].

In nickel-based superalloys the slip systems are $< 111 > \{110\}$. These make 12 potential slip systems and are summarised in table 2.2. Let the plane normal and slip direction be denoted by $\mathbf{n}$ and $\mathbf{s}$, respectively. If $\boldsymbol{\sigma}$ is the local stress, then

the shear stress τ on an active slip system is given by:

$$\tau = \mathbf{s} \cdot \boldsymbol{\sigma} \cdot \mathbf{n} \tag{3.39}$$

This will provide a force on dislocations resulting in their glide. The associated shear strain rates can be expressed in terms of constitutive relations of the general form:

$$\dot{\gamma} = \dot{\gamma}\left(\tau, \tau_k, \rho_m, \phi_p, \lambda_p, T...\right) \tag{3.40}$$

$$\dot{\tau}_k = \dot{\tau}_k\left(\dot{\gamma}, \tau, \rho_m, \phi_p, \lambda_p, T...\right) \tag{3.41}$$

$$\dot{\rho}_m = \dot{\rho}_m\left(\dot{\gamma}, \tau, \tau_k, \phi_p, \lambda_p, T...\right) \tag{3.42}$$

$$\tag{3.43}$$

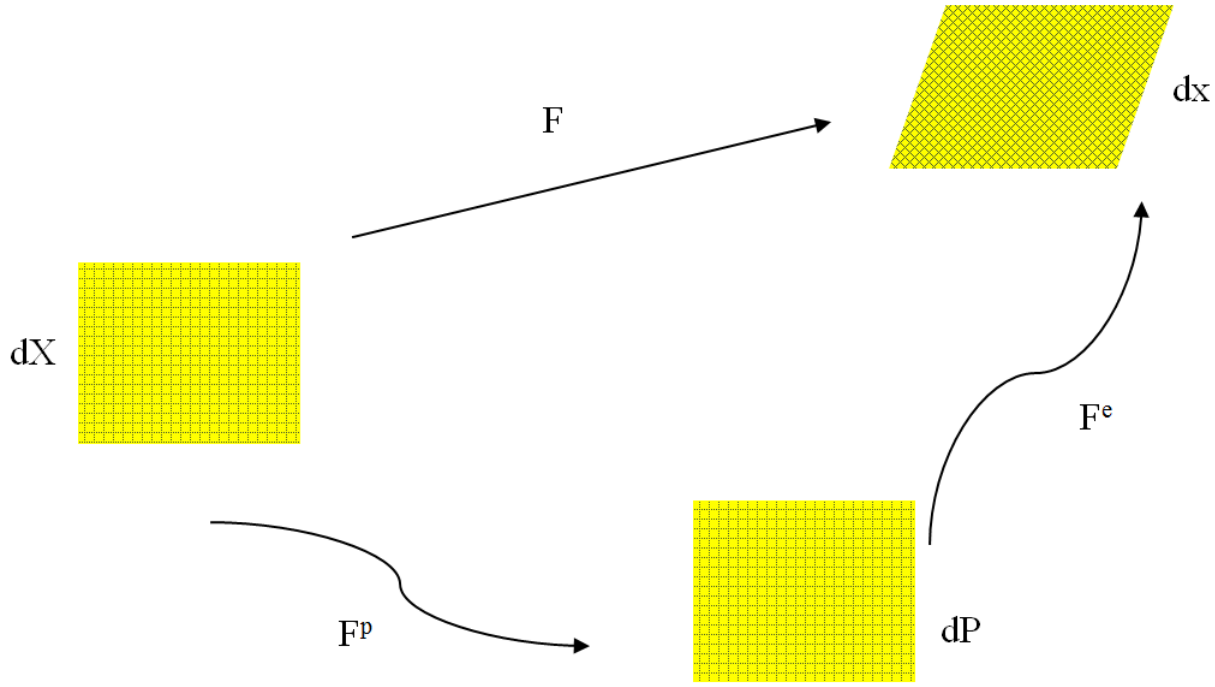


Figure 3.2: Schematic of Lee's decomposition showing breaking down the transition of deformation into plastic and elastic components

As already stated, the total deformation gradient can be decomposed into plastic and elastic parts. This is know as Lee's decomposition and requires the introduction of an intermediate configuration Ω_p. Let the $\mathbf{P} \in \Omega_p$, then we can define plastic deformation as a transformation satisfying

$$d\mathbf{P} = \frac{\partial \mathbf{P}}{\partial \mathbf{X}} \cdot d\mathbf{X} \;\Rightarrow\; d\mathbf{P} = \mathbf{F}^p \cdot d\mathbf{X} \tag{3.44}$$

where $\mathbf{F}^p$ is the plastic deformation gradient tensor. The elastic distortions are associated with a mapping from the intermediate to the current configuration:

$$d\mathbf{x} = \frac{\partial \mathbf{x}}{\partial \mathbf{P}} \cdot d\mathbf{P} \;\Rightarrow\; d\mathbf{x} = \mathbf{F}^e \cdot d\mathbf{P} \tag{3.45}$$

where $\mathbf{F}^e = d\mathbf{x}/d\mathbf{P}$ is the elastic deformation gradient tensor. By substituting in $d\mathbf{P}$ from equation (3.44) into equation (3.45) we obtain the statement of decomposition of the total deformation gradient into elastic and plastic contributions

$$\mathbf{F} = \mathbf{F}^e \cdot \mathbf{F}^p \tag{3.46}$$

The plastic part of the velocity gradient tensor $\mathbf{L}^p$ is given by

$$\mathbf{L}^p = \sum_\alpha \dot{\boldsymbol{\gamma}}^\alpha \left(\mathbf{s}^\alpha \otimes \mathbf{n}^\alpha\right) \tag{3.47}$$

where the summation is over all active slip systems. From the definition of L^p the following differential equation is obtained for the plastic part of the deformation gradient tensor:

$$\dot{\mathbf{F}}^p = \mathbf{F}^p \cdot \mathbf{L}^p \tag{3.48}$$

For small time increment δt equation (3.48) has the following solution:

$$\dot{\mathbf{F}}^p(t + \delta t) = (\mathbf{1} + \mathbf{L}^p \delta t) \cdot \dot{\mathbf{F}}^p(t) \tag{3.49}$$

Once $\mathbf{F}^p$ has been calculated then $\mathbf{F}^e$ can be determined from equation (3.46):

$$\mathbf{F}^e = \mathbf{F} \cdot \mathbf{F}^{p-1} \tag{3.50}$$

The elastic strain tensor can now be calculated using the relation for small strains

$$\boldsymbol{\varepsilon} = \frac{1}{2}\left(\mathbf{F}^{eT} \cdot \mathbf{F}^e - \mathbf{1}\right) \tag{3.51}$$

With the strain now calculated the stress can now be updated:

$$\boldsymbol{\sigma} = \mathbf{C} : \boldsymbol{\varepsilon} \tag{3.52}$$

3.2.1 Taylor Factor

The Taylor factor is a parameter that scales up material behaviour defined on the material slip systems and up-scales to macroscale behaviour. The work by Havner [64] explains Taylor's work [55] and starts off by analysing potential activity on the slip systems analysing the resultant stretch $\mathbf{D}$ and spin $\mathbf{W}$ on the slip systems:

$$\begin{aligned}
\sqrt{6}D_{11} &= ([01\bar{1}],[01\bar{1}],[01\bar{1}],[01\bar{1}])\,\dot{\gamma} \\
\sqrt{6}D_{22} &= ([\bar{1}01],[\bar{1}01],[\bar{1}01],[\bar{1}01])\,\dot{\gamma} \\
\sqrt{6}D_{33} &= ([1\bar{1}0],[1\bar{1}0],[1\bar{1}0],[1\bar{1}0])\,\dot{\gamma} \\
\sqrt{6}D_{23} &= ([0\bar{1}1],[01\bar{1}],[0\bar{1}1],[01\bar{1}])\,\dot{\gamma} \\
\sqrt{6}D_{13} &= ([10\bar{1}],[\bar{1}01],[\bar{1}01],[10\bar{1}])\,\dot{\gamma} \\
\sqrt{6}D_{12} &= ([\bar{1}10],[\bar{1}10],[1\bar{1}0],[1\bar{1}0])\,\dot{\gamma}
\end{aligned} \tag{3.53}$$

and

$$\begin{aligned}
\sqrt{6}W_{32} &= ([2\bar{1}\bar{1}], [\bar{2}11], [2\bar{1}\bar{1}], [\bar{2}11])\,\dot{\gamma} \\
\sqrt{6}W_{13} &= ([\bar{1}2\bar{1}], [1\bar{2}1], [1\bar{2}1], [\bar{1}2\bar{1}])\,\dot{\gamma} \\
\sqrt{6}W_{12} &= ([\bar{1}\bar{1}2], [[\bar{1}\bar{1}2], [11\bar{2}], [11\bar{2}])\,\dot{\gamma}
\end{aligned} \tag{3.54}$$

Where $\dot{\gamma}$ is a vector with the 12 possible slip rates in an FCC crystal. The conditions are such that every grain within the polycrystalline material is assumed to have uniform macroscopic deformation and the same rigid body motion ensured by having a reference frame which each grain can be verified against. The Euler-angles θ_L, ψ_L, ϕ_L:

$$\begin{aligned}
e_1 &= (e_u \cos\theta_L - e_z \sin\theta_L)\cos\psi_L + e_v \sin\psi_L \\
e_2 &= -(e_u \cos\theta_L - e_z \sin\theta_L)\sin\psi_L + e_v \cos\psi_L \\
e_3 &= e_u \sin\theta_L + e_z \cos\theta_L \\
&\textit{where} \\
e_u &= e_x \cos\phi_L + e_y \sin\phi_L,\; e_v = -e_x \sin\phi_L + e_y \cos\phi_L
\end{aligned} \tag{3.55}$$

Are used to create the transformation matrix $\mathbf{Q}$

$$\mathbf{Q} = \begin{bmatrix}
\cos\phi\cos\theta\cos\psi - \sin\phi\sin\psi, & \sin\phi\cos\theta\cos psi + \cos\phi\sin\psi, & -\sin\theta\cos\psi \\
\cos\phi\cos\theta\sin\psi - \sin\phi\cos\psi, & -\sin\phi\cos\theta\sin\psi + \cos\phi\cos\psi, & \sin\theta\sin\psi \\
\cos\phi\sin\theta, & \sin\phi\sin\theta, & \cos\theta
\end{bmatrix} \tag{3.56}$$

This is used to rotate the strains generated along the slip system along the local crystal system and translate those strains along the entire specimen.

$$\mathbf{D} = \mathbf{Q}\bar{\mathbf{D}}\mathbf{Q}^T \tag{3.57}$$

For equation (3.53) and equation (3.54) to be valid there would have to be at least 5 slip systems active in each grain. Relating the strain in the grain with the mechanics of frictional systems Taylor assumes that there are exactly 5 systems active in each grain. It can be determined using binomial theorem:

$$ {}_nC_k = \frac{n!}{(n-k)!k!} $$

Where $n = 12$ and $k = 5$ it shows that there are a possibility of 792 different slip combinations. Further work by Taylor [37] showed that this number of sets could be reduced to 384 independent sets. The entire crystal slip from all the applied systems is based on doing the least incremental work based on Taylor's principle of minimum shears:

$$ tr(\bar{\sigma}\bar{D}) =< \dot{W} >= \left\langle \sum (\tau\dot{\gamma})_j \right\rangle = \left\langle t_c (min \sum |\dot{\gamma}_j| \right\rangle \tag{3.58} $$

The average critical stress in the aggregate can be determined to be:

$$ d\dot{W} =< dW >= \left\langle \tau_c \left(min \sum |d\dot{\gamma}_j| \right) \right\rangle = \bar{\tau}_c \left\langle min \sum |\dot{\gamma}_j| \right\rangle \tag{3.59} $$

Restricting the work to axisymmetric deformation 'Tension' such that $d\bar{W} = \bar{\sigma}_a d\bar{e}_L$, $\bar{d}_{xx} = (\bar{e}_L)$ and $\bar{d}_{yy} = \bar{d}_{zz} = -\frac{1}{2}(\bar{e}_L)$, from equation (3.59)

$$ \frac{\bar{\sigma}_a}{\bar{\tau}_c} = \bar{M} = \frac{\langle min \sum |d\dot{\gamma}_j| \rangle}{d\bar{e}_L} \tag{3.60} $$

The resultant examination (concluding 168 slip sets are geometrically admissible) determined $\bar{M} = 3.1$. Havner explains that later work by Bishop and Hill [65] did include the the admissible slip systems, which did not make a significant difference (found to be $\bar{M} = 3.06$) [64].

3.2.2 J2 theory and Scale invariance

At the macroscale, the plastic response of an isotropic material is described by J2-theory. In the framework the plastic stretch tensor $\mathbf{D}^p$ is given by

$$\mathbf{D}^p = \frac{3}{2}\left(\frac{\dot{\varepsilon}^p}{\sigma_{mises}}\right)\mathbf{S} \tag{3.61}$$

where $\dot{\varepsilon}^p$ and σ_{mises} are the effective uniaxial plastic strain rate and effective stress, respectively. The effective stress is defined as

$$\sigma_{mises} = \sqrt{\frac{(\sigma_{11}-\sigma_{22})^2 + (\sigma_{22}-\sigma_{33})^2 + (\sigma_{33}-\sigma_{22})^2 + 6(\sigma_{12}^2+\sigma_{23}^2+\sigma_{31}^2)^2}{2}} \tag{3.62}$$

The deviatoric stress $\mathbf{S}$ is given by

$$\mathbf{S} = \boldsymbol{\sigma} - \frac{1}{3}\sigma^H\mathbf{1} \tag{3.63}$$

where

$$\sigma^H = (\sigma_{11}+\sigma_{22}+\sigma_{33})$$

The principle of scale invariance states that the form of the macroscale plastic rate has the same functional dependencies on stress, temperature and microstructure as the plastic shear rates on active slip systems. Using this principle, then effective plastic strain rate $\dot{\varepsilon}^p$ and stress σ are related to the shear rate γ^p and shear stress τ through the scaling relations:

$$\sigma = \tau\bar{M}\ ,\ \varepsilon^p = \frac{\gamma^p}{\bar{M}} \tag{3.64}$$

where $\bar{M}$ is the Taylor factor introduced in the previous section.

3.3 Microstructure explicit shear rate model

In precipitate strengthened nickel-based superalloys, the γ' dispersion acts a barrier to dislocation motion in the austenitic γ matrix. At any given moment in time the mobile dislocation segment will either be gliding in the matrix or waiting at a particle/matrix interface. At high enough temperatures the waiting segments can overcome the pinning particle through dislocation climb. With these considerations, it is useful to decompose the mobile scalar dislocation density into gliding ρ_g and waiting (or climbing) ρ_c densities

$$\rho_m = \rho_g + \rho_c \tag{3.65}$$

The evolution of the gliding dislocations density can be modelled as a continuity condition, where the rate of change of ρ_g is expressed in terms of generation $\dot{\rho}_g^+$ and trapping $\dot{\rho}_g^-$ rates. These represent escape of waiting/climbing dislocations from a particle and the intersection of gliding dislocations by a γ' particle. The continuity condition is given by

$$\dot{\rho}_g = \dot{\rho}_g^+ - \dot{\rho}_g^- \tag{3.66}$$

The generation and annihilation process can be both described as:

$$\dot{\rho}_g^{\pm} = number\ available \times probability(\pm) \times frequency\ of\ event$$

The trapping rate is the rate of interception of gliding dislocations, which occurs at a frequency given by $\bar{v}_g/\lambda_p$, where $\bar{v}_g$ is the mean glide velocity and λ_p is the mean free path of a gliding dislocation. The latter will be assumed to equal to the inter-particle spacing. So for this case we have the following for the trapping rate

$$\dot{\rho}_g^- = \rho_g \frac{\bar{v}_g}{\lambda_p} \tag{3.67}$$

Although three populations of γ' are present in fine grain RR1000, only the secondary and tertiary populations will interact with gliding dislocations. As such the mean free path will be a function of their spacings, i.e., $\lambda_p = f(\lambda_{p,2}\ ,\ \lambda_{p,3})$, where $\lambda_{p,2}$ and $\lambda_{p,3}$ are the secondary and tertiary particle spacings, respectively.

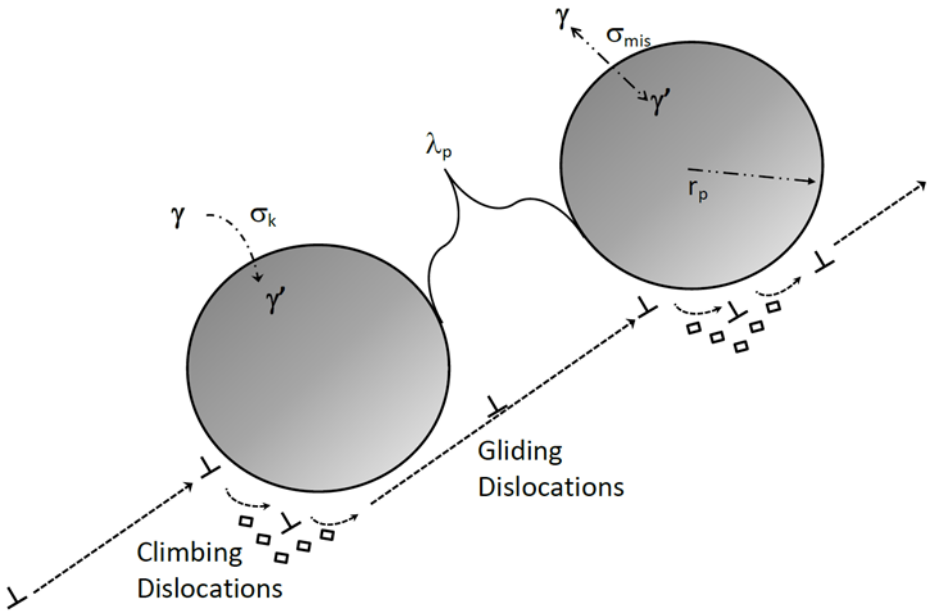


Figure 3.3: Image showing all the combined constitutive effects in the proposed creep formulation

In the present treatment, the generation rate is the frequency of waiting dislocation escaping a particle through local climb. Consider for the moment a regular particle dispersion, composed of particles with size $2r_p$ separated by λ_p. Suppose that a dislocation is located at some position y and is moving along the x-axis. The probability density of a dislocation being intercepted by a particle at y is $f(y) = r_p/\lambda_p$. Therefore, the probability that a dislocation is waiting at a particle if it is located between the interval $y_1 < y \leq y_1 + 2r_p$ is given by

$$P\left[y_1 < y \leq y_1 + 2r_p\right] = \int_{y_1}^{y_1+2r_p} f(y)dy = \frac{2r_p}{\lambda_p}$$

Let ϕ_s be the area fraction of particles, $\phi_s = (2r_p/\lambda_p)^2$. Then it follows that the

probability of having a waiting dislocation is given by

$$P\left[y_1 < y \leq y_1 + 2r_p\right] = \phi_s^{\frac{1}{2}}$$

Now consider a distribution of particle size $2r_{p,1}, 2r_{p,2}, ...$ separated by $\lambda_{p,1}, \lambda_{p,2}, ...$ Performing a similar procedure as before the probability of a dislocation waiting at a particle of size $2r_{p,i}$ is $P_i[waiting] = n_i \frac{2r_{p,i}}{\lambda_{p,i}} = \phi_{s,i}^{\frac{1}{2}}$, where n_i is the number density of particles with size $2r_{p,i}$. If we assume that most of the mobile dislocations are waiting, then number of waiting dislocations at the i-th particle population is $\rho_m \, P_i[waiting]$. The probability that the dislocation is at the top of the particle and ready to be released by a climb is $b/r_{p,i}$ where b is the Burgers magnitude. Then the probability that a dislocation will escape from a particle in the i-th population is $\phi_{s,i}^{\frac{1}{2}} \, b/r_{p,i}$ Thus the total density of waiting dislocations is $\rho_m \, \left(\phi_{s,1}^{\frac{1}{2}} \, b/r_{p,1} + \phi_{s,2}^{\frac{1}{2}} \, b/r_{p,2} + ...\right)$ If the escape frequency is v_c/b then the generation rate

$$\dot{\rho}_g^+ = \rho_m \, \left(\frac{\phi_{s,1}^{\frac{1}{2}}}{r_{p,1}} + \frac{\phi_{s,2}^{\frac{1}{2}}}{r_{p,2}} + ... \right) \, v_c \tag{3.68}$$

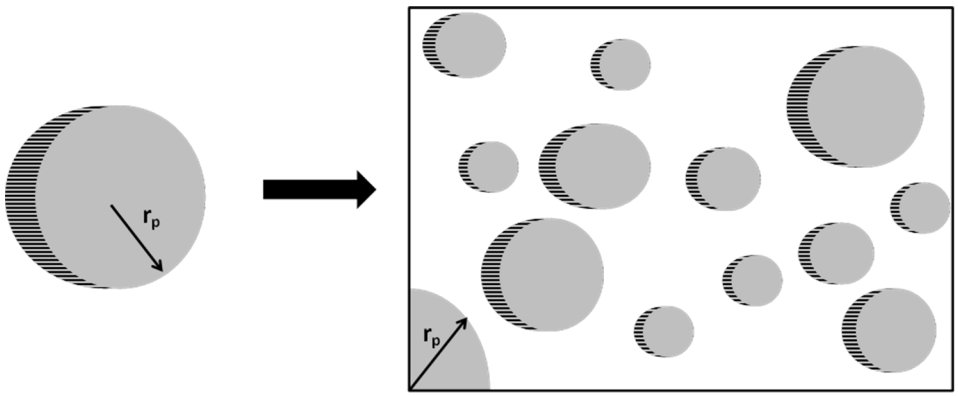


Figure 3.4: Distribution of particle spheres on a plane

The evolution of the gliding dislocations becomes

$$\dot{\rho}_g = \rho_m \left(\frac{\sqrt{\phi_{p,2}}}{r_{p,2}} + \frac{\sqrt{\phi_{p,3}}}{r_{p,3}} \right) v_c - \rho_g \frac{\bar{v}_g}{\lambda_p} \tag{3.69}$$

By integrating equation (3.69) the temporal solution for the gliding dislocation density is given by

$$\rho_g = \frac{\rho_m \lambda_p \left(\frac{\sqrt{\phi_{p,2}}}{r_{p,2}} + \frac{\sqrt{\phi_{p,3}}}{r_{p,3}} \right) v_c}{\bar{v}_g} \left[1 - \exp\left(-\frac{\bar{v}_g}{\lambda_p} t \right) \right] \tag{3.70}$$

Multiplying the above equation by the mean glide velocity $\bar{v}_g$ and using the Orowan relation equation (2.34), an expression for the shear rate is derived and assuming that $\frac{\bar{v}_g}{\lambda_p}$ is large the exponential term in the [ ] vanishes and equation (3.70) becomes:

$$\dot{\gamma} = b \rho_m \lambda_p \left(\frac{\sqrt{\phi_{p,2}}}{r_{p,2}} + \frac{\sqrt{\phi_{p,3}}}{r_{p,3}} \right) v_c \tag{3.71}$$

where $\bar{v}_g / \lambda_p$ has been assumed to be large. This will in general be true since λ_p is small (nm scale) compared to the glide velocity.

The climb rate of a waiting dislocation is governed by vacancy assisted diffusion [66]. The climbing velocity is:

$$v_c = \frac{4\pi D_v c_j}{b} \sinh\left(\frac{\tau \lambda b^2}{K_B T} \right) \tag{3.72}$$

where the jog concentration during the creep process is assumed to be a constant value c_j [66]. K_B is Boltzmann's constant. Using equation (3.72) into equation (3.71) and cancelling out the b,

$$\dot{\gamma} = 4\pi \lambda_p \rho_m D_v c_j \left(\frac{\sqrt{\phi_{p,2}}}{r_{p,2}} + \frac{\sqrt{\phi_{p,3}}}{r_{p,3}} \right) \sinh\left(\frac{\tau \lambda_p b^2}{K_B T} \right) \tag{3.73}$$

Since only the matrix is deforming plastically the term $(1 - \phi_p)$ is added to account for matrix only deformation so that the creep constitutive equation becomes:

$$\dot{\gamma} = 4\pi \lambda_p \rho_m D_v c_j (1 - \phi_p) \left(\frac{\sqrt{\phi_{p,2}}}{r_{p,2}} + \frac{\sqrt{\phi_{p,3}}}{r_{p,3}} \right) \sinh\left(\frac{\tau \lambda_p b^2}{K_B T} \right) \tag{3.74}$$

3.4 Stress Partitioning

3.4.1 Back Stress

Stress transfer between the γ and γ' phases during creep deformation will result in a reduction in the matrix stress, which in turn will reduce the shear rate in an active slip system. This back stress is a mechanism proposed by Ion et al [6] as a way of explaining the primary evolution of creep in Nickel based superalloys; utilising the influence of the γ' rather than work hardening models previously used for pure metals.

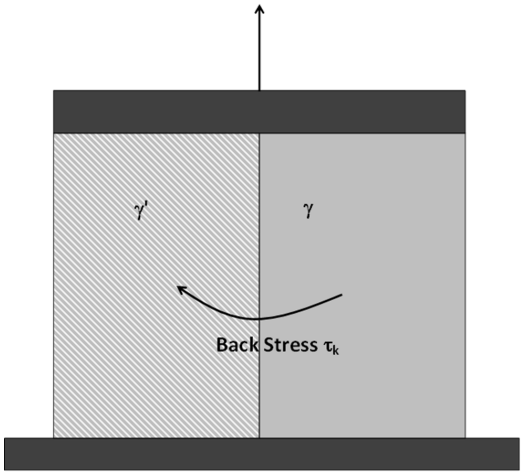


Figure 3.5: Figure of loading effect on γ and γ'

The loading at a stress τ can be split into two portions; the elastically deforming particle:

$$\gamma_p^T = \frac{\dot{\tau}_p}{G_p} \tag{3.75}$$

and the plastically deforming matrix:

$$\gamma_m^T = \frac{\dot{\tau}_m}{G_m} + \dot{\gamma}_m^c \tag{3.76}$$

In order to maintain the rule of compatibility the total strain is the same in the

matrix as in the particle as shown in figure 3.5:

$$\gamma^T = \gamma_m^T = \gamma_p^T \tag{3.77}$$

Combining equations (3.75) to (3.77) we have:

$$\frac{\dot{\tau}_p}{G_p} = \frac{\dot{\tau}_m}{G_m} + \dot{\gamma}_m^c \tag{3.78}$$

Rearranging we obtain the evolution of the stress in the γ' particles

$$\dot{\tau}_p = \frac{G_p}{G_m}\dot{\tau}_m + G_p\dot{\gamma}_m^c \tag{3.79}$$

or in the γ matrix

$$\dot{\tau}_m = \frac{G_m}{G_p}\dot{\tau}_p - G_p\dot{\gamma}_m^c \tag{3.80}$$

At the instance of loading $t = 0$: $\tau_p(0) = \tau$ and $\tau_m(0) = \tau$. From the last expression it can be seen that the particles take an increased stress whilst in the matrix this decreases. It is useful to introduce a stress τ_k defined as

$$\dot{\tau_m} = \dot{\tau} - \dot{\tau_k} \tag{3.81}$$

Such a stress acts as a back stress since it opposes the applied stress. Putting equation (3.81) into equation (3.79) to get:

$$\dot{\tau}_p = \frac{G_p}{G_m}\left(\dot{\tau} - \dot{\tau}_k\right) + G_m\dot{\gamma}_m^c \tag{3.82}$$

The equilibrium conditions:

$$\begin{aligned} \tau &= \phi_p\tau_p + \phi_m\tau_m \\ 1 &= \phi_p + \phi_m \end{aligned} \tag{3.83}$$

in rate form:

$$\dot{\tau} = \phi_p \dot{\tau}_p + \phi_m \dot{\tau}_m \tag{3.84}$$

Multiply equation (3.82) by ϕ_p

$$\phi_p \dot{\tau}_p = \phi_p \frac{G_p}{G_m} \left(\dot{\tau} - \dot{\tau}_k \right) + G_m \dot{\gamma}_m^c \phi_p \tag{3.85}$$

Putting equation equation (3.84) into equation (3.85)

$$\dot{\tau} - \phi_m \dot{\tau}_m = \phi_p \frac{G_p}{G_m} \left(\dot{\tau} - \dot{\tau}_k \right) + G_m \dot{\gamma}_m^c \phi_p \tag{3.86}$$

$$\dot{\tau} - \phi_m \left(\dot{\tau} - \dot{\tau}_k \right) = \phi_p \frac{G_p}{G_m} \left(\dot{\tau} - \dot{\tau}_k \right) + G_m \dot{\gamma}_m^c \phi_p \tag{3.87}$$

$$\dot{\tau} - \phi_m \dot{\tau} + \phi_m \dot{\tau}_k = \phi_p \frac{G_p}{G_m} \dot{\tau} - \phi_p \frac{G_m}{G_p} \dot{\tau}_k + G_m \dot{\gamma}_m^c \phi_p \tag{3.88}$$

$$(1 - \phi_m) \dot{\tau} + \left(\phi_m + \frac{G_p}{G_m} \phi_p \right) \dot{\tau}_k = \phi_p \frac{G_p}{G_m} \dot{\tau} + G_m \dot{\gamma}_m^c \phi_p \tag{3.89}$$

$$\phi_p \dot{\tau} + \left(\phi_m + \frac{G_p}{G_m} \phi_p \right) \dot{\tau}_k = \phi_p \frac{G_p}{G_m} \dot{\tau} + G_m \dot{\gamma}_m^c \phi_p \tag{3.90}$$

$$\left(\phi_m + \frac{G_p}{G_m} \phi_p \right) \dot{\tau}_k = \phi_p \left(\frac{G_p}{G_m} - 1 \right) \dot{\tau} + G_m \dot{\gamma}_m^c \phi_p \tag{3.91}$$

$$\dot{\tau}_k = \frac{\phi_p \left(\frac{G_p}{G_m} - 1 \right)}{\left(\phi_m + \frac{G_p}{G_m} \phi_p \right)} \dot{\tau} + \frac{G_m \phi_p}{\left(\phi_m + \frac{G_p}{G_m} \phi_p \right)} \dot{\gamma}_m^c \tag{3.92}$$

For creep under a constant stress $\dot{\tau} = 0$

$$\dot{\tau}_k = \frac{G_m \phi_p}{\left(\phi_m + \frac{G_p}{G_m} \phi_p \right)} \dot{\gamma}_m^c \tag{3.93}$$

If we assume both moduli are equal or that the materials macroscale shear value G is a valid replacement for both values $G_p = G_m = G$

$$\dot{\tau}_k = G\phi_p \dot{\gamma}_m^c \tag{3.94}$$

Over time the back stress evolution becomes:

$$\dot{\tau}_k = G\phi_p \left(1 - \frac{\tau_k}{H^*}\right) \dot{\gamma}_m^c \tag{3.95}$$

Work by Ashby and Johnson [67] outlined that the misfit stress of an inserted particle in the matrix acts as a stress concentrator that nucleates dislocations at the boundary. If the stress is high enough dislocations will relax the stress state at the boundary indicating that there is an upper bound. This saturation term is known as H^*. The magnitude is is heavily dependent on the geometry of the particle. If the particle is spherical as explained by Dyson [9] this saturation term is:

$$H^* = \frac{2\phi_p}{1 + 2\phi_p} \tag{3.96}$$

If the particle is cuboidal then:

$$H^* = \frac{6\phi_p}{1 + 6\phi_p} \tag{3.97}$$

3.4.2 Misfit

Due to the different lattice parameter between the γ and γ' phases, a misfit strain is introduced into the matrix to accommodate the γ' precipitates. This misfit is alleviated by the movement of dislocations around the particles and local deformation. For RR1000 experimental measurements have been used so that the initial misfit

value can be calculated by a temperature dependent empirical formulation [1]

$$\begin{aligned} \varepsilon_{mis} &= -1.772 \times 10^{-6} T + 1.596 \times 10^{-3} \\ \sigma_{mis} &= -\varepsilon_{mis} \frac{E}{(1-\nu^2)} \end{aligned} \tag{3.98}$$

This misfit will decrease during creep. The expression used to describe this effect is slightly different in formulation than that found in equation (2.62), but the scientific principle is similar. Matter flow associated with the climbing of dislocations will relieve this misfit strain. This new formulation introduces the particle size, but will only consider secondary γ' as they are significantly larger in both size and volume fraction than tertiary γ' to be the majority misfit contributor.

$$\dot{\sigma}_{mis} = \frac{D_v E b^3}{K_B T r_{p,2}^3} \sigma_{mis} \tag{3.99}$$

As with the work presented by [43] with equation (2.62) the back stress is also modified to include a similar Nabarro-Herrring diffusion formulation

$$\dot{\sigma}_k = E \phi_t \left(1 - \frac{\sigma_k}{H^* \sigma}\right) + A \exp\left(\frac{-Q}{RT}\right) \sigma_{mis} \tag{3.100}$$

3.5 Dislocation Density

The dislocation density evolution was described by Kocks, McMecking and colleagues [18]. Their work looks at the rate of change in the dislocation density based on generation (FR-sources and free gliding dislocations) figure 2.18 and annihilation (opposite dislocation attracting and pinning from dipoles) figures 2.16 and 2.17.

$$\dot{\rho}_m = \dot{\rho_m}^+ - \dot{\rho}_m^- \tag{3.101}$$

If annihilation is based on the trapping of dipoles:

$$\dot{\rho}_m = \dot{\rho}_m^+ - \rho_m \frac{\bar{v}_g}{\lambda^*} \tag{3.102}$$

In this case λ^* is the dipole trapping distance. Generation is modelled to be from Frank-Read sources as shown in figure 2.18. The dislocation loop is formed from the bowing of a dislocation line between two pinning points. As the line forms a loop the ends annihilate creating a dislocation loop free to expand throughout the crystal; this will only happen once a critical stress τ_{FR} which is dependent on the pinning point distance is reached:

$$\tau_{FR} \geq \frac{Gb}{2\pi\lambda_{FR}} \tag{3.103}$$

Generation is dependent on the number of sources ρ_s in the materials and the frequency at which they generate. This frequency is dependent on the dislocation density (more dislocations the greater potential impedance in new dislocation forming) and the dislocation gliding velocity (faster the dislocations glide the faster a dislocation loop is formed):

$$\Gamma^+ = \frac{\bar{v}_g}{\rho} \tag{3.104}$$

This is the frequency of release events where ρ could be because of the dislocation network and hence $\rho = \frac{1}{\sqrt{\rho_m}}$ The work by Kocks and Mecking [19, 20] shows two different assumptions. The first case is if the number of sources is proportional to the dislocation density $\rho_s \propto \rho_m$ so:

$$\rho_s = k\rho_m \tag{3.105}$$

So generation now becomes:

$$\rho_m^+ = k\rho_m \bar{v}_g \sqrt{\rho_m} \; = \; k\rho_m^{\frac{3}{2}} \bar{v}_g \tag{3.106}$$

Put equation (3.106) in equation (3.102)

$$\dot{\rho}_m = k\rho_m^{\frac{3}{2}}\bar{v}_g - \rho_m\frac{\bar{v}_g}{\lambda^*} \tag{3.107}$$

The effect dipole formation (trapping term)

$$\begin{aligned} 2\lambda^* h\rho_m &\simeq 2 \\ \lambda^* &= \frac{1}{h\rho_m} \end{aligned} \tag{3.108}$$

The dipole height 'h' which will determine the maximum separation height of two dislocations for a dipole to form is defined as:

$$\tau \leq \frac{Gb}{4\pi h} \;\Rightarrow\; \frac{1}{h} \geq \frac{\tau 4\pi}{Gb} \tag{3.109}$$

Put equation (3.109) into equation (3.108) and using minimum dipole height criteria:

$$\lambda^* = \frac{\tau 4\pi}{Gb}\frac{1}{\rho_m} \tag{3.110}$$

which can now go into equation (3.107)

$$\dot{\rho}_m = k\rho_m^{\frac{3}{2}}\bar{v} - \rho_m^2\bar{v}\frac{Gb}{4\pi\tau} \tag{3.111}$$

Due to the Orowan relation ($\dot{\gamma} = b\rho_m\bar{v}$) then equation (3.111)can be re-written as:

$$\dot{\rho}_m = k\rho_m^{\frac{1}{2}}(\rho_m\bar{v}) - \rho_m\frac{Gb}{4\pi\tau}(\rho_m\bar{v}) \tag{3.112}$$

$$\begin{aligned}\dot{\rho}_m &= \frac{k}{b}\rho_m^{\frac{1}{2}}(b\rho_m\bar{v}) - \rho_m\frac{G}{4\pi\tau}(b\rho_m\bar{v}) \\ &= \left(\frac{k}{b}\rho_m^{\frac{1}{2}} - \rho_m\frac{G}{4\pi\tau}\right)\dot{\gamma} \\ &= \frac{k}{b}\rho_m^{\frac{1}{2}}\left(1 - \rho_m^{\frac{1}{2}}\frac{Gb}{k4\pi\tau}\right)\dot{\gamma} \\ \dot{\rho}_m &= k\rho_m^{\frac{1}{2}}\left(1 - \sqrt{\frac{\rho_m}{\rho_{ss}}}\right)\dot{\gamma}\end{aligned} \tag{3.113}$$

where:

$$\rho_{ss} = \left(\frac{\tau}{\alpha G b}\right)^2$$

Under uniaxial loading (addition of Taylor factor equation (3.64))

$$\dot{\rho}_m = k\bar{M}\rho_m^{\frac{1}{2}}\left(1 - \sqrt{\frac{\rho_m}{\rho_{ss}}}\right)\dot{\varepsilon} \tag{3.114}$$

In this case

$$\rho_{ss} = \left(\frac{\sigma}{\bar{M}\alpha G b}\right)^2$$

3.6 Spacing

The extent of plastic deformation is determined by how far the gliding dislocations can travel before being pinned. This pinning distance works out the mean distance travelled by the dislocations. In order to accurately capture creep deformation this parameter is defined in this section.

3.6.1 Lattice Square Spacing

The lattice square spacing assumes that particles of similar size are evenly distributed in the matrix. A cross section of this 3 dimensional particle distribution where the area fraction is the space in the cross section taken up by the particles,

assuming that the area fraction is equal to the volume fraction, which is:

$$\phi_p = \frac{N_p \pi \bar{r}^2}{A} \tag{3.115}$$

Rearranging equation (3.115) the number of particles representing becomes:

$$N_p = \frac{\phi_p A}{\pi \bar{r}^2} \tag{3.116}$$

Assuming a square lattice arrangement of the particles the particle centre to centre spacing is proportional to the inverse square root of the number of particles per unit area $N_{p,A} = \frac{N_p}{A}$:

$$\zeta_p = \frac{1}{\sqrt{N_{p,A}}} \tag{3.117}$$

Edge to edge spacing takes into account the particle sizes to form:

$$\lambda_p = \frac{1}{\sqrt{N_{p,A}}} - 2\bar{r} \tag{3.118}$$

Substituting equation (3.116) into equation (3.118) to form

$$\lambda_p = \sqrt{\frac{\pi \bar{r}^2}{\phi_p A}} - 2\bar{r} \tag{3.119}$$

$$\lambda_p = 2\bar{r}\left(\sqrt{\frac{\pi}{4\phi_p A}} - 1\right) \tag{3.120}$$

The cross sectional area can be assumed to be unity (1 m^2) and removed so equation 3.120 becomes

$$\lambda_p = 2\bar{r}\left(\sqrt{\frac{\pi}{4\phi_p}} - 1\right) \tag{3.121}$$

Where the cross sectional plane intercepts 3 dimensional space we can determine the size of the particles. The average particle radius is related to the average particle radius in the cross section:

$$\bar{r} = \sqrt{\frac{2}{3}} r_p \tag{3.122}$$

Substituting this into equation (3.121) the square spacing becomes:

$$\lambda_p = 2\sqrt{\frac{2}{3}} r_p \left(\sqrt{\frac{\pi}{4\phi_p}} - 1 \right) \tag{3.123}$$

3.6.2 Freidel spacing

The square lattice spacing with respect to being used in the creep formulation is only valid when there is minimum bowing of the dislocation line. It is usually rationalised by Dyson and colleagues [9,40,44,68] that during creep the strain rates are low enough and the temperature is high enough that before the dislocation line has bowed significantly it will climb or cut the particle. In regards to RR1000 this may not be the case and there may be significant bowing of the dislocation line: if so the Freidel spacing may be a better physical representation of the particle spacing.

$$\lambda_f = \left(\frac{2T\pi r_p^2}{\phi_p \tau b} \right)^{\frac{1}{3}} \left(1 - \frac{4\phi_p}{\pi} \left(\sqrt{\frac{\pi}{\phi_p}} - 1 \right) \right)^{\frac{1}{3}} \tag{3.124}$$

where the Friedel spacing is no longer from particle to particle but rather from the peak of one dislocation bow to the peak of another.

3.6.3 Spacing in a multimodal system

The above spacing formulations are all based on the same assumption that the particles are the same size, which assumes a unimodal distribution; this is not the case for RR1000. Since it contains both secondary and tertiary γ' distributions, the method used is similar to that done by Coakley et al [69] where by the spacing is worked out for both distributions separately. An additional effect included is the effect of dislocations acting as their own pinning points which is a function of

the dislocation density. The total spacing calculation therefore becomes:

$$\left(\frac{1}{\lambda_p}\right)^2 = \left(\frac{1}{\lambda_{p,3}}\right)^2 + \left(\frac{1}{\lambda_{p,2}}\right)^2 + \frac{A}{\sqrt{\rho_m}} \tag{3.125}$$

During creep, especially at high temperatures and low stresses, the tertiary γ' will initially have the greatest effect in the creep strength; as it coarsens, secondary γ' becomes the primary strengthening mechanism.

Chapter 4

Experimental Procedure

4.1 Theoretical basis for experimental programme

A number of high temperature experiments have been carried out as part of this study to support the development and validation of the constitutive modelling framework presented in chapter 3. The proposed model is aimed at capturing the viscoplastic response of RR1000 over a wide range of applied strain rate conditions, ranging from creep dominated behaviour ($\sim 10^{-12} - 10^{-6}$ s^{-1}) to uniaxial flow stress response ($\geq 10^{-4}$ s^{-1}). The constitutive description assumes a number of micromechanisms to operate: (i) dislocation activity within the γ matrix; (ii) climb of dislocations around γ' particles; (iii) Particles deforming elastically to take up load during deformation; (iv) evolution of the multimodal γ' distribution. A key element of the theory is that the tertiary particles, when present, dominate the yield and creep strength. Back stresses arise from stress partitioning between the γ/γ' phases and the theory predicts that the extent of this stress redistribution is dependent to a first order approximation on the total volume fraction of particles present. The model also predicts that the plastic strain increments scale up with the shortest mean free path available, which for FG-RR1000 is the tertiary inter-particle spacing. The creep rate, however, is controlled by diffusion assisted dislocation climb around particles.

These mechanisms can operate over the entire stress/temperature range of interest or may dominate over certain ranges. For example, evolution of the particle dispersion will be slow at low temperatures, whereas at high enough temperatures, coarsening/dissolution of the tertiary particles will be rapid and will modify the strength of the alloy significantly. At low stresses dislocations will by-pass particles by a local climb mechanism. At high stresses and low temperatures, Orowan looping and cutting of the particles will occur. Incorporation of these mechanism into a climb-based theory is necessary in extending the constitutive relations to cover a wider range of conditions. While particle cutting was not addressed in Basoalto et al. [70] its importance in understanding the material behaviour cannot be ignored. This is especially relevant at high stress regimes where this cutting can have a great impact on the amount of stress transferred to the precipitates. It is anticipated that studying the flow stress behaviour at different strain rates and temperatures for the two microstructures will provide information to develop and validate the γ' cutting model.

The objective of the experimental programme is to establish how a multimodal particle dispersion determines the constitutive response in nickel-based superalloys. In particular, the experimental study is targeted to provide information on the following:

- The proposed microstructure-sensitive constitutive model requires information on the tertiary and secondary γ' size and spatial distributions as a function of temperature. These will be characterised.

- The stability of the tertiary particles in RR1000 is sensitive to temperature. This was demonstrated in the PANACEA programme [1], which measured the tertiary γ' particle size during thermal exposure for a range of temperatures and times. In order to assess the influence of the γ' dispersion on kinetics as well as deformation, two different γ' distributions will be studied: one based on the standard heat treatment (SHT) and the other on a modified

HT (aged). These will be referred to as SHT and MHT, respectively.

- An extended form of mean field theory has been developed, which the deformation model uses to predict the creep and flow stress behaviour of the material. Numerical solution of the mean field equations requires a knowledge of the initial size distributions. These can be taken from the two heat treatments under consideration and aid to fine tune the mean field parameters to predict the evolution of the multimodal particle size distribution accurately. Also, to get reasonable changes to the γ' dispersion, tests will be carried out at higher temperatures than have been considered in previous programmes.

- As the applied stress approaches yield, cutting of the γ' particles will take place and this will affect the flow stress and creep behaviour of the alloy. Thus, creep test conditions at or near yield are proposed.

- Extending the current theoretical framework to lower temperatures is a challenge. The objective of the theoretical work is not, therefore, to account for the localisation of deformation observed at lower temperatures. Also, the extent of localisation is anticipated to be affected by the spatial distribution of particles. In order to provide some insights into these questions, in-situ experiments that aim to measure strain maps of grains during cyclic loading have been carried out.

Figure 4.1 gives an overview of the existing Rolls-Royce creep database together with the testing matrix defined in this test programme. Based on the above points the experimental conditions within this programme have extended the existing creep database to high temperatures ≥ 750°C, high stresses at 700°C and a low temperature creep test 600°C 500 MPa. Some conditions in this programme will repeat conditions within the existing Rolls-Royce creep database (700°C 700 MPa) and add additional comparative information when comparing the creep behaviour

with the modified heat treatment condition (750°C 460 MPa).

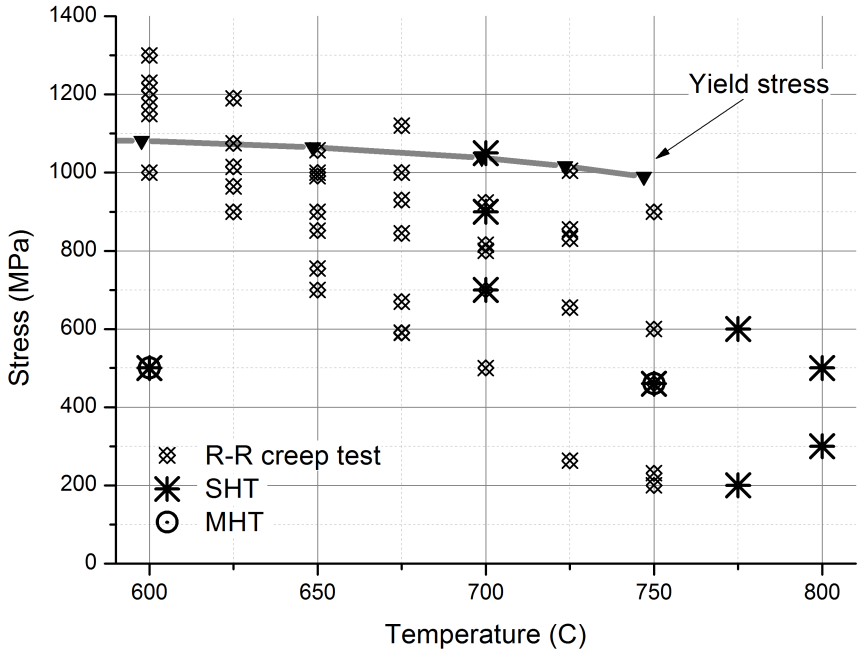


Figure 4.1: Creep tests done in this project and given in the PANACEA project [1]

4.2 Method

4.2.1 Creep tests

For the creep test programme 11 test conditions were investigated. Creep specimens were machined from a FG-RR1000 test ring. Figure 4.2 shows a drawing of the creep specimen geometry.

Samples were given one of the following heat treatments:

1. Standard heat treatment (SHT): 2 hour heat treatment at 1120°C, Cooling rate 0.5-1°C/sec, 16 hours at 760°C

2. Modified heat treatment (MHT): 2 hour heat treatment at 1120°C, Cooling rate 0.5-1°C/sec, 24 hours at 800°C

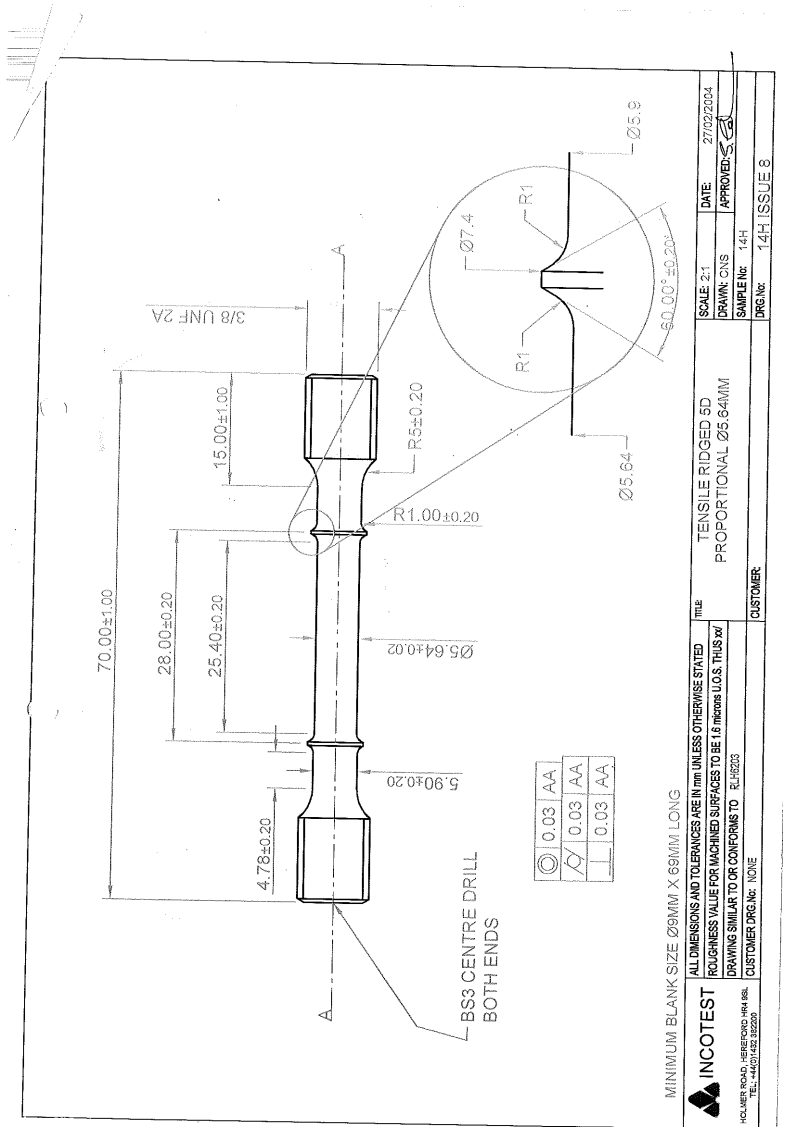


Figure 4.2: Creep test piece geometry.

Table 4.1 lists all creep test conditions carried out in this work, which cover a temperature range from 600° to 800°. For the 700°C test conditions stresses at 900 MPa and 1050 MPa are included to assess the creep response near and beyond yield to meet model requirements outlined in the previous section. Creep conditions 600°C/500 MPa and 750°C/460 MPa are targeted to provide information on the influence of γ' dispersion on the creep behaviour.

Test $N°$	Temperature (°C)	Stress (MPa)	HT	Max test time	Part $N°$	Inco ID
1	600	500	x	4 months	SEC 1 1-6	
2	600	500	o	4 months	SEC 4 4-1	
3	700	700	x	250 hours	SEC 2 2-3	J29980A101
4	700	900	x	250 hours	SEC 2 2-2	J29990A101
5	700	1050	x	200 hours	SEC 2 2-1	
6	750	460	x	200 hours	SEC 1 1-5	J29992A101
7	750	460	o	200 hours	SEC 3 3-1	J29993A101
8	775	200	x	200 hours	SEC 1 1-4	J29994A101
9	775	600	x	200 hours	SEC 1 1-3	J29995A101
10	800	300	x	200 hours	SEC 1 1-2	J29996A101
11	800	500	x	200 hours	SEC 1 1-1	J29997A101

Table 4.1: Creep test matrix x = SHT and o = MHT

All creep tests were carried out by INCOTEST and tested following the British standard BS EN 2002-5:2007 FEB 09 [71].

4.2.2 Tensile tests

For the flow stress characterisation 19 samples were extracted from a RR1000 pancake forging. The standard heat treatment was given to 11 samples, with the remaining 8 samples given the MHT (see Table 4.2). The tensile test piece geometry is shown in Figure 4.3.

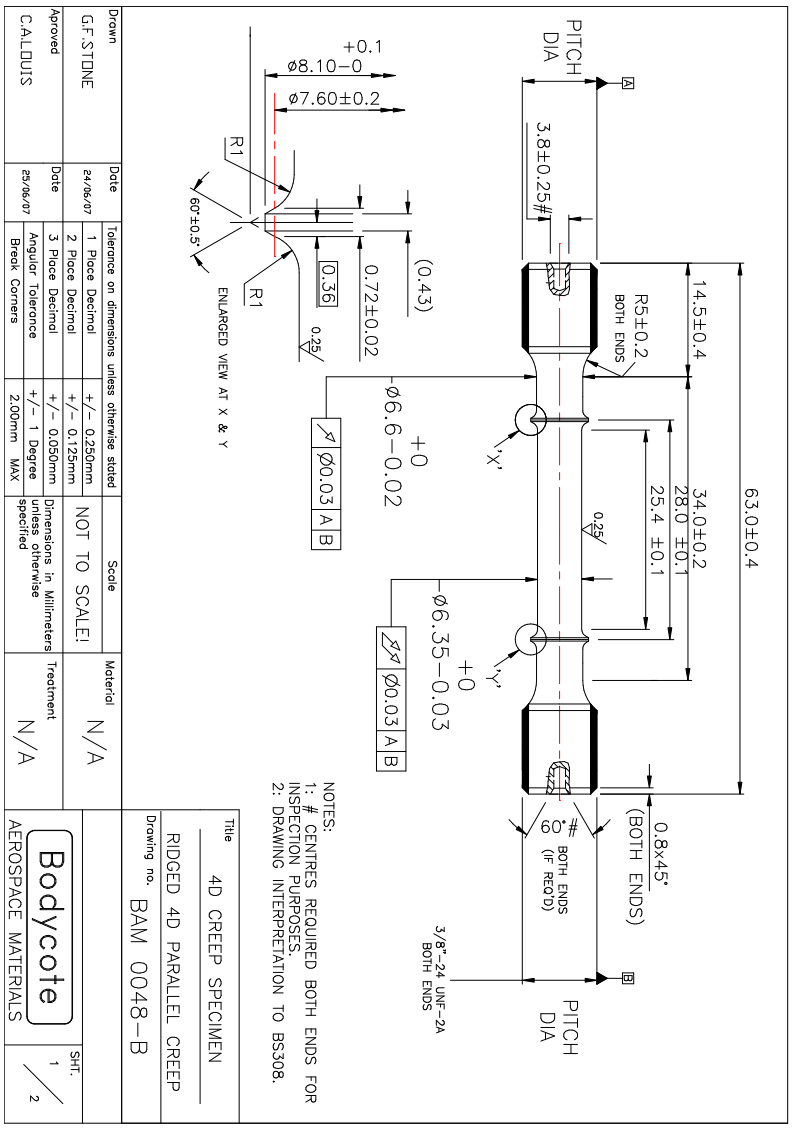


Figure 4.3: Uniaxial tensile test piece geometry.

Figure 4.4 is from one of the samples being prepared with a line of best fit to the cooling rate shown. The result shows that depending on the examined area the cooling rate (ignoring below 400 °C where the kinetics are too slow) can be said to range from 1.03 to 0.51 $°C\,s^{-1}$ with the overall average cooling rate being $0.71°C\,s^{-1}$. This is important to notice that the upper and lower bound measurement are close to the required cooling rate for the heat treatments.

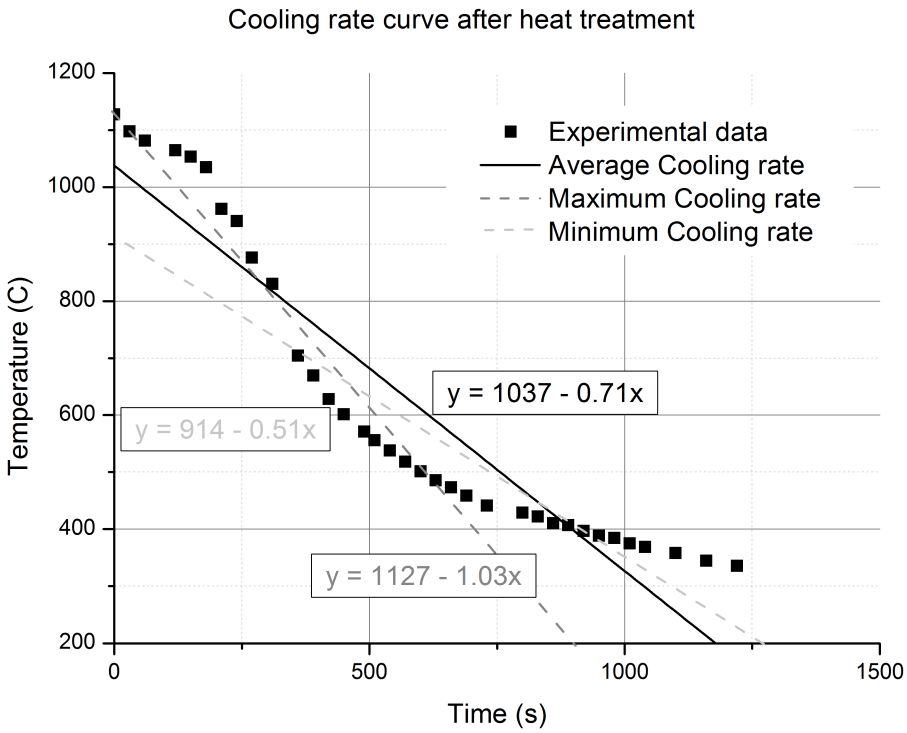


Figure 4.4: Temperature measurements to ensue sample reaches correct cooling rate

Table 4.2 gives a summary of the flow stress test matrix. Conditions considered range from 650°C to 800°C and strain rates of 10^{-4} s^{-1} to 1 s^{-1}.

	Rate (s^{-1})			
Temp ($°C$)	10^{-4}	10^{-3}	10^{-2}	1
650			x	x,o
700	x,o	x,o	x	x,o
750	x,o		x	x,o
800	x,o	x,o		

Table 4.2: Tensile test plan x = SHT and o = MHT

Figure 4.5 gives an overview of this test programme showing existing Rolls-Royce flow stress data.

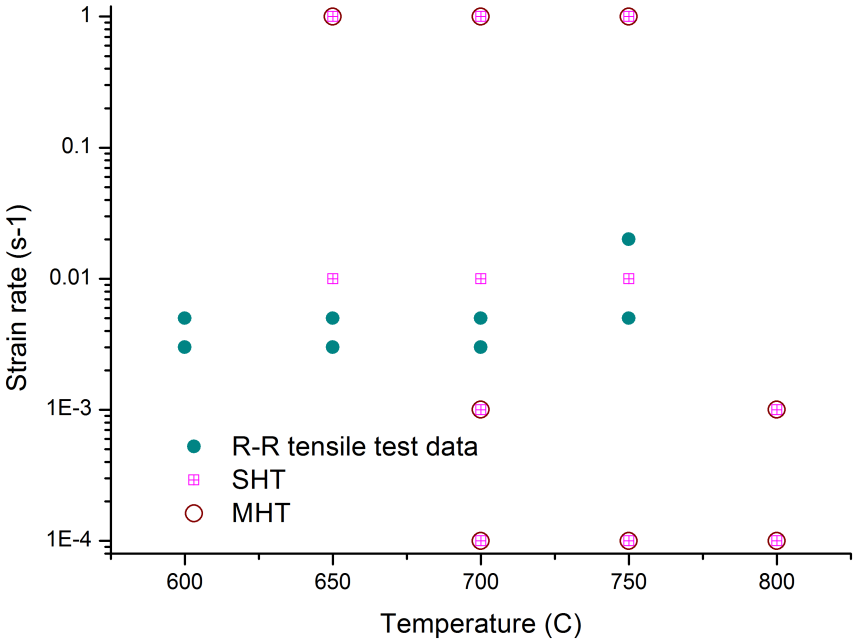


Figure 4.5: Flow stress test matrix for this study. Also indicated are exisiting Rolls-Royce plc. data.

The samples were machined and tested at Exova to the specification ASTM E21:09 [72].

4.2.3 Pre-strained Creep tests

Four standard heat treated samples from the RR1000 pancake forging were machined to the test-piece geometry shown in figure 4.3. The samples were pre-strained under a uniaxial tensile load at room temperature and at 800°C to 1% strain. The pre-strained samples were then tested under the creep conditions listed in table 4.3. The pre-strain creep tests were sub-contracted to Exova. The pre-strains samples were carried out under specification ASTM E21:09 [72] whilst the creep tests followed according to ASTM E139:11 [73].

Tensile			Creep	
Temp ($^{\circ}C$)	Rate (s^{-1})	Strain (%)	Temp ($^{\circ}C$)	Stress (MPa)
800	10^{-3}	1	750	231
800	10^{-3}	1	750	460
RT	10^{-3}	1	750	231
RT	10^{-3}	1	750	460

Table 4.3: Test for sample which would first undergo a 1% tensile test pre-strain then a creep test

4.2.4 Microstructure analysis

Scanning electron microscopy (SEM) and transmission electron microscopy (TEM) was undertaken to characterise the initial microstructure and define the grain size and primary γ' size from SEM and the tertiary and secondary γ' size from the TEM.

TEM

Samples were taken from both the test ring and the pancake forging and given SHT and MHT. Thin sections were cut ∼50 mm in length and a thickness less than a millimetre using electrical discharge machining (EDM). From these sections 5-6 3 mm discs were cut out using spark erosion. The discs were ground to 80-130 μm and were twin jet polished with a solution of 10% perchloric acid 90% ethanol at 20 V, 0.6 A and -15°C . This process both polishes and etches the sample leaving a convex surface with a small hole in the center; enabling it to be put into the TEM. The method for analysing the microstructure is based on the work of Payton et al [74] and is based on automating image analysis using matlab and makes spherical approximations of all the precipitates.

SEM

From the same EDM sections used for the TEM samples, sections that were left over were cut again using the EDM. These newly cut samples were mounted in

Bakelite, ground, polished and electro-etched in a solution of 10 % phosphoric acid 90 % water at 3.5 V.

Chapter 5

Experimental Results

5.1 Creep experimental results

A combined plot of the rupture life against the stress and strain to failure is shown in figure 5.1, with the individual curves shown in figures 5.2 to 5.10.

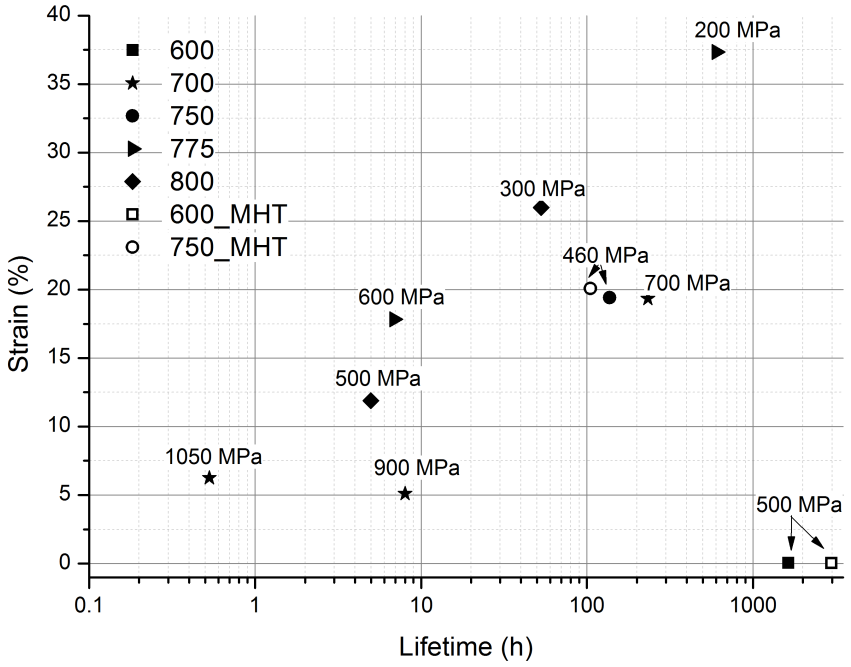


Figure 5.1: All experimental lifetime data against amount of elongation

The creep behaviour at 700°C/700 MPa is shown in figure 5.2. The strain-time

trajectory shows no significant primary creep transient and the curve is dominated by an increasing creep strain rate until failure. It is only from zooming in on figure 5.2(b) that the primary transient is observed to reach a peak creep strain of ∼0.05% after 15 hours followed by tertiary creep. For the first 60 hours there is very little creep strain accumulation. The sample ruptured after ∼300 hours with a rupture creep strain of 15%.

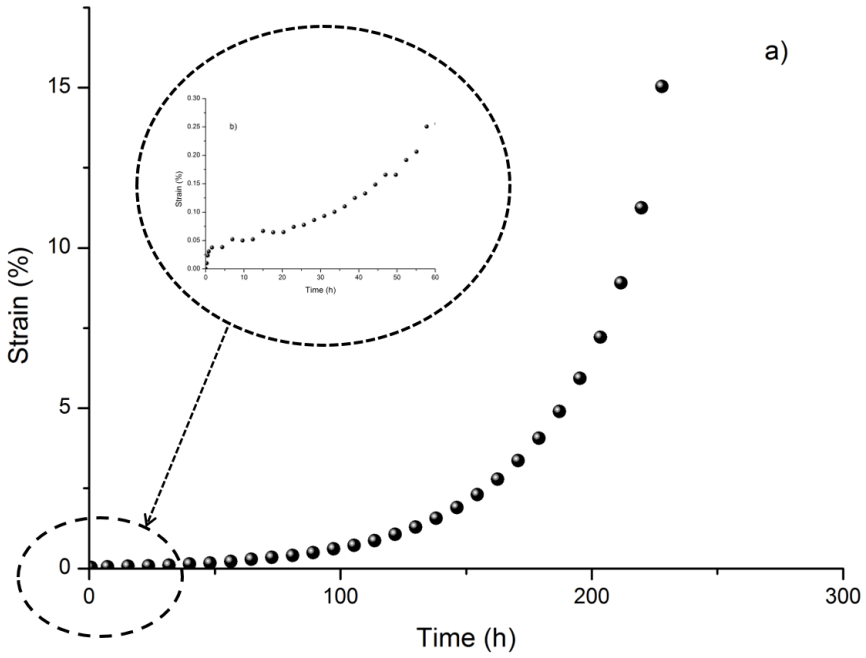


Figure 5.2: Creep experimental results 700°C 700 MPa

At 700°C/900 MPa the strain-time trajectory is different from that at 700 MPa at the same temperature, which has a higher initial creep rate but shows a less pronounced tertiary, see figure 5.3. The creep ductility is significantly less reaching 5% after ∼8.5 hours. A primary transient is observed as indicated in figure 5.3(b) which is a lot less pronounced, as it occurs over a much shorter time period. Reaching a higher strain of 0.1% in 0.3 hours.

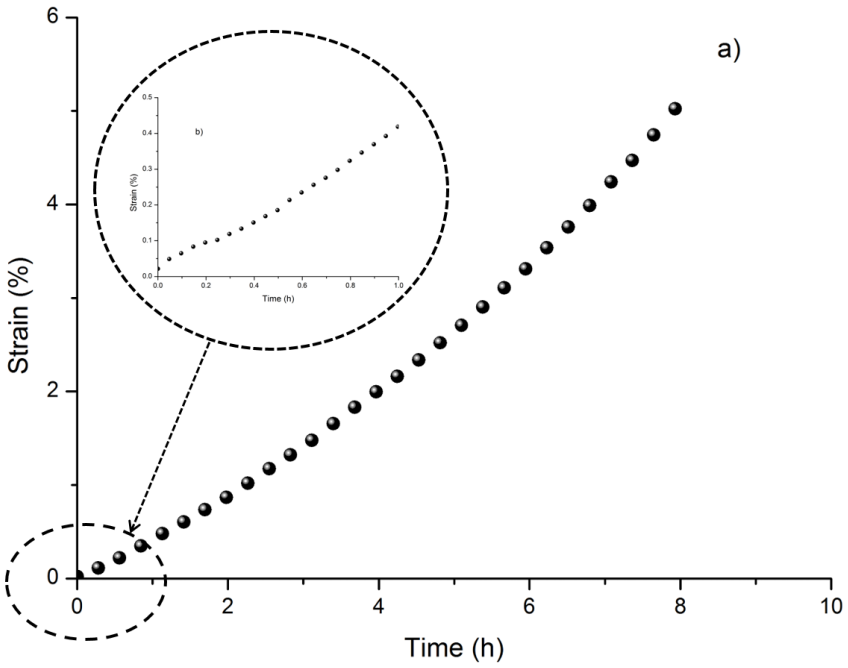


Figure 5.3: Creep experimental results 700°C 900 MPa

Figure 5.4 is another progression of the effect of increased stress (1050 MPa) at the same temperature (700°C). The increased stress further linearises the creep curve and reduces the life (∼0.6 hours) when compared against figures 5.2 and 5.3. The result does produce a slightly higher ductility of 6% compared to figure 5.3 and the primary regime reaches a higher strain of ∼0.38%, but it happens almost instantly upon loading.

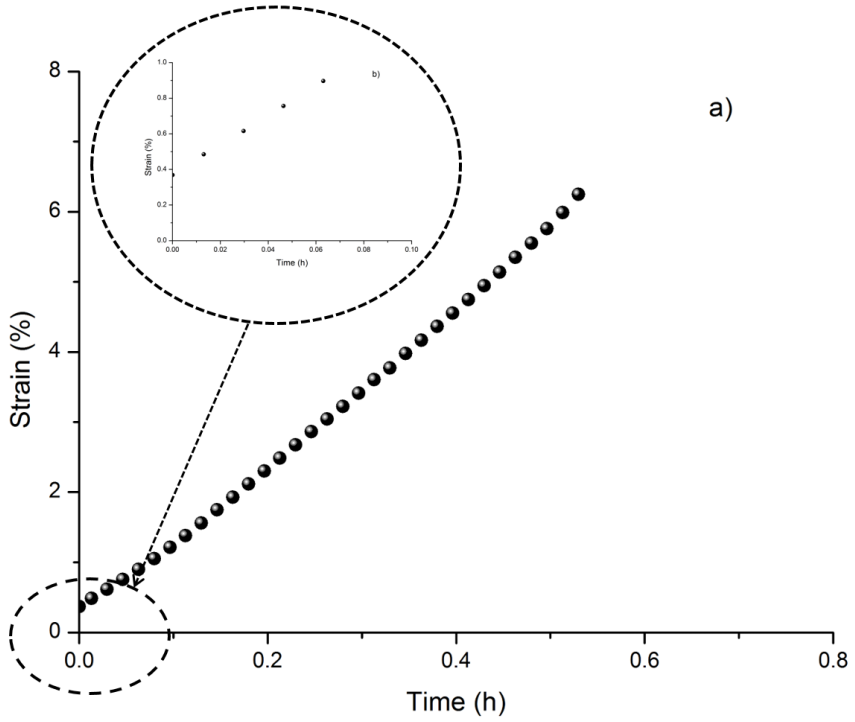


Figure 5.4: Creep experimental results 700°C 1050 MPa

The creep responses from the SHT and MHT samples at 750°C/460 MPa are shown in figure 5.5. Both curves are characterised by a tertiary transient dominating the entire creep life. During the early stages of creep, the response of the SHT and MHT samples are very different, as shown in figure 5.5(b). The MHT sample shows a typical primary transient over the first few hours; however, the SHT sample after a rapid increase in strain, shows a drop in creep strain over ∼10 hours before increasing again, due to this effect only being present in this one condition it is thought to be an issue with the sample set up. The MHT failed at a shorter time of ∼104 hours compared with the SHT sample which failed at ∼136 hours.

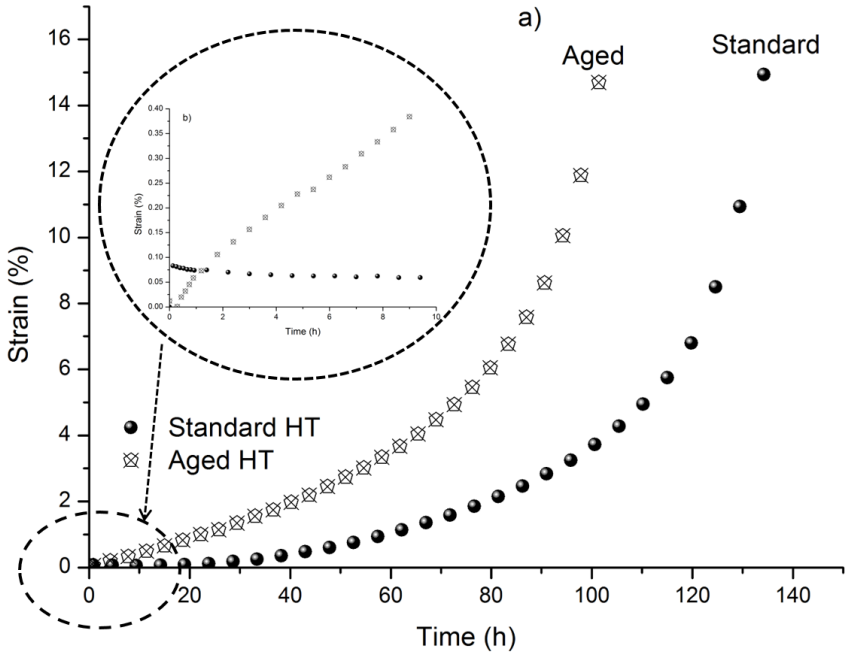


Figure 5.5: Creep experimental results 750°C 460 MPa for both SHT and MHT

The creep response at 775°C/200 MPa is shown in figure 5.6. At this condition the rupture ductility was 37% and the lifetime was 603 hours. The strain-time trajectory is dominated by a tertiary transient. A primary creep strain is observed with peak creep strains of ∼0.011% achieved at ∼1 hour.

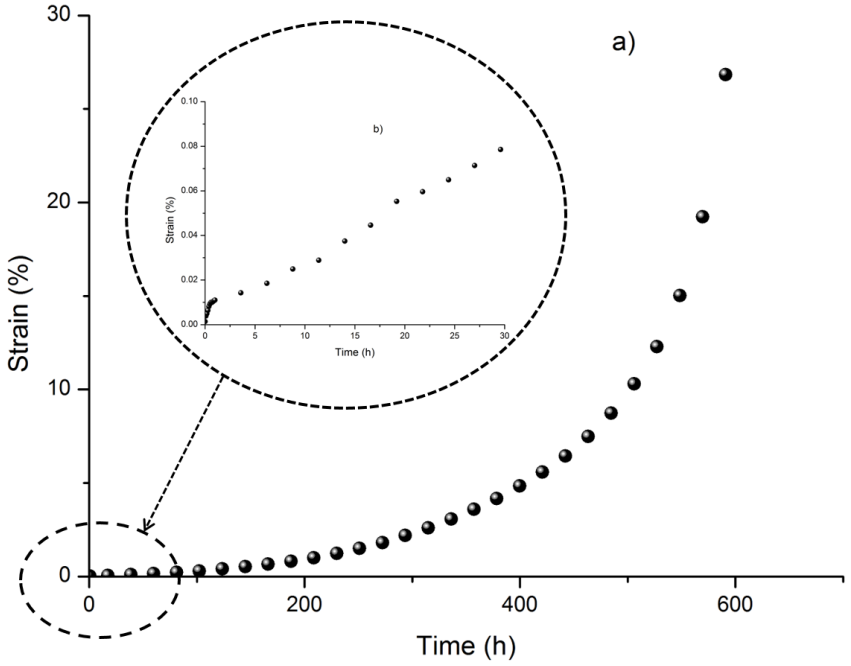


Figure 5.6: Creep experimental results 775°C 200 MPa

Figure 5.7 shows the creep response at 775°C/600 MPa, which has a rupture strain of 17% and a lifetime of 6.8 hours. Once again a primary transient is present, although it is less marked than that observed at 200 MPa at the same temperature.

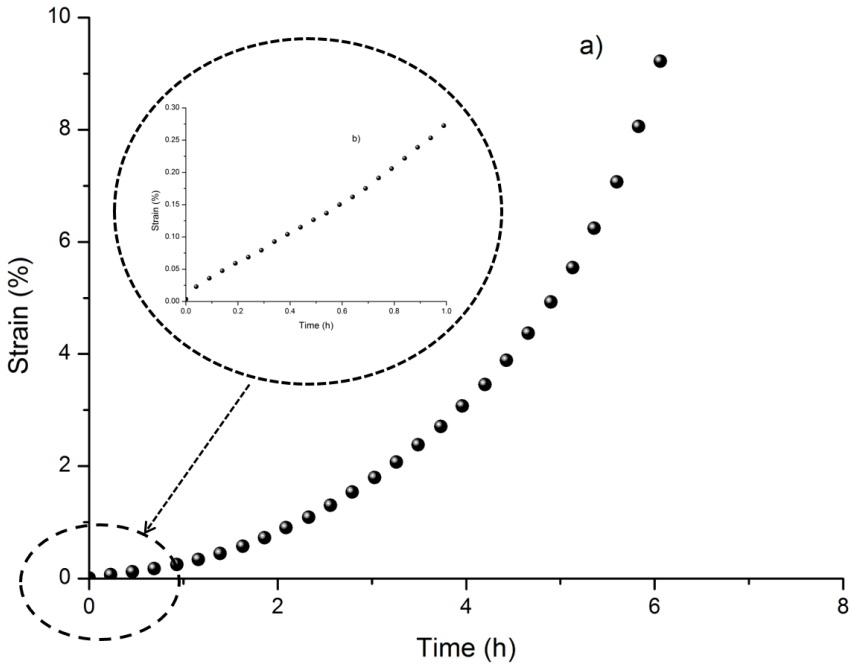


Figure 5.7: Creep experimental results 775°C 600 MPa

The creep strain curve at 800°C/300 MPa is shown in figure 5.8. Once again the strain-time trajectory is characterised by a tertiary dominated creep response. For this sample a lifetime of 52 hours with a rupture creep strain of 26% is recorded. The primary transient extends for < 1 hour.

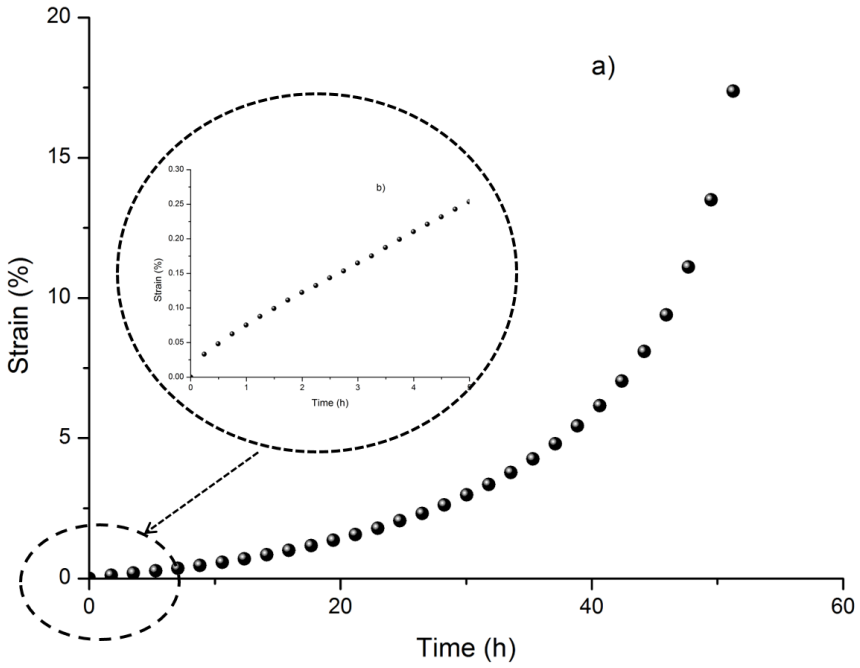


Figure 5.8: Creep experimental results 800°C 300 MPa

The creep response at 800°C/500 MPa is shown in figure 5.9, which has a lifetime of 5 hours and rupture strain of 12%. The primary creep transient is shown in figure 5.9(b), reaches a higher strain ∼0.5% over a shorter time period 0.2 hours than that observed at 300 MPa.

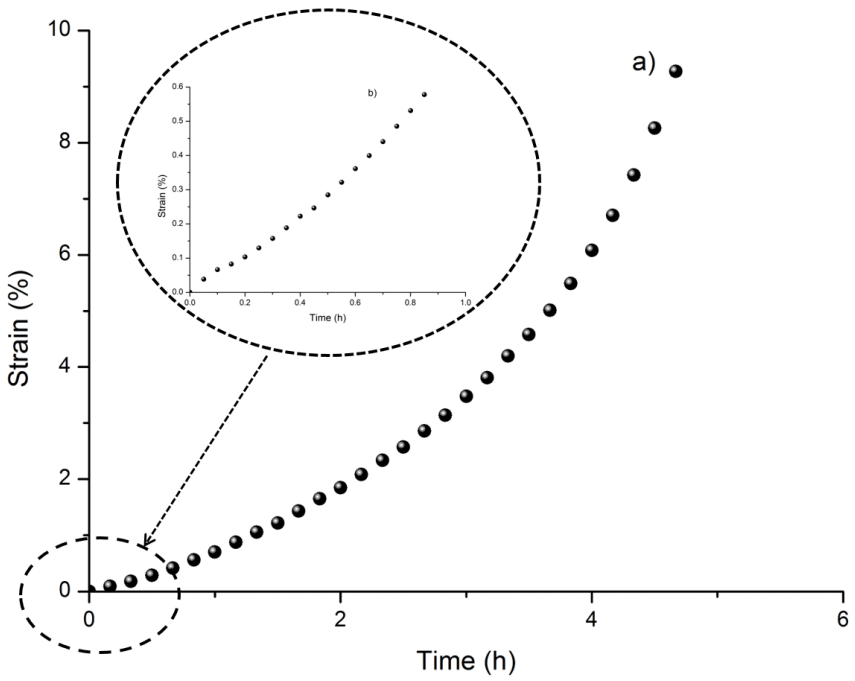


Figure 5.9: Creep experimental results 800°C 500 MPa

Figure 5.10 is both a low temperature and fairly low stress test condition as such both samples did not creep until failure instead stopping based on equipment time constraints. Both the SHT and MHT conditions are still in the region or just exiting the primary creep regimes and in both cases there is a large amount of scatter present in data recordings. What can be gained from comparing both samples is that the SHT has a much higher primary creep strain reaching 0.55% compared to 0.25% in the MHT. Both did reach this strain at around the same time of 500 hours.

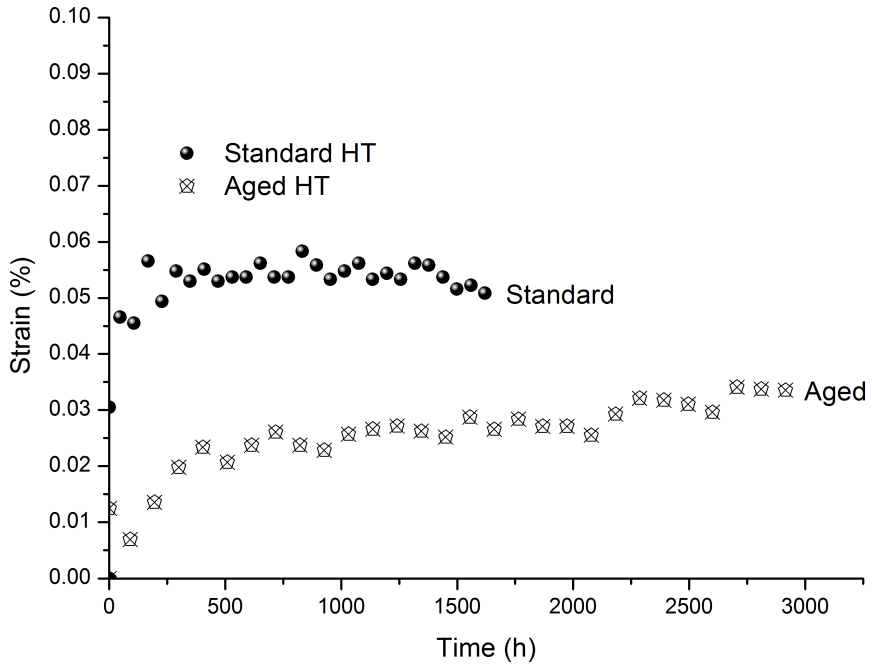


Figure 5.10: Creep experimental results 600°C 500 MPa for both SHT and MHT

5.2 Tensile Flow Stress

The flow stress responses for 10^{-2} s^{-1} and 10^{-1} s^{-1} at 650°C tests are shown in figures 5.11 and 5.12, respectively. At these conditions the stress-strain curves show strain-hardening behaviour. For the 10^{-1} s^{-1} test the tensile response for the SHT and MHT samples are plotted, with the MHT sample having a slightly higher flow stress response than the SHT. The 0.2% yield stresses at 10^{-1} s^{-1} for the SHT and MHT samples are 966 MPa and 1006 MPa, respectively. The measured maximum stresses for the SHT and MHT tests are 1374 MPa and 1418 MPa, respectively. Thus, comparing the effect of heat treatment the MHT sample produced an increased strength in the measured flow stress response at this condition.

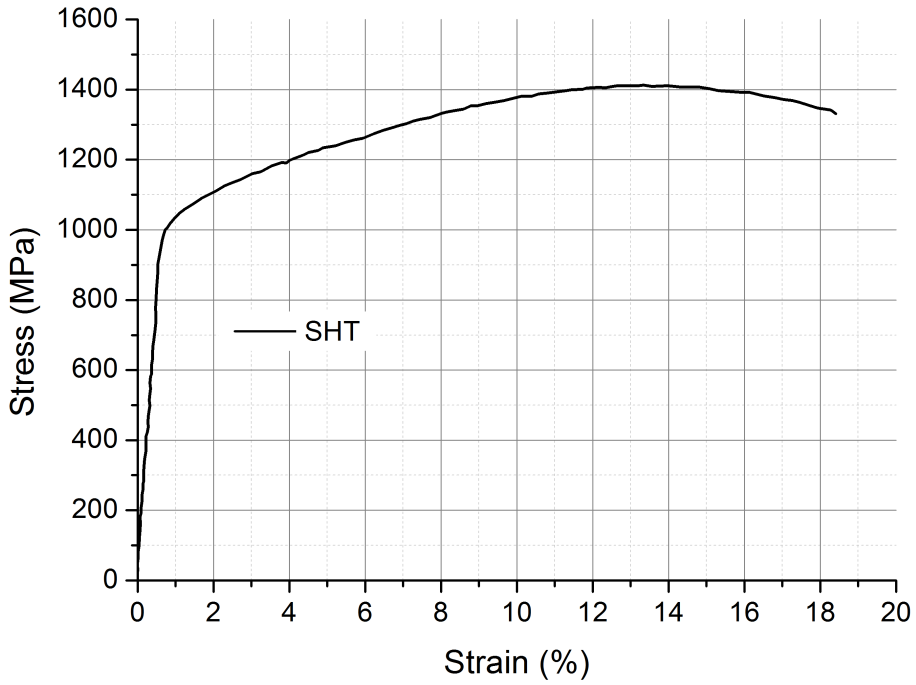


Figure 5.11: Tensile 650°C, $\dot{\varepsilon} = 0.01s^{-1}$

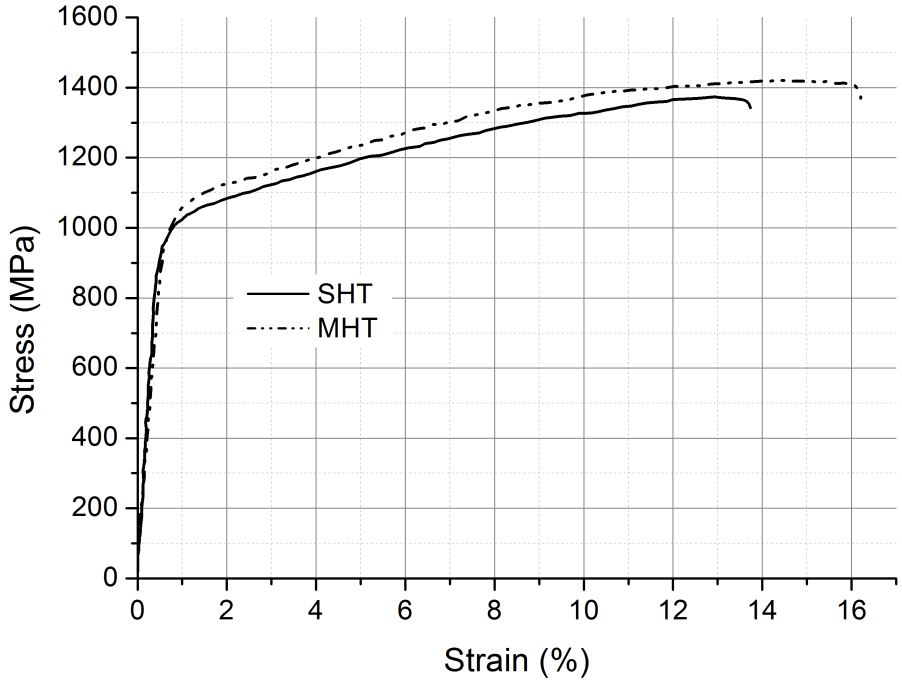


Figure 5.12: Tensile 650°C, $\dot{\varepsilon} = 1s^{-1}$

The flow stress behaviour at 700°C is shown in figures 5.13 to 5.16. Increasing the applied strain rate does not appear to influence yield significantly. However, the level of work hardening is increased with increasing strain rate. At low strain rates the SHT results in a lower yield stress than the MHT: this difference reduces with increasing strain rate. The rupture strains of the SHT samples also appear to be sensitive to the strain rate, with increasing rupture strains with increasing strain rate.

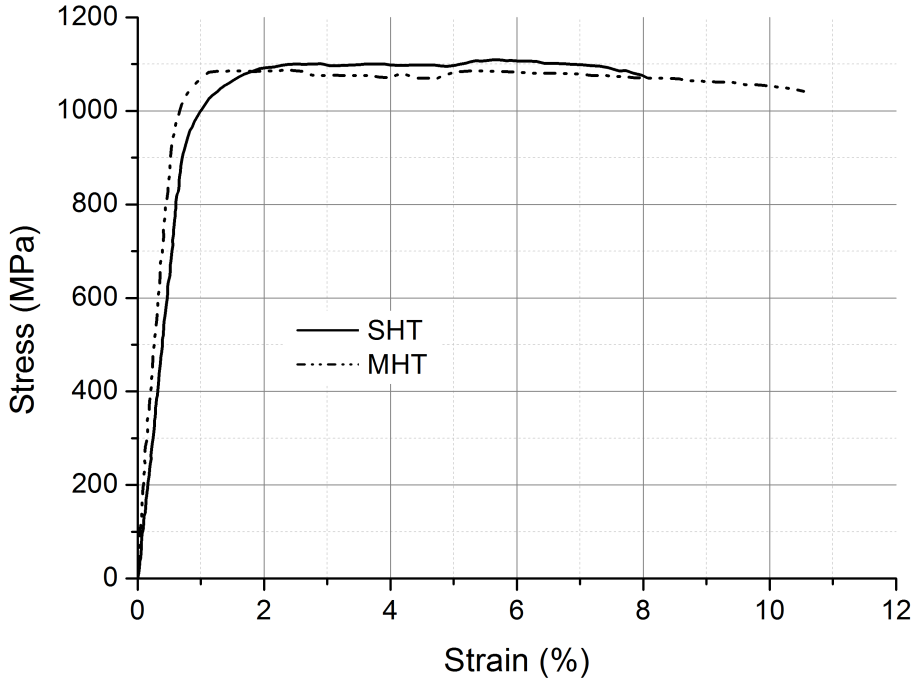


Figure 5.13: Tensile 700°C, $\dot{\varepsilon} = 10^{-4}s^{-1}$ both SHT and MHT

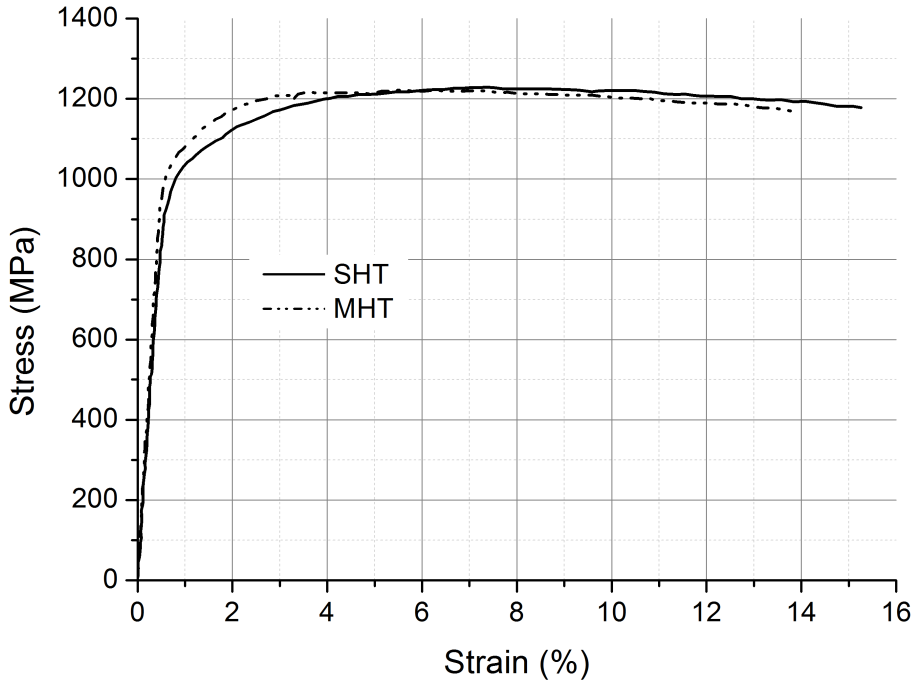


Figure 5.14: Tensile 700°C, $\dot{\varepsilon} = 10^{-3}s^{-1}$ both SHT and MHT

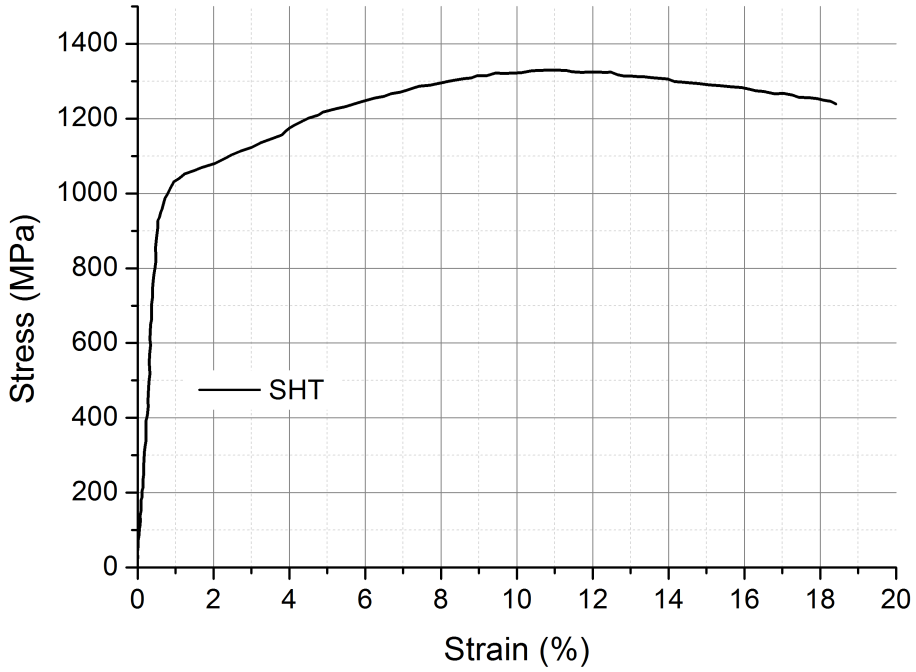


Figure 5.15: Tensile 700°C, $\dot{\varepsilon} = 0.01s^{-1}$

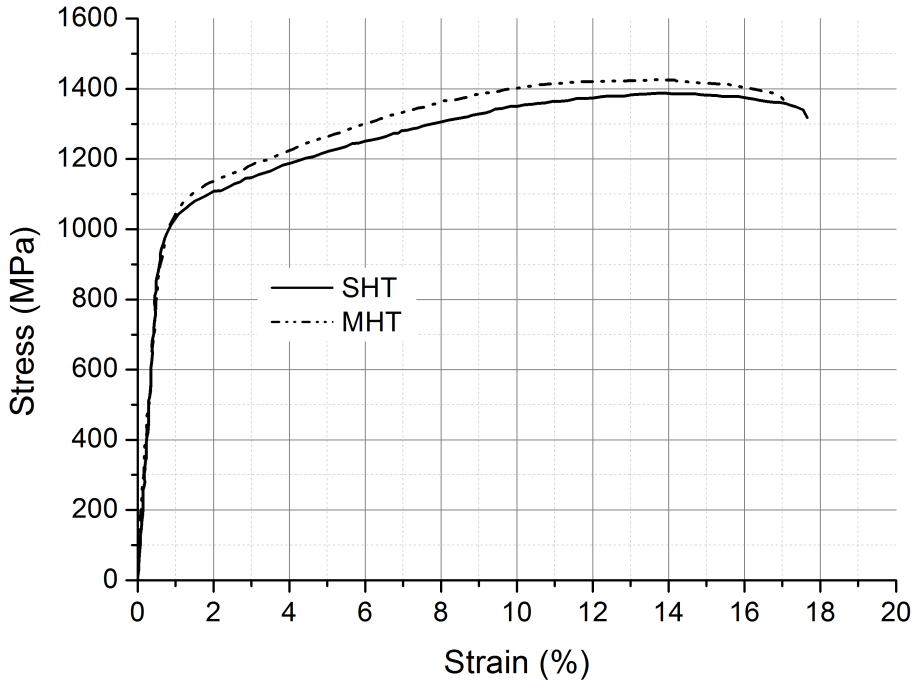


Figure 5.16: Tensile 700°C, $\dot{\varepsilon} = 1s^{-1}$ both SHT and MHT

Figures 5.17 to 5.19 show the stress-strain response at 750°C for strain rates at $10^{-4}s^{-1}$,$10^{-2}s^{-1}$ and $1s^{-1}$. The shape of the flow stress curves changes with increasing strain rate. At $10^{-4}s^{-1}$ to $1s^{-1}$ a peak stress is observed before reaching ∼1% strain followed by limited softening then reaching a steady state. At higher strain rates a strain hardening behaviour is observed until a maximum stress at ∼8% strain followed by softening until failure. Differences between the SHT and MHT are not significant at 750°C.

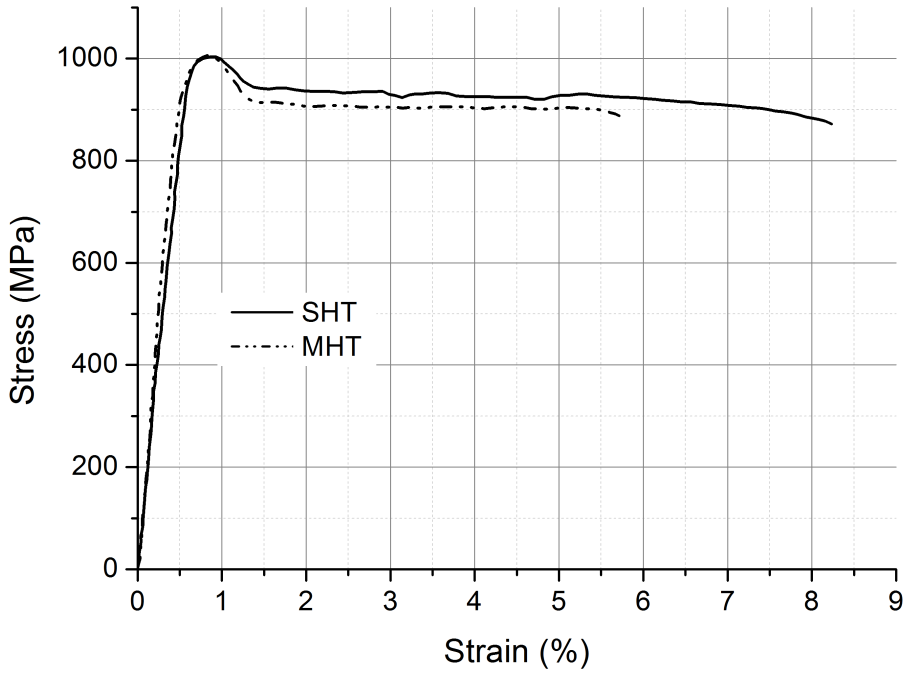


Figure 5.17: Tensile 750°C, $\dot{\varepsilon} = 10^{-4}s^{-1}$ both SHT and MHT

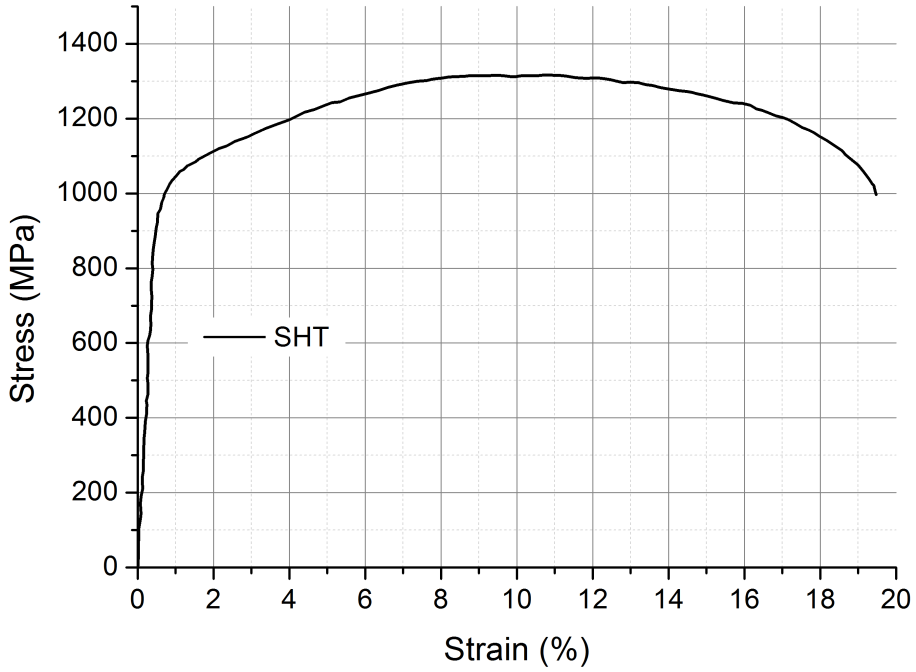


Figure 5.18: Tensile 750°C, $\dot{\varepsilon} = 0.01s^{-1}$

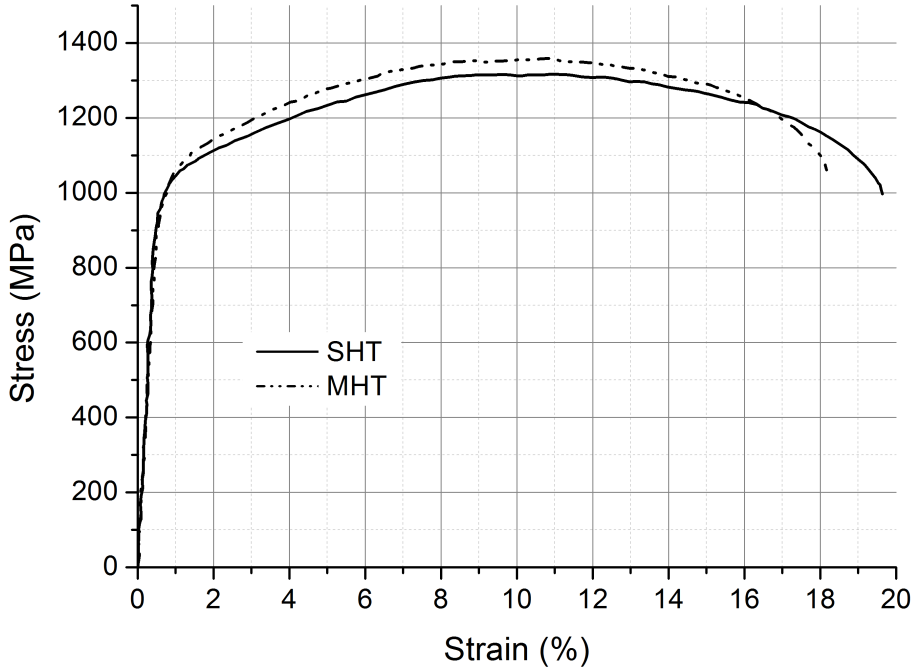


Figure 5.19: Tensile 750°C, $\dot{\varepsilon} = 1s^{-1}$ both SHT and MHT

The 800°C tensile data at $10^{-4}s^{-1}$ and $10^{-3}s^{-1}$ are shown in figures 5.20 and 5.21, respectively. Once again at the slowest strain rate the curves for both SHT and MHT show softening of the flow stress after a peak stress followed by a steady state. At $10^{-3}s^{-1}$ the softening rate is slower that at $10^{-4}s^{-1}$. In both cases the MHT gives a higher flow stress behaviour, although at $10^{-3}s^{-1}$ this is only up to a strain of around 3% then the curves match the response.

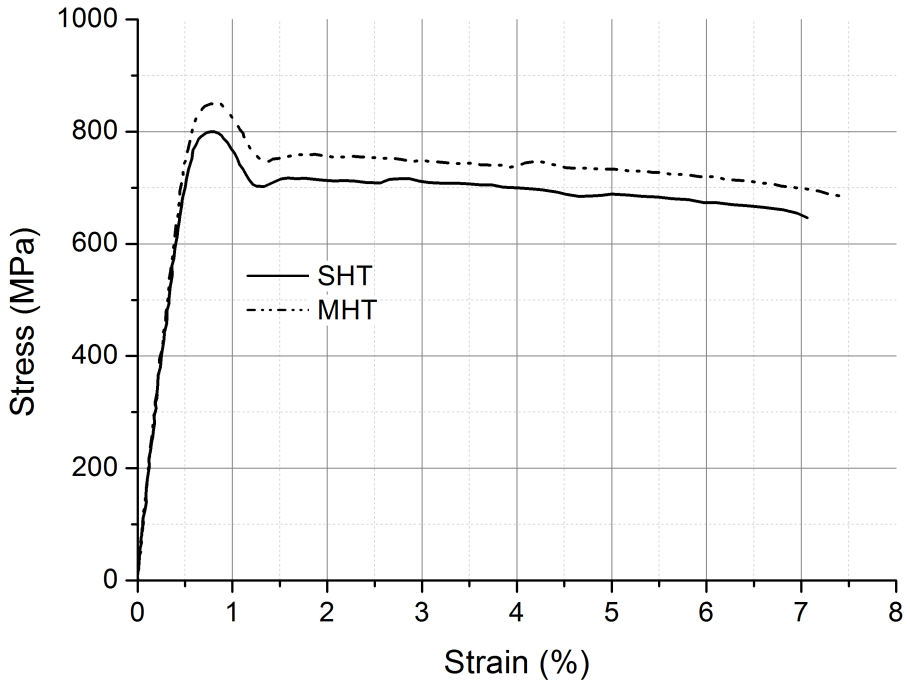


Figure 5.20: Tensile 800°C, $\dot{\varepsilon} = 10^{-4}s^{-1}$ both SHT and MHT

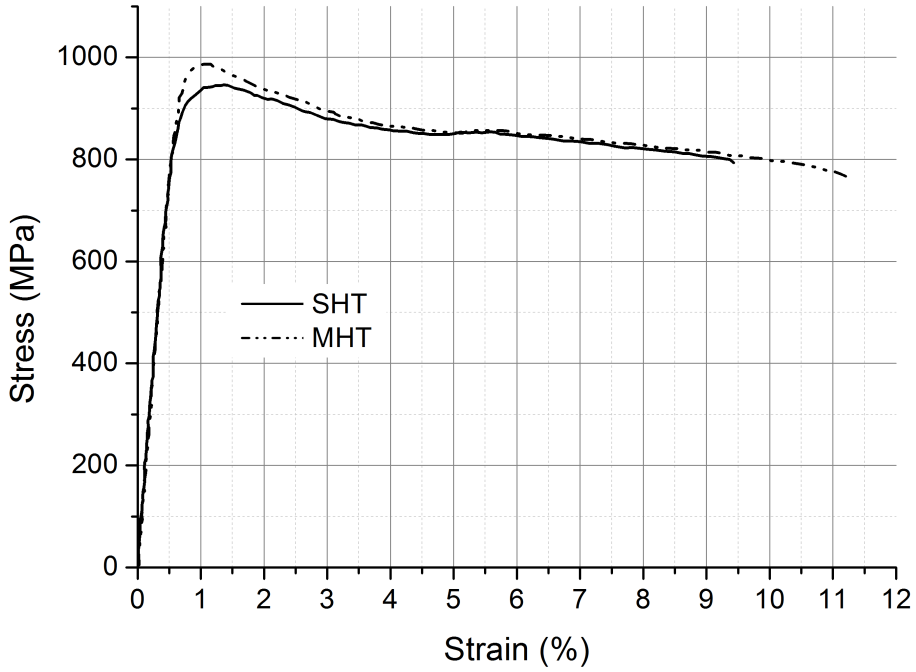


Figure 5.21: Tensile 800°C, $\dot{\varepsilon} = 10^{-3}s^{-1}$ both SHT and MHT

Figure 5.22 shows the effect of temperature on material response at 10^{-4}s showing a decrease in the yield stress and increases in softening with temperature. Going from a near linear plastic response at 700°C to a curve that presents an upper and lower yield point before reaching a steady state at 750°C. 800°C is very similar to 750°C, except it does not reach a steady state and begins to soften until fracture.

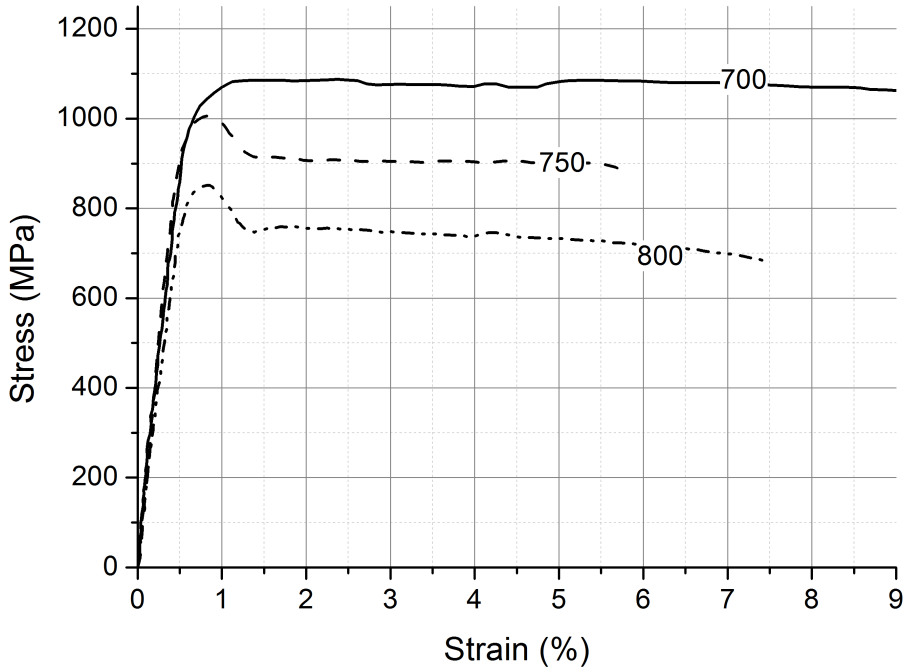


Figure 5.22: Flow stress experimental curves for 700°C,750°C and 800°C all with a strain rate of 10^{-4} s^{-1}

5.3 Pre-strained Creep tests

The results showing the effect of pre-straining the material before the creep test are shown in figures 5.23 and 5.24. The creep response of both an 800°C and room temperature 1% pre-strain and creep test at 750°C/231 MPa creep test are shown in figure 5.23. This test was not completed due to the long creep lifetime with a strain of 1.5% reached in 760 hours for the 800°C pre-strain and 1% for the same time in the room temperature pre-strain. The tertiary region is not very pronounced which is expected considering the relatively low final strain. The primary region in figure 5.23(b) reaches a low strain of around 0.02%, for both conditions. The room temperature pre-strain condition achieving this primary strain in the first hour compared to around 5 hours for the 800°C condition. Once the primary is reached the 800°C pre-strain exhibits a more rapid tertiary region compared to the behaviour at room temperature.

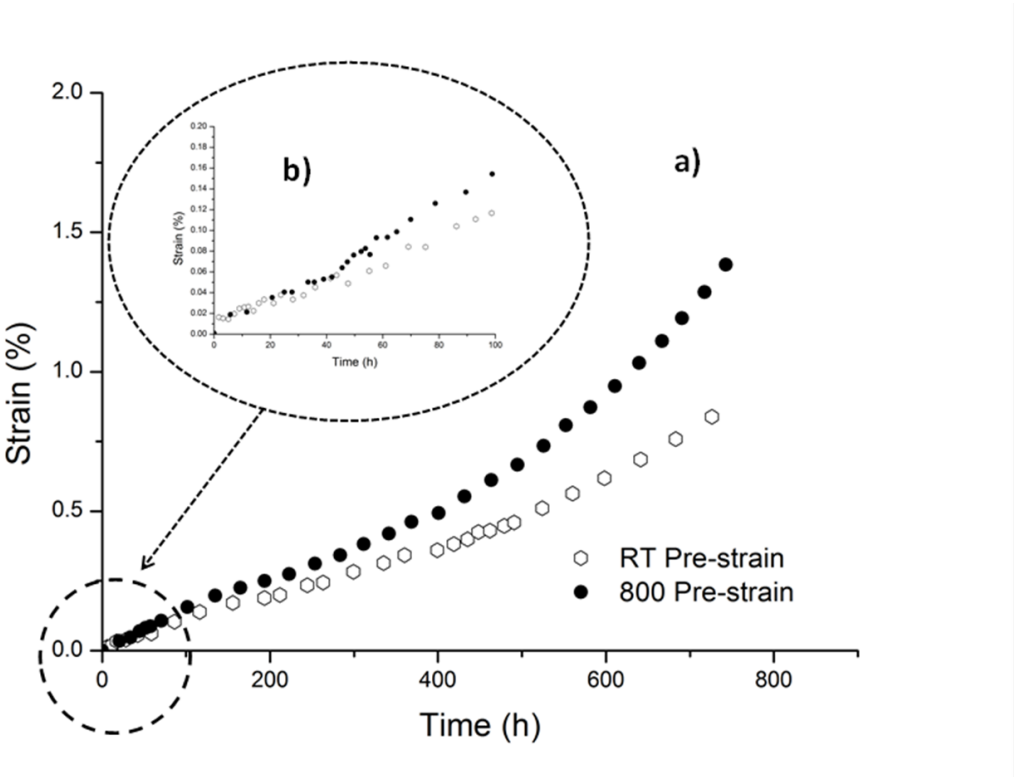


Figure 5.23: 1 % pre-strain at both room temperature and 800°C and creep tested at 750°C 231 MPa

Figure 5.24 shows creep response at 750°C/460 MPa for both 800°C and RT pre-strained tests. There was very little difference in their tertiary response behaviour, but a significant difference in their strain to failure with the room temperature pre-strained test failing earlier at 12% at 86 hours compared to 19% in just under 100 hours. Examining the primary creep region in figure 5.24 (b) there is a reduction in the 800°C pre-strained test at 0.02% compared to 0.04% in the room temperature test, though both had a very short primary region of less than an hour. This difference in primary behaviour due to pre-straining temperature is the same in figure 5.24(b) as in figure 5.23(b).

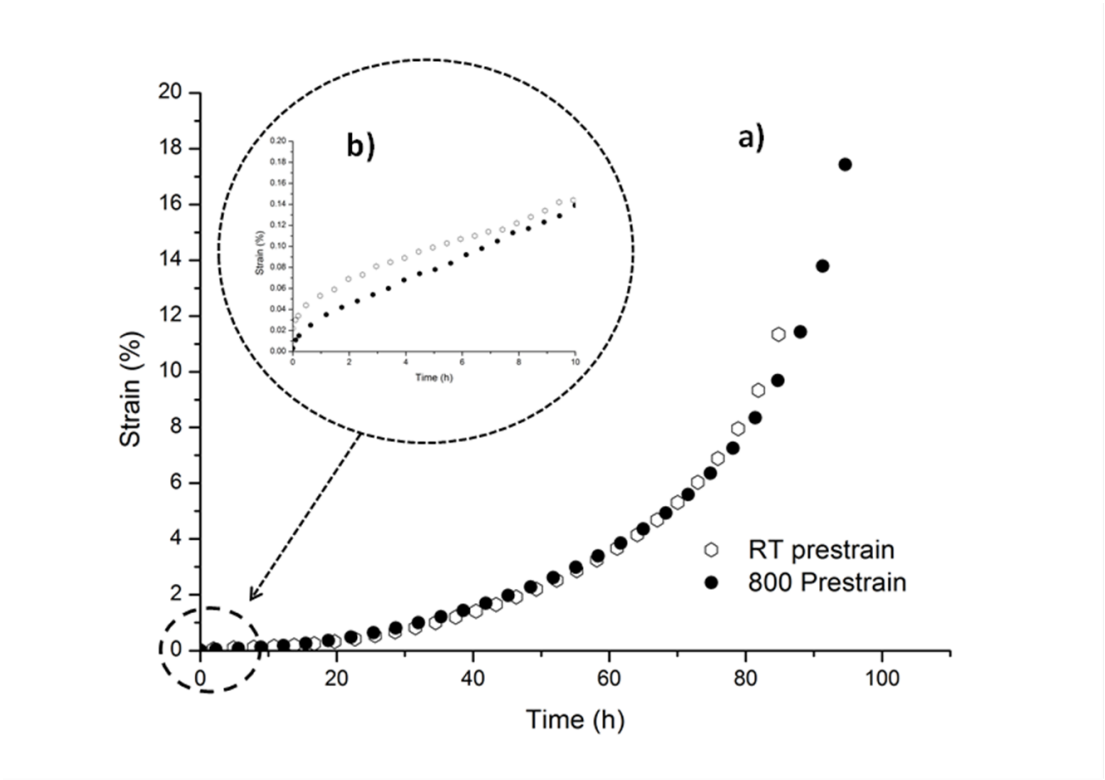


Figure 5.24: 1 % pre-strain at both room temperature and 800°C and creep tested at 750°C 460 MPa

Combining figure 5.5 with figure 5.24 to show how pre-straining compared with a standard test is shown in figure 5.25. The result shows the effect of pre-straining in this case has reduced the overall material lifetime with the 800°C ending over 36 hours less than the standard heat treated test, but having the largest strain to failure. The room temperature pre-strain failed with the earliest and the least strain. The primary behaviour in figure 5.25 is where the effect of pre-straining is most pronounced with the primary transient being reduced more than that found in both the SHT and MHT tests.

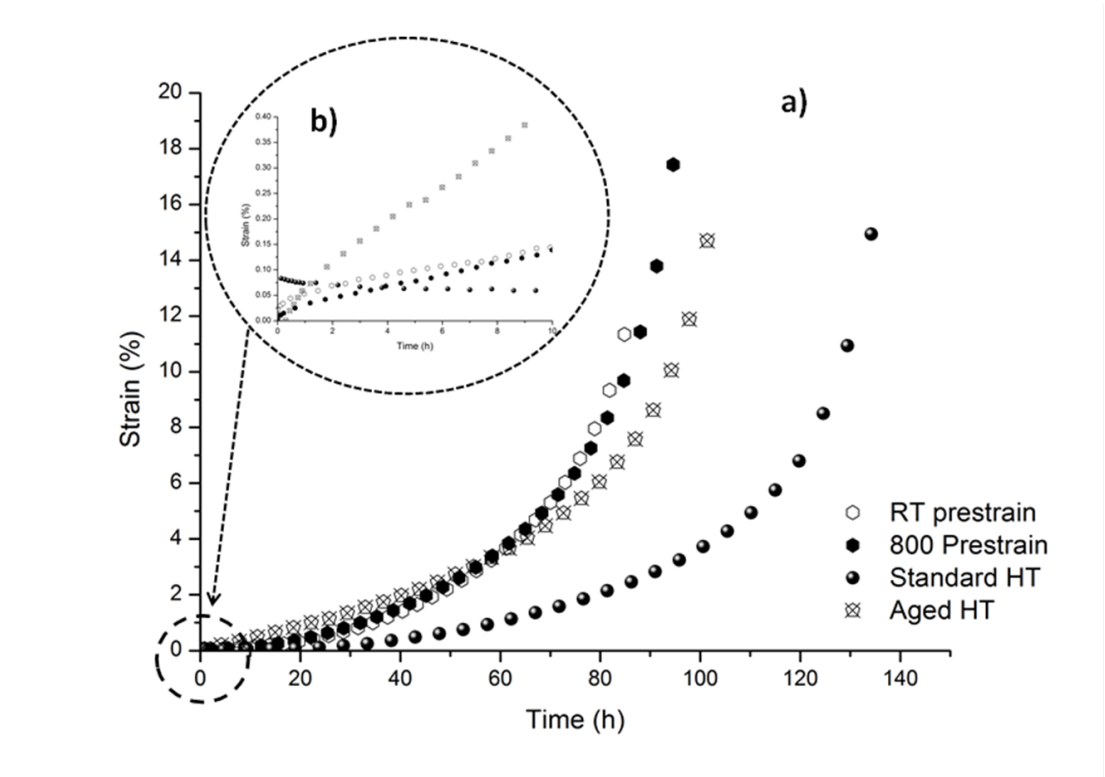


Figure 5.25: All the experimental data including old and new, and the effect of ageing temperature at the condition 750 $^{\circ}C$ 460 MPa

5.4 Microstructure Characterisation

Transmission electron microscopy (TEM) images of the γ' dispersion were taken from a subset of the creep and tensile test samples to: (i) extract information on the precipitate distributions required by the model; and (ii) investigate the influence of load and temperature on the tertiary and secondary γ' dispersion parameters. As described in the previous chapter, samples were extracted from the gauge length (near the fracture surface) and the threaded area of crept and tensile test-piece specimens. Figures 5.26 and 5.27 where samples taken from a pancake forging and given the subsequent heat treatments, these were then used for dispersion characterisation to give a rough idea what the initial microstructure was for SHT and MHT specimens.

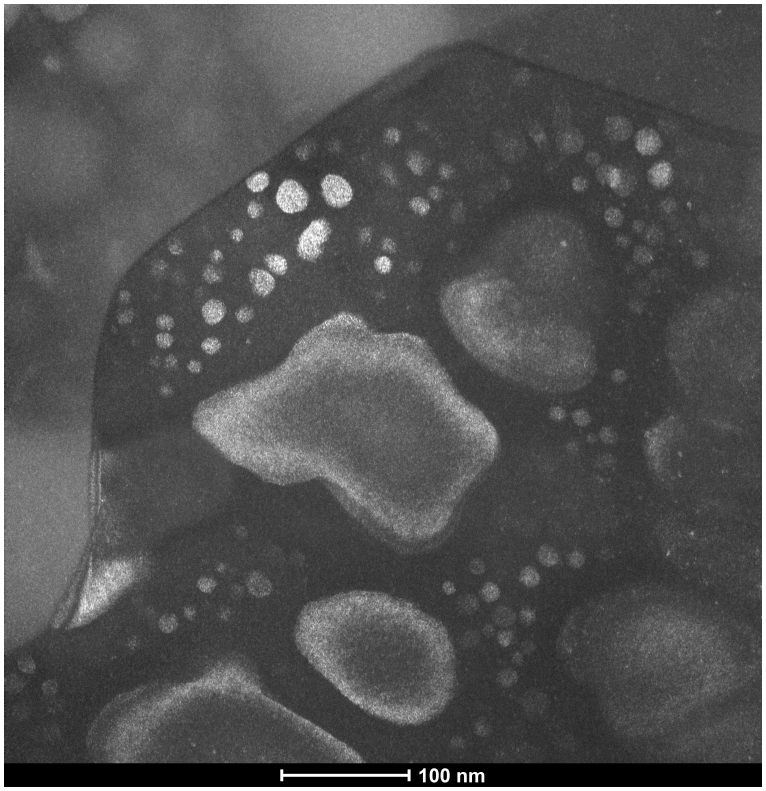


Figure 5.26: TEM image of SHT from pancake forging at 74000× (1)

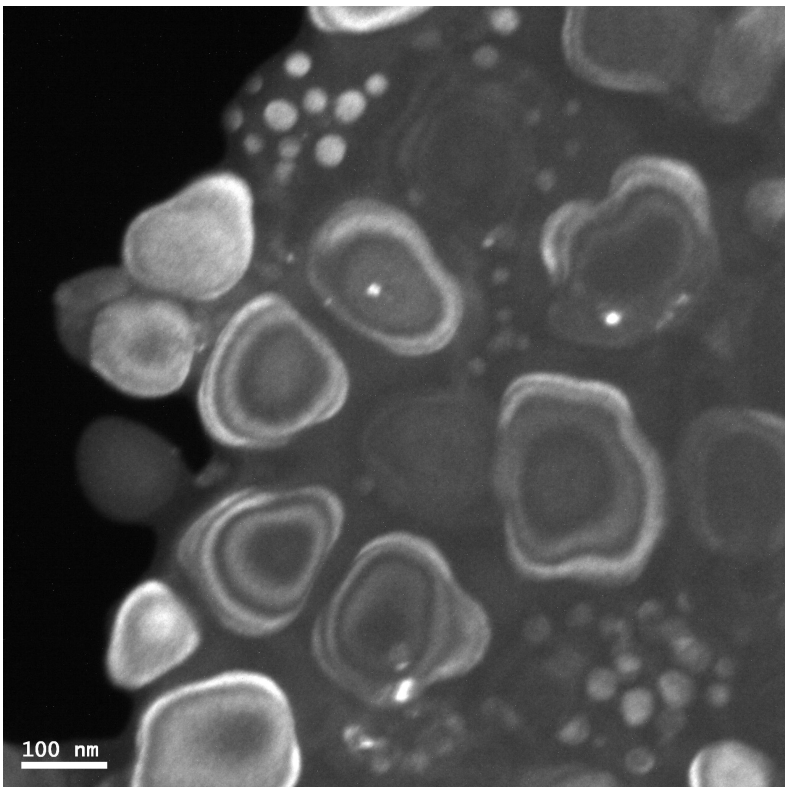


Figure 5.27: TEM image of MHT from pancake forging at 12000× (2)

The γ' microstructure corresponding to the interrupted 650°C/500MPa condition at the thread and test area for the SHT are shown in figures 5.28 and 5.29, while that for the MHT are given in figures 5.30 to 5.32.

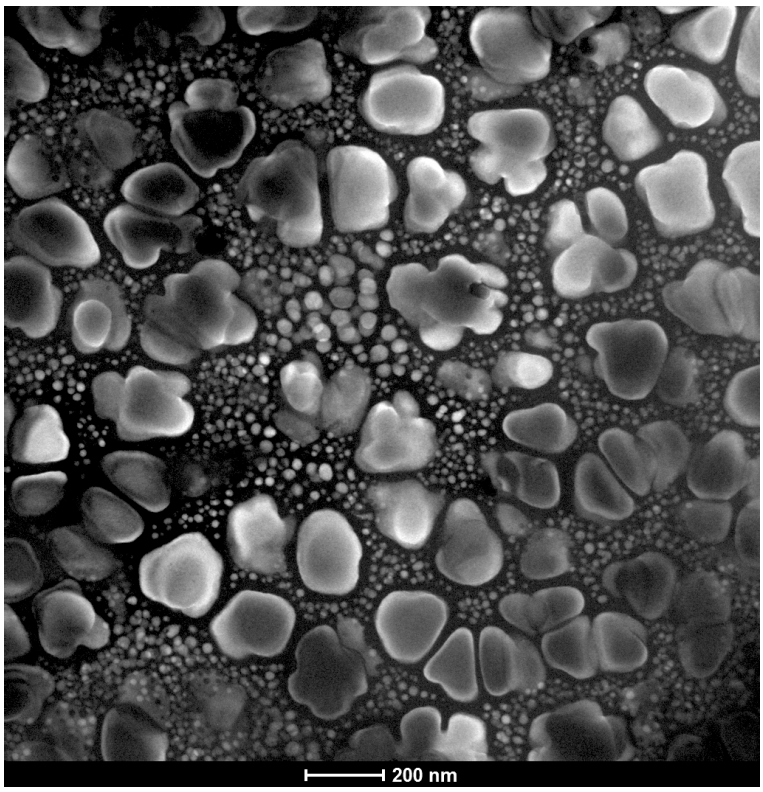


Figure 5.28: TEM image of thread area for 600°C 500 MPa at 22500x SHT

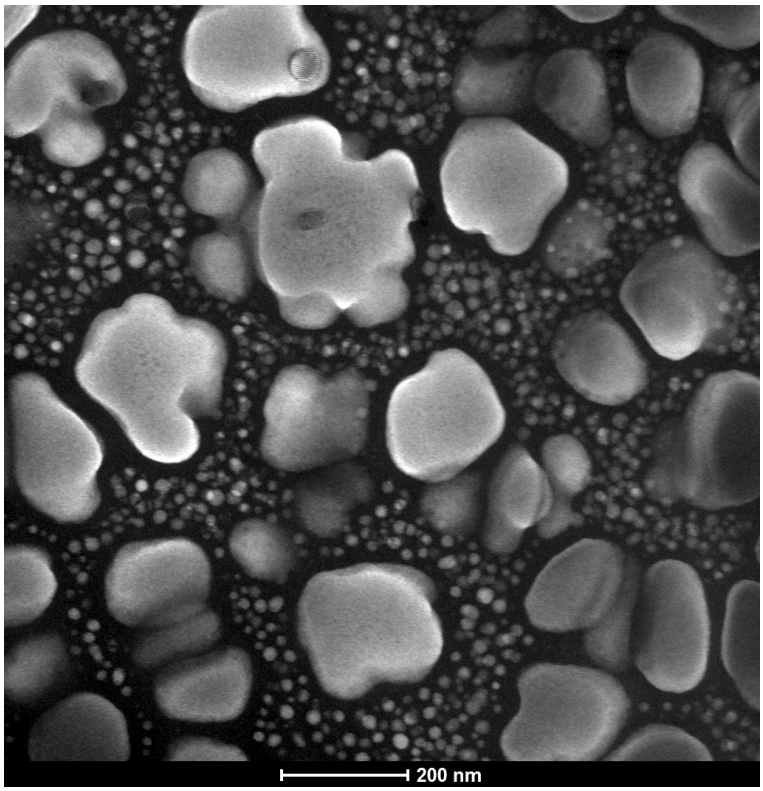


Figure 5.29: TEM image of test area for 600°C 500 MPa at 36000x SHT (2)

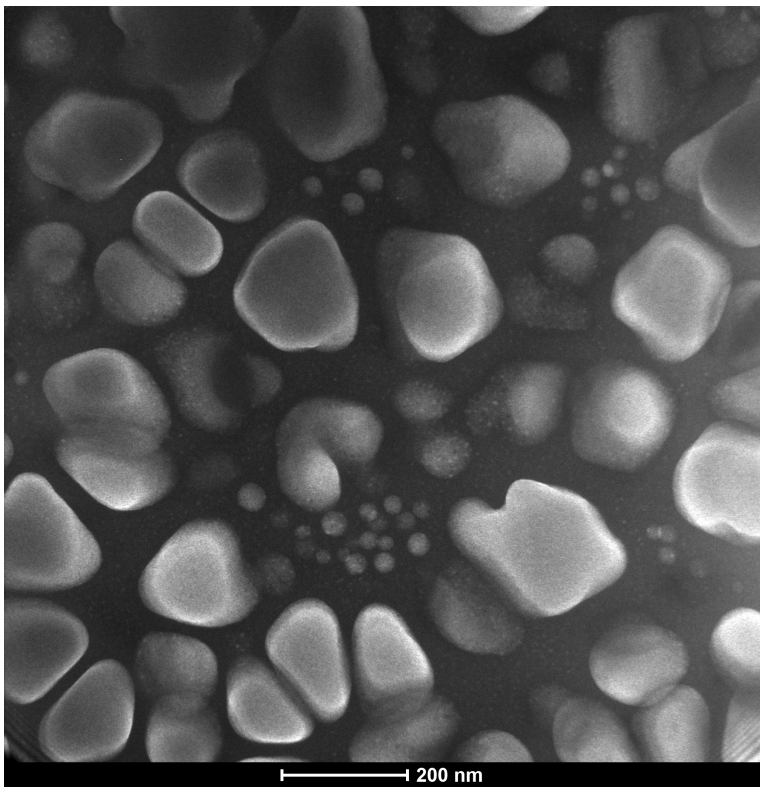


Figure 5.30: TEM image of thread area for 600°C 500 MPa at 36000x MHT

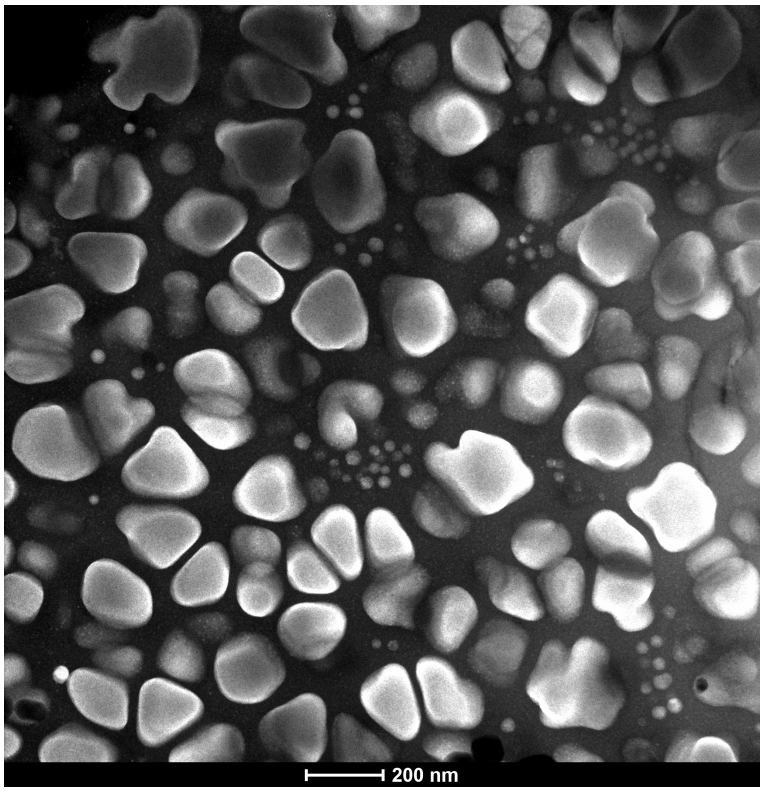


Figure 5.31: TEM image of thread area for 600°C 500 MPa at 22500x MHT

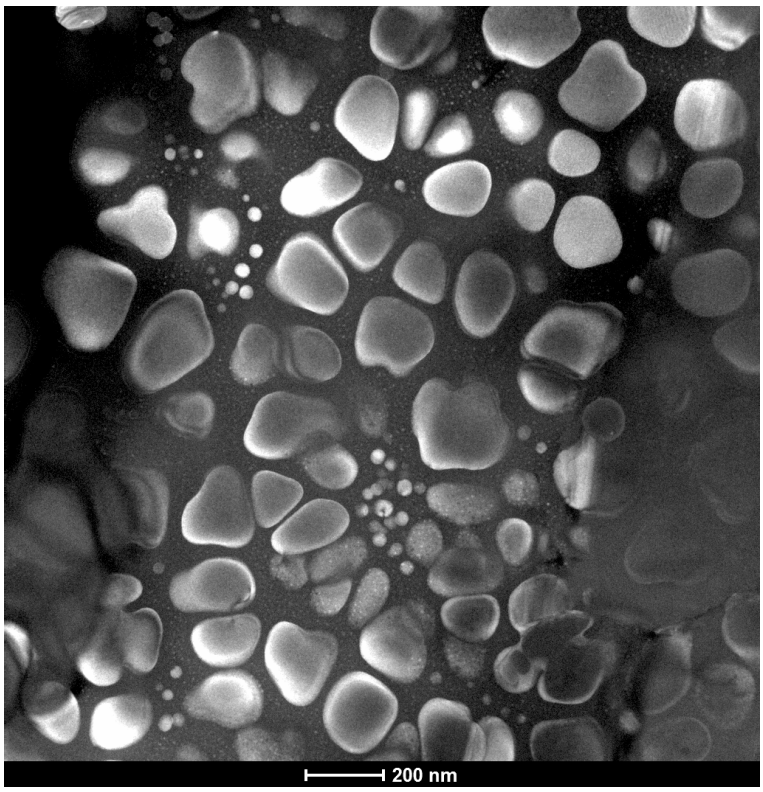


Figure 5.32: TEM image of test area for 600°C 500 MPa at 22500x MHT

It can be seen that the number density of tertiary γ' particles is smaller for the MHT sample, but larger in size as a result of coarsening they have undergone during the additional ageing.

For the 775°C/200 MPa samples the microstructures from the thread and gauge length are shown in figures 5.33 and 5.34.

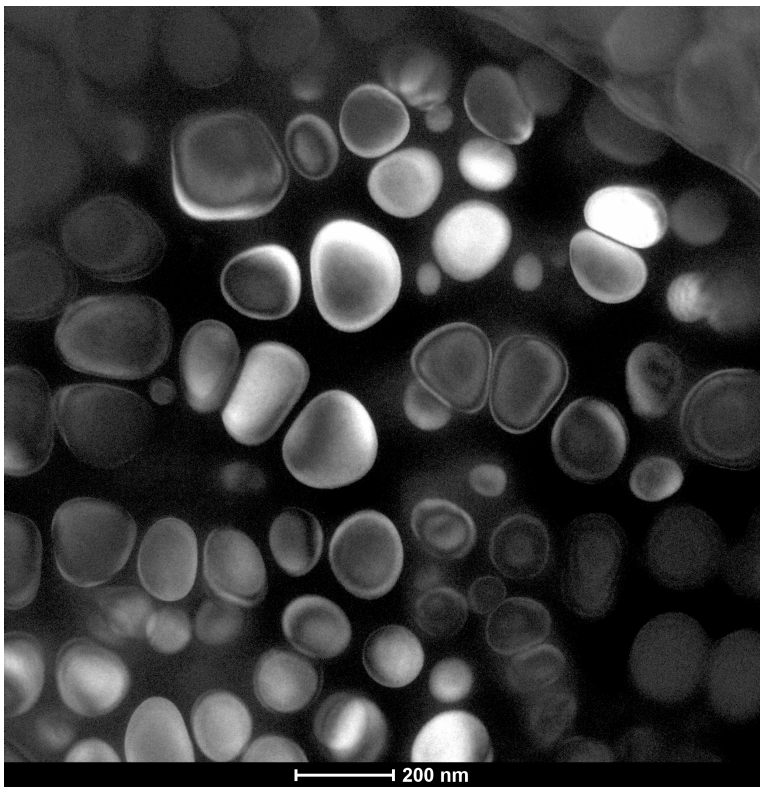


Figure 5.33: TEM image of thread area for 775°C 200 MPa at 28500x

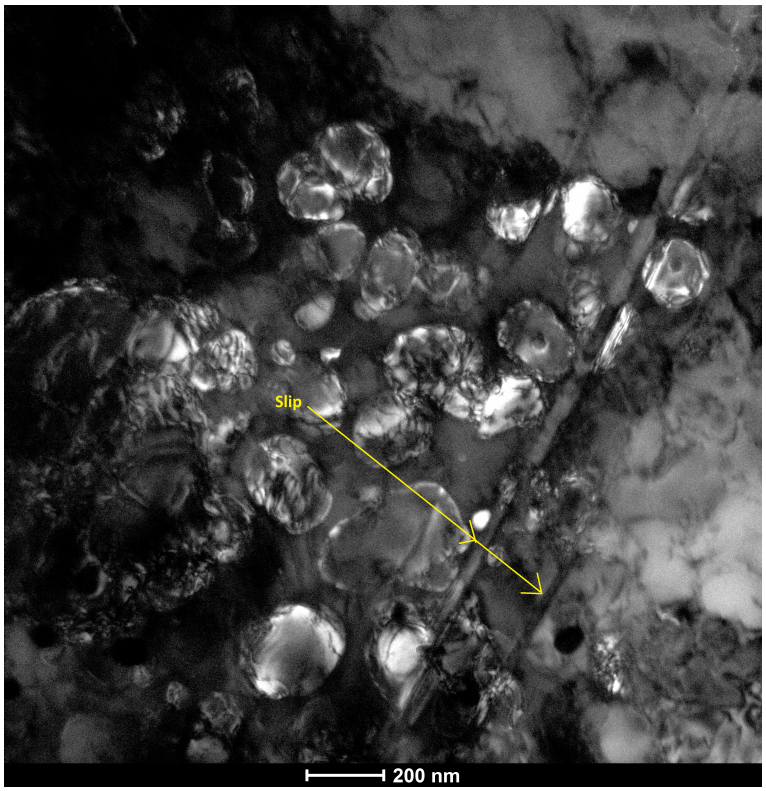


Figure 5.34: TEM image of test area for 775°C 200 MPa at 22500x

A greater amount of dislocation activity is observed in the gauge area for this case compared to 650°C/500 MPa. Dislocations are clearly visible in figure 5.34.

Similar observations are seen for the 1% pre-strain tests crept at 750°C/460 MPa. The room temperature pre-strain and the 800°C pre-strain thread and gauge microstructures are shown in figures 5.35 to 5.38.

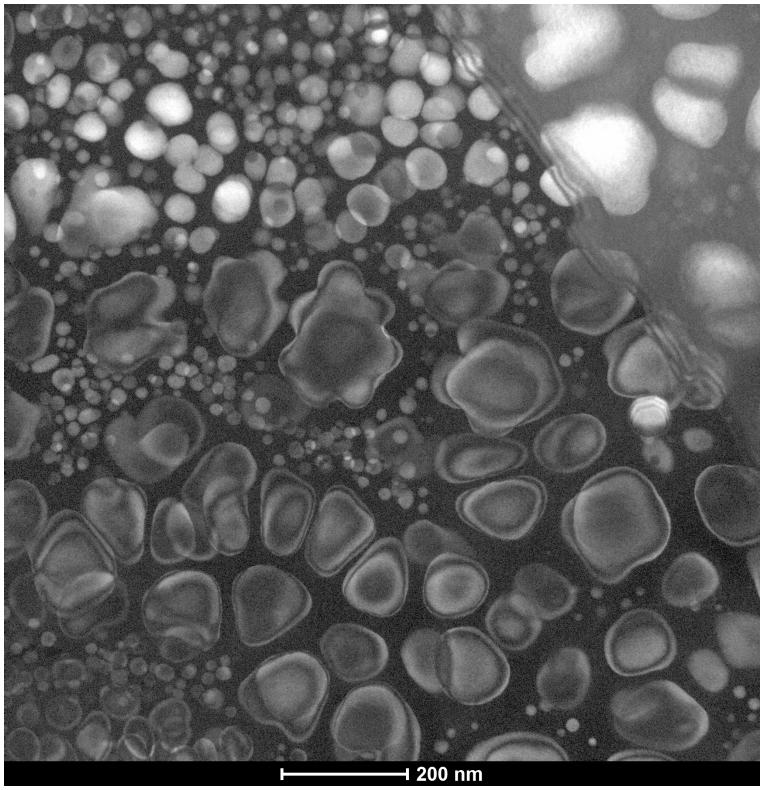


Figure 5.35: TEM image of thread area for 750°C 460 MPa RT pre-strain at 36000x

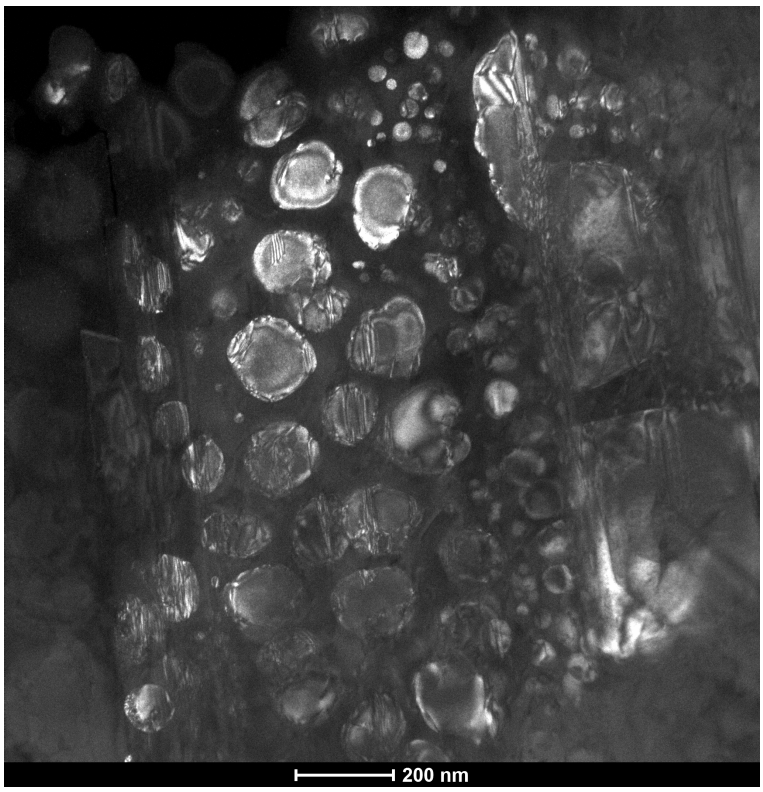


Figure 5.36: TEM image of test area for 750°C 460 MPa RT pre-strain at 28500x

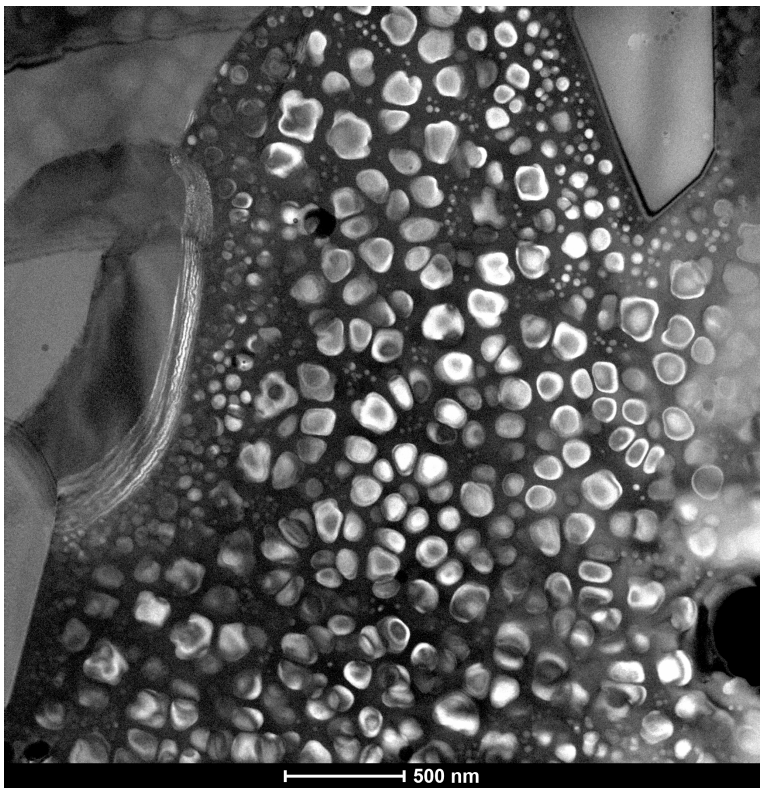


Figure 5.37: TEM image of thread area for 750°C 460 MPa 800°C pre-strain at 14000x

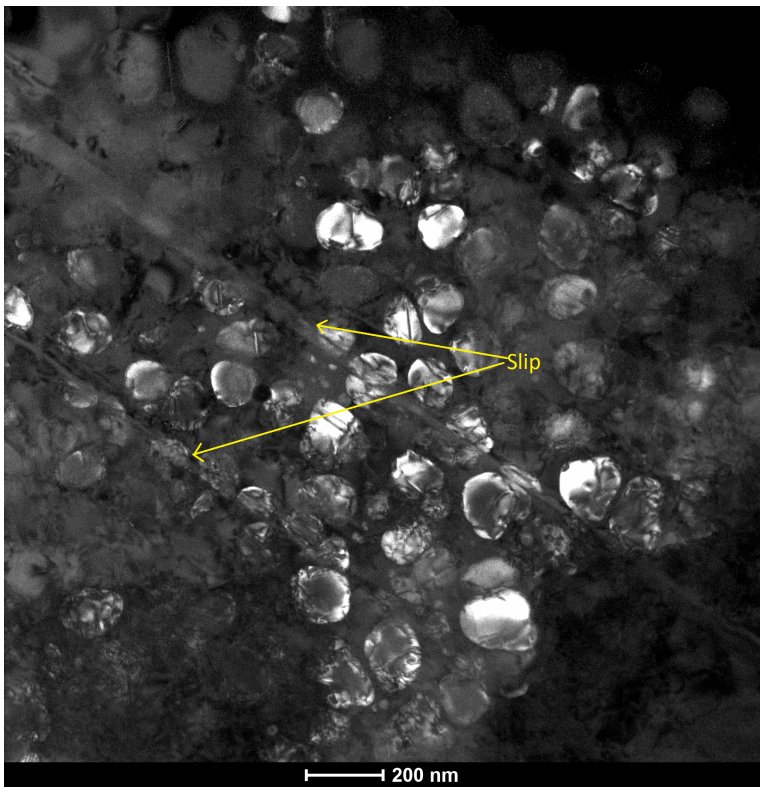


Figure 5.38: TEM image of test area for 750°C 460 MPa 800°C pre-strain at 22500x

TEM images for the room temperature pre-strained creep test are shown in figures 5.35 and 5.36 for the SHT materials and figures 5.37 and 5.38 for the 800°C prestrain samples. As for the 600°C/500 MPa case, the γ' from the thread of the MHT samples appears to have larger tertiary γ' with a smaller number density than the SHT case.

In the pre-strain samples there is no visual difference between the room temperature figures 5.35 and 5.36 and the 800°C figures 5.37 and 5.38 1% pre-strained samples. In both cases there is extensive amount of shear, with the pre-strained samples showing a greater amount of dislocation than the creep only case figures 5.33 and 5.34, but this could be due to the difference in loading conditions.

The γ' dispersion for the 800°C at 10^{-3} s^{-1} tensile test-piece was also examined. Figures 5.39 to 5.41 show micrographs taken at the thread.

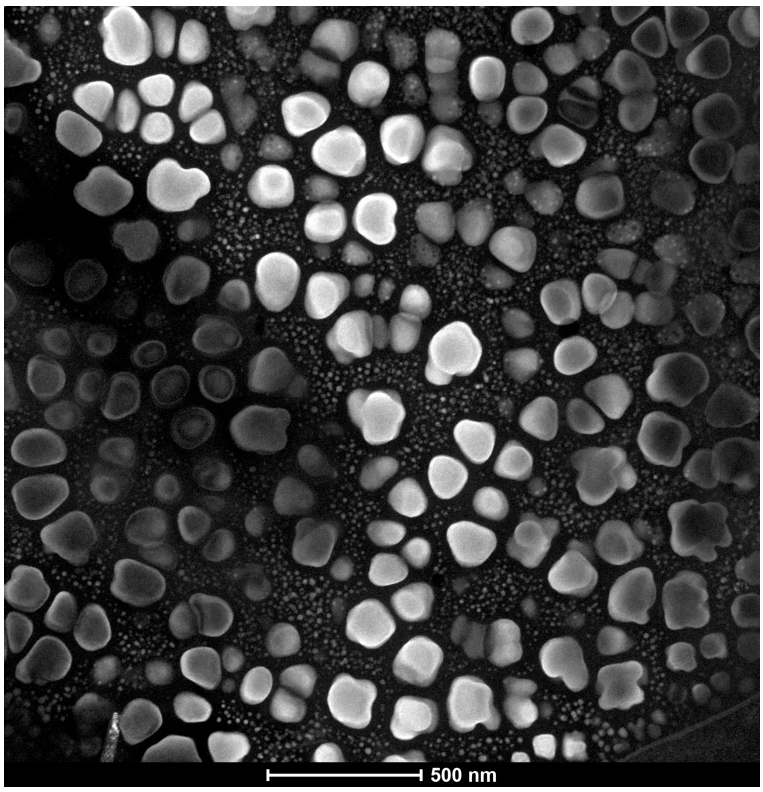


Figure 5.39: TEM image of thread area for 800°C $\dot{\varepsilon} = 10^{-3}$ at 17500x

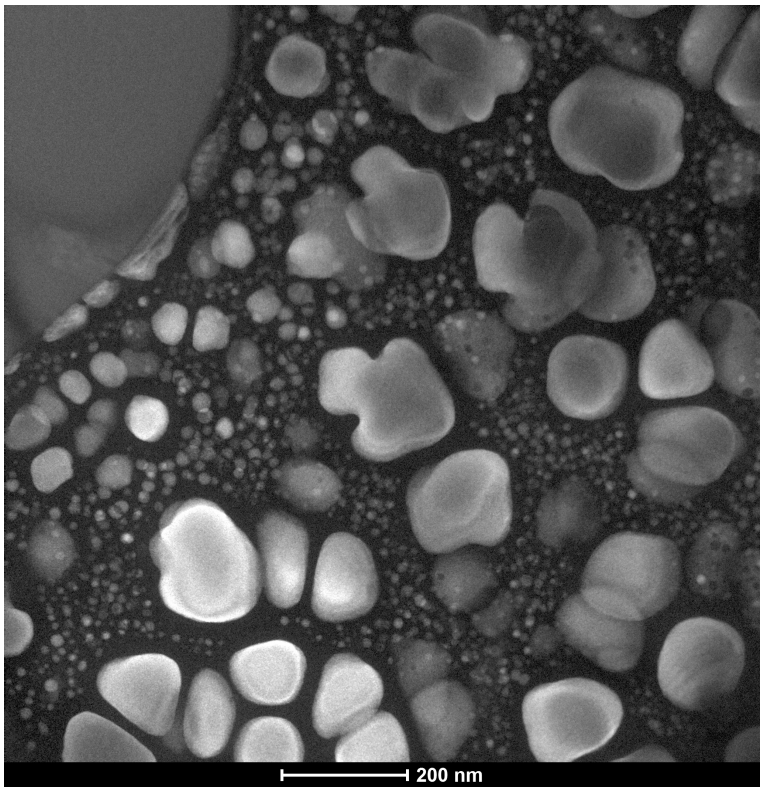


Figure 5.40: TEM image of thread area for 800°C $\dot{\varepsilon} = 10^{-3}$ at 36000x (1)

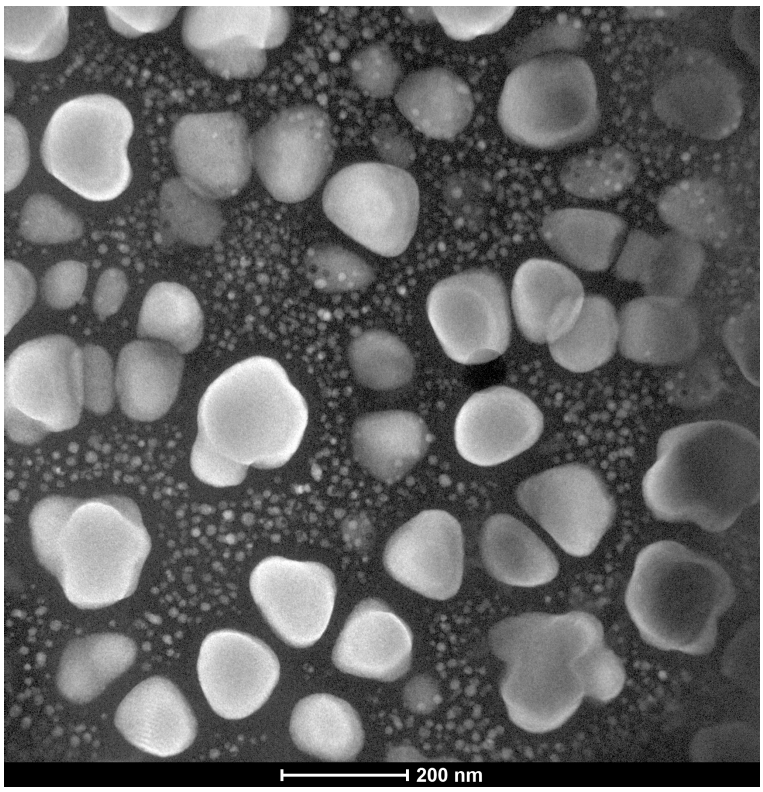


Figure 5.41: TEM image of thread area for 800°C $\dot{\varepsilon} = 10^{-3}$ at 36000x (2)

These clearly show the bimodal particle distribution consistent with that observed in the creep samples. This gives confidence that the heat treatment given to the tensile samples reproduced the desired γ' dispersion. Validating the microstructure of the heat treated pancake forging and that from the FG RR1000 test ring.

The microstructures near the fracture surface are shown in figures 5.42 to 5.44 and as expected extensive dislocation activity is observed within the γ matrix. Some of the γ' particles appear to have lost coherency indicating that they have been sheared.

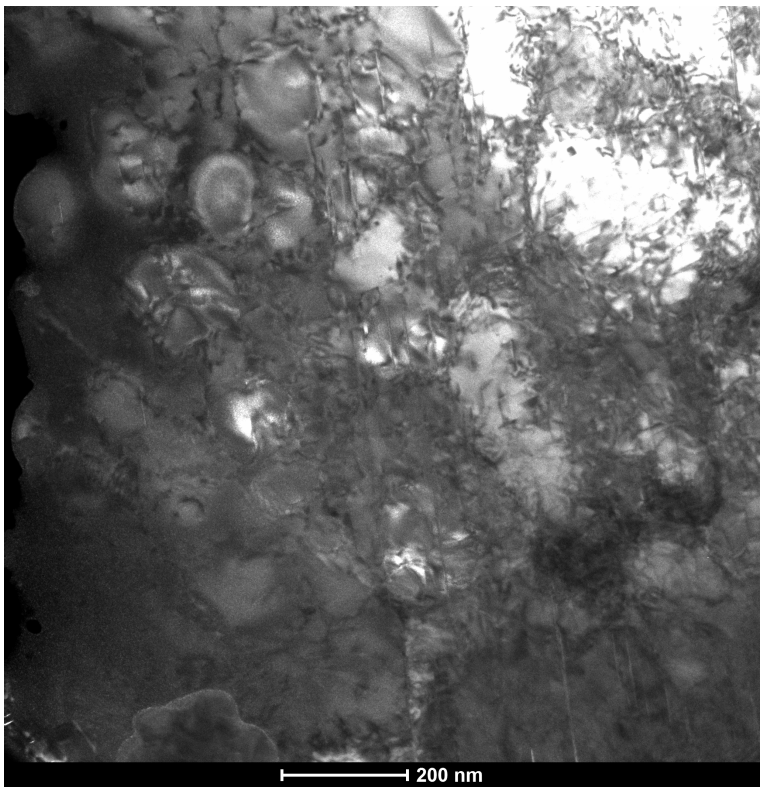


Figure 5.42: TEM image of test area for 800°C $\dot{\varepsilon} = 10^{-3}$ at 36000x (1)

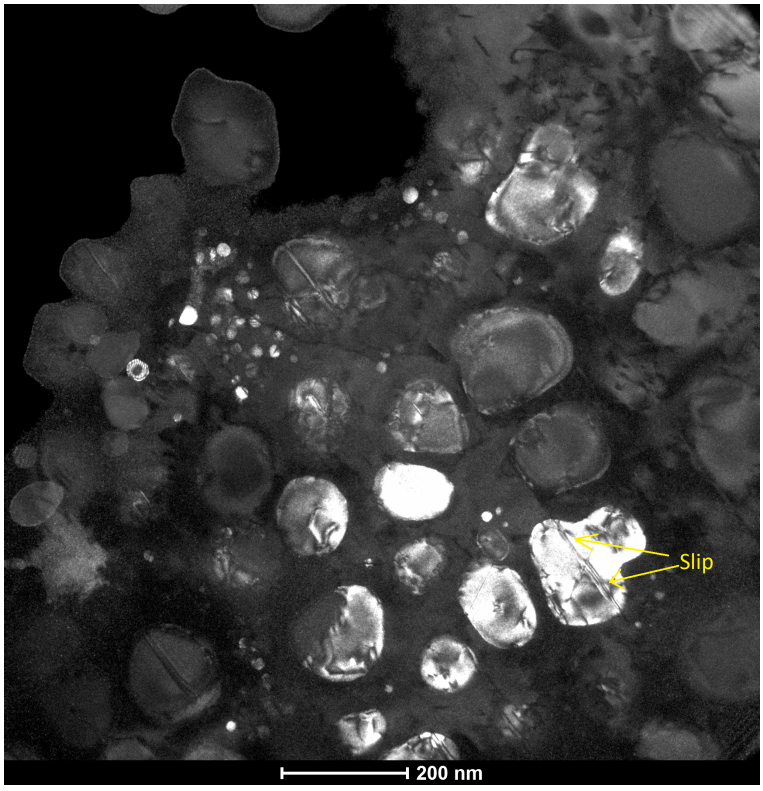


Figure 5.43: TEM image of test area for 800°C $\dot{\varepsilon} = 10^{-3}$ at 36000x (2)

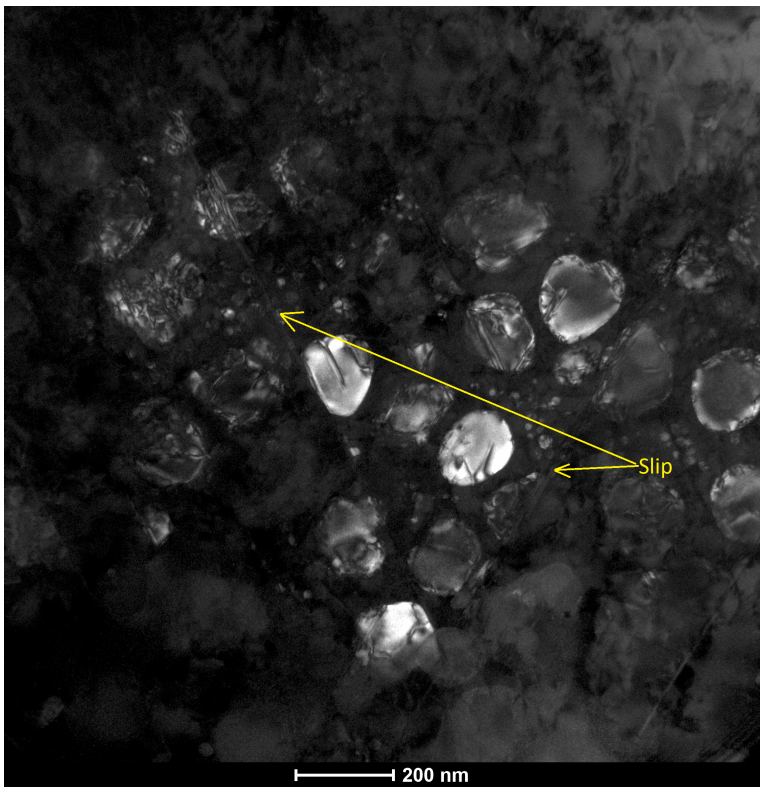


Figure 5.44: TEM image of test area for 800°C $\dot{\varepsilon} = 10^{-3}$ at 28500x

The measured size distributions for the secondary and tertiary particle populations from the test ring samples with the SHT and MHT are shown in figures 5.45 and 5.46. Also shown are the number densities for the two particle populations. For secondary γ' the Standard-HT (sample 1) had a minimum particle radius of 30 nm and a maximum of 130 nm. For the MHT (sample 2) a minimum size of $\sim$30 nm and a maximum of slightly over 100 nm were observed. The two secondary particle distributions of the SHT and MHT are not very different, although that of the SHT sample appear to be more uniform over the size range. The tertiary sizes for the test ring are in figure 5.46. The SHT sample has a minimum particle radius of 2 nm and a maximum of 22 nm. The MHT on the other hand has a minimum of 4 nm and a maximum of 26 nm. Comparing both data sets together the MHT has a larger frequency of larger tertiary precipitates.

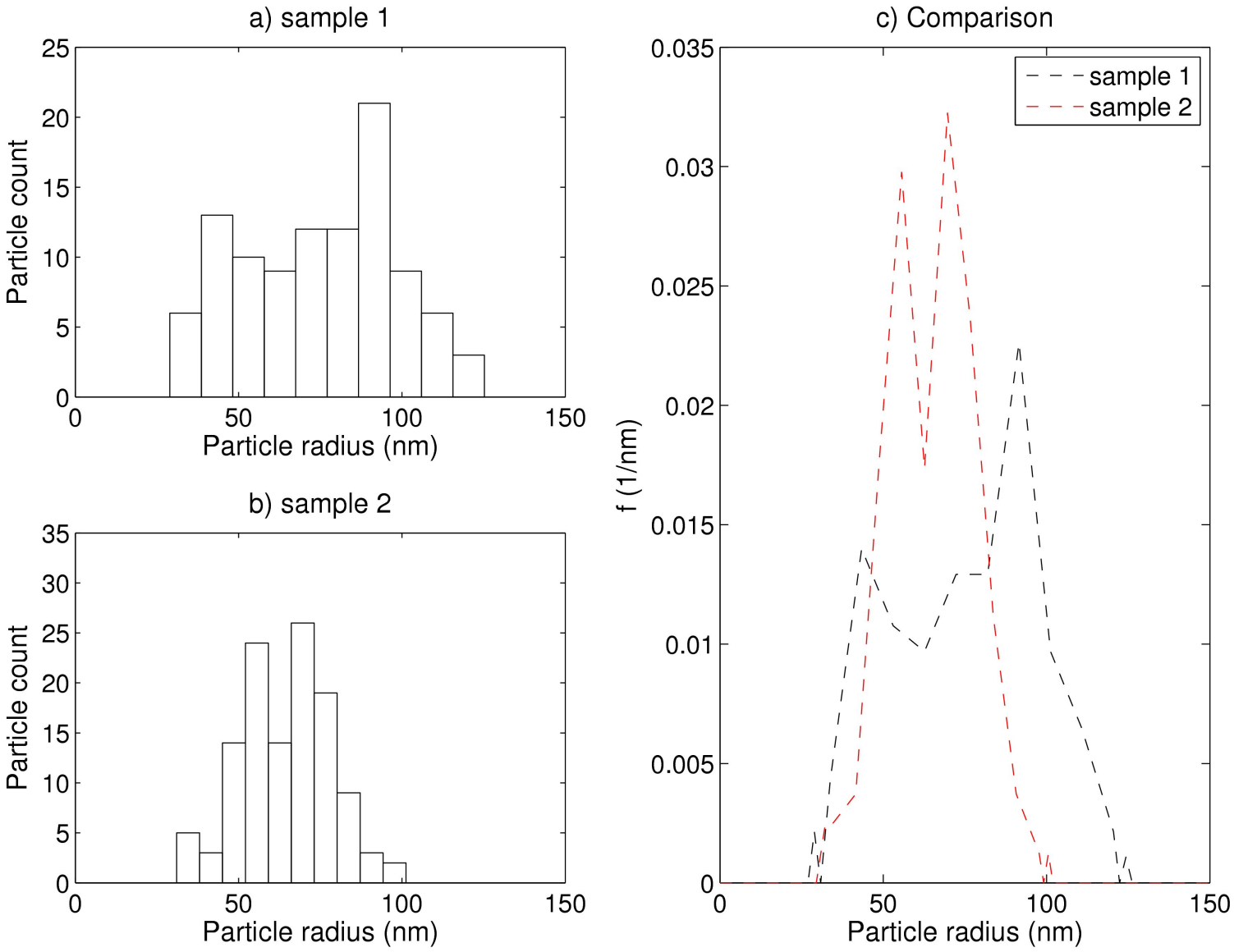


Figure 5.45: Size distribution of secondary γ' from the test ring: (a) SHT sample, (b) MHT sample; and (c) number density distribution

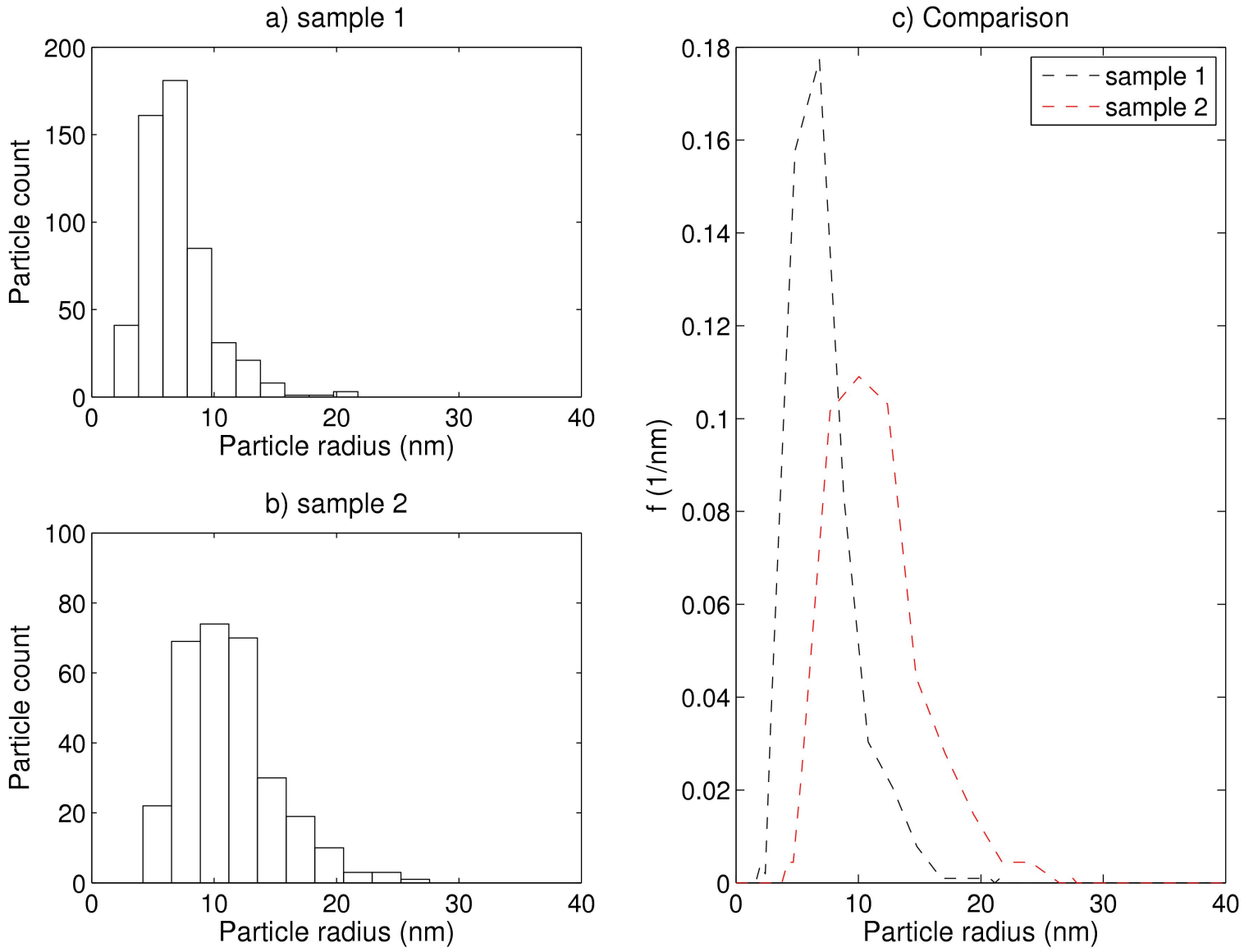


Figure 5.46: Size distribution of tertiary γ' from the test ring: (a) SHT sample (b) MHT sample; and (c) number density distribution

TEM images of the secondary and tertiary γ' particles taken from the pancake forging are presented in figure 5.47 and figure 5.48, respectively. The MHT sample shows a coarser secondary γ' distribution compared with that corresponding to the SHT. For SHT the minimum size was 28 nm radius and the maximum was 105 nm, compared with the MHT which had a minimum size of 35 nm and a maximum of 115 nm. Comparing the tertiary particle size distribution there are clear differences between the standard and modified heat treatments, see figure 5.48. In the SHT condition a minimum size of 7 nm and a maximum of 40 nnm were observed for the tertiary particles. MHT samples had a minimum size of 4 nm and a maximum of 18 nm.

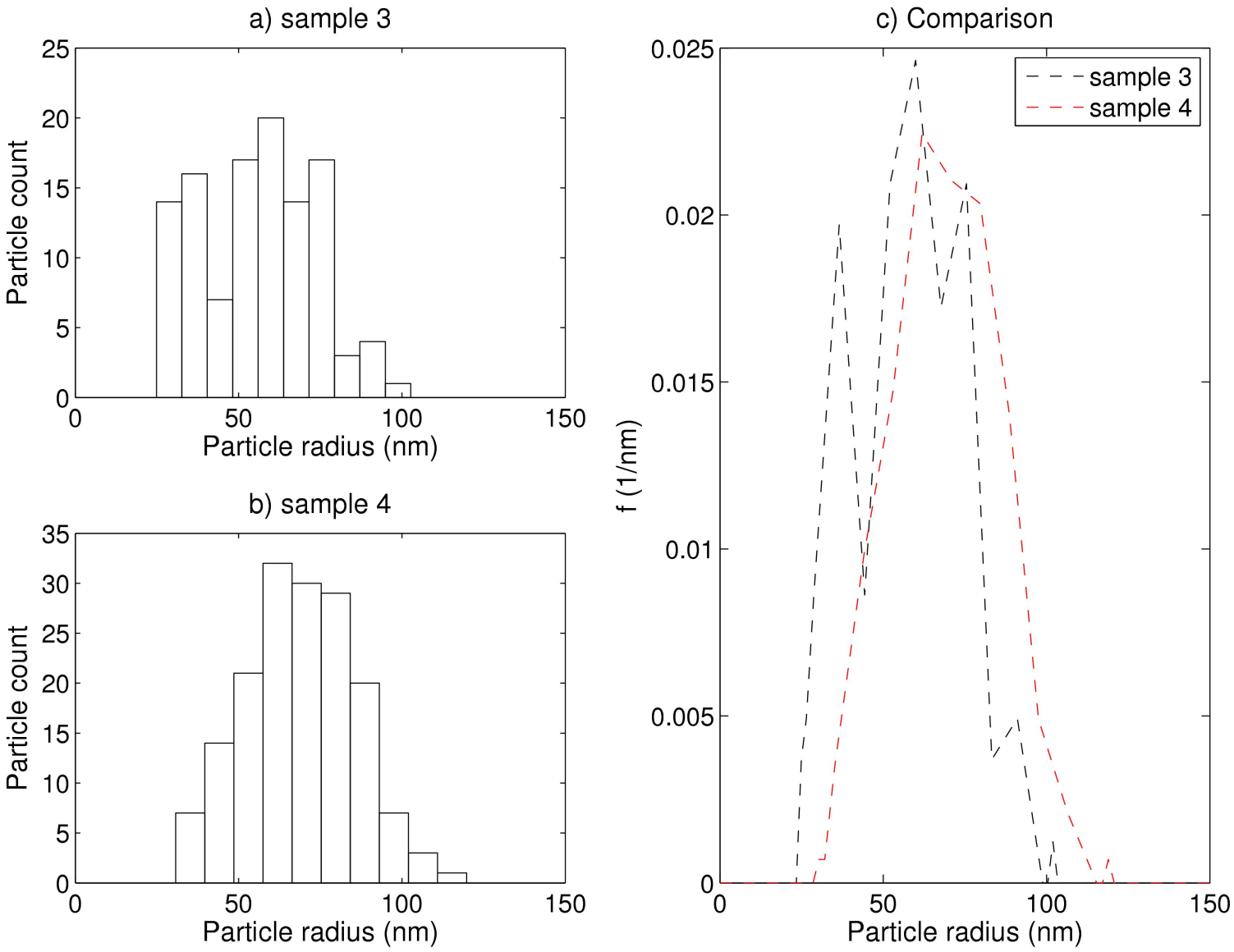


Figure 5.47: Size distribution of secondary γ' from the pancake forging: (a) SHT sample; (b) MHT sample; and (c) number density distribution

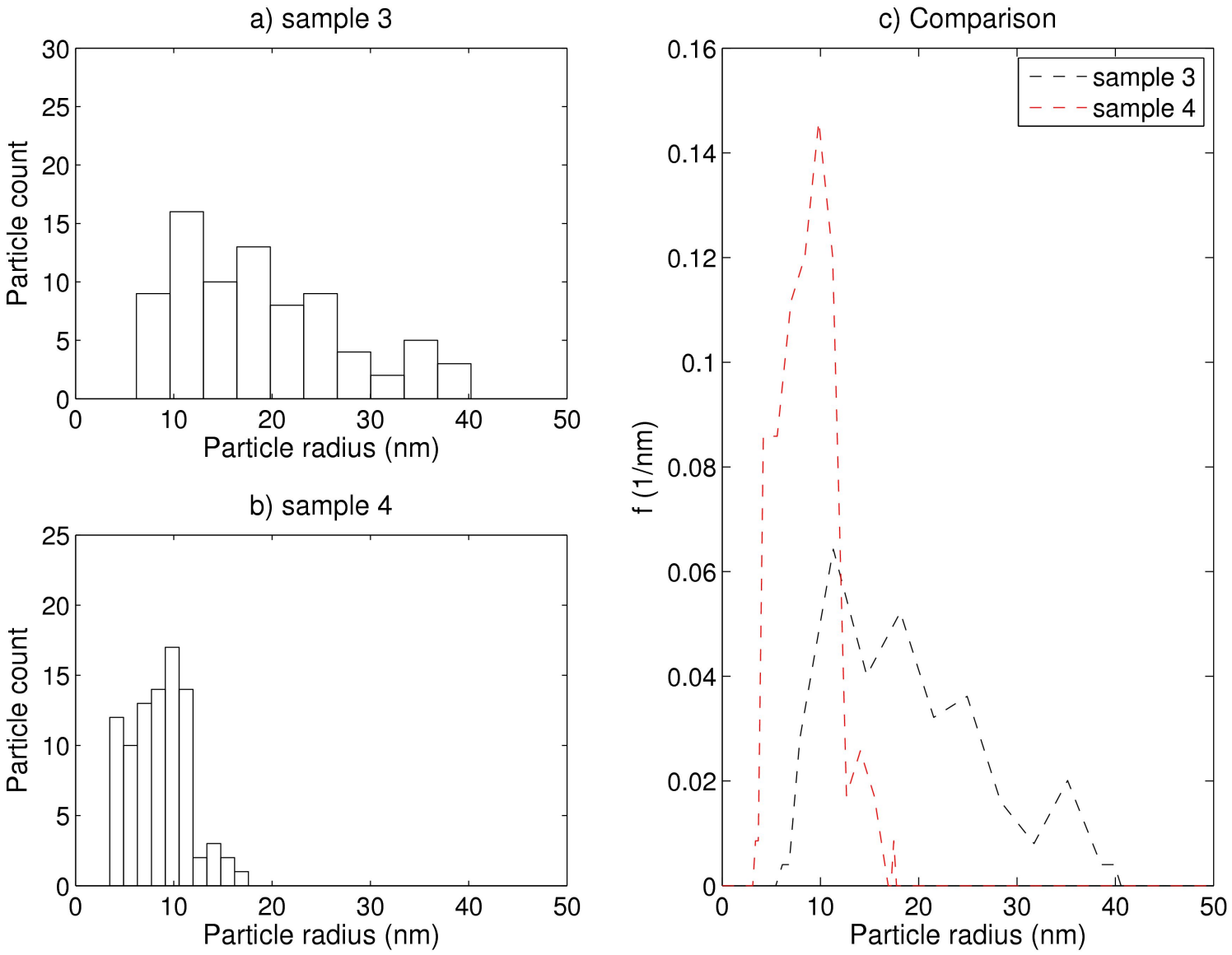


Figure 5.48: Size distribution of tertiary γ' from the pancake forging: (a) SHT sample; (b) MHT sample; and (c) number density distribution

The volume fractions for the tertiary precipitates were calculated from the TEM images using the software Digitise to manually shade in particles and calculating the proportion of the image shaded. Assuming that due to their small size the tertiary precipitates area fraction is equivalent to the volume fraction. However, for the secondary precipitates, due to the thickness of the samples, only the area fraction of the could be calculated. The results are summarised in table 5.1.

Table 5.1: Volume fraction of tertiary γ' and area fraction for secondary γ' for each of the different samples

sample	min tertiary vf	max tertiary vf	secondary af
1	0.0156	0.0290	0.4255
2	0.0336	0.0624	0.4862
3	0.0517	0.0921	0.4939
4	0.0042	0.0077	0.4707

Chapter 6

Numerical implementation and results

6.1 Identification of model parameters

A microstructure-explicit viscoplastic model for γ' strengthened nickel-based superalloys has been presented in chapter 3, which is coupled to a mean field description of the temporal γ' size distribution evolution. These models require specification of a number of parameters, and the procedure for their identification will now be described.

The first step is calibration of the mean field model parameters. These parameters are associated with the particle growth rate given by equation (2.66) which is based on minimisation of interface curvature. Olson *et al.* [75] measured values for the interfacial energy from RR1000 and we have taken these values as representative in this work. For the diffusivity parameters $D_{v,0}$ and Q seen in equation (2.44) the starting values are those corresponding to pure nickel which are $D_{v,0} \sim 1.9 \times 10^{-4}\mathrm{m}^2\mathrm{s}^{-1}$ and $Q \sim 284\mathrm{kJmol}^{-1}$ [76]. Since we are dealing with an alloy with complex chemistry, the increased solid solution and will result in reduced diffusion rates. From coarsening data of a number of nickel-based superalloys the pre-exponential factor takes on values in range $D_{v,0} \sim 10^{-4} - 10^{-6}\mathrm{m}^2\mathrm{s}^{-1}$

while the activation energy $Q \sim 300\text{kJmol}^{-1}$ [76]. These were adjusted until the average particle size and volume fraction at different temperatures and exposure times matched experimentally available data (see section 6.2). The mean field model parameters used for the prediction of the γ' size distribution are listed in section 6.1

Molar volume m^3	Interfacial area Jm^{-2}	Lattice misfit strain	D_{v0} $m^2 s^{-1}$	Q_v $kJmol^{-1}$
2.72×10^{-5}	0.0225	7.3×10^{-4}	10^{-4}	300

Table 6.1: Mean field parameters

The micromechanistic modelling approach outlined in chapter 3, naturally introduced a number of parameters that have direct physical meaning and therefore provides in principle an initial parameter-set that can be used for model predictions of strain-time trajectories. This is in contrast to existing empirical or phenomenological modelling approaches where model parameters have no or little physical meaning. In such cases there is a lack of uniqueness in the model parameter-sets, since theoretically an infinite number of parameter combinations can be used to represent a creep database.

For the diffusivity parameters $D_{v,0}$ and Q controlling the temperature dependence of the creep model, the starting values are those driving γ' growth rate in the mean field model.

It was found that a lower effective diffusivity was needed to describe the creep data, in particular a large activation energy $Q \sim 309\text{kJmol}^{-1}$. The difference in activation energies is assumed to be a result of the formation of jogs. The jogs are created to enable the dislocation to climb pass the γ' particles at high temperatures. The particle growth rate involves self-diffusion only.

The diffusivity parameters were identified with the constraint to be within these ranges and that best represent the lifetime database. The Burgers vector for nickel is taken to be $b \sim 2.54 \times 10^{-10}$ m and the Taylor factor $\bar{M}$ has been

estimated to take a value of 3.1 for fcc crystals.

Evolution of the dislocation density requires specification of a multiplication parameter C. Previous work using similar state variable models suggest $C \sim 10^2$ [9] [77] [40] whilst theoretical estimations C is a lot larger. The theory assumes the entire mobile dislocation network acts as sources and gives $C = \bar{M}/b$ and under this assumption we estimate $C \sim 10^{10}$, this value was found to be too small This discrepancy between the theoretical estimate and 'measured' value for C will be addressed in the discussion. For the initial dislocation density it is assumed that at least one source is operational per grain. Taking a grain size of $d_g = 10\mu$m as representative for fine grain RR1000, then the initial mobile density is assumed that initially no dislocations are moving $\rho_{m,0} = 1\text{m}^{-2}$. The final parameter-set is listed in section 6.1.

$D_{v,0}$ $m^2 s^{-1}$	Q $kJmol^{-1}$	b nm	$\bar{M}$	C	$\rho_{m,0}$ m^{-2}	α
10^{-5}	309	2.54	3.1	$1E14$	1	0.5

Table 6.2: List of creep model parameters

The temperature dependent Poisson's ratio, Young's modulus and the misfit strain are plotted in figure 6.1.

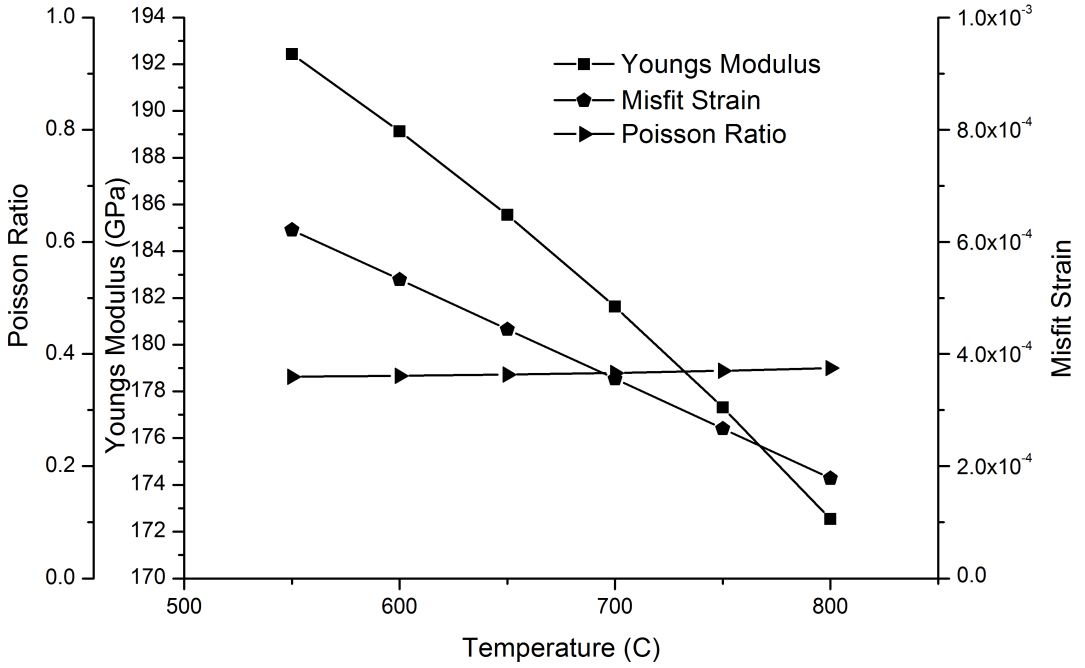


Figure 6.1: Data capturing RR1000 Young's modulus, Poisson's ratio and Misfit strain and how these vary with temperature

These were taken from the PANACEA program [1] and can be represented with following polynomial fits over temperature:

$$E(GPa) = -8.1836 \times 10^{-8}T^3 + 9.1952 \times 10^{-5}T^2 - 9.0545 \times 10^{-2}T + 228.04 \tag{6.1}$$

$$\nu = 2.3755 \times 10^{-10}T^3 - 3.2605 \times 10^{-7}T^2 + 1.7383 \times 10^{-4}T + 0.32275 \tag{6.2}$$

$$\varepsilon_{misfit} = -1.772 \times 10^{-6}T + 1.596 \times 10^{-3} \tag{6.3}$$

For the crystal plasticity simulations, the stiffness tensor needs to be specified. No values for this tensor are available for RR1000 in the scientific literature. However, there are a number of papers reporting on single crystal superalloys. Due

to the lack of information for the stiffness tensor for RR1000, this work will use values measured for CMSX4 at room temperature by Dye et al [78]. The work collected a table of values from various sources this was averaged to get: C_{11} = 233GPa, C_{12} = 146GPa and C_{44} = 133GPa. This is due to the extensive amount of work of stiffness constants for CMSX-4 compared to RR1000, both are nickel based superalloys strength dependant on the γ' phase. There are significant differences in volume fraction and microstructure morphology, the similarities are deemed significant enough to allow these values to be used to be able to gauge model behaviour.

6.2 Mean field predictions of the γ' evolution

Figure 6.2 shows a comparison of the calibrated mean field predictions for the average tertiary γ' particle radius as a function of time with experimentally measured values within the temperature range 680-840°C. The experimental data was taken from the PANACEA programme [1] with the error bars showing the scatter in measured tertiary size are compared against the prediction lines. It can be seen that the simulated tertiary γ' evolution is in good agreement with the available experimental data. The predictions where using the parameters in section 6.1 and equations (2.65) to (2.67).

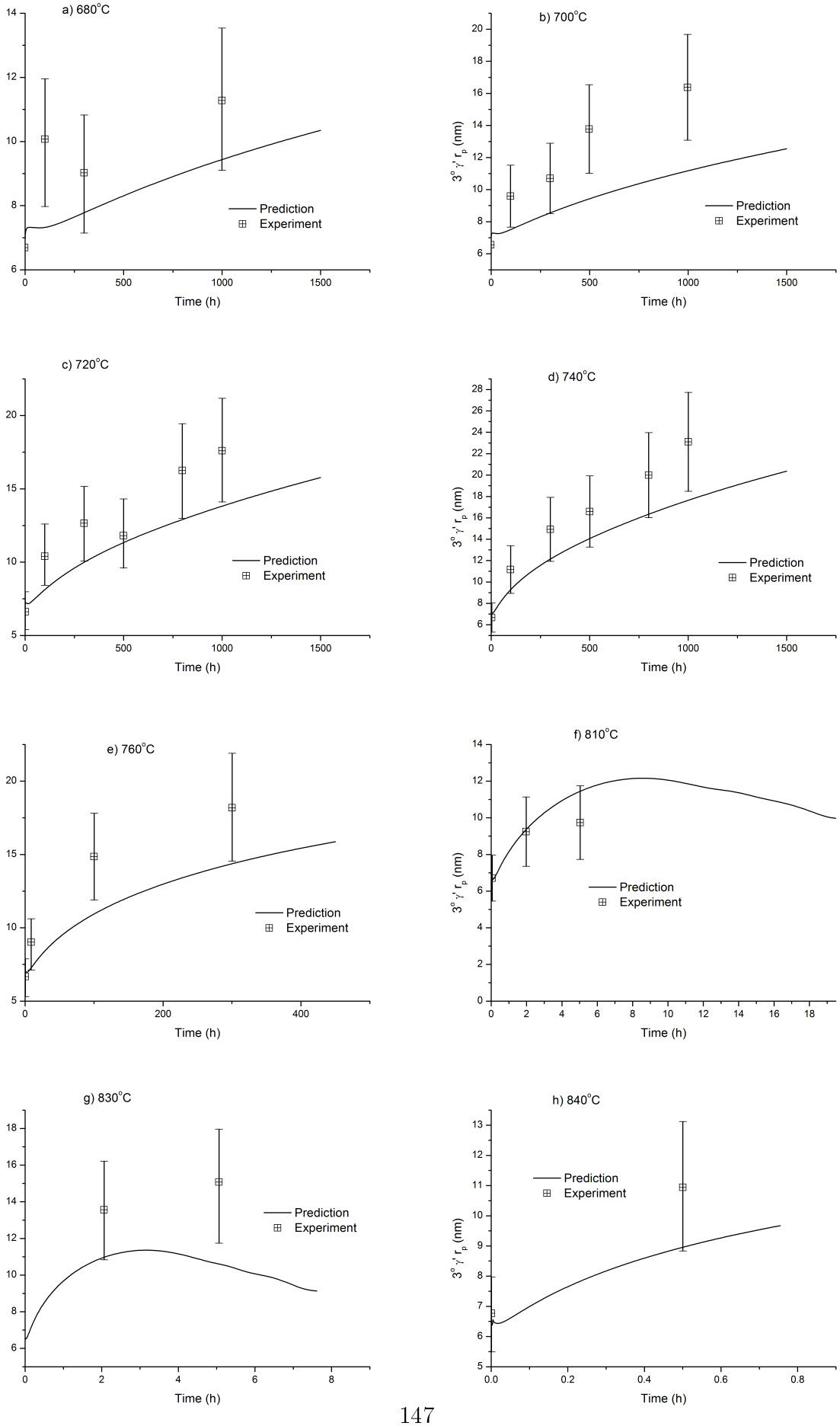


Figure 6.2: Tertiary γ' size distribution, showing mean field predictions and experimental data from the PANACEA programme [[1]].

Figure 6.3 shows the evolution of tertiary γ' particle radius distribution for a range of temperatures $650 - 800°$C. At low temperatures $< 750°$C, the particle size remains approximately unchanged for the thermal exposures considered in the present calculations. However, for temperatures $\geq 750°$C the particle growth rates are significantly increased and the tertiary γ' particles are predicted to coarsen with the development of a spreading of the number density.

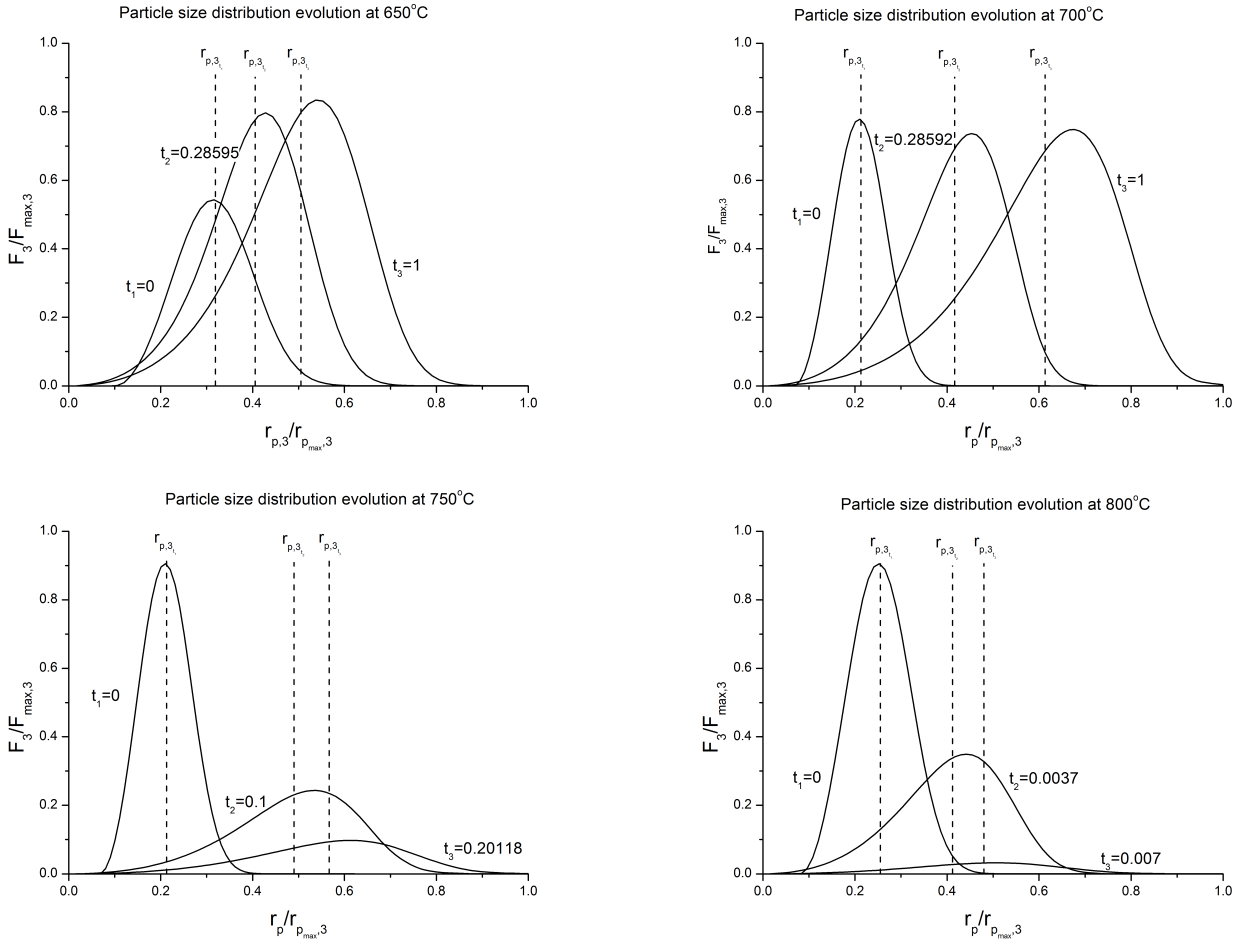


Figure 6.3: Mean Field predictions of γ' evolution predictions validated against PANACEA experimental data in [1]

Although the tested samples were RR1000, the secondary γ' was not examined; the main focus of the work in [1] was to characterise the tertiary γ' in the temperature range of 680-840°C. Combined with the belief that at those conditions examined the secondary γ' does not change significantly and any such change would be difficult to measure. Since the model predicts the entire microstructure

evolution, not just tertiaries it can be assumed to accurately predict the tertiary behaviour the secondary behaviour is also being captured as well.

With the Mean Field model validated it will be used to create the microstructure for which the creep model will be designed for, assuming this was the initial microstructure for all the experimental samples.

6.3 Experimentally derived distributions

Using the the experimentally measured microstructure, size distribution were generated using a Weibull function:

$$F(R) = \frac{\alpha_w}{\beta_w}\left(\frac{R-\gamma_w}{\beta_w}\right)^{\alpha_w-1} exp^{-\left(\frac{R-\gamma_w}{\beta_w}\right)^{\alpha_w}} \tag{6.4}$$

For each Weibull distribution the parameters α_w, β_w and γ_w in equation (6.4) were modified in Matlab until the right distributions matched the experimental data. In all the prediction cases the Mean Field predictions to represent the PANACEA data which was used for the model callibration and main creep predictions are compared against the experimental derived distributions in figures 6.4 to 6.11. In all cases it can be seen for the case of the tertiary distributions each distribution is broader than the PANACEA calibration distribution. For figures 6.7, 6.9 and 6.11 the distributions are also shifted to cover larger precipitates and have a larger average tertiary size.

Comparing the secondary γ' distributions the calibration distribution is more narrow compared to the experimentally obtained distributions in figures 6.4, 6.6, 6.8 and 6.10. In the case of figures 6.4, 6.8 and 6.10 the distribution is shifted to the left to encompass a much greater amount of smaller particles. Due to restrictions in how the model differentiates between secondary and tertiary γ' when creating distributions which is purely by size, the best match for the experimental data causes the tertiary distribution to end abruptly figure 6.9. This is not considered

a problem as this cut-off does not actually exist when the mean field runs it tracks the evolution of each distribution by following the inflection points combining together both figures 6.8 and 6.9 creates the same inflection points as in all the other cases.

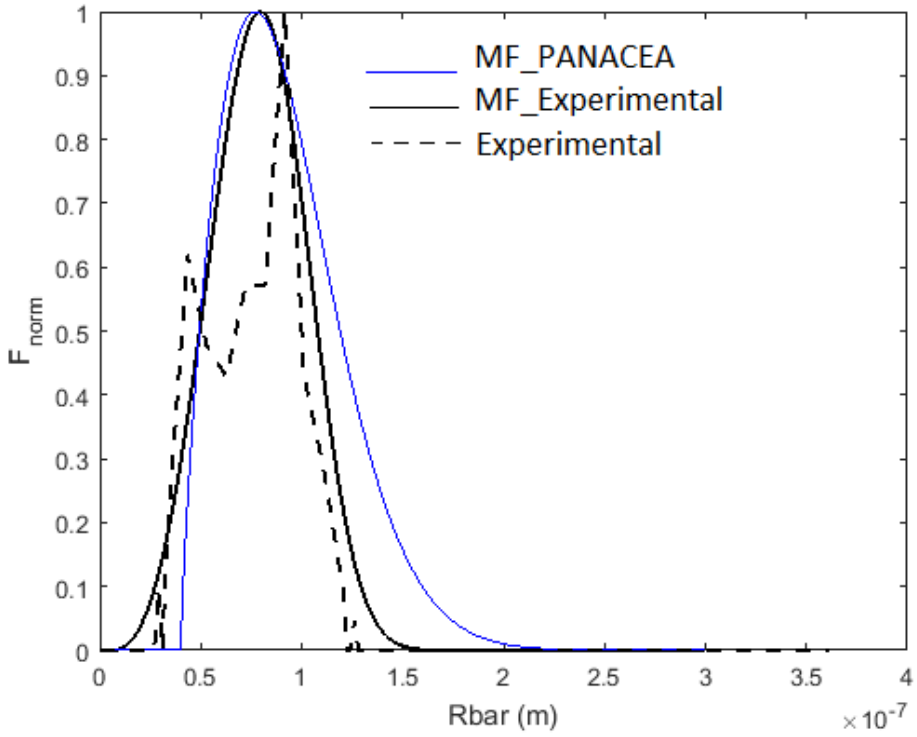


Figure 6.4: Distribution for secondary γ' measurements from sample 1 figure 5.45

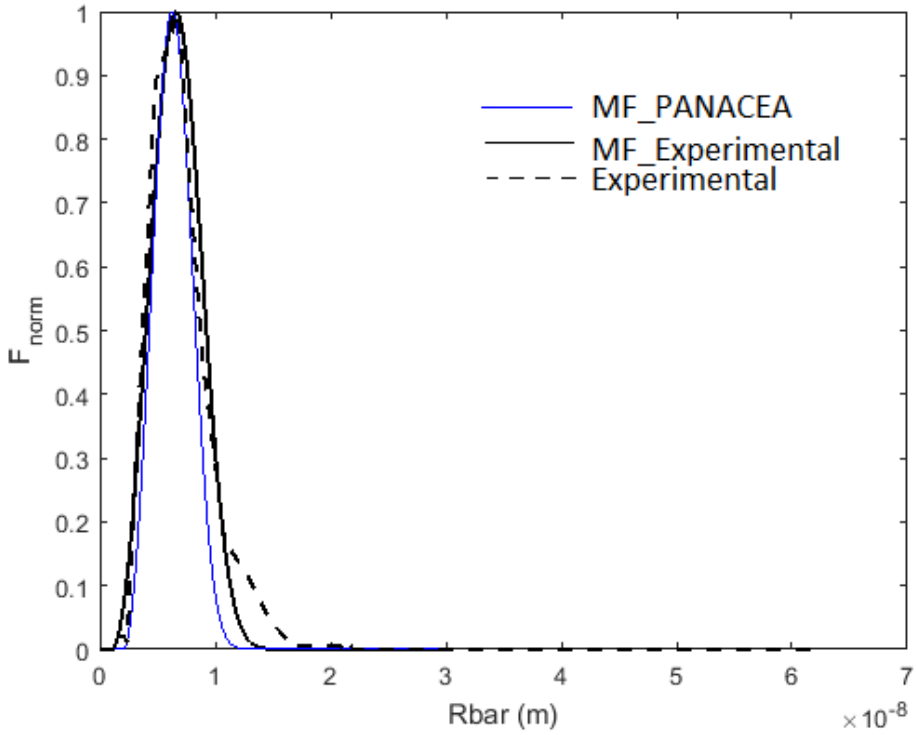


Figure 6.5: Distribution for tertiary γ' measurements from sample 1 figure 5.46

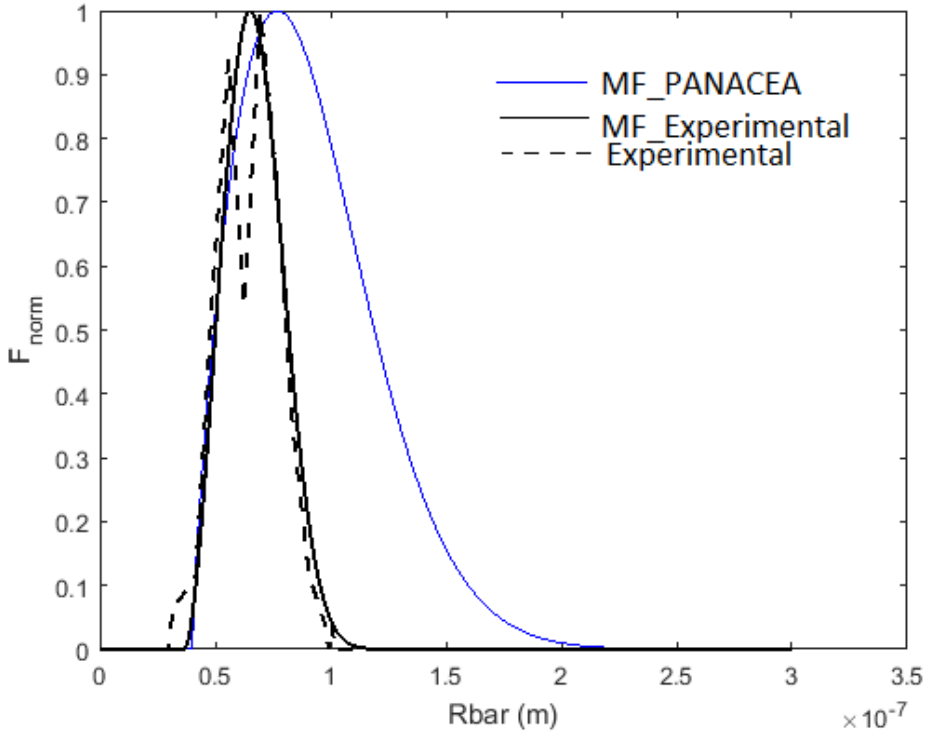


Figure 6.6: Distribution for secondary γ' measurements from sample 2 figure 5.45.

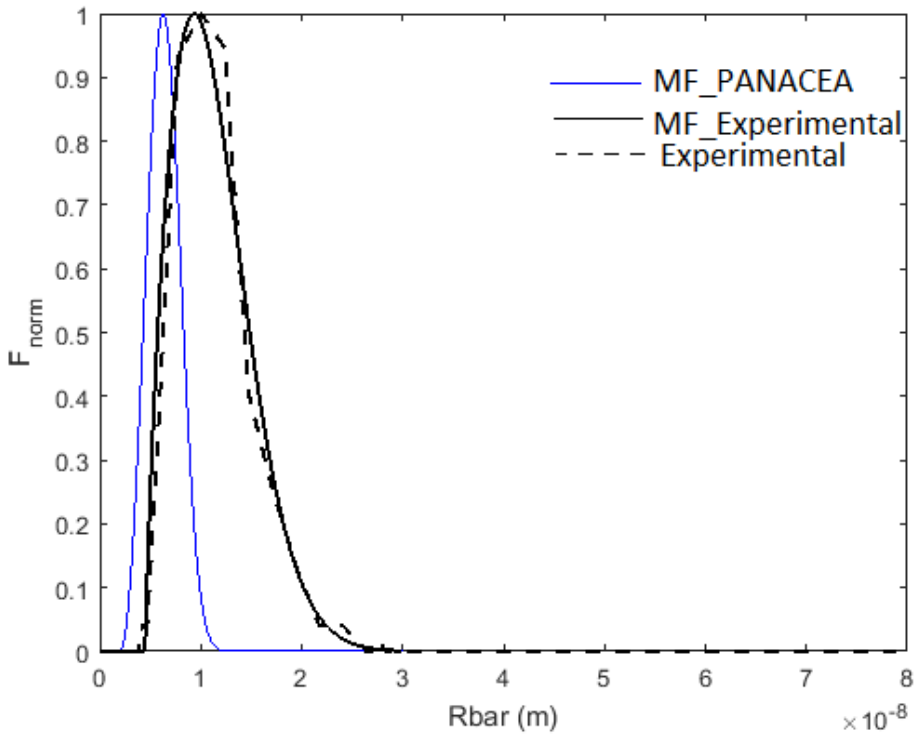


Figure 6.7: Distribution for tertiary γ' measurements from sample 2 figure 5.46

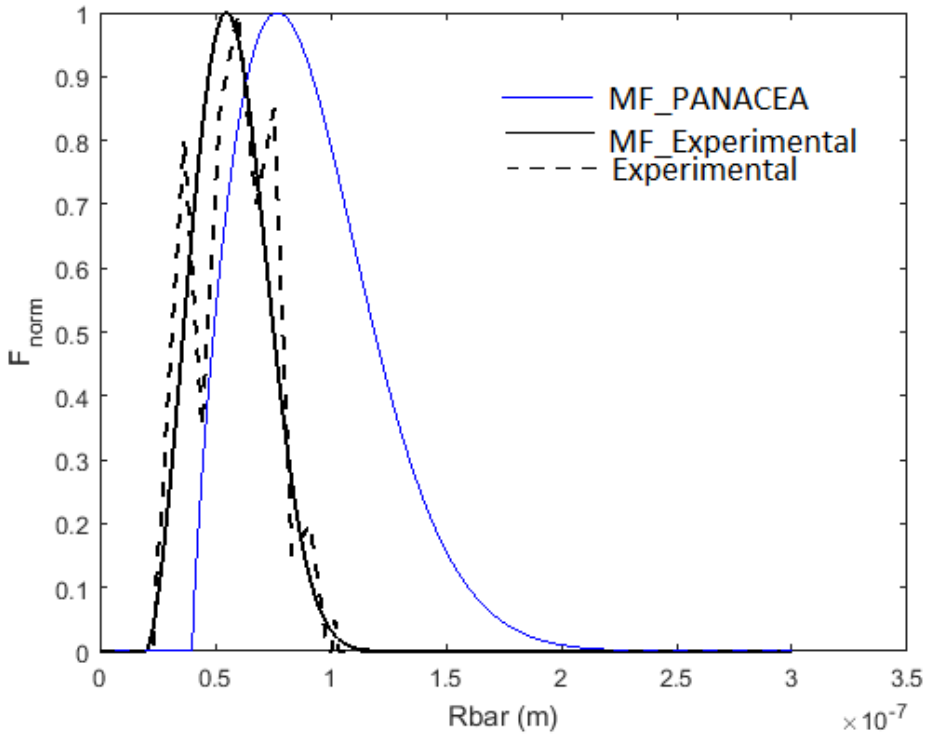


Figure 6.8: Distribution for secondary γ' measurements from sample 3 figure 5.47

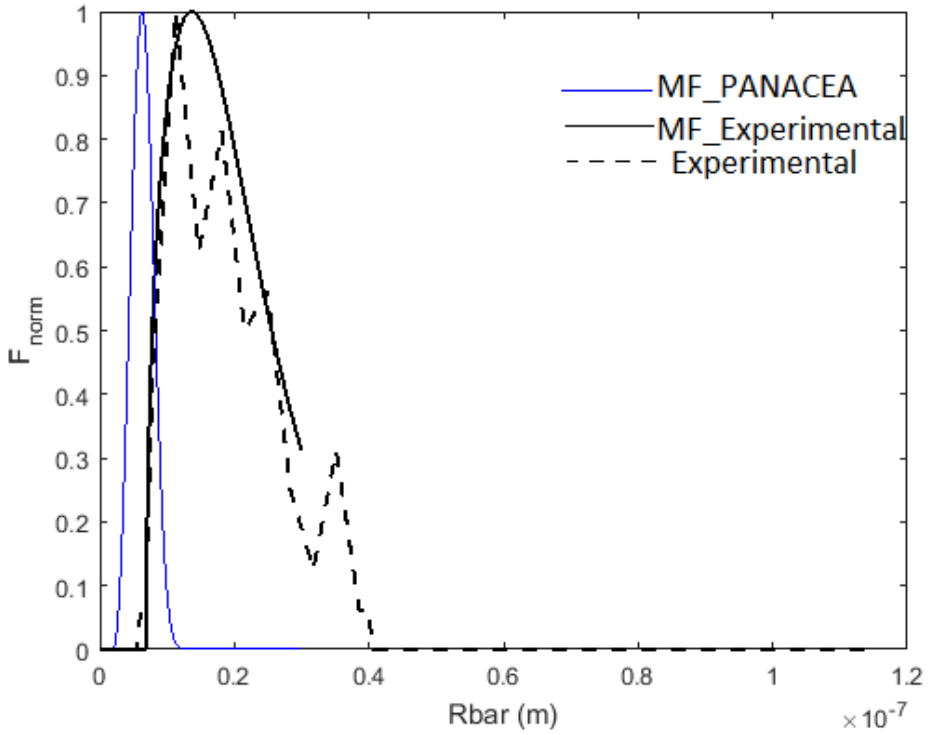


Figure 6.9: Distribution for tertiary γ' measurements from sample 3 figure 5.48

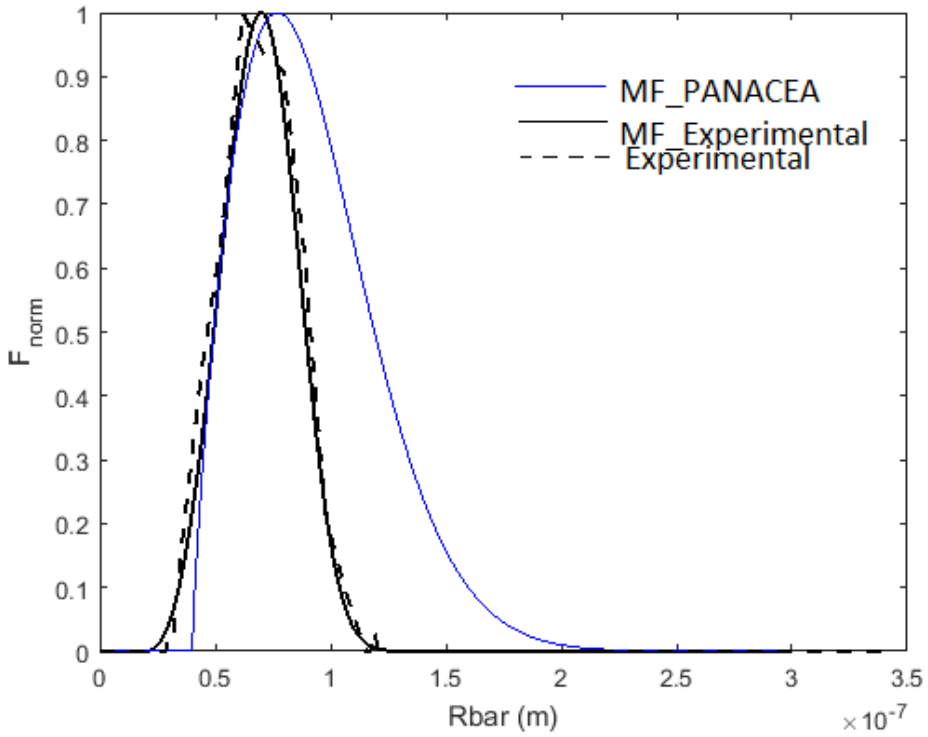


Figure 6.10: Distribution for secondary γ' measurements from sample 4 figure 5.47

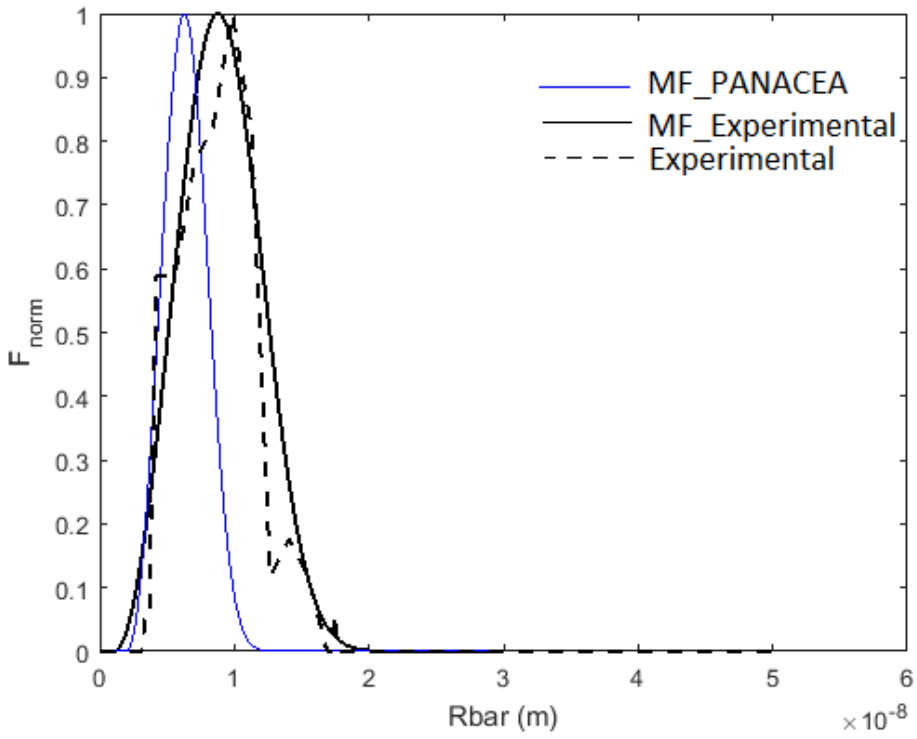


Figure 6.11: Distribution for tertiary γ' measurements from sample 4 figure 5.48

For each case these distributions were used as the starting points for the Mean Field model to predict how they will evolve over the experimental data range. This could then be used in the creep model to see how each size distribution effects the model predictions. Below is a table showing the mean values for each distribution case. There is a discrepancy with the measured values of the secondary γ' area fraction in figures 5.45 and 5.47 and the volume fraction used in the mean field model is due to two reasons. First is that what was measured was the area fraction which is normally larger than the volume fraction, second to successfully create a model for RR1000 the material must have a specific chemistry range, the maximum volume fraction was used which would successfully recreate RR1000.

Table 6.3: Mean values from each microstructure distribution

Distribution	$\phi_{p,2}$	$r_{p,2}$ (nm)	$\phi_{p,3}$	$r_p p, 3$ (nm)
MF PANACEA	0.29	91.8	0.053	6.38
MF1	0.32	79.7	0.023	6.72
MF2	0.3	67.2	0.043	11.3
MF3	0.28	58.1	0.073	17.3
MF4	0.34	69.5	0.006	9.1

6.4 Lifetime and MCR

Model predictions of the creep lifetimes are shown in figure 6.12 together with experimental data for fine grain RR1000. These were determined as the time taken to reach 10% creep strain. The first thing to notice is the wide scatter in measured lifetimes which can be as large as an order of magnitude ($750°C$ 600 MPa). Model predictions are in good agreement with the available experimental data for temperatures $\geq 650°C$. For this temperature range the predicted lifetime plots show a sigmoidal dependence with stress. This is attributed to the influence of the γ' distribution on the simulated creep response. The evolution of the particle dispersion, initially characterised as a bimodal size distribution evolves towards a unimodal size dispersion for long thermal exposures i.e., low stress, high temperature conditions. In the current framework the creep strength scales with the particle spacing for a given volume fraction. Consequently, a coarser particle microstructure is predicted to have larger creep rates than a finer particle dispersion and hence a shorter life than it would otherwise have if the particles did not coarsen. At 600°C the model under-predicts substantially the lifetimes compared to the measured values. However, the experimental stress range at 600°C is in excess of 1000 MPa, which corresponds to conditions at and above the mechanical threshold (creep considered operating at stresses 0.8 of yield) for RR1000. Hence these conditions are not under a creep dominated domain and athermal plasticity effects cannot be ignored. Such effects will include the formation of dislocation

substructures [56] [79] and extensive interaction between dislocation and stacking faults generated by shearing of the γ' particles [80]. These mechanisms have not been taken into account in the current creep formulation.

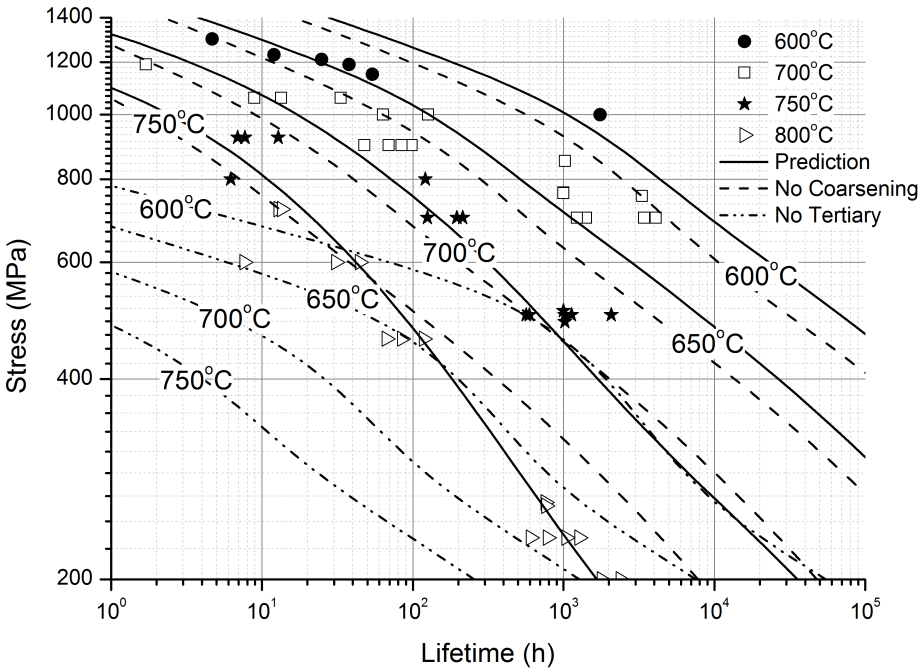


Figure 6.12: Lifetime model predictions against experimental data, also showing the effect of no tertiary γ' and no coarsening on lifetime predictions

With the global parameters shown to represent the lifetime database, it is possible to simulate the influence of the various γ' particle populations on predicted lifetimes. Predictions of the rupture lifetimes for a static particle dispersion (dashed lines) and one for which the tertiary γ' are removed (broken lines) are also shown in figure 6.12. The removal of tertiary γ' will result in an increase in the mean free path for the gliding dislocation segments. Consequently, the creep rate will increase and lead to a reduction in the predicted time to failure. If the particle dispersion is treated as static, the predicted lifetimes are increased.

Simulated minimum creep rates (MCRs) and the corresponding measured values are presented in figure 6.13 while no experimental data is provided the examination of the MCR is a good indicator if the model is showing the right trends.

In terms of a power law creep model, the simulated MCRs show a variable n dependence with stress. This is interesting since creep models based on a power law formulation require a variable n to describe the MCRs over some stress range, which is linked to changes in micromechanisms driving creep. These variations arise naturally in the current formulations and are associated with varying contributions of the dislocation density, particle dispersion and stress transfer from the matrix to the particles on the creep rates. At low temperatures coarsening of the γ' particles is expected to be minimal and the creep response will be dominated by dislocation activity and stress partitioning between the austenitic γ matrix and γ' particles. This is the case at 600°C. However, as the temperature increases the sigmoidal MCRs variations with stress must be linked to changes in the simulated γ' dispersion.

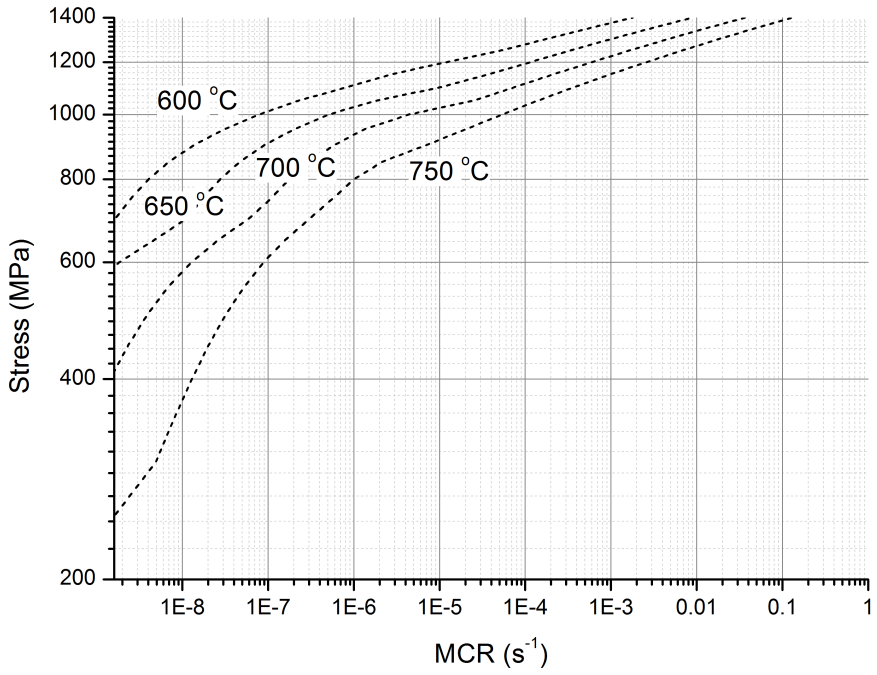


Figure 6.13: Minimum creep rate predictions from the constitutive equation description

6.5 Prediction of strain-time trajectories

Under creep conditions, defined here by stresses below the mechanical threshold, the model is able to reasonably predict the strain-time trajectories over the temperature regime of 650-800°C investigated in this study. Figures 6.14 to 6.24 show a number of model predictions and available from the PANACEA experimental data. Overall predicted trends are: (i) the extent of primary creep increases with increasing stress level; (ii) the simulated creep curves are mainly dominated by a tertiary regime becoming more pronounced as the temperature is increased. Where possible, experimental data of repeated creep tests has been included in order to gauge the variability of measured strain-time trajectories.

For all conditions, although the model captures the tertiary response it over-predicts the extent of the primary transient. There may be two possible contributions to this difference. The first is at low temperatures, where the shearing of the γ' particles may be more pronounced than expected. Within the current constitutive description, cutting of the the γ' particles will limit the extent of stress partitioning form the austenitic γ matrix to the γ' particles. Limiting stress partitioning will result in a large effective stress driving dislocation motion in the γ phase and therefore reduce the extent of primary creep strain. The second potential contribution is the creeping of the material while loading to the creep stress conditions in the experiments. Whilst the model is within a reasonable margin of error for most of the data there is common trend for lower temperatures to slightly under-predict and for higher stresses to over-predict. The latter effect is linked to the over-predicted primary region in the curves and would be reduced with the inclusion of γ' shearing. The low temperature behaviour can be linked to the fact that there was no tertiary experirmental data for the mean field and could therfore be describing the microstructure evolution incorrectly.

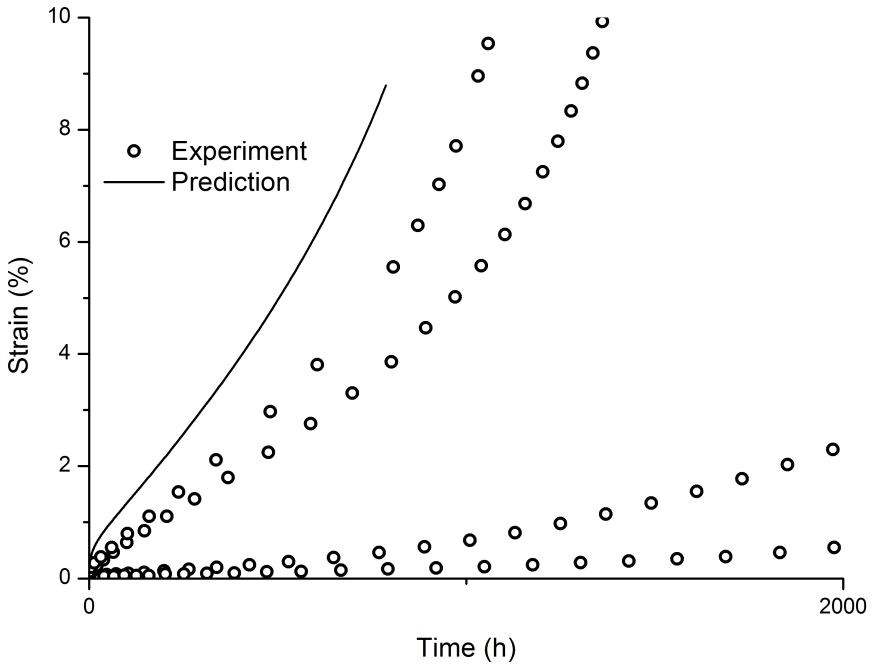


Figure 6.14: Creep prediction at 650°C 700 MPa

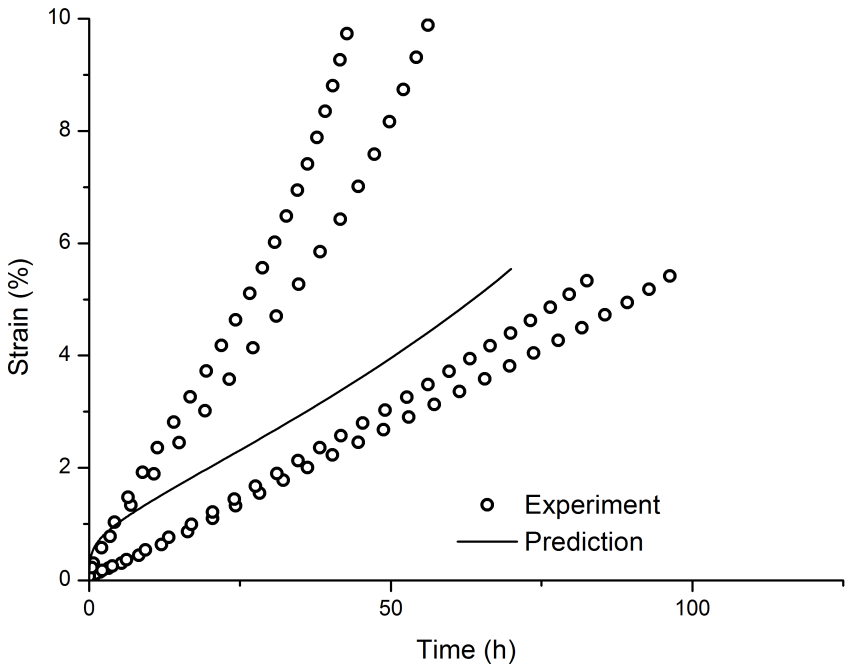


Figure 6.15: Creep prediction at 650°C 900 MPa

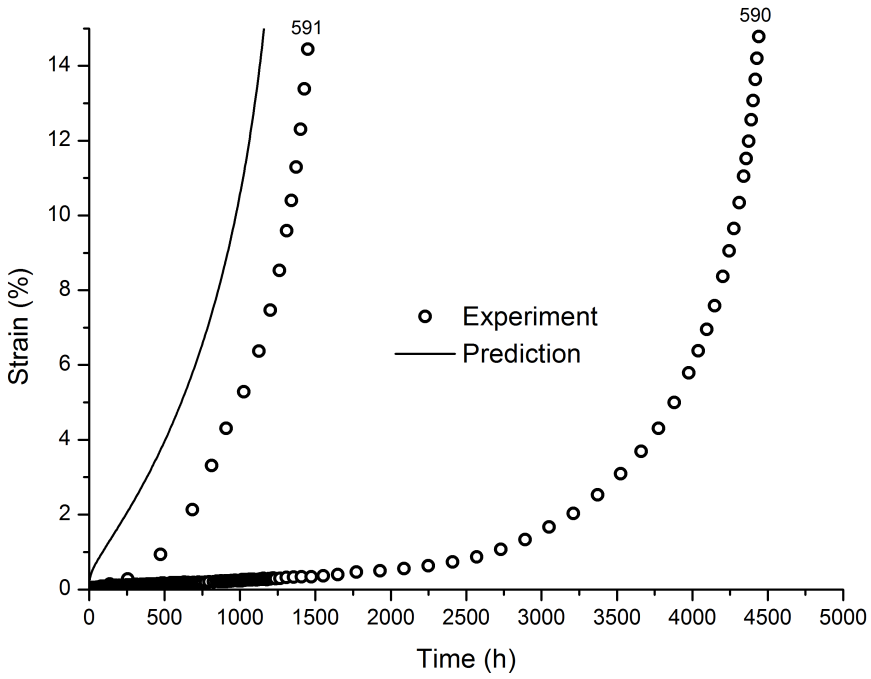


Figure 6.16: Creep prediction at 675°C 590 MPa

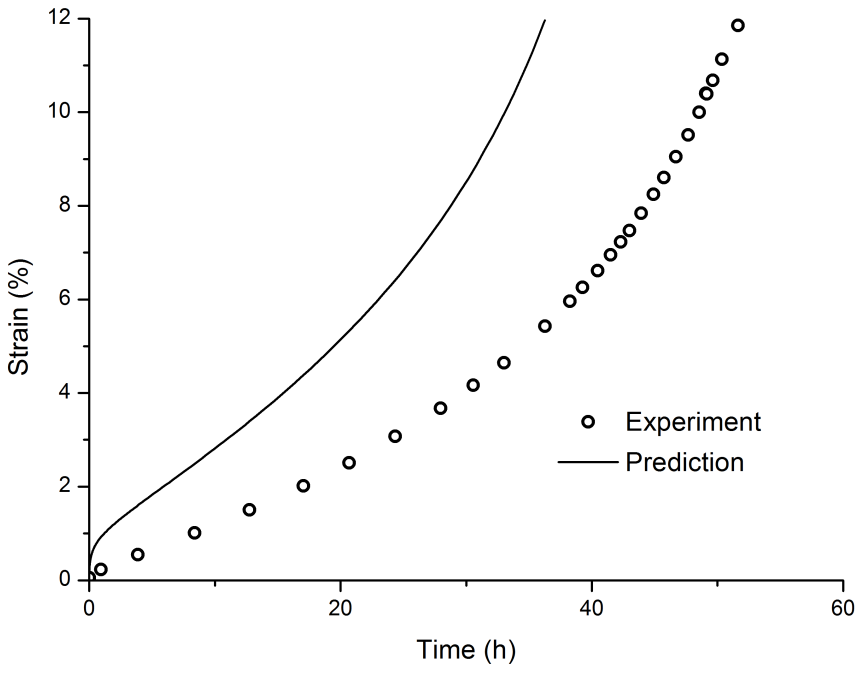


Figure 6.17: Creep prediction at 675°C 930 MPa

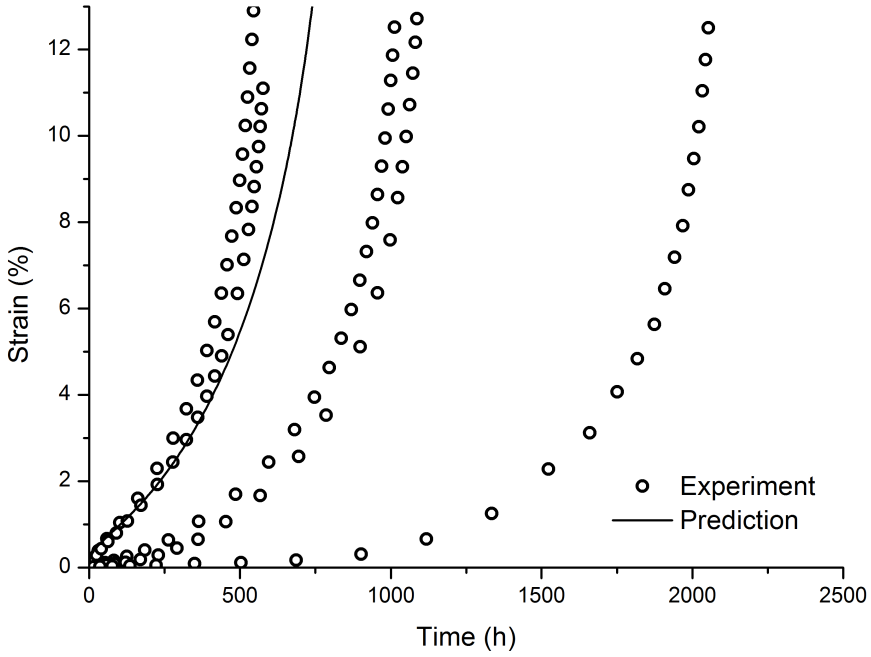


Figure 6.18: Creep prediction at 700°C 500 MPa

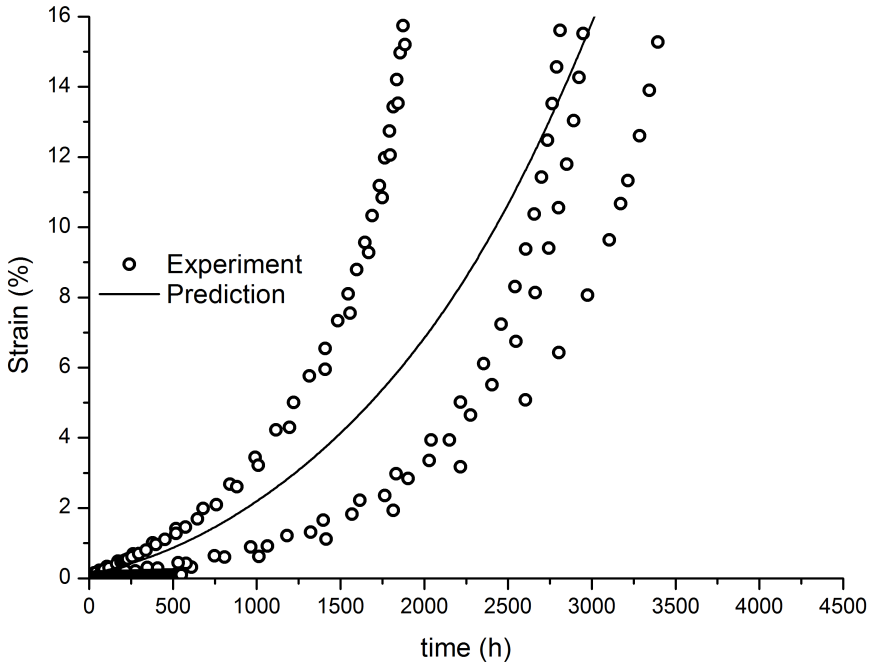


Figure 6.19: Creep prediction at 725°C 263 MPa

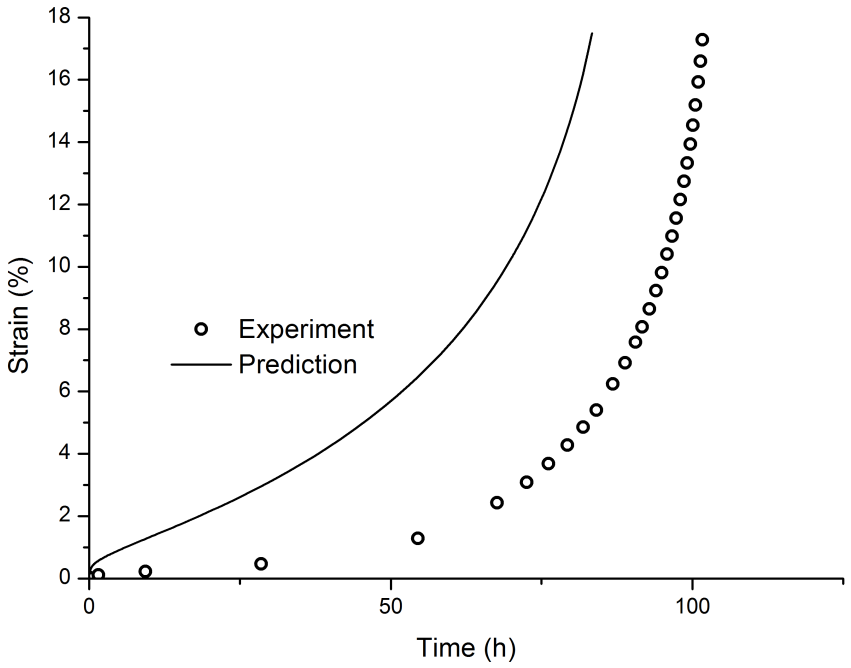


Figure 6.20: Creep prediction at 725°C 655 MPa

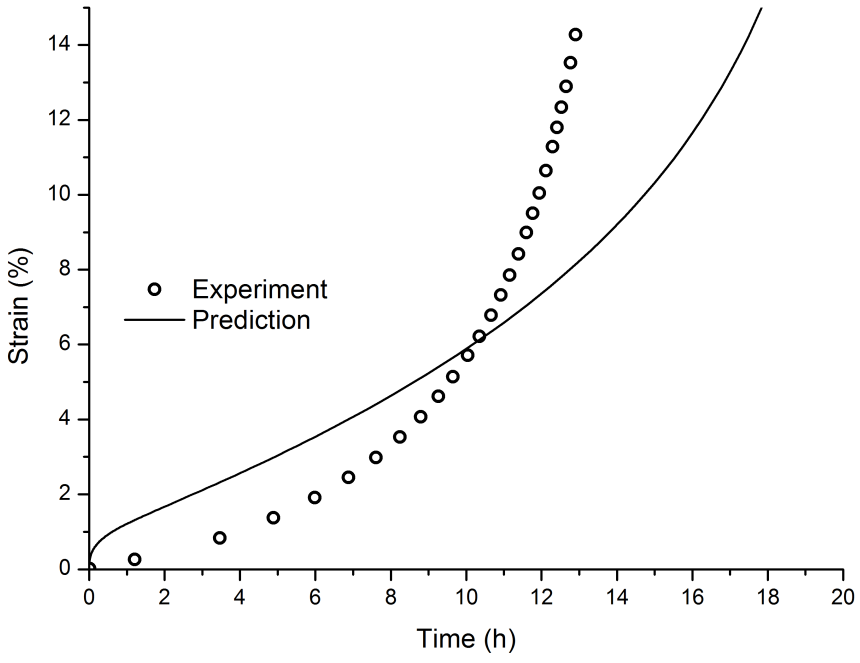


Figure 6.21: Creep prediction at 725°C 831 MPa

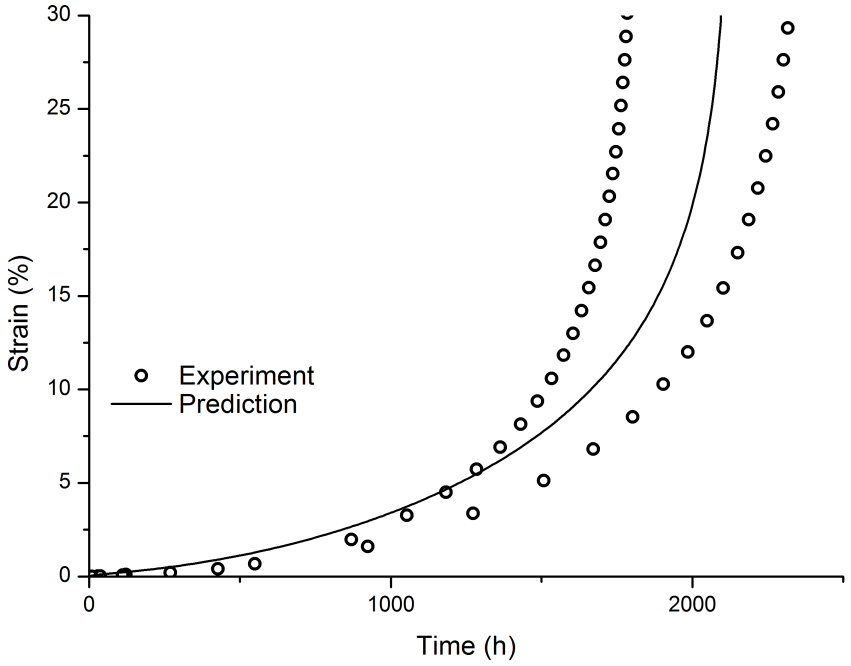


Figure 6.22: Creep prediction at 750°C 200 MPa

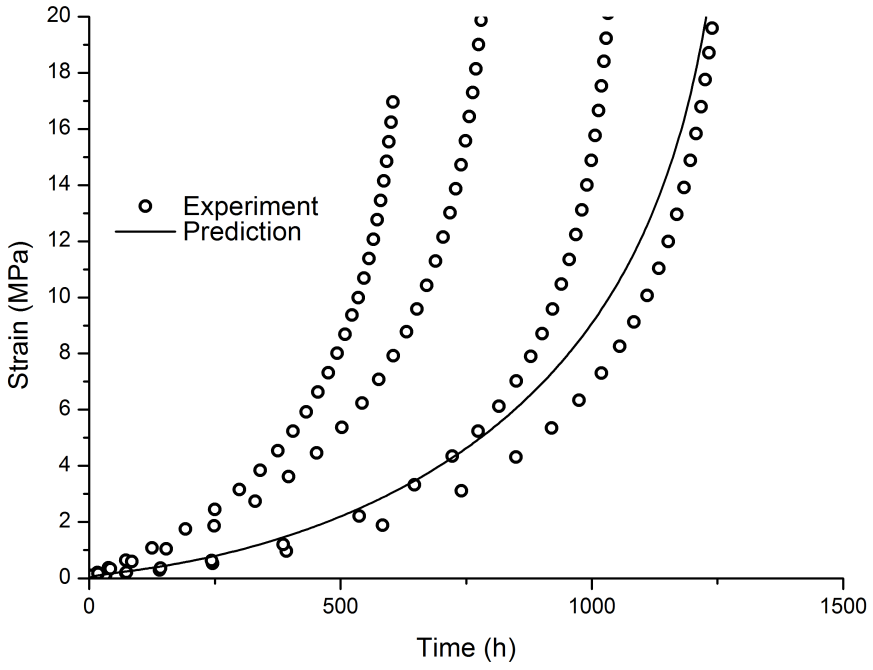


Figure 6.23: Creep prediction at 750°C 231 MPa

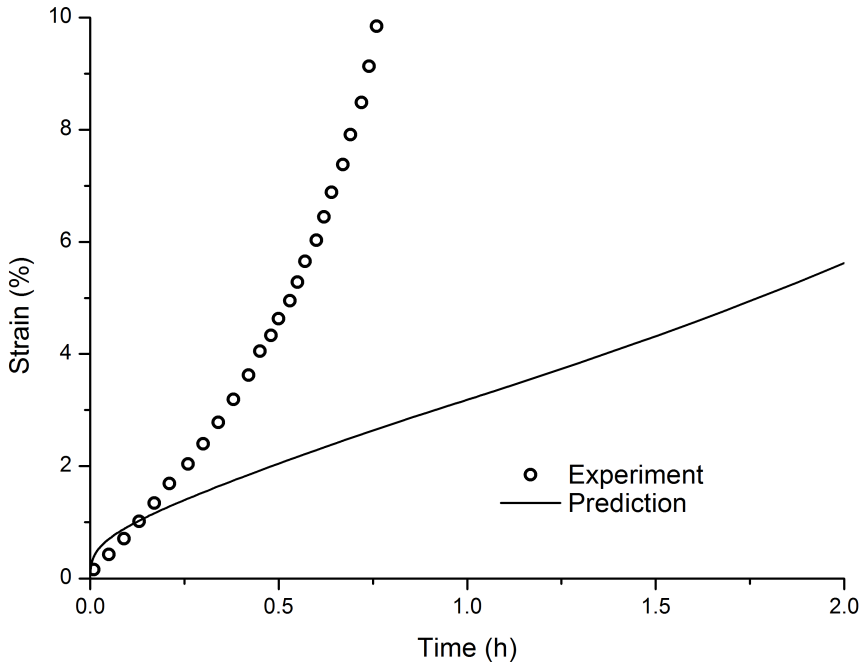


Figure 6.24: Creep prediction at 750°C 900 MPa

The microstructure variations in a nickel-based superalloy disc can be significant as outlined in the introduction. To assess the influence of the γ' variation on the creep response, a number of γ' particle size distributions from different locations on a disc have been provided by Rolls-Royce plc. The measured distributions will be used as input into the precipitate mean field model, which will predict their temporal evolution at temperature. The measured initial secondary and tertiary γ' distributions are shown in figures 6.25 and 6.26, respectively. It is important to note that these distributions have similar mean size and volume fractions, however, they differ in the spread of the distribution and number density. These have been labelled base-line (1), narrow (2) and broad (3). Note that the base-line distribution is the one used in the previous simulations of the creep response and the mean field predictions in section 6.2.

The creep prediction corresponding to 700°C at 500 MPa for these three γ' dispersions are shown in figure 6.27. The simulations predict different creep responses

for each particle distribution, differing mainly in the tertiary response. The simulations indicate that dispersions with broad particle size distributions about their mean size will have reduced lifetimes compared to a narrow distribution. Also, it is interesting to note that the predicted creep scatter appears to capture the experimentally measured spread of the strain-time trajectories.

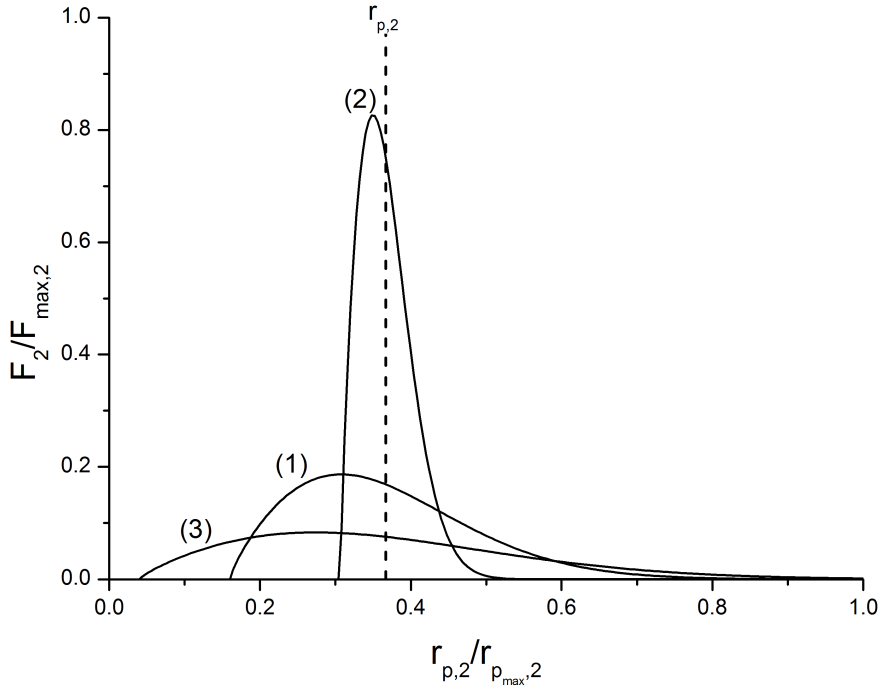


Figure 6.25: Mean Field prediction of secondary γ' at 700°C showing the different distribution shapes: (1) = Base, (2) = Narrow and (3) = Broad, all with the same mean size and volume fraction

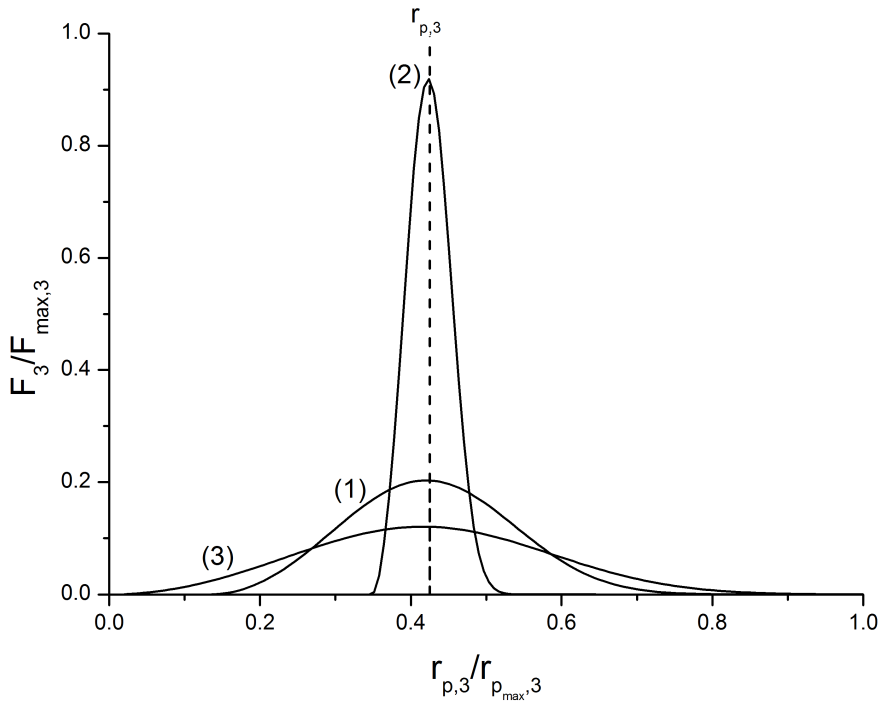


Figure 6.26: Mean Field prediction of tertiary γ' at 700°C showing the different distribution shapes: (1) = Base, (2) = Narrow and (3) = Broad, all with the same mean size and volume fraction

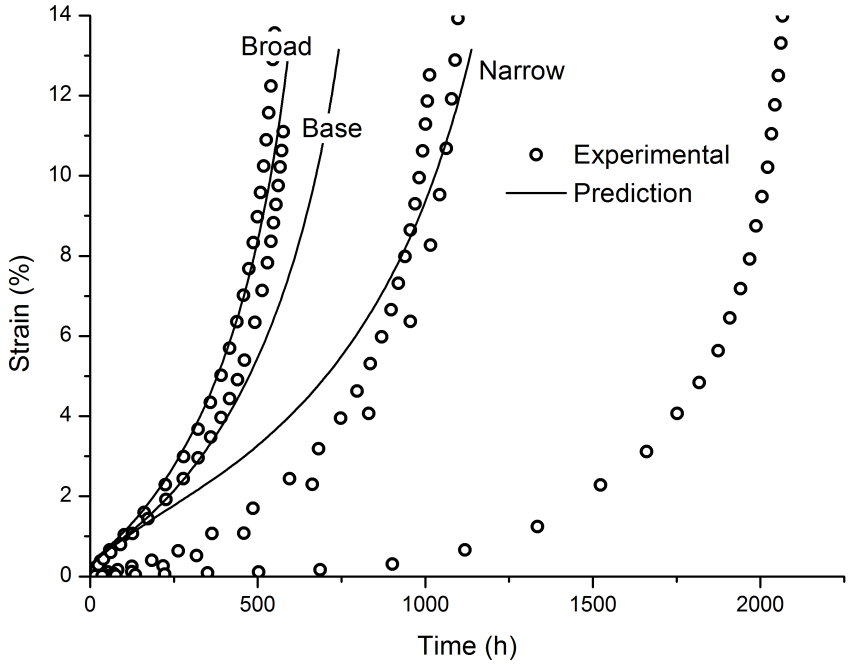


Figure 6.27: Creep prediction at 700°C 500 MPa from different distribution sizes (1) = Base, (2) = Narrow and (3) = Broad, all with the same mean size and volume fraction

The experimental distributions were used as starting distributions for the mean field model. The model then predicted how those distributions would evolve with regards to both size and volume fraction. This information has then been utilise for the creep model to show and compare how the individual distributions effect the model behaviour. Also compared is mean field prediction for the PANACEA data which the model has been calibrated against. Where MF1 is the initial distribution representing SHT in figures 5.45 and 5.46 and MF2 is MHT. MF3 describes SHT in figures 5.47 and 5.48, MF4 represents the MHT and MFP is the distribution used for the PANACEA data.

Figure 6.28 is unique as due to the large discrepancy, between the experimental data and the predictions, the experimental data (seen in figure 5.10) was left off. MFP has the slowest creep strain accumulation, but the 35 hours is a lot further away than the 1000s of hours seen in the experimental data. The 2 conditions

representing the SHT (MF1 and MF3) had the next slowest creep rates though the difference between MF2 and those is very slight, this behaviour is in line with the experimental predictions where the MHT has a faster creep rate than the SHT.

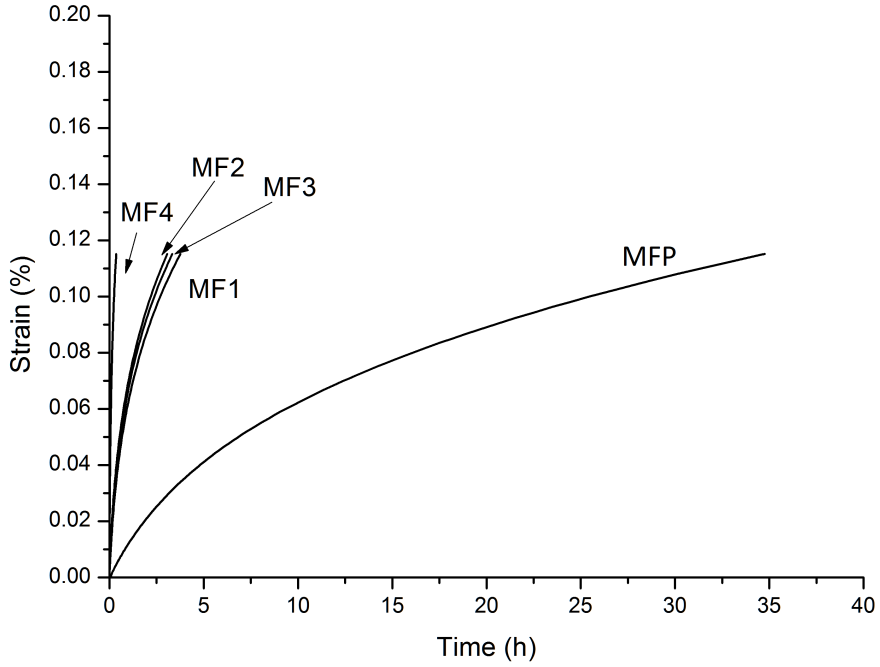


Figure 6.28: Prediction of creep behaviour at $600°C$ 500 MPa with different starting particle size distributions

At 700°C 700 MPa shown in figure 6.29, combines the experimental work done in the PANACEA program [1] with work done in this program. This conditions shows that there is a large scatter with the experimental data, but the test done in this program very closely matches one of the PANACEA test conditions. The predictions all fall short of the experimental data, but MFP does approach the shortest experimental test which ends a lot shorter than the other data points. All the other mean field conditions are a lot shorter than the data and the calibration prediction, with MF4 being the shortest, MF1 being the longest and MF3 being the next longest and also being very close to MF2.

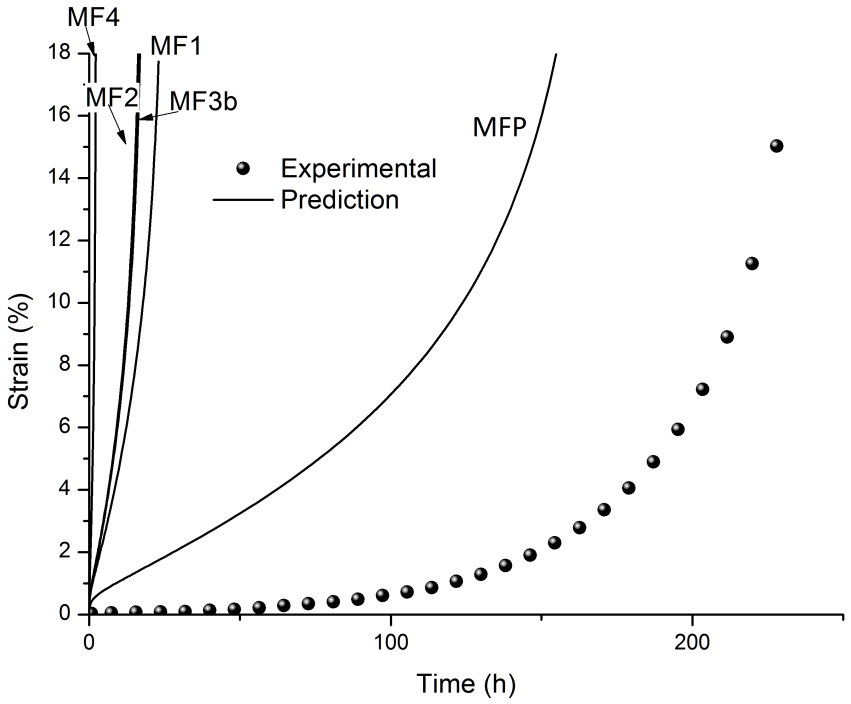


Figure 6.29: Prediction of creep behaviour at $700°C$ 700 MPa with different starting particle size distributions

The description of the model predictions in figure 6.29 is similar to the higher stress condition in figure 6.30 with the only difference being the that MFP is closer to the experimental data and ends up over-predicting slightly. The predictions also show similar behaviour as seen in the experimental data where the higher the stress the more linear the tertiary region in the creep curve.

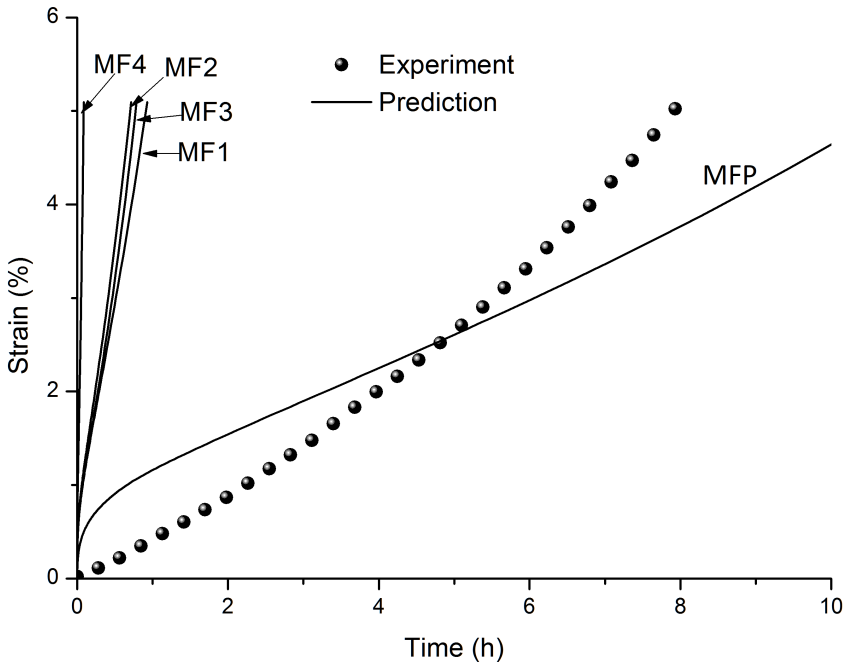


Figure 6.30: Prediction of creep behaviour at 700°C 900 MPa with different starting particle size distributions

Figure 6.31 is the highest stress condition examined and it is different from the other conditions at 700°C, MFP over predicts a lot more (only relatively due to the short time of the test $<$ 1 hour). The other conditions all under predict and MF1 and MF4 have their same respective places in overall lifetime predictions as in figures 6.29 and 6.30 with increasing the stress the difference in predictions between MF2 and MF3.

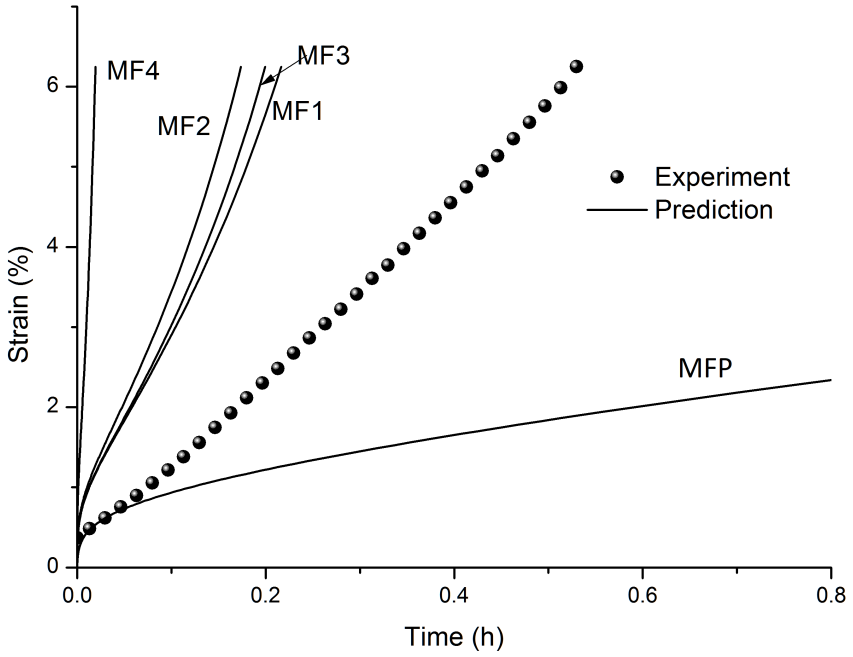


Figure 6.31: Prediction of creep behaviour at 700°C 1050 MPa with different starting particle size distributions

At 750°C 460 MPa the predictions shown in figure 6.32 shows different behaviour than that found at the lower temperature conditions. The experimental data shows a large scatter in the prediction behaviour with both the SHT and MHT experimental data lying with the PANACEA data scatter. The only difference is the the MHT data having a larger primary creep regime which is presented in the predicted results to a greater extent. The overall lifetime conditions MF4 and MF1 fall outside the experimental data range with MF1 having an initial creep rate less than MF2 and MF3 but at around 30 hours increases much faster. MF3 has the best lifetime being within the PANACEA experimental range.

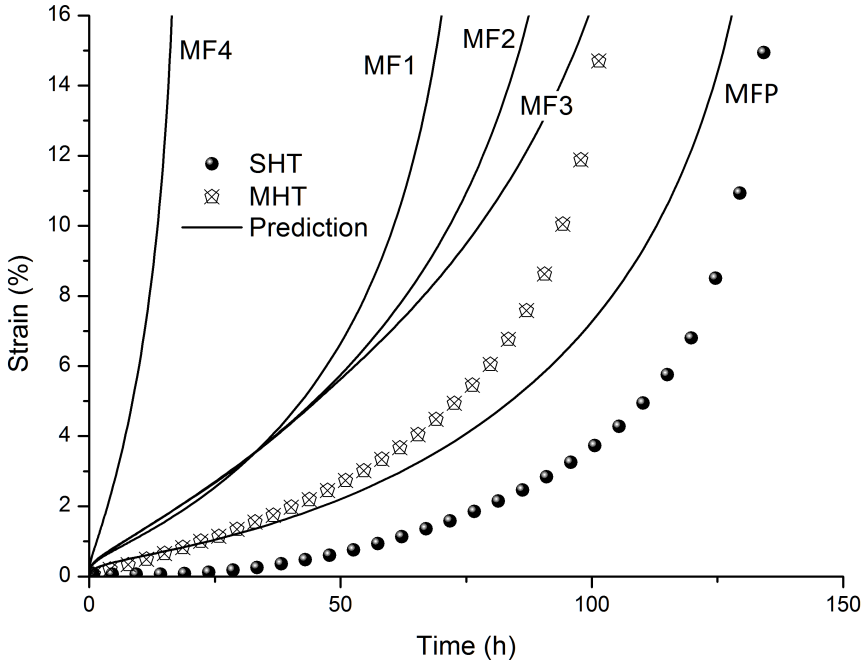


Figure 6.32: Prediction of creep behaviour at 750°C 460 MPa with different starting particle size distributions

The low stress condition at 775°C 200 MPa in figure 6.33 the behaviour is completely different to the other conditions, here MFP follows the experimental data very well but are a lot less than the other predictions. MF1 is next in lifetime and is close to the experimental data next is MF4 which has a lot slower creep rate than the other conditions. MF3 and MF2 are the furthest out from the experimental data MF3 initially has the slowest creep rate, but at around 1500 hours its creep rate speeds up and MF2 then has the slowest creep rate.

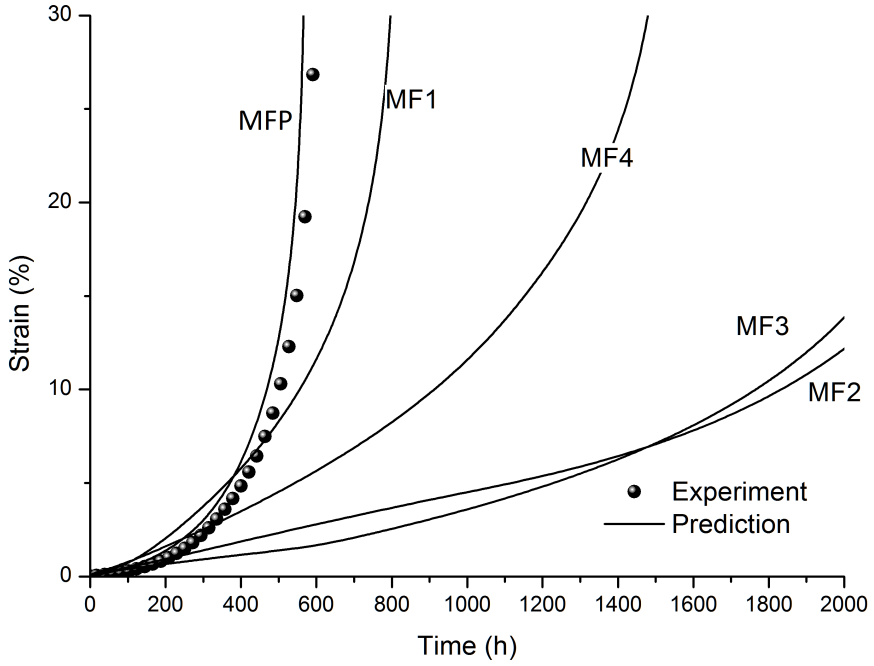


Figure 6.33: Prediction of creep behaviour at 775°C 200 MPa with different starting particle size distributions

The high stress condition 600 MPa at 775°C shown in figure 6.34, MFP slightly over-predicts from the experimental data (it seems larger due to the short lifetime of the test). The other conditions are shorter lifetimes than the experimental data with MF4 having the fastest creep rate and MF1 has the slowest creep rate and is the closest to the experimental data. This prediction result is very similar to figure 6.29 except MF2 is slightly ahead of MF3.

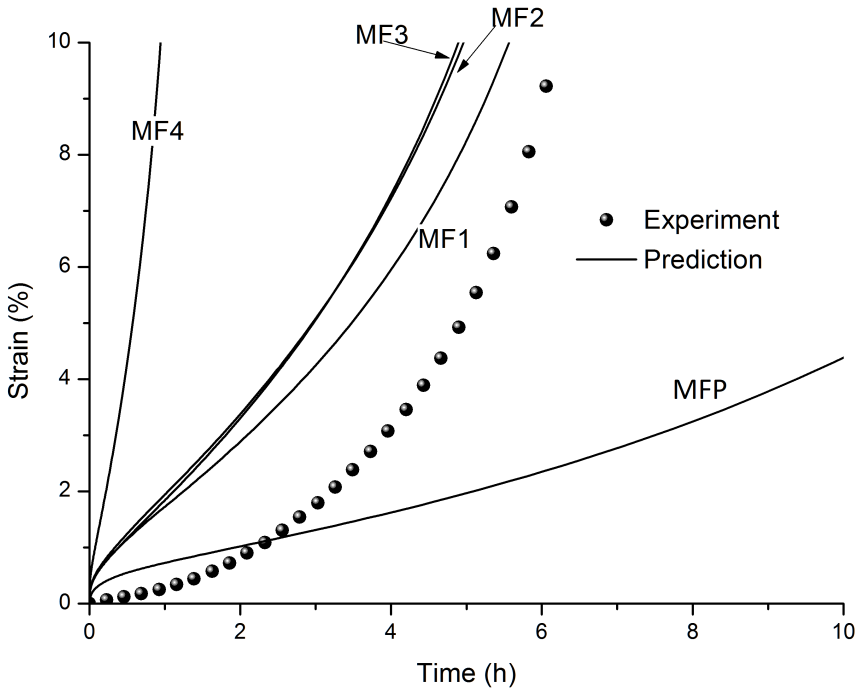


Figure 6.34: Prediction of creep behaviour at 775°C 600 MPa with different starting particle size distributions

Figure 6.35 is the highest temperature prediction at 800°C and is 300 MPa, here MF1, MF4 and MFP are all close to the experimental data. MF2 and MF3 have the slower creep rates and have a lot longer lifetimes than the others with MF3 having over 5 times the lifetime of MF1.

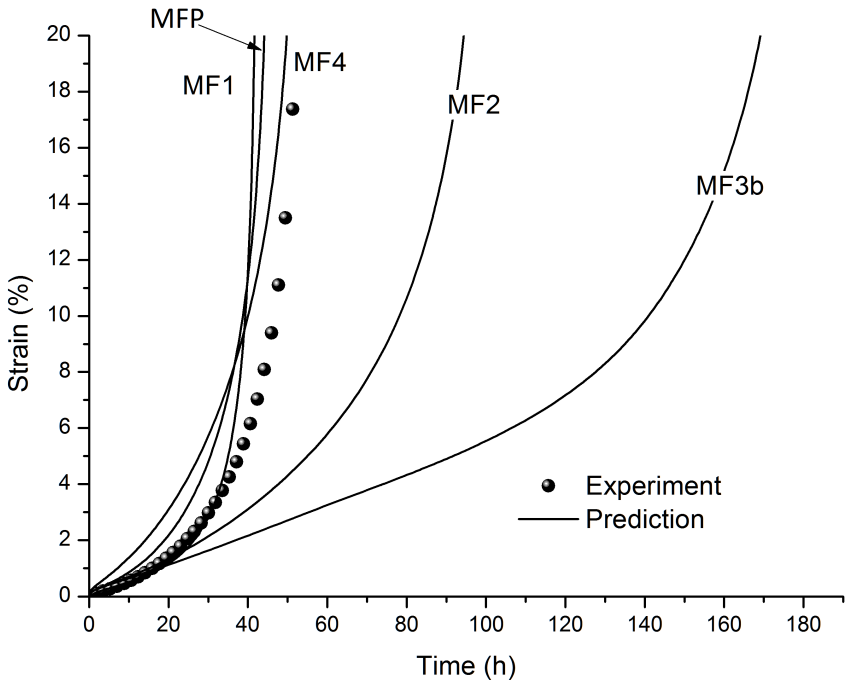


Figure 6.35: Prediction of creep behaviour at $800°C$ 300 MPa with different starting particle size distributions

The high stress condition of 500 MPa and at the highest temperature is shown in figure 6.36 MFP has the longest lifetime and over-predicts the creep behaviour, MF4 has the fastest creep rate resulting in the shortest lifetime, MF1, MF2 and MF3 are close to the experimental data increasing in lifetime in the stated order.

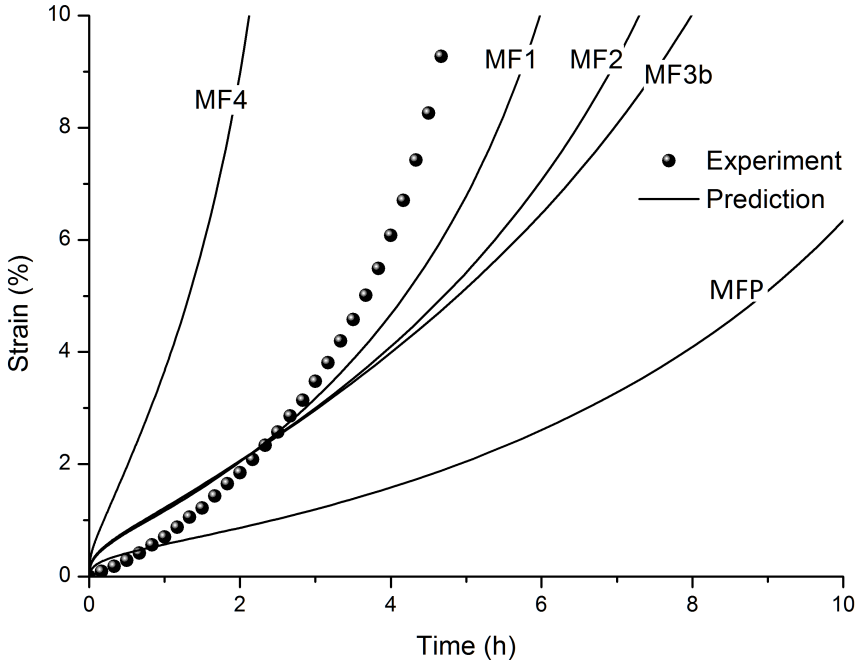


Figure 6.36: Prediction of creep behaviour at 800°C 500 MPa with different starting particle size distributions

From using the experiment based distributions there are a few common trends independent of the loading conditions. MF4 has the highest primary creep regime and MFP has the lowest and is consistently close to the experimental data. At low temperatures 700°C (little microstructural evolution) the experiment based distributions consistently under-predict, but with the introduction of more thermally activated purpose it affect the creep rate greatly with MF1 seeming to be influenced the most by temperature.

6.6 Simulations of the flow stress

Crystal plasticity simulations were run using three different RVEs corresponding to: a single crystal, 100 grains and 1000 grains agglomerate. The partitioning of the RVE into a distribution of subdomains representing grains was accomplished using the open source software Neper. Periodic boundary conditions have been

used in all crystal plasticity simulations and are shown in figure 6.37.

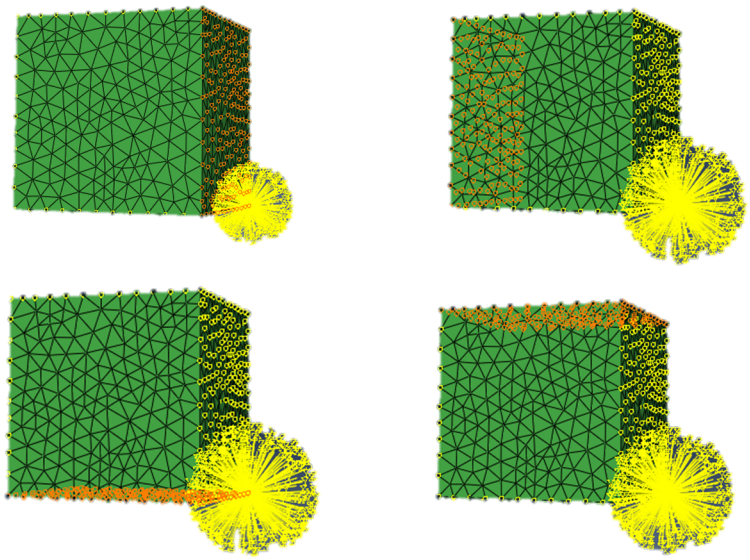


Figure 6.37: Boundary conditions used in crystal plasticity model

Prediction of the flow stress at $700°C/10^{-3}s^{-1}$ for the RVEs are shown in figure 6.38.

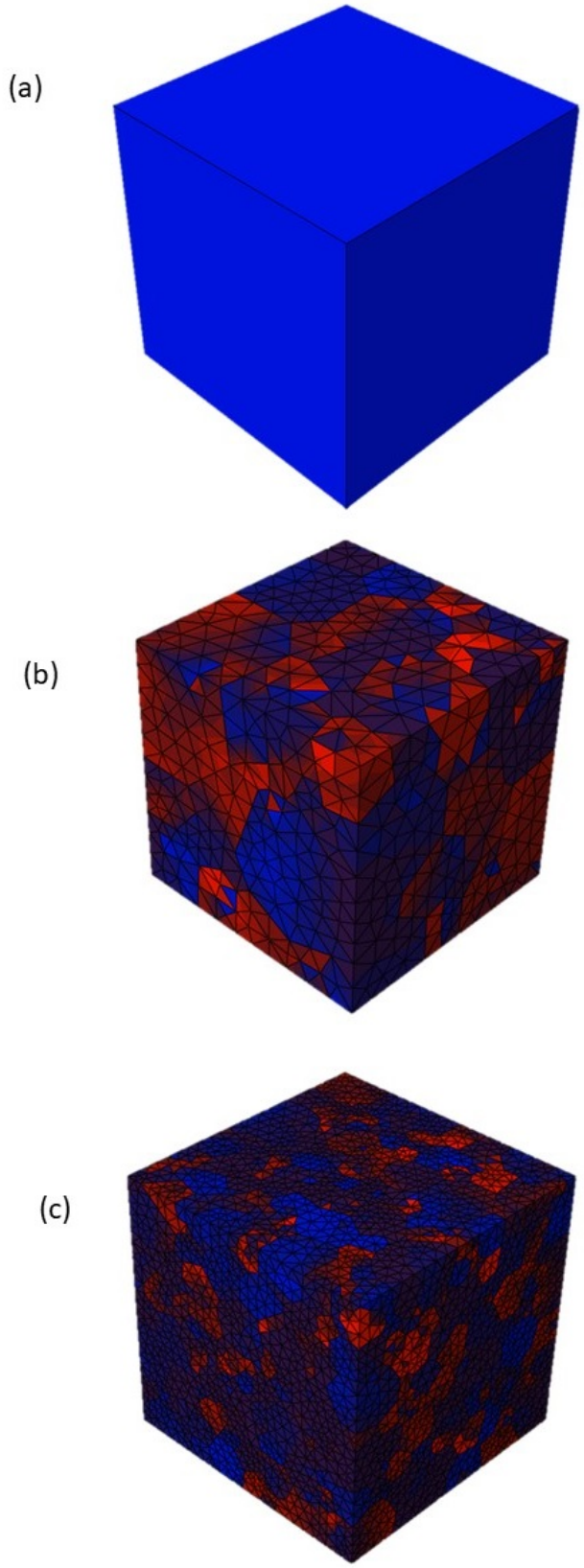


Figure 6.38: Crystal plasticity simulations showing stress using creep constitutive equations: (a) [001] orientated single crystal, (b) 100 grains RVE and (c) 1000 grains RVE. All simulations correspond to an applied strain rate of $10^{-3}s^{-1}$ at 700°C.

A uniform stress state is achieved for the single crystal simulation loaded along an [001] direction. For the 100 and 1000 grain RVE simulations the characteristic non-homogeneous distribution of micro-stress fields associated with variations in crystallographic orientation within the RVE are predicted. The localisation of deformation is associated with plastically soft and hard grains as a result of their orientation relative to the global references frame. Comparing the predicted flow stresses for the [001] single crystal, 100 and 1000 grain RVEs, it can be seen that increasing the number of grains per unit volume reduces the macroscale stress. Also the initial stiffness is reduced within increasing grain density.

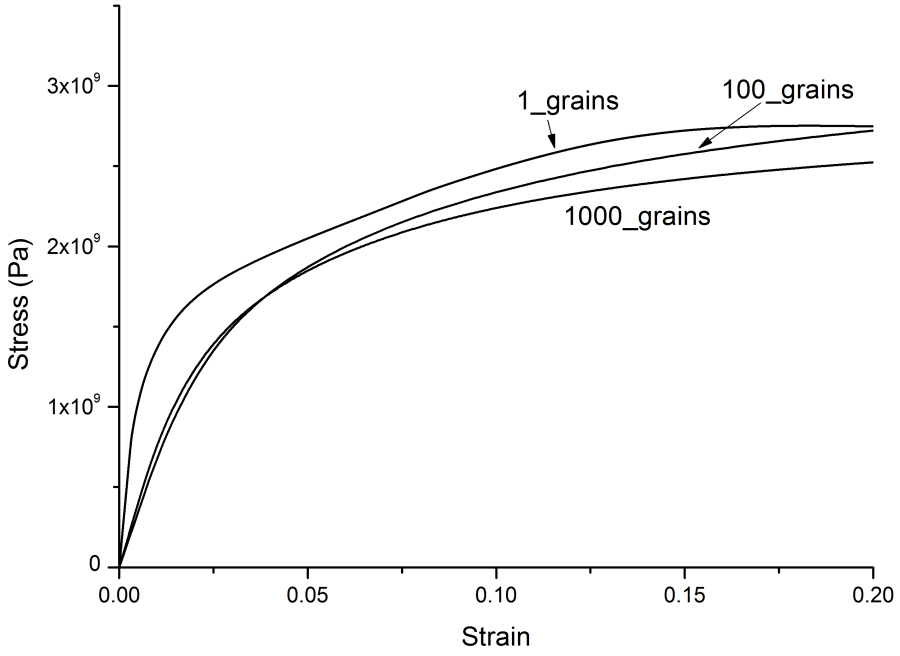


Figure 6.39: Comparing grain size effects to tensile load at $700°C$ and $\dot{\varepsilon} = 10^{-3}$

It is possible to analyse the predicted slip activity within grains making up the RVE, defined in this work as the volume average of the shear strain rate on a given slip system slip system per grain. These are presented in figures 6.40 to 6.44 for five randomly selected grains from the 1000 grain RVE. In these simulations 4 to 7 systems dominate the plastic response per grain.

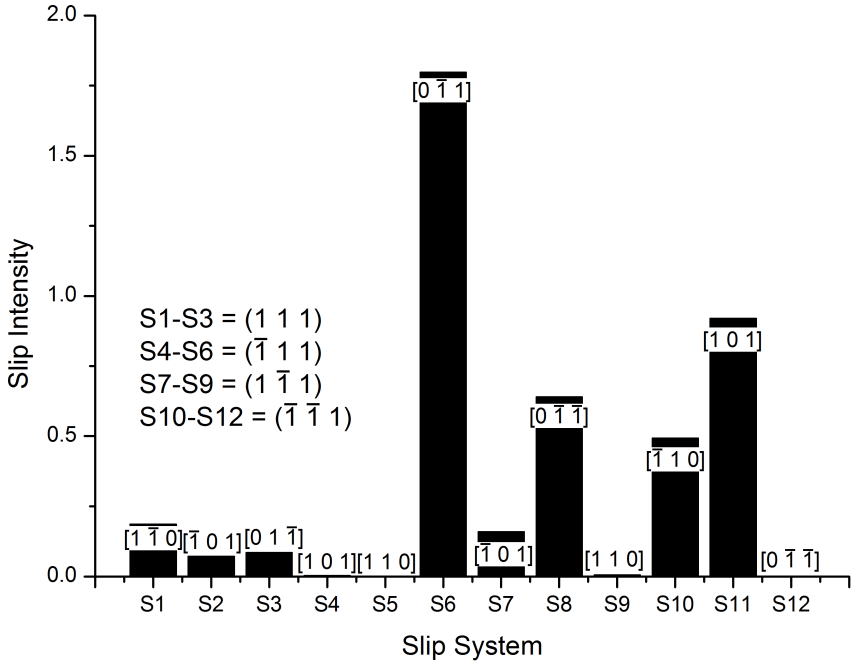


Figure 6.40: Slip activity in a random grain (1)

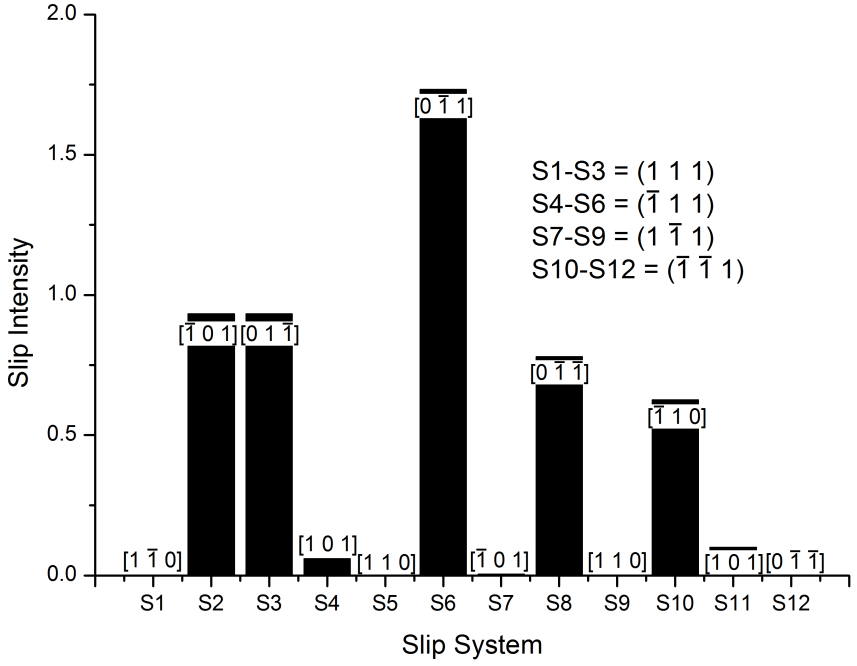


Figure 6.41: Slip activity in a random grain (2)

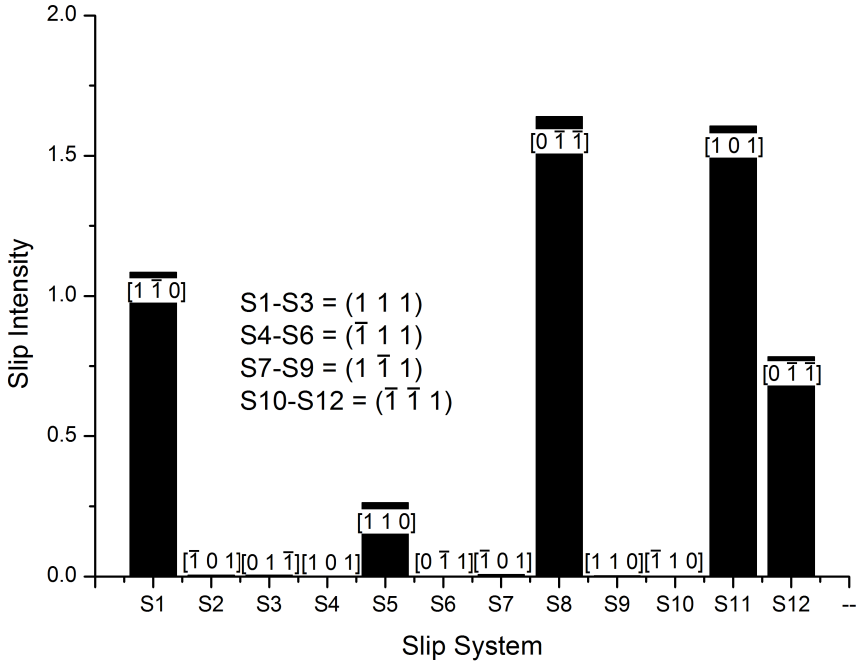


Figure 6.42: Slip activity in a random grain (3)

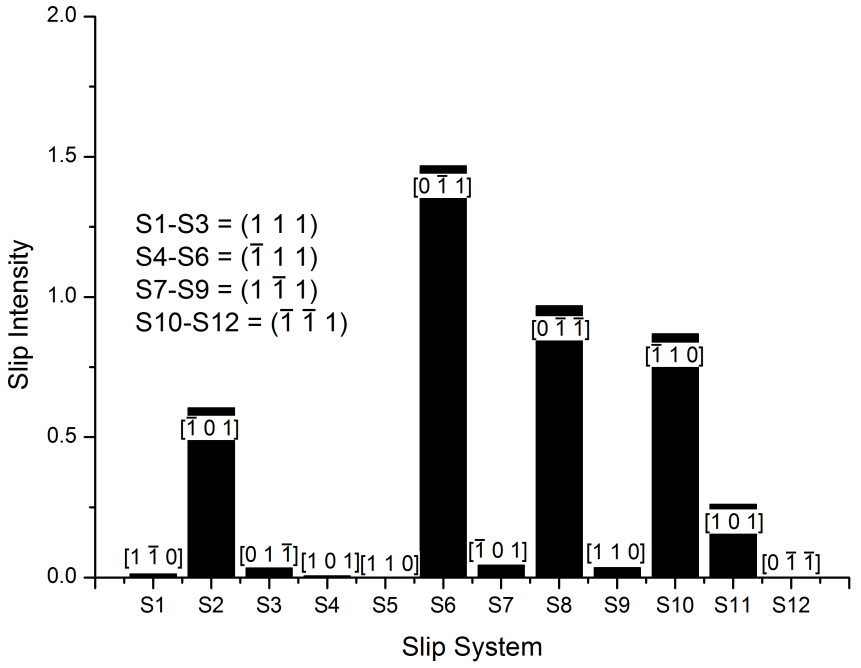


Figure 6.43: Slip activity in a random grain (4)

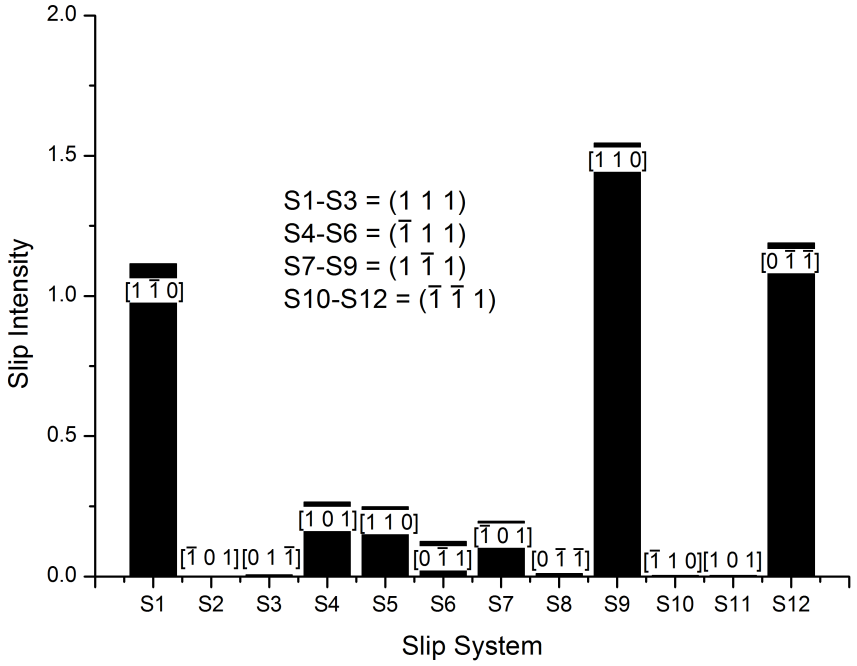


Figure 6.44: Slip activity in a random grain (5)

It is interesting to compare the predicted grain slip activities to that of the entire RVE. This is shown in figure 6.45 and it can be seen that for this case a more uniform distribution of the slip activity per slip system is generated. However, for this particular case we see $[1\bar{1}0]$ and $[0\bar{1}\bar{1}]$ slip systems provide the largest contributions to the total deformation.

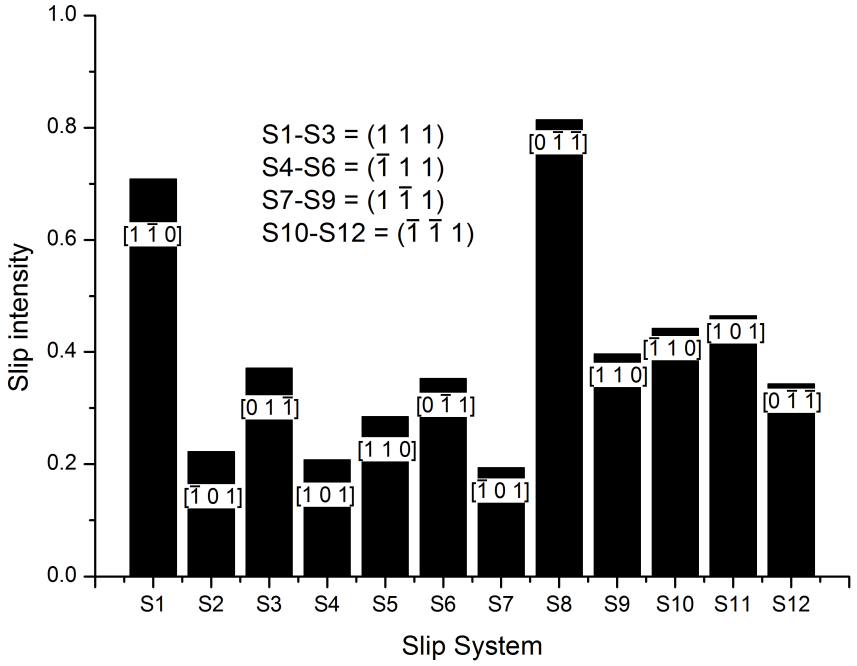


Figure 6.45: Average slip activity in polycrystalline CP simulations

Chapter 7

Discussion on experiments

7.1 Mechanical characterisation

The creep responses of FG-RR1000 for a number of stress and temperature conditions have been presented in Chapter 5. All strain-time trajectories studied so far are characterised by a small primary transient followed by a tertiary creep regime that dominates most of the creep life. For γ' strengthened nickel-based superalloys there are a number of micromechanisms that can result in a tertiary creep response. These are: (i) dislocation activity in the γ matrix; (ii) Ostwald ripening of particles; and (iii) growth and coalescence of grain boundary voids. Of these three mechanisms, grain boundary cavitation is not believed to play a significant role at the temperatures investigated in this study, as the diffusion fluxes of vacancies along grain boundaries at these conditions are relatively slow. Consequently, this micromechanism has been ignored.

Coarsening kinetics of the tertiary particles in FG-RR1000 are fast enough under certain conditions examined in this study that may suggest this mechanism may be important to tertiary creep. From figure 6.2, for temperatures below 740°C the coarsening rates are very slow. At 700°C it takes ∼1000 hours for the fine γ' particles to double in size, which suggests that for the stress conditions examined at this temperature (with lifetimes much shorter than this) it is not coarsening

of particles that gives rise to the tertiary creep transient. As the temperature is increased the coarsening kinetics of the the tertiary γ' particles will become significant. For temperatures between 740°C to 760°C the tertiary particles will have doubled in size after ∼30 to 100 hours respectively. Figure 5.5 shows the 750°C/460 MPa creep data. For the SHT it is observed that there is a region of close to no creep strain accumulation lasting a period of 20-30 hours.

The tertiary γ' particles double in size after ∼3 hours at 810°C (figure 6.2). Thus, at 800°C/300MPa, which has a lifetime of ∼50 hours, changes in the fine particle dispersion are expected to affect the strain-time trajectories. However, at 800°C/500MPa with a lifetime of 5 hours, changes of the tertiary dispersion are not believed to affect the creep response strongly. In this case it is the build up of the dislocation density that will result in an increasing creep rate.

Under creep conditions (stress levels well below yield) the dislocation build-up in the γ matrix has been shown by Dyson and McLean [81] to contribute to tertiary creep in nickel-based superalloys. Mechanistically, because these alloys are dislocation lean, the accumulation of plastic strain will be determined by the mean free path of gliding dislocations, since their interactions will be weak. This is supported in this study through measured differences in creep behaviour of the SHT and MHT samples, where the coarser microstructure is demonstrated to produce faster creep rates (figure 5.5). This implies that the mean free path scales-up with the tertiary γ' particle spacing. However, as the applied stress approaches yield the creep response of the material was found to produce a less pronounced tertiary transient as shown in figure 5.3. This behaviour indicates that dislocation interactions can no longer be ignored. Such interactions are known to influence the rate of accumulation of creep strain through the development of kinematic and isotropic stresses. The kinematic contribution is associated with stress field interactions between dislocations, while the second corresponds to a forest hardening mechanism. Thus, in moving away from creep conditions the mean free path can not be described by the smallest inter-particle spacing.

The flow stress response between 650°C to 800°C was presented in Section 5.2 for strain rates between 10^{-4} s^{-1} to 1 s^{-1}. The γ' dispersion was found to affect the stress-strain curve, with all the aged samples (MHT) showing higher flow stresses than the samples with the standard heat treatment (SHT). Thus, under high strain rates (compared to creep) the effect of a coarser particle dispersion is to make the alloy stronger in terms of yield behaviour. This is opposite to the effect on creep, where a coarser particle microstructure results in a loss of creep strength. The micromechanism consistent with the flow stress data is cutting of the γ' particles by mobile dislocation segments, since at high strain rates most of the mobile dislocation network will be piled up against the γ' particles. At high enough stresses the mechanical work done by the applied stress on the dislocation will be enough to off set the energy barrier to shear the γ particles. The stress required to shear particles scales as $\sigma_c \sim R^{1/2}$, where σ is the stress required for cutting and R the particle size.

The shape of the stress-strain curves is different at low strain rates to that observed at higher strain rates. The data shows that at strain rates of 10^{-4} s^{-1} and 10^{-3} s^{-1} the stress-strain curve increases to a peak stress at $\sim$1% total strain, followed by strain softening before settling down to a steady state. At higher strain rates the flow stress is described to have increased hardening. The following physics is proposed to rationalise these differences in behaviour. For slow strain rates, although cutting of particles will occur, most of the plastic deformation is confined to the γ matrix. If this holds, then stress redistribution between phases will take place in order to maintain compatibility. This produces a kinematic back stress that reduces the effective stress driving plastic deformation. As dislocations will continue to generate while the dislocation mean free path is the particle spacing, strain softening will occur. However, as deformation proceeds dislocation density ρ will increase dramatically and the the mean free path λ_m will correlate with the mean dislocation spacing in the matrix, i.e., $\lambda_m \approx 1/\sqrt{\rho}$. At this point the theory of generation/trapping dislocation networks suggest that the dislocation density

will reach a steady state condition. At this point the mean free path is constant - it is proposed that this corresponds to the steady state in the flow stress curves.

At high strain rates both the γ' particles and the γ matrix will plastically deform. Stress partitioning between the matrix and particle will be limited and the stress-strain curve must be determined by dislocation interactions and the evolution of shear bands, which are known to lead to increased hardening behaviour. This is supported by the similar flow stress behaviour of the SHT and MHT samples observed at 750°C/1 s^{-1}.

Similar trends of the shape of the flow stress curves on strain rate are observed with temperature. Figure 5.22 show the tensile flow stress response at 10^{-4} s^{-1} at 700°C,750°C and 800°C. At 700°C the stress-strain curve shows hardening over the first ~2% of strain before remaining constant. For the 750°C and 800°C conditions, the curves show a peak in stress followed by strain softening. These results are consistent with the extent of dislocations shearing particles reducing with increased temperature.

7.2 Microstructure characterisation

The TEM images give an initial look at how the material behaves during creep. The results give a clear insight into which mechanisms have the most significance and when they take effect. Figures 5.28 to 5.31 show that during the primary creep regime which the test covers, there is no apparent significant change to the microstructure; which is what would be expected at this temperature. The Mean Field prediction figure 6.3 indicates that nucleation of γ' at elevated temperatures should occur, but quantification of the microstructure is difficult. Whilst there does appear to be an increase in the amount of tertiary γ' present as with examining the thread at 650°C with the thread at 775°C the microstructure can change locally. An early assessment of the microstructure was done using offcuts of the SHT and MHT samples used in the creep tests. The results are only preliminary as not

a large enough sample area was chosen for it to be definitive. Ideally multiple micrographs from multiple grains should be taken > 10 compared to 2 done in figures 5.45 to 5.48. As such it is still unconfirmed if nucleation has occurred or the microstructural change is location variance.

Dislocation content shows from the experimental results that in the primary creep regime there is not a significant change in the dislocation density none seen in figures 5.28 to 5.31. From the other samples which were tested to failure, and it since the secondary creep regime does not exist in complex alloys examined. It can be assumed that the large amount of dislocations seen in other creep samples occur in the tertiary creep regime. Due to the large dislocation density present in figures 5.33 and 5.34, figures 5.36 and 5.38 and figures 5.42 to 5.44 it is difficult to see the microstructure in any detail. Although it is difficult to see it appears that the effect of pre-straining does increase the dislocation density, though this difference could be between the loading conditions of 750°C 460 MPa and 775°C 200 MPa.

Cutting of the γ' can be seen occurring in all the loading conditions where the material failed. Figure 5.34 is of particular importance as it shows γ' has been cut and this process is happening at a much lower stress than expected. The cutting though is not widespread and is probably caused by localised stress concentrations in the material. This shearing though prevalent in all samples that were tested to failure was seen in greatest effect in the 800°C and $\dot{\varepsilon} = 1 \times 10^{-3}$ s^{-1} test. In this condition slip bands can be seen and two of the three slip directions can be seen to have been activated in slip plane figures 5.42 to 5.44 with an example of single slip in figures 5.34 and 5.38 and 2 slip directions highlighted in figure 5.43.

Chapter 8

Discussion on numerical simulations

The results show that the creep model has successfully been able to predict creep behaviour over the majority of the experimental conditions. To understand where the creep model performed well and areas for improvement it is best to look at the constitutive equations individually and assess their effect on the creep model predictions.

8.1 Constitutive modelling

8.1.1 Stress Partitioning

In many of the simulations of the strain-time trajectories the model over predicts the extent of the primary creep. Although in some cases the primary creep strains are not too different to the experimental data as in figure 6.18 in other cases the predictions do not capture the initial stages of creep correctly. There are a number of factors that may contribute to this discrepancy between theory and experiment and include: (i) influence of a bimodal dispersion on the stress partitioning; (ii) the influence of particle shearing on stress transfer. These will now be addressed.

The primary creep transients in the proposed constitutive description arise mainly from the stress partitioning between the γ and γ' phases. As outlined in the theoretical framework chapter, this is a consequence of assuming that under creep loading conditions most of the deformation is confined to the γ matrix with the particles behaving as though they are plastically hard. Such a configuration forms a composite system with load transfer arising as a mechanism to maintain comparability between phases.

Figure 8.1 shows the effect of stress and temperature on the misfit σ_{mis} and the kinematic back stress σ_k. Three different applied conditions are considered to demonstrate the evolution of σ_{mis} and σ_k. These are 750°C/460 MPa, 750°C/200 MPa and 700°C/500 MPa.

The model predictions show that the higher the applied stress the faster the rate of stress transfer between the γ and γ' phases (figure 8.1 the σ_k predictions corresponding to 750°C/460 MPa against 750°C/200 MPa).

Comparing the 750°C/460 MPa and 700°C/500 MPa conditions the evolution of σ_k are similar. This is a reflection of the weak temperature dependency of σ_k on the γ' volume fraction and elastic constants figure 6.1. It is the plastic strain rate that has the most significant influence on stress partitioning between phases. In contrast, the misfit stress evolution is strongly influenced by the time at temperature. This is because within the framework it was assumed that stress relaxation at the matrix/precipitate interface is governed by diffusion.

The maximum stress transfer is determined by the volume fraction through the parameter H^* (see equation (3.96)). The derivation of H^* assumes stress transfer is limited by plastic punching of spherical precipitates. Where the stress distribution is relates to the immediate area around the particle and was first derived from assuming holes instead of particles to grasp to stress field around certain shapes. This links the maximum amount of stress the matrix can load onto particles as dependent to the geometry of the particles. TEM images such as those given in figures 5.33 and 5.34 show that the precipitates are not spherical.

Cuboidal precipitates can take on more stress than the spherical precipitates, as the corresponding expression for H^* (see equation (3.97)) yields higher values. This would mean that the particles could take up more stress resulting in a lower relative stress in the matrix. With a lower relative stress there is less plasticity reducing the amount of strain whilst increasing the time in the primary regime.

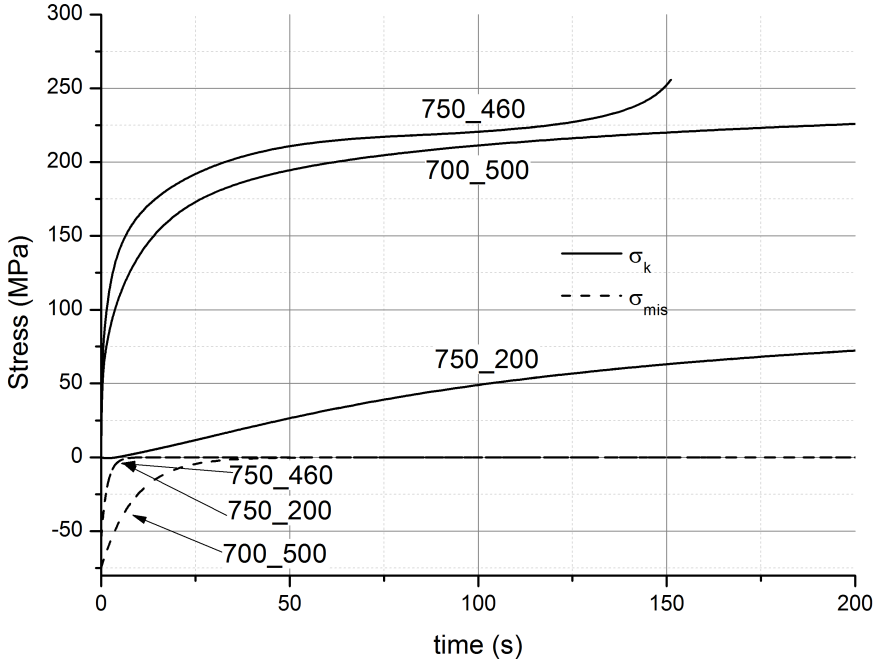


Figure 8.1: Plot showing the effect of temperature and stress on stress partition parameters σ_k and σ_{mis}

TEM analysis of crept and tensile test-pieces near the fracture surface show that the γ' particles have been heavily deformed. This is the case even for loading conditions which are well below the yield stress (see figures 5.34 and 5.38). Slip transmission of $< 110 >$ dislocations across the γ/γ' interface, will result in deformation of the precipitates, which in turn will limit the extent of stress transfer between phases. Taking the limit that the γ' particles provide no resistance to dislocations, no stress partitioning will occur.

Another possible contribution for overestimating the primary region is the simulation loading conditions. The simulation assumes instantaneous application of

the creep stress and temperature. This is not true in creep testing, since the test-piece is first brought up to temperature and then loaded until the desired stress is reached.

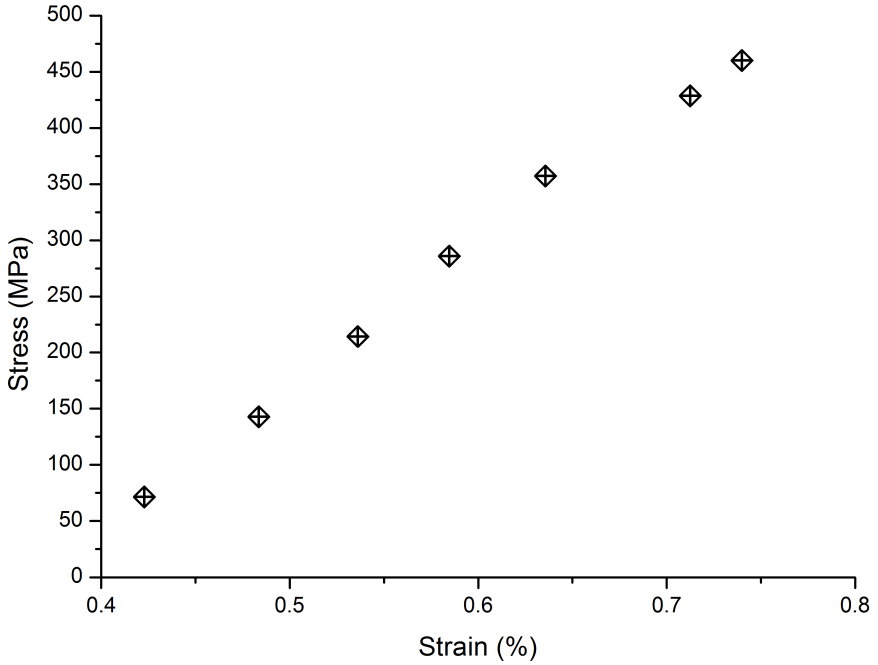


Figure 8.2: Loading of test piece for creep at 750°C/460MPa.

Figure 8.2 shows the total strain accumulation during loading for the 750°C/460 MPa test. At the required stress the extensometer is then set back to zero, but in reality the test piece has already reached a strain of 0.8%. The magnitude of the strain is very high at low stresses and indicates that a portion of the hot load measured strain is probably due to the set up of the test. Even then there is still some initial strain in loading that would have resulted in some stress transfer in the model and consequently a smaller primary then what the model is predicting.

8.1.2 Mobile dislocation density

The mobile dislocation density evolution has been treated as a continuity condition, where the density of mobile dislocation per unit time is given by the balance

between generation through the operation of Frank-Read sources and trapping of mobile segments as a result of dipole formation. The theory predicts an initially linear increase in the scalar dislocation density with strain which saturates at some steady state value, which is inversely proportional to the square root of the applied stress. The TEM images show initially no or very little dislocation activity (figure 5.33) and then after testing there are a large amount dislocations (figure 5.34). The interesting thing is that results at the condition 600°C 500 MPa show that there is not significant dislocation evolution in the primary creep region comparing figure 5.28 with figure 5.29. This shows that the density evolution is most significant in the tertiary region. This is what the dislocation constitutive equation (3.114) shows, but there is a question on the total dislocation density generated.

The dislocation multiplication parameter C defined in section 6.1 was found to have value of $\sim 10^{14} m^{-1}$ to represent the creep database. This value is a lot larger than the value found in a lot of literature [9, 40, 44, 70] and in the theoretical value based on the original assumptions made by Kocks et al [18]. The discrepency could be because the dislocation source unit cell, has the addition of being generated from precipitates. If it is assumed that each secondary precipitate acts as a source, then the source density is related to the average area of the secondary γ' if this is the case the mean value is $r_{p,2} \sim 90\ nm$ then the dislocation multiplication parameter $C = \sim \frac{1}{r_{p,2}}^2 = 10^{14}$.

8.2 Towards location specific property predictions

The microstructure throughout creep is changing and its evolution has a major contribution to tertiary creep especially at higher temperatures. Figure 6.12 shows the effect of microstructure evolution on the lifetime predictions. The influence of

tertiary γ' on creep lifetimes is significant, even though they have a much lower volume fraction compared to the secondary γ' particles (5% compared to 29%, respectively). However, there is a large number density of the tertiary particles compared to secondary, and it is this that limits the dislocation mean free path and thereby gives the alloys their good creep resistance. While the model has been shown to simulate the tertiary transient accurately for a number of conditions (such as figure 6.22), there are instances at the higher stresses the model tends to over-predicts the creep response as in figure 6.31 one likely reason for this is the model currently has not introduced cutting of the γ', this would have a large effect on the high stress predictions reducing both the primary creep strain and the lifetime predictions.

Switching off the γ' evolution resulted in unexpected shorter lifetimes at high stresses, see figure 6.12. The reason for this simulated response is that the mean field precipitation model predicts nucleation of γ' particles in addition to their coarsening. This is illustrated in figure 6.2 where the tertiary volume fraction (given by area under the graph) increases with time at 650°C.

The model predictions for temperature at and below 650°C under predict the rupture lives. The experimental data corresponds to stresses well above the yield stress and athermal plasticity will play a role. In particular, during loading the alloy will undergo plastic deformation which will alter the initial conditions for the back stress and dislocation density. Even so, if such changes are accounted for the increase in life is not significant. At these stress levels, the micromechanics are different. Dislocation interactions are expected to dominate the creep response and the mean free path will no longer be determined by the γ' dispersion but instead by some aspect of the dislocation substructure.

Rationalisation of the scatter in the creep data present in figures 6.14 to 6.16, 6.18, 6.19, 6.22, 6.23, 6.29 and 6.32 will now be addressed in terms of the proposed theory. As already stated, under loading conditions below yield, the creep response

of the material will be governed by the tertiary γ' dispersion. It has been shown in chapter 5, that the evolution of the precipitate dispersion depends on the shape of the particle size distribution. Calculations based on mean field theories have shown this to be the case such as the work of Chen and Vorhees [51], where they demonstrate how distributions having different shapes, but the same mean volumes can evolve differently. The mean field framework in this workapplies this for the same volume fraction and mean particle radius and predicts similar behaviour. Simulations were run to generate three different distributions at 700 °C shown in figures 6.25 and 6.26. The 'base' distribution is the dispersion used in the simulating all of the strain-trajectories in this work. The other two distributions were obtained from a disc and are representative of a wide and narrow distributions. All of these size distributions have similar mean values for the size and volume fraction. This was found to influence the predicted creep curves. These distributions were used in simulating the creep response at 700 °C/500MPa are shown in figures 6.18 and 6.27. The narrow distribution produces the creep curve with the longest lifetime. The broad distribution approaches the experimental data with the shortest lifetime and the base is representative of an in-between solution. The simulations represent the range of experimental curves reasonably well, and consequently, it may be inferred that such scatter in the creep response may be attributed to variations in the γ' distribution. The explanation for this phenomenon is given by the work of Chen and Vorhees [51] where they found numerically that the further a distribution is from the steady state unimodal distribution (the LSW limit) the faster it will approach this state. In the present study, it means a broad γ' size distribution will evolve the fastest which means the mean free path increases and more plasticity accumulates as a result of more slip.

These simulations are encouraging in that the proposed creep theory provides a foundation for the development of location specific property predictions. The current simulations clearly show that having mean values to represent the γ' dispersion is not enough to rationalise variations in the measured creep response. The

way the precipitate size distribution is arranged as well as the density of particles are important parameters in the accumulation of creep strain. In the manufacture of disc components, the thermomechanical history will not be uniform across the component. This will result in thermal and strain rate fields across the component during hot forming. In addition, variations in chemistry from point to point may also be present. These factors will determine the extent and rate of precipitation and result in differences in the γ' size distribution.

Simulations based on the experimental microstructure measurements, show a framework for how the model can be used to predict behaviour based on various microstructures. Even though the predictions from the experiment distriburtions on most cases were far out from the experiental data this is to be expected considering the limited information provided. TEM is neccessary to gain accurate measurements of tertiary γ', but for secondary γ' SEM would be sufficient and provide information over a larger area. There were some trends that could be seen from the predictions that generally match well with the experimental data, both MHT samples had a lower primary creep regime in the predictions just as in the experimental data.

8.3 Microscale to macroscale transition: Scale Invariance

In the development of the creep constitutive model a number of assumptions were made made to construct the macroscale creep rates. Of these the following are fundamental in derivation: (i) the form of the shear rate on activity slip systems is reflected at the macroscale; and (ii) the slip systems contribute to the macroscale creep rate. The first of these assumptions is referred to as scale invariance of the constitutive relations. To test these assumptions a crystal plasticity formulation was developed that simulated the viscoplastic behaviour of an agglomerate of

grains, from which the macroscale properties are derived from the volume average of the microscale fields. Simulations were carried out on a single crystal, a 100 and 1000 grain RVE at 700°C at an applied strain rate of $10^{-3}s^{-1}$. s.

The CP simulations show differences in the predicted flow stress response as the number of grains per volume is increased. It was found that an RVE with 1000 grains was required to generated isotropic macroscale flow stress properties. Increasing the grain size resulted in a reduced flow stress. This is associated with an increase in volume fraction of soft grains as the number density of grains is increased.

From the 1000 grain simulations, information on the slip intensity on slip systems over the entire RVE have been extracted. It was found that on a grain level, 4 to 7 slip systems dominate, while over the RVE the all slip systems contribute to the macroscale behaviour (see figures 6.40 to 6.44). This supports the application of scale invariance of the constitutive relations using a Taylor factor to scale the shear rates and shear stress to their corresponding macroscale values.

Chapter 9

Conclusion and Future work

9.1 Conclusion

- This work has outlined a general physics based creep model to predict creep behaviour in a multi-modal system, focussing on the nickel based superalloy RR1000 to compare against.

- Experimental data from the PANACEA project [1] was utilised and extra experiments were done. This was to extend the experimental range examining high temperature and low temperature creep behaviour. This data was also extended via experiments in this work which also looked at the effect of ageing on the material microstructure and creep and flow stress results. Analysis of the microstructure under TEM showed an increase in tertiary size, but an overall reduction in number density. The impact for creep resulted in a reduced primary region and a shortened lifetime at 750°C 460 MPa. The flow stress experiments show the impacting of further ageing the material, which coarsens the tertiary γ'. Larger particles are harder to cut this effect is seen when comparing MHT and SHT tests the MHT with the larger tertiaries displayed a higher yield and a greater amount of hardening. The two microstructures is strain rate sensitive.

- The effect of pre-straining to 1% strain had the effect of having a lower primary region and reduced ductility when compared to the standard test at 750°C and 460 MPa. The difference between the temperature of pre-straining gives an increased primary region for room temperature when compared to 800°C, but also a reduced strain to failure. This effect could be due to the low temperature effect on the mobility of dislocations causing high stress local regions in the room temperature pre-strain. Care must be taken with any assessment as the effects are slight and are not as great as the general scatter seen other tests at this condition.

- The TEM images enabled a measurement of the distributions for both the SHT and MHT samples. Examining test samples show that upon failure there are a large amount of dislocations. The 600°C 500 MPa sample which was still in the primary regime when the test stopped indicates that the majority of the dislocation evolution is occurring in the tertiary regime. The effect of pre-straining appears to increase the dislocation density when compared to other tests, but does not seem to greatly effect the creep response.

- The predicted primary transients tend to be over-predicted when compared to experimental data. The probable causes have been outlined from slip transfer between the γ/γ' phases and the influence of including a loading step to decrease the primary region in the model.

- The tertiary creep regime has been seen to be heavily dependent on the evolution of the dislocations and of the microstructure. Lifetime plots indicate how greatly the lifetime predictions are reduced with no tertiary γ' and how coarsening will cause the model to greatly over predict particularly at high temperatures.

- Under the same creep conditions there has been variation in the creep strength in the material which can be of an order of magnitude difference. The model

managed to successfully predict all the scatter data at 700°C 500 MPa, by keeping mean size and volume fraction the same, but changing the particle size distribution shape. This provides a foundation for location specific property predictions and it outlines that relying on mean field information is not enough to predict and capture the material behaviour.

- In developing the creep constitutive model scale invariance was used to enable macroscopic creep rate predictions. A CP formulation was developed that simulated viscoplastic behaviour; this was carried out with a single crystal, 100 grains and 1000 grain RVE at 700°C, $\dot{\varepsilon} = 10^{-3}$ s^{-1}. It was found that the greater the number of grains the greater the softening, due to the volume fraction of soft grains increasing with increasing with number of grains.

- With the 1000 grain RVE slip intensity data was extracted from 5 random grains, showing for each grain a similar number of slip systems were active (4-7), whilst over the macroscale this effect is being averaged out. This supports the scale invariance approach and the validates the use of a Taylor factor.

9.2 Future Work

9.2.1 Crystal Plasticity

Further refinement of the crystal plasticity model. It is recommended that this should focus on a better understanding of the grain-to-grain interactions associated with stress redistribution within the RVE models. It is anticipated that these stresses will impact the predicted flow stress evolution and consequently the calibrated model parameter values. From the present study, it is also recognised that better stiffness matrix values are needed to improve prediction at early stages of deformation.

9.2.2 Primary Creep

The primary creep regime in the model is consistently over-predicted. A potential reason for this may be due to the details on how dislocation segments percolate through a field of hard precipitates. If these process is difficult then a transient will existing before reaching a steady state dislocation flux. This is described in section 3.3 equation (3.71). Here it assumed that the term

$$\left[1 - \exp\left(-\frac{\bar{v}_g}{\lambda_p}t\right)\right]$$

can be ignored due to $\frac{\bar{v}_g}{\lambda_p}$ being considered large. However, this term may persists over a significant time and lead to impedance to the initial creep rate. It is proposed that in cases where there is a low creep rate the following term be included in the creep rate equation.

$$\left[1 - \exp\left(-\rho_I\frac{\bar{v}_g}{\lambda_p}t\right)\right]$$

where ρ_I is the impedance factor which should evolve in time before reaching a maximum value of 1.

9.2.3 Cutting γ'

Cutting of γ' occurs when for a given particle size a critical stress is reached. It is argued in [82] that the cutting reduces the amount of stress partitioning in the material as well as increasing the mean free path travelled by the dislocations. The effect would reduce the creep lifetime, lower the primary creep region and reduce the amount of hardening in a tensile situation (as in CP). Whilst its importance has been stressed throughout this work there is difficulty in implementing it. Based on the theory proposed in [82], cutting of the γ' particle may be treated as follows: in visualising cutting of the γ' the 3 dimensional particle is first cut into 2 dimensional planes.

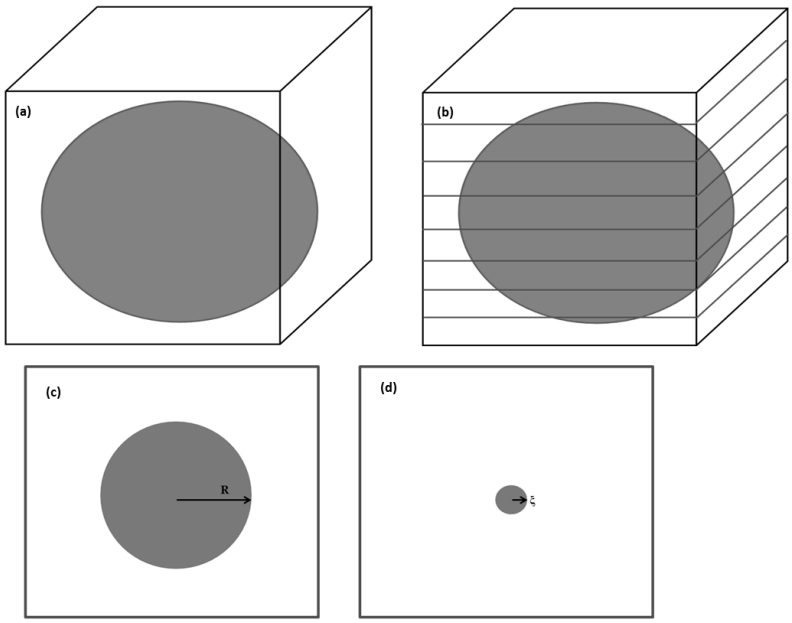


Figure 9.1: Sphere being cut into planes (a) shows the sphere (b) the appearance of planes on the 3d structure. (c) and (d) show depending where the plane is that the size of the visible particle can change

With a single particle it can be cut into many planes of thickness dh such that a distribution of particle sizes can be obtained: $\xi_1 < \xi_2 < \xi_3 < \ldots < \xi_m$ where $\xi_m = R$. With a new distribution of particle sizes a mean size can be obtained:

$$\bar{\xi} = \sum_{k=1}^{m} \xi_k \frac{n_k}{N} \tag{9.1}$$

where $N = n_1 + n_2 + \ldots n_m$ is the total number of particles. From geometry of a single particle it is known that $\frac{n_k}{N} = \frac{dh}{R}$. Substituting this into (equation (9.1)) and having the limit $dh \to 0$ on the sum the particle size becomes:

$$\bar{\xi} = \int_0^R \frac{\xi^2}{R\sqrt{1 - \left(\frac{\xi}{R}\right)^2}} \tag{9.2}$$

Probability density function on a plane is found to be:

$$f_{plane}\left(\xi, R\right) = \frac{\xi}{R\sqrt{1 - \left(\frac{\xi}{R}\right)^2}} \tag{9.3}$$

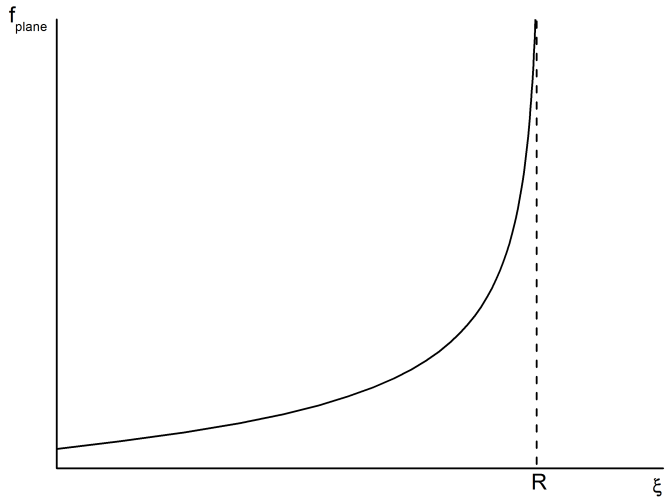


Figure 9.2: Logarithmic CDF of the sizes gathered through the 2D planes for a 3D spherical particle

Calculating the cutting radius

$$r_c = r_c\left(\sigma_c, R\right)$$

There are many cutting equations which can be used and rearranged to determine the cutting radius e.g.

$$r_c = \left(\frac{\sigma_{eff} b}{\bar{M}\gamma^{\frac{3}{2}}}\right)^2 \frac{\pi T \eta}{4\phi_p} \tag{9.4}$$

where

$$\eta = 1 - \frac{4\phi_p}{\pi}\left(\sqrt{\frac{\pi}{\phi_p}} - 1\right)$$

Calculating the effective area fraction left after cutting:

$$\begin{aligned} \phi_a\left(r_c, R\right) = \frac{\int_{rc}^{R} \xi^2 f_{plane}\left(\xi, R\right) d\xi}{\int_0^R \xi^2 f_{plane}\left(\xi, R\right) d\xi} &= \frac{\sqrt{\left(R - r_c\right)\left(R + r_c\right)}\left(2R^2 + r_c^2\right)}{2R^3} \\ &= \frac{\sqrt{\left(1 - \frac{r_c}{R}\right)\left(1 + \frac{r_c}{R}\right)}\, 2 + \left(\frac{r_c}{R}\right)^2}{2R} \end{aligned} \tag{9.5}$$

The fraction of particles cut is $1 - \phi_a\left(r_c, R\right)$

The work from the above section which was for a single particle and can be applied for a distribution of particles.

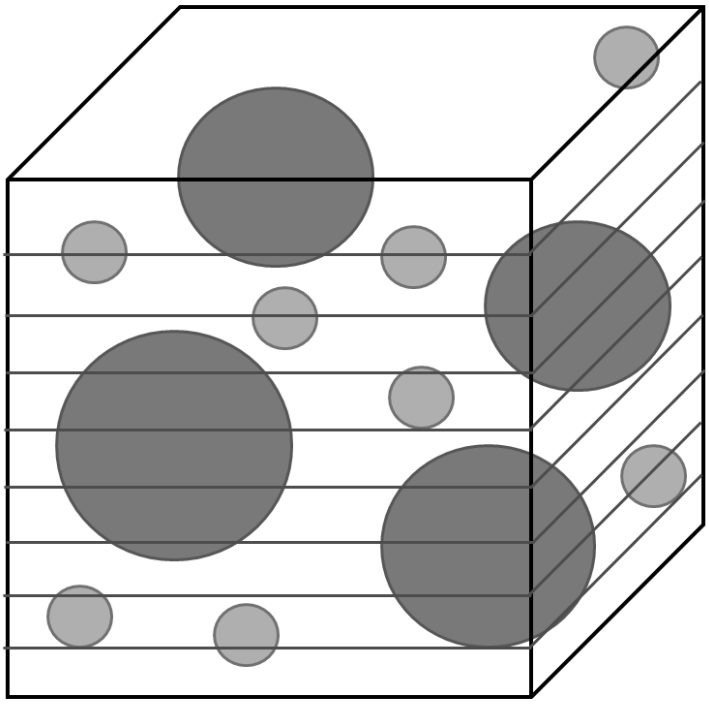


Figure 9.3: Situation for a bimodal distribution

This can create its own size distribution $F(r)$

All populations can be counted in a number per unit volume N_v

$$N_v = \int_0^\infty F\left(r,t\right) dr \tag{9.6}$$

$$dN_v(r) = F\left(r,t\right) dr \tag{9.7}$$

Therefore the number of particles remaining is:

$$dN_v = F_{plane}\left(r,t\right) dr \tag{9.8}$$

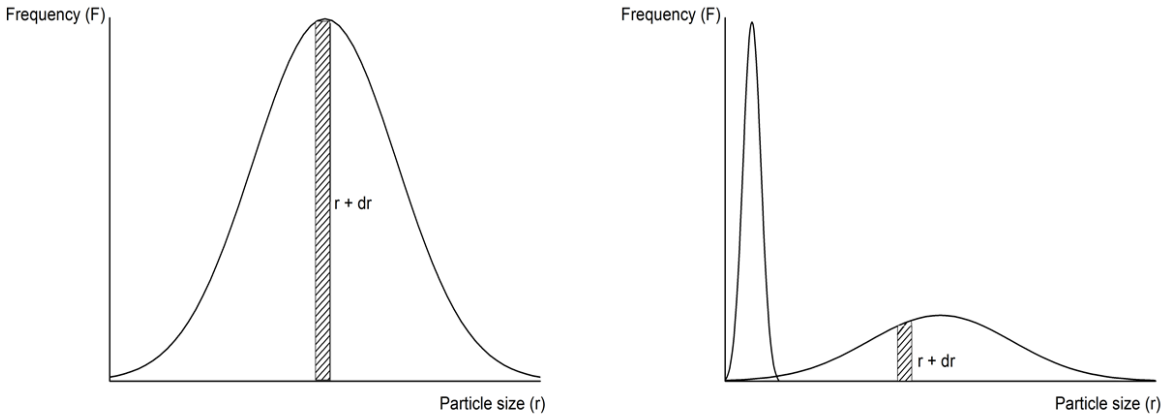


Figure 9.4: When there is a size distribution of particles both unimodal and bi-modal

where

$$F_{plane}\left(r,t\right)=\phi_{a}\left(r_{c},r\right)\ F\left(r,t\right) \tag{9.9}$$

resulting change in volume fraction and mean particle radius being:

$$\phi_{v}=4\pi\int_{0}^{\infty}r^{3}F_{plane}\left(r,t\right)dr \tag{9.10}$$

$$r_{p}=\int_{0}^{\infty}rF_{plane}\left(r,t\right)dr \tag{9.11}$$

This will be applied in the case of a multi-modal situation to each individual volume fraction to determine which are cut, by the proportion of the mean size of each population and how it compares to the cut radius.

Whilst displaying the theoretical basis for implementing cutting of the γ' the difficulty is with coding this work in an efficient way. Combining this cutting

formulation with the mean field predictions requires interaction: opening, loading and interpolating of large amounts of data, that have currently been too time costly to produce results in this work.

Chapter 10

Bibliography

Bibliography

[1] M. C. Hardy, R. M. Mitchell, H. Y. Li, J. P. Jones, and H. Kitaguchi. Charcterising the effect of thermal exposure on the microstructure and mechanical properties of coarse grain rr1000. PANACEA Milestone M5 DHC326411, Rolls-Royce, 2009.

[2] R. J. Mitchell, J. A. Lempsky, R. Ramanathan, H. Y. Li, K. M. Perkins, and L. D. Connor. Process development and microstructure and mechanical property evaluation of a dual microstructure heat treated advanced nickel disc alloy. In *Superalloys 2008*, pages 347–356, 2008.

[3] A. Graham and K. F. A. Walles. Relationships between long- and short-time creep and tensile properties of a commercial alloy. *J. Iron Steel Inst.*, 179:105–120, 1955.

[4] G. F. Harrison. Structural Materials Centre, DERA, Farnborough Hants,, 1982. private communication.

[5] R. W. Evans and B. Wilshire. Creep behaviour of superalloy blade materials. *Material Science and Technology*, 3:701–705, 1987.

[6] J. C. Ion, A. Barbosa, M. F. Ashby, B. F. Dyson, and M. McLean. Report dma (a115). Technical report, NPL, 1986.

[7] M. F. Ashby and B. F. Dyson. *Creep Damage Mechanics and Micromechanisms, in Advance in Fracture Research in Advances in Fracture Research.* Pergamon press, 1 edition, 1984.

[8] B. F. Dyson. Use of cdm in marterials modelling and component creep life prediction. *Journal of Pressure Vessel Technology*, 122:281–296, 2000.

[9] B.F. Dyson. Microstructure based creep constittutive model for precipitation strengthened alloys: Theory and application. *Material Science and Technology*, 25(2):213–220, 2009.

[10] M. J. Donachie and S. J. Donachie. *Superalloys a technical guide*. The Materials Information Society. ASM international, 2002.

[11] N. S. Stoloff. Fundamentals of strengthening. In C. T. Sims, N. S. Stoloff, and W. C. Hagel, editors, *Superalloys II*, pages 61–96. John Wiley and Sons, 1987.

[12] A. M. Goodman. In J. Bressers, editor, *Creep and Fatigue in High Temperature Alloys*. London Applied Science, 1981.

[13] F. R. N. Nabarro and H. L. Villiers. *The physics of creep*. Taylor and Francis Ltd, 1995.

[14] M. Whittaker, W. Harrison, C. Deen, C. Rae, and S. Williams. Creep deformation by dislocation movement in waspaloy. *Materials*, 10(61), 1982.

[15] Oleg D. Sherby and Peter M. Burke. Mechanical behavior of crystalline solids at elevated temperature. *Progress in Materials Science*, 13:323 – 390, 1968.

[16] J. Weertman. Theory of steady-state creep based on dislocation climb. *Journal of Applied Physics*, 26(10), 1955.

[17] J.E. Dorn. Some fundamental experiments on high temperature creep. *Journal of the Mechanics and Physics of Solids*, 3(2):85 – 116, 1955.

[18] U. F. Kocks, A. S. Argon, and M. F. Ashby. Thermodynamics and kinetics of slip. *Prog. Mater. Sci.*, 19, 1975.

[19] U.F Kocks and R.O Scattergood. Elastic interactions between dislocations in a finite body. *Acta Metallurgica*, 17(9):1161 – 1168, 1969.

[20] H. Mecking and U.F. Kocks. Kinetics of flow and strain-hardening. *Acta Metallurgica*, 29(11):1865 – 1875, 1981.

[21] J. Weertman. Strady-state creep through dislocation climb. *Journal of Applied Physics*, 28(3), 1957.

[22] A. J. Ardell and O. D. Sherby. Strady-state creep of polycristaline alpha zirconium at elevated temperatures. *Transactions of the Metallurgical Society of AIM*, 239(10):1547, 1967.

[23] J. J. Gilman. Plastic anisotropy of zinc monocrystals. *Tranactions of the American Institute of Mining and Metallurgical Engineers*, 206:1326–1336, 1956.

[24] J. Weertman and P. Shahinian. Creep of polycrystalline nickel. *Transactions of the American Institute of Mining and Metallurgical Engineers*, 206(10), 1956.

[25] J. Weertman. Theory of influence of stacking-fault width of split dislocations on high temperature creep rate. *Transactions of the American Institute of Mining and Metallurgical Engineers*, 233(12):2069, 1965.

[26] G. S. Ansell and J. Weertman. Creep of a dispersion hardened aluminum alloy. *Transactions of the American Institute of Mining and Metallurgical Engineers*, 215(5):838–843, 1959.

[27] D. McLean. Fundsamentals of creep and creep-rupture in metals. *Journal of teh Institute of Metals*, 93:1099, 1965.

[28] N. J. Grant. *The Strengthening of Metals.* Reinhold, 5 edition, 1964.

[29] Brown A. M. and M. F. Ashby. On the power-law creep equation. *Scripta Metallurgica*, 14:1297–1302, 1980.

[30] F. S. Furillo, S. Purushothaman, and J. K. Tien. Understanding the larson-miller parameter. *Scripta Metallurgica*, 11:493–496, 1977.

[31] L. M. Kachanov. On creep rupture time. *Izv. Ak. Nauk. SSSR Otdel. Tekh. Nauk*, 8:26–31, 1958.

[32] S. G. R. Brown, R. W. Evans, and B. Wilshire. Alternative methods of parameter estimation in exponential descriptions of normal creep curves. *Scripta Metallurgica*, 21:239–242, 1987.

[33] P. W. Davies, R. W. Evans, K. R. Williams, and B. Wilshire. An equation to represent strain/time relationships during high temperature creep. *Scripta Metallurgica*, 3:671–674, 1969.

[34] *ASM Pressure Vessel Piping Conf*, volume 288, 1994.

[35] Jong-Taek Yeom, Jong-Yup Kim, Young-Sang Na, and Nho-Kwang Park. Creep strain and creep-life prediction for alloy 718 using the omega method. *Metals and Materials International*, 9(6):555–560, 2003.

[36] M. McLean and B. F. Dyson. Modelling the effects of damage and microstructure evolution on the creep behaviour of engineering alloys. *Journal of Engineering Materials and Technology*, 122:273–278, 2000.

[37] G. I. Taylor. Plastic strain in metals. *Journal of the institute of metals*, 62:307–324, 1938.

[38] J. Heslop and W. Betteridge. *The nimonic alloys*. Edward Arnold, London, 2 edition, 1974.

[39] T. B. Gibbons and B. E. Hopkins. The creep behaviour and structure of ni-cr base alloys. Report DMA 253, NPL, 1976.

[40] H. C. Basoalto, S. K. Sondhi, B. F. Dyson, and M. McLean. A generic microstructure-explicit model of creep in nickel-based superalloys. In T. M. et al Pollock, editor, *Superalloys 2004*, page 897. TMS, 2004.

[41] T.M. Pollock and A. S. Argon. Creep resistance of cmsx-3 nickel-based superalloy single crystal. *Acta metall. mater*, 40(1):1–20, 1992.

[42] M. Palumbo, D. Baldissin, L. Battezzati, O. Tassa, R. Wunderlich, H.-J Fecht, R Brooks, and K Mills. Thermodynamic properties of cmsx-4 superalloy: Results from the thermolab project. *Materials Science Forum*, 508:591, 01 2006.

[43] H. C. Basoalto, J. W. Brooks, and I. Di Martino. Multiscale microstructure modelling for nickel based superalloys. *Materials Science and Technology*, 25(2):221–227, 2009.

[44] J. Coakley, D. Dye, and H. C. Basoalto. Creep and creep modelling of a multimodal nickel-based superalloy. *Acta Materialia*, 59:854–863, 2011.

[45] L. Brownl and R. Ham. Dislocation-particle interactions. In A. Kelly and Nicholson R., editors, *Strengthening Methods in Crystals*, London, 1971. Applied Science Publishers.

[46] I. M. Lifshitz and V. V. Slyozov. The kinetics of precipitation from supersaturated solid solutions. *Journal of Physics and Chemistry of Solids*, 19(1-2):35–50, 1961.

[47] C. Z. Wagner. Theorie de alterung von niederschlagen durch umlosen. *Zeitschrift Fur Elektrochemie*, 65:581–591, 1961.

[48] P. W. Voorhees. Ostwald ripening of 2-phase mixtures. *Annu. Rev. Mater. Sci*, 22:197–215, 1992.

[49] A. Baldan. Review progress in ostwald ripening theories and their applications to nickel-base superalloys part 1: Ostwald ripening theories. *Kluer Academic Publishers*, pages 2171–2202, 2001.

[50] I. M. Lifshitz and V. V. Slyozov. *Idem. Sov. Phys: Solid State*, 1, 1960.

[51] C. K. Chen and P. W. Voorhees. The dynamics of transient ostwald ripening. *Modelling and Simulation in Material Science and Engineering*, 1(5):591–612, 1993.

[52] J. A. Marqusee and J. Ross. Theory of ostwald ripeening - competitive growth and its dependence on volume fraction. *Journal of Chemical Physics*, 80(1):536–543, 1984.

[53] A. H. E. Love. *A treatise on the Mathematical theory of elasticty.* University Press, Cambridge, 4 (1952) edition, 1926.

[54] I. Kovacs and L. Zsoldos. *Dislocations and plastic deformation.* Pergamon press, 1 edition, 1973.

[55] G. I. Taylor. The mechanism of plastic deformation of crystals. part i.—theoretical. *Proceedings of the Royal Society of London. Series A, Containing Papers of a Mathematical and Physical Character*, 145(855):362–387, 1934.

[56] H. Mughrabi. Dislocation wall and cell structures and long-range internal stresses in deformed metal crystals. *Acta Metallurgica*, 31(9):1367 – 1379, 1983.

[57] H. Wilsdorf and D. Kuhlmann-Wilsdorf. Direct evidence for dislocations in aluminium copper alloys. *Philosophical magazine.*, 45(369), 1954.

[58] C. W. Dash. Copper precipitation on dislocations in silicon. *Journal of Applied Physics*, 27(10):1193–1195, 1956.

[59] B. Jaoul. *Bull. Soc. Fr. Mecan*, 2(5):69, 1952.

[60] D. Hull and D. J. Bacon. *Introduction to dislocations.* Butterworth-Heienmann, Oxford, 5 edition, 1965.

[61] F. R. N. Nabarro. *Theory of crystal dislocations.* Oxford: Clarendon Press, 1967.

[62] J. R. Rice. Inelastic constitutive relations for solids: An internal-variable theory and its application to metal plasticity. 19(6):433–455, 1971.

[63] F. Dunne and N. Petrinic. *Introduction to Computational Plasticity.* Oxford University Press, Oxford, 5 edition, 2005.

[64] K. S. Havner. *Finite Plastic Deformation of Crystalline Solids.* Cambridge University press, 1 edition, 1992.

[65] J. F. W. Bishop and R. Hill. A theoretical derivation of the plastic properties of a polycrystalline face-centered metal. *The London, Edinburgh, and Dublin Philosophical Magazine and Journal of Science*, 42(334):1298–1307, 1951.

[66] J. Friedel. *Dislocations.* Pergamin Press, 1 edition, 1964.

[67] M. F. Ashby and L. Johnson. On the generation of dislocations at misfitting particles in a ductile matrix. *The Philosophical Magazine: A Journal of Theoretical Experimental and Applied Physics*, 20(167):1009–1022, 1969.

[68] H. C. Basoalto, B. F. Dyson, and M. McLean. A quantitative physics-based approach to creep and lcf life prediction: Application to nickel-base superalloys. In Fuchs et al, editor, *Advance Materials and Processes for Gas Turbines*, page 53. TMS, 2003.

[69] James Coakley, Hector Basoalto, and David Dye. Coarsening of a multimodal nickel-base superalloy. *Acta Materialia*, 58(11):4019–4028, 2010.

[70] M. R. Ahmadi, E. Povoden-Karadeniz, K. I. ksz, A. Falahati, and E. Kozeschnik. Role of athermal yield mechanisms on the creep behaviour of nickel-based superalloys. 2008.

[71] *Aerospace series. Test methods for metallic materials. Uninterrupted creep and stress-rupture testing.* BSI, 2009.

[72] *Standard Test Methods for Elevated Temperature Tension Tests of Metallic Masterails*, West Conshohocken, PA, 2009. ASTM international.

[73] *Standard Test Methods for Conducting Creep, Creep-Rupture, and Stress-Rupture Tests of Metallic Materials*, West Conshohocken, PA, 2018. ASTM international.

[74] E. J. Payton, P. J. Phillips, and M. J. Mills. Semi-automated characterization of the phase in ni-based superalloys via high-resolution backscatter imaging. *Materials Science and Engineering: A*, 527(10-11):2684–2692, 2010.

[75] G. B. Olson and J. H. Jou. Precipitation model validation in 3rd generation aeroturbine disc alloys. In *Superalloys 2008*. TMS, 2008.

[76] H. J. Frost and M. F. Ashby. *Deformation-mechanism maps*. Pergamon press, 1 edition, 1982.

[77] H. C. Basoalto, M. G. Ardakani, B. A. Shollock, and M. McLean. Variable and multiaxial loading. In *Proceedings of the. 9th International Conference on Creep and Fracture Engineering Materials and Structures,*, Swansea, 2001.

[78] D. Dye, J. Coakley, V. A. Vorontsov, H. J. Stone, and R. B. Rogge. Elastic modulii and load partitioning in a single-crystal nickel superalloy. *Scripta Materialia*, 61:109–112, 2009.

[79] H. Mughrabi. A two-parameter description of heterogeneous dislocation distributions in deformed metal crystals. *Materials Science and Engineering*, 85:15 – 31, 1987.

[80] L. Agudo Jcome, P. Nrtershuser, C. Somsen, A. Dlouh, and G. Eggeler. On the nature of phase cutting and its effect on high temperature and low stress creep anisotropy of ni-base single crystal superalloys. *Acta Materialia*, 69(0):246 – 264, 2014.

[81] B. F. Dyson and M. McLean. Particle coarsening, and tertiary creep. *Acta Materialia*, 31:17–27, 1982.

[82] Basoalto H.C. Yearwood, G. Effect of dislocation shearing og γ' on creep of nickel-based superalloys. 2019.